Diagnosis of the atmospheric hydrological cycle and its variability in the present-day climate

A thesis submitted to the School of Environmental Science
of the University of East Anglia in partial fulfilment
of the requirements for the degree of Doctor of Philosophy

Guangzhi XU

May 2016

Abstract

This thesis investigates some important aspects of the atmospheric branch of the hydrological cycle in the modern day climate from an observational perspective. Data quality is evaluated, focusing on two state-of-the-art reanalysis products, ERA-I and JRA-55. Regional-scale discrepancies among reanalyses and observations, especially in their annual cycles, are found in the warm pool, Amazon, Gulf stream and Indian subcontinent regions. In the tropics, oceanic evaporation and its temporal variability are notably greater in JRA-55 than in ERA-I and satellite-based estimates, while both reanalyses overestimate precipitation. Higher tropical precipitation and evaporation, accompanied by a slightly lower level of total column water (TCW), might suggest a more intense hydrological cycle, but this can be an ill-defined concept especially when analysis increments mask "spin-down" errors in reanalysis models. Analysis increments arise to remove unphysical residuals in the atmospheric water budget, and these are explored via a cluster analysis to identify regimes with common behavior. Consistent for ERA-I and JRA-55, the regime with the largest negative residuals (greater moisture outputs than inputs) exceeding 50 % of mean precipitation occurs during the dry season of some low latitude regions that feature strong seasonality, high evapotranspiration and high moisture divergence. Errors in the moisture divergence are likely responsible because they correlate strongly with the budget residual.

Empirical Orthogonal Function (EOF) and Self Organizing Map (SOM) analyses are applied to identify the dominant inter-annual patterns of vertically-integrated moisture divergence variability. They reveal that the transition from strong La Niña through to extreme El Niño events is not a linear one and that the EOF orthogonality constraint results in the patterns being split between leading EOFs that are non-linearly related. The SOM analysis captures the range of responses to the El Niño-Southern Oscillation (ENSO), indicating that the distinction between the moderate and extreme El Niños can be as great as the difference between La Niña and moderate El Niños, from a moisture divergence point of view.

On diurnal time scales, horizontal moisture fluxes vary in response to thermodynamic and dynamic effects. TCW shows a global scale diurnal cycle that peaks around $\sim$ 1800 $-$ 2100 local time with a peak-to-trough magnitude of $\sim 0.4\,mm$. Semi-diurnal variations in surface winds and pressure,

consistent with atmospheric tidal theory, create a westward propagating moisture convergence/divergence wave along the equator.

Finally, the importance of Tropical Cyclones (TCs) as a source of freshwater for the North American continent is estimated using an ensemble of schemes designed to attribute onshore moisture fluxes to TCs. Averaged over the 2004–2012 hurricane seasons and integrated over the western, southern and eastern coasts of North America, the seven schemes attribute 7 to 18 % (mean 14 %) of total net onshore flux to Atlantic TCs. A reduced contribution of 10 % (range 9 to 11 %) was found for the 1980–2003 period, though only two schemes could be applied to this earlier period. Over the whole 1980–2012 period, a further 8 % (range 6 to 9 % from two schemes) was attributed to East Pacific TCs, resulting in a total TC contribution of 19 % (range 17 to 22 %) to the ocean-to-land moisture transport onto the North American continent between May and November. The inter-annual variability does not appear to be strongly related to ENSO.

Acronyms

E/ET	Evaporation/Evapo-Transpiration
ENSO	El Niño-Southern Oscillations
EOF	Empirical Orthogonal Functions
ERA-I	European Centre for Medium Range Weather Forecast (ECMWF) ERA-Interim reanalysis
ITCZ	Intertropical Convergence Zone
JRA-55	Japanese 55-year Reanalysis
MJO	Madden-Julian Oscillation
OLR	Outgoing Longwave Radiation
PC	Principle Component
QBO	Quasi-Biennial Oscillation
SOM	Self-Organizing Maps
SST	Sea Surface Temperature
SPCZ	South Pacific Convergence Zone
TC	Tropical Cyclones
TCW	Total Column Water

Acknowledgements

Firstly I owe a great deal of gratitude to all members in my supervisory team at the University of East Anglia: Prof. Tim Osborn, Prof. Adrian Matthews and Dr. Manoj Joshi, for all their invaluable support, help and guidances throughout the process of my Ph.D. Special thanks to Prof. Tim Osborn, for his patience and understanding in supporting and encouraging me on various occasions, and numerous hours he spent on answering my odd questions and discussing with me on subjects relevant and irrelevant to the project. Many thanks to Prof. Adrian Matthews for guiding me through the computing and data analysis training and providing valuable comments at some critical moments in my research. Dr. Manoj Joshi has also been of great help in giving me deeper insights into the subject, and a considerable part of the thesis was inspired by his suggestions. Finally I'd like to thank all of them for being co-authors and contributing to the two manuscripts that I submitted. Also many thanks go to members in the Climatic Research Unit especially Mike Salmon who has saved me out of tricky computing situations on many occasions. My sincere thanks also go to Prof. Philip Jones and Prof. Richard Allan for providing valuable comments on the thesis.

Farther afield, I would like to thank Lisha Li for suggesting and guiding me into UEA, and for her generous care when I broke my hand. Her enthusiastic, considerate and inspirational character has been one of the most influential figures in my life. I wish a healthy and wealthy life for her and her new-born baby.

Thanks to the selection panel of the Derek Bryan and Liao Hongying memorial scholarship for awarding me this scholarship and alleviating my financial pressure.

Finally, I cannot thank my family enough for being supportive, understanding and patient. A special thank to Can Huang for the lovely food and loads of laughter in my difficult times.

The research in this thesis was carried out on the High Performance Computing Cluster supported by the Research and Specialist Computing Support service at the University of East Anglia.

Contents

List of figures

List of tables

Chapter 1

Introduction

1.1 Introduction

Water, in all its physical forms, plays a crucial role in modulating our climate in various ways across multiple time scales. Although it only contains a small proportion of water, the atmosphere is by far the most dynamic and far-reaching hydrological branch, bridging the oceanic net source and the terrestrial net sink of moisture. Short-term variability in precipitation, evaporation, atmospheric total column water vapour and moisture transport shape the atmospheric hydrological cycle of the modern day climate, and their long-term variations are intimately linked with the global energy budget (*Allan*, 2012; *Held and Soden*, 2006; *Allen and Ingram*, 2002) and climate change scenarios (*Allan et al.*, 2014). Theoretically, observations of all these components should lead to a closed water budget in the atmosphere, on the surface, or between ocean and land, at either global or regional scales. However, the current observation systems are found to give unsatisfactory estimates and the distribution of error/uncertainty is uneven over time, among different variables, and across different regions around the globe.

Precipitation is a crucial source of freshwater to land and on average around $114\,Eg$ ($1\,Eg = 10^{18}g$) of water is precipitated over global land every year (*Trenberth et al.*, 2011). The spatial distribution of this quantity, and perhaps more importantly its temporal variability, have a profound impact on humanity, society, agriculture and all other life forms on or beyond land. Its predicted change under global warming has attracted much attention from both within and outside the scientific community, and a broad consensus has been reached

regarding first order global precipitation changes, such as the "wet getting wetter and dry getting drier" response (*Kirtman et al.*, 2013), and the moistening of the mid-latitudes (*Hartmann et al.*, 2013). However, even state-of-art climate models are still much less consistent in predicting precipitation changes than temperature. Insufficient observations, understanding and models of dynamic processes hamper our ability to confidently predict future changes (*Shepherd*, 2014; *Flato et al.*, 2013; *Demory et al.*, 2014). First and foremost, monitoring of precipitation is unsatisfactory. Currently there are still large areas over ocean and land where precipitation is most intense but direct observation is sparse. This deficiency affects not only in situ observations, but subsequently leads to greater uncertainties in remote sensing and model (including reanalysis) precipitation estimates.

Water in its gas form, a quantity often measured as specific humidity, is an important factor in the formation of clouds and precipitation, the redistribution of water and energy, the modulations of the atmospheric radiative forcing, and numerous air-borne chemical reactions. As the largest greenhouse gas, water vapour both contributes positively to radiative forcing and responds positively to a warming surface, making it a critical chain linking the energy and water cycles. Although vapour accounts for only about 0.25 % of the mass of the atmosphere (*Gimeno et al.*, 2012), around 40 Eg of water is transported in vapour form from ocean to land every year, replenishing terrestrial hydrology (*Trenberth et al.*, 2007, 2011). As the growing human population is becoming increasingly reliant on freshwater security, and is faced with future changes to the hydrological regimes that we have already adapted to, understanding this transport process is of great importance.

Solid-form water that covers the sea or land surfaces exerts a strong control on the surface albedo. Polar amplification and to a lesser extent, altitude amplification effects (*Serreze and Barry*, 2011; *Pepin and Lundquist*, 2008) are closely related to the albedo feedbacks due to seasonal snow and ice retreat. Cryosphere dynamics impact global sea level, ocean circulation, marine ecosystems and ocean productivity (*Vaughan et al.*, 2013), and better representation of this component is being incorporated into Earth System Models (ESMs) (*Flato et al.*, 2013).

Lastly, phase transitions, e.g. evaporation and condensation, bridge the energy and water cycles (*Liu et al.*, 2015). Globally, recycling of continental evaporation/evapotranspiration (E/ET) is responsible for 67 % of rainfall over land (*van der Ent et al.*, 2010) and over 50 % of the solar energy absorbed by

land is converted to latent heat through ET (*Jung et al.*, 2010; *Hartmann et al.*, 2013), thus making it an important modulator of the soil moisture, surface temperature and precipitation (*Wang and Dickinson*, 2012; *Jung et al.*, 2010; *Koster et al.*, 2004). However, benchmark large-scale ET observations are still lacking, and large uncertainties are found among available datasets.

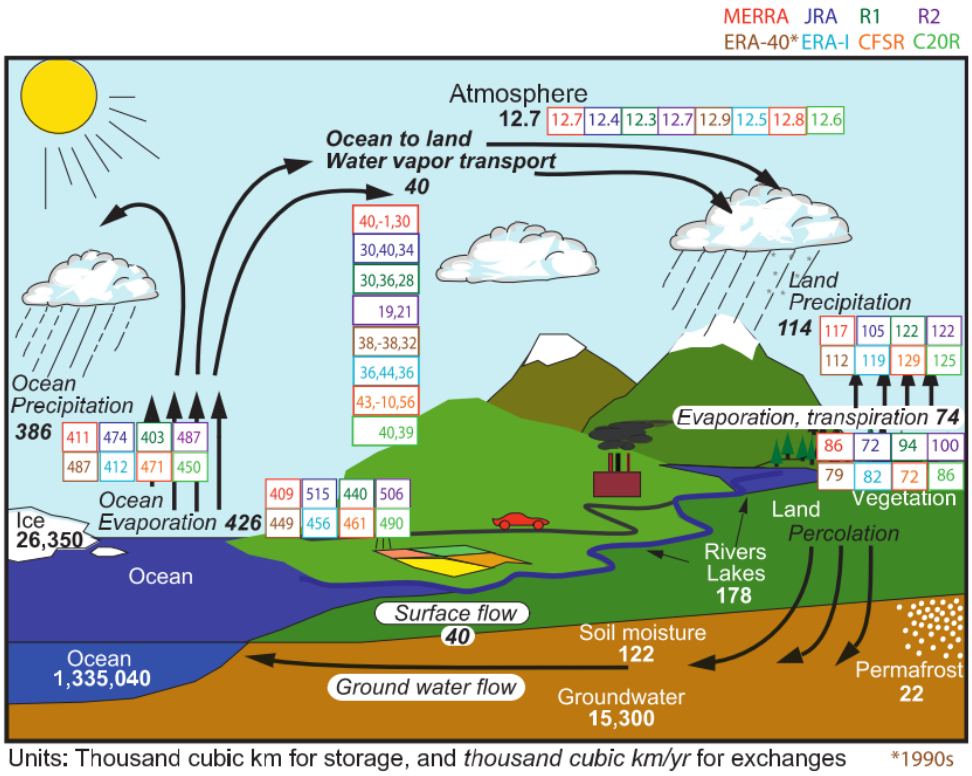

Figure 1.1: Global observed hydrological cycle. The background figure shows the estimates of the observed hydrological cycle adjusted from (*Trenberth et al.*, 2007) to apply to 2002-08 (1000 km^3 for storage and 1000 $km^3\,yr^{-1}$ for exchanges). Superposed are values from the eight reanalyses for 2002-2008 (colour coded as given at the top-right of the panel). The exception is for ERA-40, which is for the 1990s. For the water vapour transport from ocean to land, the three estimates given for each are (i) the actual transport estimated from the moisture budget (based on analyzed winds and moisture). (ii) the E-P from the ocean, and (iii) P - E from the land, which should be identical. Figure adopted from *Trenberth et al.* (2011).

Putting all components together, *Gimeno et al.* (2012) states: "The hydrological cycle may be summarized as the evaporation of moisture at one location and precipitation elsewhere, balanced by the atmospheric, oceanic, and hydrological transport of water." Fig. 1.1 (*Trenberth et al.*, 2011) gives a schematic illustration of this picture, with variables quantified from best observations available at the time, but with various degrees of uncertainties among them. On average, 426 *Eg* of water vapour is evaporated from the ocean surface in a year, of which 386 *Eg*

(90 %) returns to the ocean as oceanic precipitation, and the remaining 40 Eg (10 %) gets transported onto land. To close the budget in the long run, an equal amount of water should return from land to ocean in the form of surface flow and ground water flow. In addition to this ocean-land water balance, closure in atmospheric water budget should be observed in an air column of arbitrary shape and size, from the scale of a grid cell, to a watershed, or up to a continent, all governed by the following equation:

$$\frac{dS}{dt} = E - P - \bigtriangledown \cdot \mathbf{Q} - R \tag{1.1}$$

which expresses the storage change over time ($\frac{dS}{dt}$) as the combined effect of evaporation input (E), precipitation (P) and divergence ($\bigtriangledown \cdot \mathbf{Q}$) outputs, and a non-physical term (R) that accounts for residuals/errors. For a closed budget, $R = 0$. Taking the global land as a whole and omitting storage changes and residuals in the long-term mean, about 114 Eg of water precipitates over land every year, of which 74 Eg (65 %) is contributed by terrestrial evaporation-transpiration, and the remaining 40 Eg (35 %) is transported from ocean and converges over land (Fig. 1.1).

The above gives only a crude depiction of the global hydrological cycle, but even with our modern day technology and knowledge, quantification of the mean annual global cycle is still an ongoing challenge, let along its variability over different spatio-temporal scales. Taking the ocean-to-land moisture transport as an example, consistency is expected among these three quantities: the integrated divergence over ocean ($\bigtriangledown \cdot \mathbf{Q}$), the moisture surplus from excessive oceanic E over P ($E - P$ over ocean), and the moisture deficit from excessive terrestrial P over E ($P - E$ over land). However, as shown in Fig. 1.1, these are poorly balanced in some of the state-of-art reanalysis products. Disagreements in other variables are also present, particularly precipitation and evaporation, where the spread among reanalyses is about 20 % and 30 %, respectively. At a regional scale, datasets exhibit different biases over different time scales.

Water and energy are redistributed at a global scale by the atmospheric circulation. Fig. 1.2 shows the seasonal mean December-January-February (DJF) and June-July-August (JJA) moisture transports, computed by vertically integrating layered moisture fluxes from the NCEP/NCAR reanalysis (*Trenberth and Guillemot*, 1998). The plot summarizes the major characteristics of the global moisture flows: it is dominated by the zonal component, with easterlies in the

tropics and westerlies in mid-latitudes, and subtropical highs in-between; strong seasonality over storm track and monsoon regions; and stronger oceanic fluxes than those over land. On top of these, moisture fluxes vary substantially at different time scales with different vertical distributions as well, and it is this circulation element that poses the biggest challenge in our prediction of future hydrological cycle change (*Shepherd*, 2014; *Flato et al.*, 2013; *Demory et al.*, 2014). This thesis will revisit this global pattern and investigate some important aspects related to inter-annual variability, the diurnal cycle and tropical cyclones (TCs). The following section lists the main aims and topics of the thesis and introduces its structure.

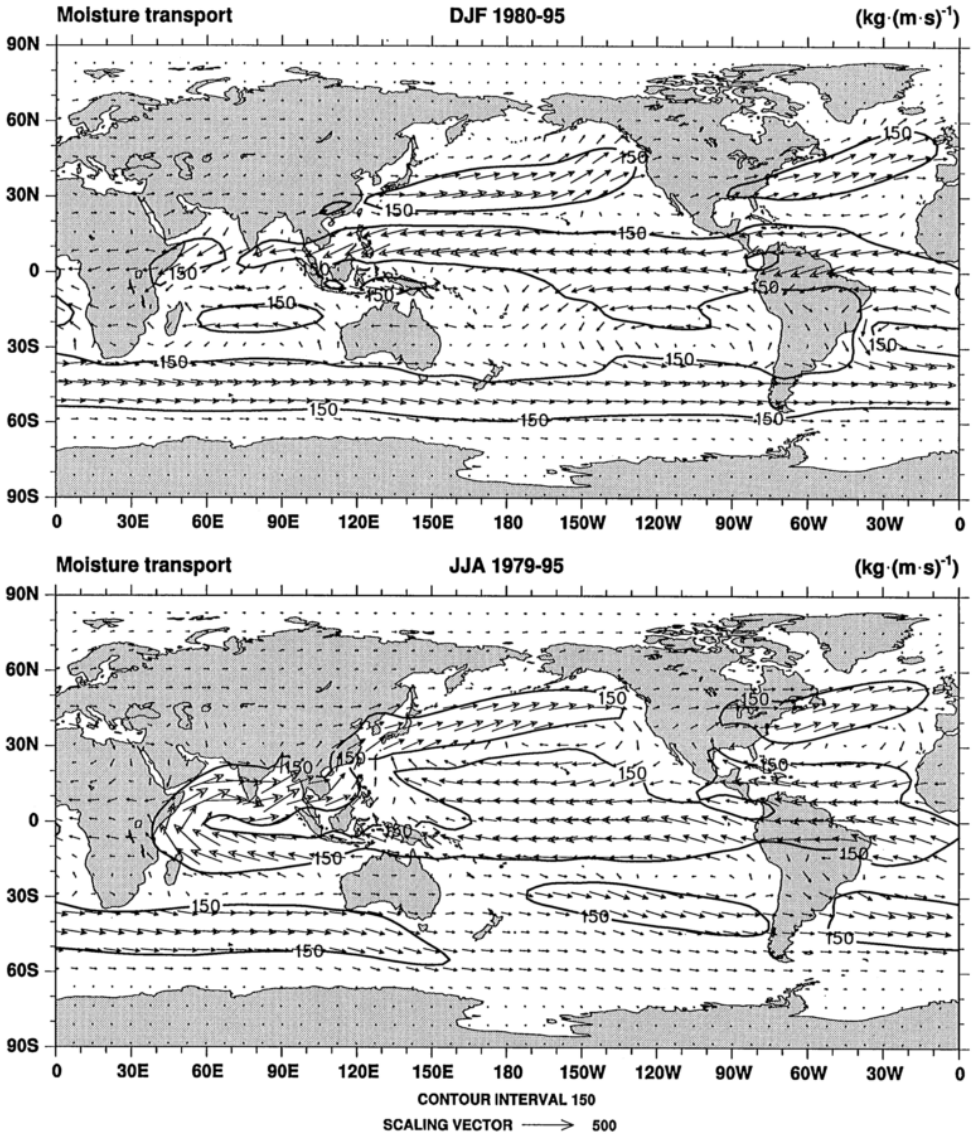

Figure 1.2: Vertically integrated moisture transport for the period 1979-1995 in DJF (top panel) and JJA (bottom panel). Figure is adopted from *Trenberth and Guillemot* (1998).

1.2 Research aims

Successful understanding and modelling of the climate system requires solid and detailed observations of the water cycle. This work aims to provide an updated assessment of some key aspects of the atmospheric hydrological cycle in the modern day climate, aspects that were selected because they offer the potential to provide new insights into identifying the capabilities and limitations of our global climate observing systems and new insights into the mechanisms that drive hydrological cycle variability on multiple time and space scales. By considering scales from the diurnal cycle and tropical cyclones up to basin-wide patterns of inter-annual variability, hydrological cycle behaviour and processes are identified that could be used to challenge climate model capabilities in a diverse range of situations.

This overarching aim is structured into a series of more specific scientific questions to be addressed:

1. How well are the key components of the atmospheric hydrological cycle monitored by observations and reanalyses? A particular motivation here is to assess the newest reanalysis product (JRA-55), which was not available to be included in the inter-comparison in Fig. 1.1 from Trenberth et al. (2011), by considering the extent to which the most modern reanalysis products agree with each other and with other ground-based or remote sensing observations. This analysis raises two related questions: how well do reanalyses close the water budget, and where do the budget residuals come from?
2. How are the temporal variations in precipitation, evaporation and moisture transports decomposed into different time scales? What are the contributions of annual cycle, diurnal cycle, intra-seasonal and interannual variabilities? Each of these components is explored in greater detail, guided by the remaining questions.
3. How does atmospheric moisture transport vary diurnally and how is it decomposed into thermodynamic versus dynamic components?
4. What are the dominant patterns of inter-annual moisture divergence and how are they linked to the El Niño Southern Oscillation (ENSO) phenomenon? Since moisture convergence and divergence are inherently linked to the atmospheric diabatic heating that creates the global teleconnections associated with the impact of ENSO events, a further

important issue to address is the dependence of the moisture divergence responses on different El Niño warming patterns.

5. Extending the temporal spectrum to cover extreme events, can the role of tropical cyclones in transporting moisture from ocean to land be quantified using reanalysis data?

To answer these wide-ranging and challenging questions, multiple state-of-art observation-based (i.e. including direct observations and reanalysis) datasets are utilized to assess the key hydrological processes including precipitation, evaporation/evapotranspiration, atmospheric humidity changes and horizontal moisture transports. First, I will present an evaluation and intercomparison of the selected datasets, taking account of dataset uncertainty assessments. Variability is then decomposed into different time scales to assess their relative magnitudes, and detailed analyses are performed for the annual and diurnal cycles. Various conventional, well-established methods such as spatial and/or temporal averages, composites, Taylor diagrams, harmonic and Empirical Orthogonal Function (EOF) analysis are used in the investigation, together with some new techniques that are explored to facilitate a better and more thorough understanding, such as the introduction of uncertainty quantification and visualization to a Taylor diagram, the application of Self-Organizing Maps (SOMs) as a complement to EOF analysis, and a set of distance-based schemes to attribute moisture transports to TCs. The "frozen" assimilation systems and complete spatio-temporal global coverage of reanalyses make them a good candidate to study short-term variability, therefore most of the analyses here are based upon the ERA-Interim reanalysis product.

The results will provide valuable information to the research community in a few areas. Firstly, the reanalysis-focused analyses serve as good complements to the study of longer-term climate changes and future predictions, by contributing to our understanding of the processes that underlie hydrological cycle changes. The assessment of the current hydrological cycle will serve as a baseline for hydroclimatic studies, climate change predictions and evaluations.

Secondly, some suggestions are offered to the user community based on the assessments of the datasets evaluated here. Due to the differences in the incorporated observations, resolutions, bias correction methods, parameterization schemes and various pre- or post-processing procedures, observational datasets and reanalyses may exhibit different features/qualities which should be taken into account in a study. In particular, the evaluation of

various hydrological variables from the newly released JRA-55 reanalysis offers helpful guidance in choosing this product according to the specific purpose of future research.

After assessing the quality of observational data, much effort is devoted to the horizontal moisture transport, a process that combines the thermodynamic and dynamic components of the hydrological cycle. Constructive new findings are reported across a spectrum of variability, ranging from climatological annual cycles based on three decades of observations, to inter-annual variations related to ENSO, to diurnal cycles stemming from humidity and/or wind fields, and finally covering the extreme water fluxes related to TC activity.

1.3 Thesis structure

The thesis is broadly divided into two parts: the first part evaluates the state-of-art observation-based estimates of the atmospheric hydrological cycle in the modern day climate. Chapter 2 considers the precipitation observations: reanalysis products ERA-I and JRA-55 are compared with gauge, satellite and combined gauge-satellite precipitation observations in their depiction of mean precipitation patterns and degrees of temporal variability. The comparison starts from global patterns and delves into regional scales where notable differences are observed. Chapter 3 applies a similar evaluation process to E/ET, total column water (TCW) and finally assesses the atmospheric hydrological cycle from a water budget perspective. Budget residuals are examined by a cluster analysis, providing evidence to develop a hypothesis for the causes of the budget residuals.

The second part focuses on horizontal atmospheric moisture flux variability across multiple time scales. Chapter 4 diagnoses two climatological variabilities: the annual and diurnal cycles, based on 34 years of reanalysis data. Chapter 5 investigates the distinct moisture divergence responses to extreme versus moderate El Niño events. The results, consistent with recent literature, suggest that the conventional El Niño-La Niño-dipole way of understanding ENSO variability needs to be updated: the difference between an extreme El Niño and a moderate El Niño is as large as, sometimes even larger than, the difference between a moderate El Niño and a La Niña in terms of their expression in the moisture divergence fields. In this chapter, I also propose SOMs as a helpful complementary method to EOFs for diagnosing non-linear behaviour. Chapter 6

shifts the scope to extreme events and quantifies onshore moisture transports by the Atlantic and Eastern Pacific tropical cyclones. An ensemble of estimates are created by applying multiple TC attribution schemes to reanalysis and best track datasets. The results provide a new quantification of the significant contribution that TCs play in supplying moisture to the North American continent, and in some cases, a key factor in the alleviation of sustained droughts.

Each chapter is relatively self-contained, guiding the reader into the topic by a literature review which sets up the research background, which is then followed by a standard data and methods-results-conclusion structure. The final chapter (Chapter 7) gives an overall summary of the thesis and proposes some suggestions for future work.

Chapter 2

Evaluation of atmospheric hydrological cycle – precipitation observations

2.1 Research Background

We will start this chapter by first reviewing the current status and challenges of global scale precipitation observations, the reliability and known issues of some major datasets. The discussion will cover observations from in situ gauge measurements, remote-sensed satellite retrievals and and those that are produced by reanalysis models. Ideally, estimates from these three major sources should reconcile with each other. However, each of them has their respective strengths and limitations, and the consistency among them is usually poor where precipitation is most intense. Moreover, the accuracy and confidence of these measurements vary spatially and temporally, mostly due to the limited monitoring techniques and our knowledge of the synoptic processes. Considerations of both factors will be taken into account when we evaluate the precipitation estimates from a newly released reanalysis product (JRA-55). Finally some suggestions will be offered to the user community based on the evaluation results.

Although monitoring of rainfall has a long history, global scale records of precipitation that cover both land and ocean didn't exist until routine satellite observations became operational. In the past four decades, global climatologies of monthly precipitation estimates have seen a dramatic improvement in both

observation quantity and quality, thanks to the superior spatial coverage of satellite remote sensing, particularly after the launch of the TRMM satellite in late 1997 (*Pan et al.*, 2012; *Dai*, 2001). On the other hand, improved upper-air observations of other variables provides better observational constraints for model-based precipitation from reanalysis. Equipped with more advanced data assimilation schemes, the skill of precipitation estimates has also improved in newer generations of reanalyses (*Trenberth et al.*, 2011; *Bosilovich et al.*, 2008; *Knippertz et al.*, 2013; *Ebita et al.*, 2011; *Kobayashi et al.*, 2015; *Simmons et al.*, 2010). The benefits of satellite observations on reanalysis precipitation is mostly felt over ocean (*Dee et al.*, 2011), where direct ship measurements are prone to sampling errors, and fixed location in-situ observation is very much limited to several rain gauges on the Tropical Atmosphere-Ocean (TAO) buoys in the central Pacific (*Andersson et al.*, 2011). Over land, in-situ measurements of surface temperature and humidity impose stronger constraints on the reanalysis models, therefore precipitation estimates tends to be more reliable over land (*Dee et al.*, 2011; *Andersson et al.*, 2011). Over most of the mid-to-high latitude land areas, the magnitude of mean precipitation variability is within $1\,mm/day$ from both reanalysis-based and observation-based estimates (*Lorenz and Kunstmann*, 2012).

Despite these improvements, global observations of precipitation have substantial uncertainties, particularly convection-related precipitation in the summer hemisphere (*Adler et al.*, 2001; *Bosilovich et al.*, 2008; *Lorenz and Kunstmann*, 2012). In principle, different datasets should share consistency in precipitation estimates, but dependencies are common in precipitation inter-comparison studies, particularly in regions where surface observation coverage is sparse. The lack of in-situ observations often brings down the effectiveness of remote-sensing observations as well: due to the above mentioned difference in terrestrial and oceanic precipitation qualities, some satellite estimates are rescaled against gauge data before being combined with the surface data (e.g. GPCP, (*Huffman and Bolvin*, 2011)), so are only marginally different from in situ products at the basin and monthly scale (*Pan et al.*, 2012). On the other hand, although satellite observation has achieved near-global coverage and increases in the temporal sampling resolution, a widespread decrease in the number of assimilated gauges has occurred in recent decades. For instance, the number of rain gauges available to CPC and GPCC decreased over most of South America, Europe, Africa, Asia and Australia during the 1990s and 2000s (*Lorenz and Kunstmann*, 2012). Similar decreases also exist in the

CRUTS precipitation dataset (see Fig. 4 in *Hegerl et al.* (2015)).

Well observed regions, including North America and Europe, have much denser monitoring networks than other tropical and subtropical regions. In the upgrade from version 4.0 to 5.0 of the GPCC product, the spatial coverage was further increased in areas where monitoring had already been dense, but little improvement is seen in regions where additional observations are urgently needed (*Lorenz and Kunstmann*, 2012), particularly in the tropics where many studies have identified problems/uncertainty maxima (e.g. interpolation uncertainties) caused by a lack of surface observations (*Lorenz and Kunstmann*, 2012; *Pan et al.*, 2012; *Qian et al.*, 2006; *Bosilovich et al.*, 2008). This makes the divergence of precipitation data quality between the tropics and mid-high latitudes even larger, and hampers the overall usefulness of the datasets in faithfully quantifying large scale hydrological characteristics.

A paradoxical outcome of this surface coverage insufficiency is that sometimes datasets have better agreements over such poorly observed areas than other densely gauged basins (*Pan et al.*, 2012). This is due to a heavy overlap in the small number of available gauges being assimilated into different datasets over these poorly observed regions, and a lack of data for procedures like undercatch corrections, while in densely gauged regions the differences in gridding and various correction procedures could lead to relatively larger discrepancies. This feature adds extra complexity to our interpretation of uncertainties because small discrepancy spread does not guarantee better observational quality (*Hartmann et al.*, 2013), and adding more datasets into the uncertainties analysis would not provide much added value unless more independent observations are assimilated.

However, currently there are not many effective alternatives to simply inter-comparing as many different datasets to assess the uncertainty ranges in large scale precipitation observations (*Mo and Higgins*, 1996; *Andersson et al.*, 2011). Many previous studies have addressed this using different datasets and considering different spatio-temporal scales.

Trenberth and Guillemot (1998) validated the precipitation from the NCEP-NCAR (NR1) reanalysis against the Xie-Arkin CMAP observation, and confirmed some deficiencies of NR1 including a double SPCZ problem, tropical rainfall biased low compared with CMAP, and insufficient ENSO-related variability. *Bosilovich et al.* (2008) included NR1 alongside another four reanalyses (NR2, ERA-40, JRA-25 and GEOS4 from NASA) in their comparison, therefore putting it in

a wider context. Two points are worth mentioning. i) Although in general new reanalyses show improved skills than older ones, exceptions do exist, as in the case of NR1 and NR2: the former has both better spatial correlations and less biases than its successor. Therefore the newer-is-better rule of thumb is not always correct. ii) The low bias in tropical NR1 in *Trenberth and Guillemot* (1998) "changes" to a high bias compared with a GPCP reference, this is because of the known high bias of CMAP with respect to GPCP (more on this in section 2.2). This complexity illustrates a pitfall that although words like "biases" and "over/under-estimate" are common in such validation studies, one should always keeps in mind that the reference datasets differ from study to study and none is the absolute truth. And a comprehensive view is difficult to achieve without a comprehensive collection, which leads to another challenge in the precipitation quantification: the proliferation of existing literature on such inter-comparison studies provide valuable information and recommendations for researchers in different applications. However, the emergence of new data products and an ever increasing amount of available data collections also pose a bigger challenge for the user community to make effective selections. For the continuation of such studies, one needs to incorporate a greater number of datasets in the analysis to create a comprehensive review.

Instead of incorporating as much data into one single comparison, an alternative is to select only from the "seeded players", namely the best quality datasets based on existing knowledge in some specific fields. Comparison is then performed between the "seeds" and the newly emerging compilations. This methodology will be adopted in this study, and the "seeds" we select are the model-based ERA-I (*Dee and Uppala*, 2009), and the observation-based GPCP (*Huffman and Bolvin*, 2011).

NR1 and NR2 have been shown to have various significant deficiencies in hydrological aspects, as mentioned above. The MERRA (Modern Era Retrospecitive Reanalysis) and CFSR (Climate Forecast System Reanalysis) are both newer generation reanalyses (*Trenberth et al.*, 2011), however, global precipitation averages in both show abrupt increases around 1998 and 2001, particularly over the oceans (*Lorenz and Kunstmann*, 2012). This has been diagnosed as a satellite observation problem in MERRA: assimilation of AMSU-A data brings in excessive moisture followed by excessive oceanic precipitation (*Bosilovich et al.*, 2011; *Robertson et al.*, 2011). Since CFSR and MERRA share nearly the same analysis system and input data, the same diagnosis also applies to CFSR. The problem is severe enough to change

the ocean into a net moisture sink ($P - E > 0$), therefore rendering them unsuitable for hydrological studies (in terms of terrestrial precipitation, MERRA has performed a land-only rerun of the reanalysis and used observations to correct precipitation, making it perhaps the only global reanalysis that has observation-assimilated precipitation). In addition, CFSR also systematically over-estimates the mid-to-high latitude precipitation (*Lorenz and Kunstmann*, 2012). For the earlier ECMWF product ERA-40, there exists a large tropical wet bias (creating an oceanic moisture sink during the satellite era), and spurious temporal changes (*Andersson et al.*, 2005; *Dee et al.*, 2011; *Hagemann et al.*, 2005; *Bosilovich et al.*, 2008; *Trenberth et al.*, 2007), which has been substantially improved in its successor ERA-I (*Knippertz et al.*, 2013). ERA-I has been shown to be the best reanalysis for atmospheric branch of the hydrological cycle (*Castillo et al.*, 2014).

At the end of 2013, Japanese Meteorological Agency (JMA) released its newer version of atmospheric reanalysis dataset–JRA-55–to supersede its predecessor JRA-25. JRA-55 benefits from third generation reanalysis techniques, and achieved some improvements such as increased model resolution (T319L60 with a reduced Gaussian grid system vs T106L40 in JRA-25), the introduction of 4D-VAR assimilation scheme (thus making it the first global reanlaysis applying 4D-VAR to the second half of the 20th century), a revised radiation scheme and variational bias correction (VarBC) for satellite radiances (*Ebita et al.*, 2011; *Kobayashi et al.*, 2015). The extended temporal span further back in time to cover the pre-satellite 1958-1979 period makes it more suitable for studies of climate change or multi-decadal variability, compared with the shorter JRA-25 (1979-2004). A couple of studies have reported some preliminary assessments of this new product, and confirmed improvements with respect to JRA-25, such as alleviating a dry bias over the Amazon region and the cold bias in the lower stratosphere (*Ebita et al.*, 2011; *Kobayashi et al.*, 2015) and better temporal homogeneity of temperature structure (*Kobayashi et al.*, 2015). The global precipitation anomalies also show better agreement with observations (*Kobayashi et al.*, 2015).

However, a careful and detailed assessment of various hydrological related variables in JRA-55 has not been published yet. Therefore we include it in our dataset selection and compare against ERA-I, as well as observation-based estimates (the rationale for selecting GPCP will be explained in the Data and Methods section). Our objective is to give a brief review of the reasonableness and usefulness of these most modern reanalysis datasets in realistically

depicting the atmospheric hydrological cycle, which is still believed to be a challenge for the state-of-art reanalysis products. A comprehensive evaluation and explanation of the differences between reanalyses is a non-trivial task that goes beyond the scope of the study, so we provide only a summary of some selected aspects that are believed to be most important for hydrological cycle. These include precipitation P (this chapter), evaporation E, the net freshwater fluxes (E - P) and water budget residuals (all in Chapter 3). Results of the these validations will provide useful guidance on selecting an appropriate dataset for subsequent analyses.

Evaluation in this chapter covers the mean annual cycle of precipitation rates, magnitudes of variances over different time scales, and pattern correlations with independent observations. To validate the reanalysis precipitation, the observation-based GPCP dataset is used as the "truth", and extra "independent" datasets are chosen to facilitate estimations of uncertainties in observation-based products. For such purposes, the CRUTS precipitation product (version 3.1) (*Harris et al.*, 2014) is used for terrestrial precipitation, and HOAPS (version 3.2) (*Andersson et al.*, 2010) is used over the ice-free ocean. In the end, we summarize the performance of the reanalyses using Taylor diagrams, in which we explore a new method to depict the observational uncertainties on Taylor diagrams by utilizing the error estimations from the observation products.

2.2 Data and Methods

2.2.1 Precipitation observation data

For validation purposes, many good-quality observation-based products are commonly used in the research community, including CMAP (*Xie and Arkin*, 1997), PREC/L (*Chen et al.*, 2002), CRUTS (*Harris et al.*, 2014), GPCC (*Becker et al.*, 2013), and various satellite retrievals including HOAPS (*Andersson et al.*, 2010).

There are some known problems in the CMAP precipitation over oceans, especially for trends (*Trenberth et al.*, 2007). Tropical precipitation has a notable high bias resulting from unwarranted use of atoll data in CMAP (*Yin et al.*, 2004; *Bosilovich et al.*, 2008; *Edwards*, 2007), and since GPCP does not include the atoll stations, it is immune to such errors. In addition, over high latitude regions north/south of 40° N/S, CMAP relies on SSM/I alone which suffers

from coverage completeness and a dry bias at such latitudes (*Edwards*, 2007), while GPCP uses TOVS data to supplement the SSM/I (*Edwards*, 2007; *Huffman and Bolvin*, 2011). Therefore the GPCP precipitation product is preferred for validation purposes.

CRUTS (CRU Timeseries, version 3.10) (*Harris et al.*, 2014) provides monthly time series of 10 variables (including temperature and precipitation) compiled from over 4,000 weather station records and has global land coverage (except Antarctica). The high spatial resolution ($0.5° \times 0.5°$) makes it suitable for regional climate variability studies as well, and it has been used to derive gridded drought indices (e.g. *van der Schrier et al.* (2013)). The 3.1 version of CRUTS has been shown to have comparable quality with GPCC precipitation over most of the globe, despite fewer input stations, therefore it is chosen as an "independent" observation to help quantify the observational uncertainties.

GPCC provides monthly land-surface precipitation with global coverage, based on 67,200 stations world-wide that feature record durations of 10 years or longer, and is used as the land surface reference in GPCP. However, it differs from GPCP in the inclusion of various gauge bias corrections including under-catch bias in the latter (GPCC includes bias corrections in the Arctic). In addition, the merge of satellite observations in GPCP allows global ocean coverage. Therefore the GPCP data is used as the major observational reference, and some GPCC data is used to help diagnose the Indian sub-continent discrepancies observed in GPCP and CRUTS.

HOAPS was designed with the principle of retrieving multiple global ocean surface flux components consistently within one single observation framework. SSM/I is used as the common data source for all retrievals instead of combining different data sources, thus achieving better homogeneity and internal consistency (*Andersson et al.*, 2011).

Table 2.1 lists the metadata of datasets used in the following analysis.

Table 2.1: Summary of the observation datasets containing precipitation P.

Dataset	Time period	Resolution (degree)	Land/sea coverage	Data sources
GPCP (v2.2)	1979 - 2014	2.5×2.5	Global	Merged gauge and satellite
ERA-I	1979 -	0.75×0.75	Global	Forecast model
JRA-55	1958 -	1.25×1.25	Global	Forecast model
CRUTS (v3.1)	1948 - 2010	0.5×0.5	Land	Gauges
GPCC (v6.0)	1901 - 2010	0.5×0.5	Land	Gauges
HOAPS (v3.2)	July-1987 - Dec-2008	0.5×0.5	Ice-free ocean	SSM/I

2.2.2 Taylor diagram

The Taylor diagram (*Taylor*, 2001) is a useful graphical device to summarize the agreement between two patterns. By making analogous relations to the law of cosines, a Taylor diagram represents the pattern correlations (cosine of the angle), standard deviations (radial distances) and the centered root mean square (RMS) differences (distance between model and reference points) in a single plot. Spatial correlation measures the extent to which the pattern in a model matches the reference, and the standard deviation quantifies the amplitude of variances. Centered RMS differences summarizes these two quantities and provides an overall evaluation. Applied with proper area weighting and temporal weighting in computing the statistics, a Taylor diagram is especially useful in evaluating multiple aspects of complex models or in gauging the relative skill of many different models.

Extending the basic formulation of the Taylor diagram, some other statistics could be added to give a more thorough view of the relationships among the patterns being examined, such as an extra dot (or line) for each model point to represent the systematic bias (*Taylor*, 2001), and an extra "independent" observation to indicate the observational uncertainty (*Taylor*, 2001; *Bosilovich et al.*, 2008, 2011). In this chapter we will apply this technique to compare the precipitation estimates in ERA-I and JRA-55 with an observation-based dataset (GPCP v2.2). In addition to the centered RMS differences offered by a standard Taylor diagram setup, the overall biases of each reanalysis will also be quantified on the diagram. Another "independent" observation (CRUTS 3.1 and HOAPS v3.2) will be plotted alongside the GPCP reference to help quantify the uncertainties from observations. In addition, a new approach to estimate such observational uncertainty using the random error of the observational dataset will be explored.

2.2.2.1 Bias estimate on a Taylor diagram

The centered RMS difference (E) between a model point (M) and the observational reference (O) is defined as (*Wilks*, 2011, chap. 8):

$$E = MSE - (\bar{\mathbf{M}} - \bar{\mathbf{O}})^2 \tag{2.1}$$

where MSE is the mean squared error; $\bar{\mathbf{M}}$ and $\bar{\mathbf{O}}$ denote the mean of $\mathbf{M}$ and

O, respectively. Eq.2.1 shows that the Taylor diagram represents a model as the debiased MSE, which is the MSE after subtraction of contributions due to overall bias errors (*Wilks*, 2011, chap. 8). And when represented geometrically, the quantities $E^{1/2}$, $RMSE$ and $|\bar{\mathbf{M}} - \bar{\mathbf{O}}|$ form a right-angle triangle (*Taylor*, 2001).

E could be represented using a standard Taylor diagram setup as a vector ($\overrightarrow{OM}$) pointing from the reference towards the model point. To visualize the bias, one could draw another vector ($\overrightarrow{MB}$) from the model point, perpendicular to $\overrightarrow{OM}$, with a length of $\| \bar{\mathbf{M}} - \bar{\mathbf{O}} \|$. The direction of the bias arrow follows a lateral convention: leftward pointing denotes negative bias and rightward positive. When there is a relatively good match of the standard deviations between the model and reference, this scheme helps distinguish the bias directions better.

2.2.2.2 Depicting observational uncertainty on a Taylor diagram

Although used as a reference, an observation of a variable is itself uncertain. Various sources of uncertainties and biases add up throughout the processes of monitoring, data collection and pre-processing, bias corrections, and accumulate into the final synthesized product (*Hartmann et al.*, 2013). It is usually difficult to account for all the potential error souces, which could lead to a paradoxical interpretation that small uncertainty ranges indicate a better product/estimation (*Hartmann et al.*, 2013). Observational uncertainty is typically depicted on a Taylor diagram by adding another independent observation of comparable quality, so that the difference between the two can be used as an indication of the observational uncertainty (*Taylor*, 2001; *Bosilovich et al.*, 2008).

However, this conventional approach has two main limitations. i) datasets may have common data sources and hence are not really independent. ii) it does not make use of the error estimates that some dataset developers have been able to quantify. Therefore, we intend to overcome these limitations by utilizing the error estimates provided by GPCP (this chapter) and OAflux (in next chapter) as a supplimentary uncertainty measurement, thus making full use of these valuable first-hand information from the data providers. Bias errors were neglected in the error computation in GPCP, therefore the RMS error should be interpretated as dominated by random fluctuations that arise from sampling, measurement and algorithm effects (*Janowiak et al.*, 1998; *Huffman and Bolvin*, 2011). Detailed explanation of the error derivation is missing in the OAflux

documentation (*Yu et al.*, 2008), therefore we will interpret their error data as RMS errors assuming independence between different data sources, and a larger monthly mean standard deviation at a grid box represents a larger uncertainty range among input data sources (*Yu et al.*, 2008). Given these random errors in the reference dataset, there will be a region on the Taylor Diagram around the reference point where "reality" could reasonably lie, and the purpose here is to map out this region, using the published error estimates. However it is not clear whether the errors in each grid cell are independent of each other, or there are consistent regional structures in the error field. Therefore, theoretically all possible combinations need to be enumerated to cover a full range of uncertainty estimate. Here we propose a method that allows a meaningful uncertainty range depiction using finite computations, based upon certain assumptions of the error distrubtions. The statistical interpretation of the results will also be discussed in the end.

This method to estimate an uncertainty range involves some manipulation of the RMS error **E** (note this is the observational RMS error offered by the data provider, and it is distinct from the RMS between the model and reference on a Taylor diagram): $\mathbf{E_x} = f(\mathbf{E})$. The effect of function $f()$ is to give a particular redirection of the error field, ranging from completely coherent errors chosen to maximise the difference from the reference field in some metric, to assigning completely random errors at each grid box. When added to the observation (**O**), the resultant Uncertainty Variable (UV) $\mathbf{U} = \mathbf{O} + \mathbf{E_x}$ represents one possible realization of the error-contaminated observation, and could be plotted out on the Taylor diagram as another evaluation point. And a series of such realizations will delineate the range of uncertainties stemmed from random errors.

The first two realizations one could easily obtain are:

$$\begin{cases} \mathbf{U_1} &= \mathbf{O} + \mathbf{E} \\ \mathbf{U_2} &= \mathbf{O} - \mathbf{E} \end{cases} \tag{2.2}$$

where the error standard deviation at each grid box is added (subtracted) from the observation. It can be proved (not shown) that the resultant points U_1 and U_2 will be symmetrical about the vertical line going through the reference point ($x = 1$ if normalized, see a sample plot in Fig. 2.1). However, these two points are not included in the plots in the results section, as will be explained below.

The signs and magnitudes of the errors should be allowed to vary spatially.

Using the standard deviations ($\pm\mathbf{E}$) as the boundaries of the error distribution at each grid box, and assuming grid box error independency at any time, the scenarios of maximum and minimum standard deviations of a UV could be achieved using:

$$\begin{cases} \mathbf{U_3} & = \mathbf{O} + \mathbf{E_3} \\ \mathbf{U_4} & = \mathbf{O} + \mathbf{E_4} \\ \mathbf{E_3} & = [e_1 \cdot sgn(o_1 - \bar{\mathbf{O}}), e_2 \cdot sgn(o_2 - \bar{\mathbf{O}}), ..., \\ & \quad e_n \cdot sgn(o_n - \bar{\mathbf{O}})] \\ \mathbf{E_4} & = -\mathbf{E_3} \end{cases} \tag{2.3}$$

Where $\mathbf{U_3}$ and $\mathbf{U_4}$ are the Uncertainty Variables with maximum (σ_{max}) and minimum (σ_{min}) standard deviations, respectively. And $sgn()$ is the sign function. Maximum standard deviation is achieved by adding (subtracting) a capped (assuming standard deviation as the local upper boundary) positive error to (from) the grid boxs where they are above (below) average. And doing the opposite gives the UV with minimum standard deviation. Again due to the symmetrical property, U_3 and U_4 are mirror images about the $x = 1$ vertical line (see U_3 and U_4 in Fig. 2.1).

The space in between U_3 and U_4 is delineated by inserting six intermediate dots interpolated from the standard deviation range $\sigma_{max} - \sigma_{min}$:

$$\sigma_t = \sigma_{min} + f(\sigma_{max} - \sigma_{min}),\ f = \{0.10, 0.25, 0.40\} \tag{2.4}$$

Only the left half ($f < 0.5$) of the empty space is interpolated by computation, and the right half could be obtained by a symmetrical transformation.

To give a full range of uncertainty estimate, the distance between the point of U and O should be maximized, at any given target standard deviation σ_t. This is equivalent to minimizing the correlation between $\mathbf{U}$ and $\mathbf{O}$ subject to a given standard deviation of $\mathbf{U}$, thus constituting a Lagrangian multiplier problem where the target function to minimize is $f(\mathbf{U}) = corr(\mathbf{U}, \mathbf{O})$, and the equality constraint is $g(\mathbf{U}) = \sigma_{\mathbf{U}} - \sigma_t = 0$. To numerically solve this, the Augmented Lagrangian method (ALM) is applied. An ALM function is first constructed as:

$$\Phi(\mathbf{U}) = f(\mathbf{U}) + \frac{\mu_k}{2} g(\mathbf{U})^2 - \lambda_k g(\mathbf{U}) \tag{2.5}$$

where μ_k and λ_k are the penalty parameter and Lagrangian multiplier at the kth step, respectively.

During each iterative step, a gradient descent algorithm is used to solve the $\mathbf{U}$ that minimizes the ALM function:

$$\mathbf{U_k} = \underset{\mathbf{U}}{\operatorname{argmin}}\, \Phi(\mathbf{U}) \tag{2.6}$$

Where $\underset{\mathbf{U}}{\operatorname{argmin}}$ is the arg max operator. Note that u_i is always kept in the range $[-e_i, e_i]$ throughout the process (constrained by the local error standard deviation e_i). Before stepping into the next iteration, μ_k and λ_k are updated following:

$$\begin{cases} \mu_{k+1} & := 30 \times (k+1) \\ \lambda_{k+1} & := \lambda_k - \mu_k g(\mathbf{U}) \end{cases} \tag{2.7}$$

where $:=$ denotes parameter updating.

Since the interpolated standard deviation (σ_t) only needs to be approached approximately, a relatively slow-growing penalty parameter updating function is adopted here. Experiments show that a few iterations are usually sufficient to reach convergence at a reasonable level (see a sample in Fig. 2.2).

The area delineated by the above derived UVs form a section-like shape in the Taylor diagram (Fig. 2.1), and represents the range of uncertainties stemming from the observational error. Care needs to be taken in its statistical interpretation: at each designated standard deviation level σ_t, the correlation $corr(\mathbf{U}, \mathbf{O})$ has been deliberately minimized, so that the resultant UVs encompass the largest area possible surronding the reference point, therefore representing the largest possible uncertainty spread given the observational error. However, at grid box level an arbitrary boundary $\pm e_i$ is set to the local error's distribution, although the range $[-e_i, e_i]$ only accounts for around 68 % of probabilities in a Normal distribution. Moreover, after the minimization process, the errors $\mathbf{E_x}$ are mostly distributed at their extremes: e_{xi} being close to $\pm e_i$ or 0 (see Fig. 2.2d, the author is unable to give a sound mathematical explanation to this). Therefore, the uncertainty range estimated above is a combination of locally constrained random error distribution (within $[-e_i, e_i]$), and a globally deliberated spatial pattern. However, the following Monte Carlo experiment suggests that the local error distribution constraint has little effect on the error's

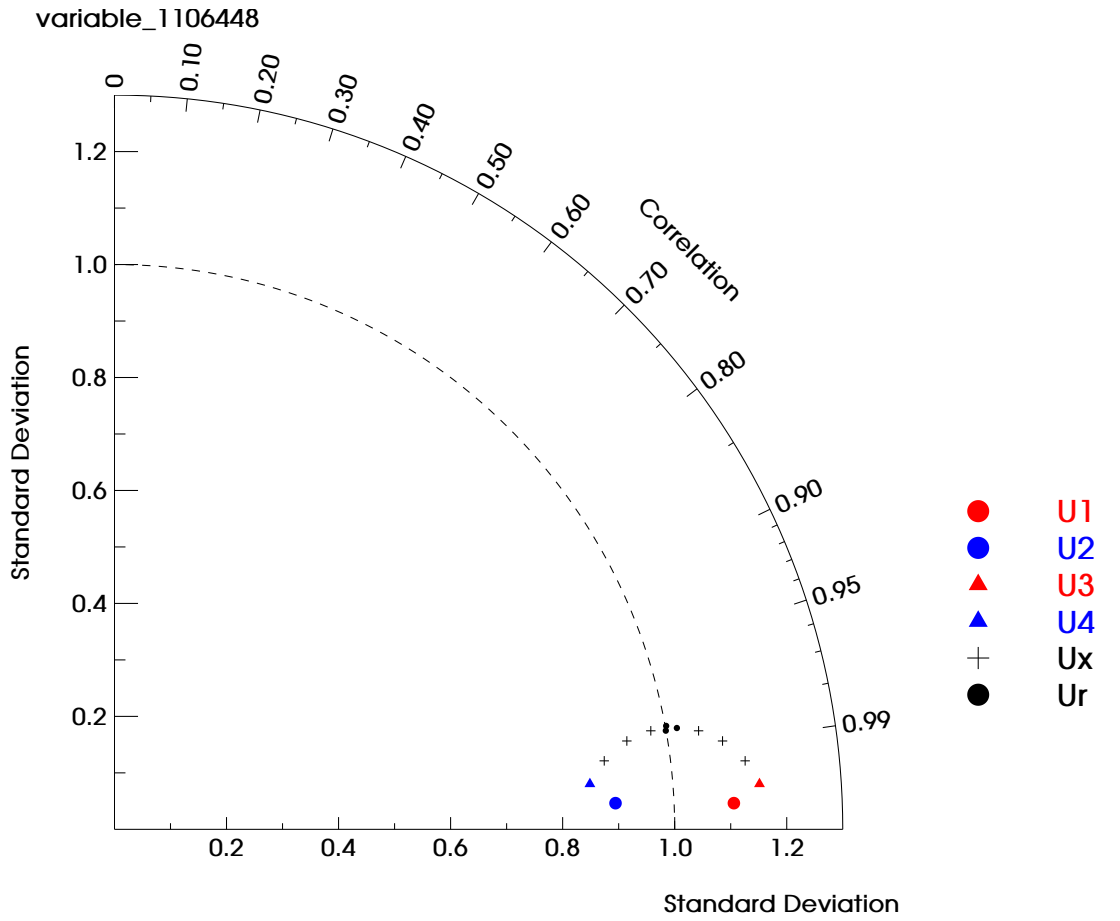

Figure 2.1: A sample plot of the observational uncertainties estimated from the random error on a Taylor diagram. Data used to generate the plot are the tropical precipitation from GPCP (v2.2) in JJA season, during the period of 1988-2008, and the RMS error data provided by GPCP for the same spatio-temporal region. U_1 is the Uncertainty Variable (UV) obtained by adding the RMS error onto the observation: $\mathbf{U_1} = \mathbf{O} + \mathbf{E}$, and U_2 is $\mathbf{U_2} = \mathbf{O} - \mathbf{E}$. U_3 and U_4 are the UVs with maximum and minimum standard deviations, respectively. U_x are the correlation-minimized UVs interpolating the space between U_3 and U_4. Three random UVs (U_r) obtained by randomly sampling a Normal distribution at each grid box are shown as small black dots.

size (variance of $\mathbf{E_x}$).

Assuming grid box errors are independent and Normally distributed at all grid boxes, a random error $\mathbf{E_r}$ can be obtained by randomly sampling a Normal distribution $\mathcal{N}(0, e_i)$ at each grid box i. The resultant UV is simply $\mathbf{U_r} = \mathbf{E_r} + \mathbf{O}$. A number of such random UVs could then be generated to form a Monte Carlo test. The results (small black dots in the sample figure Fig. 2.1 and figures in the results section) suggest that these random points are mostly distributed directly above the reference point, and aligned along the section arc formed by correlation-minimized UVs. The former property is a result of the grid box independence assumption and therefore the random error has near zero

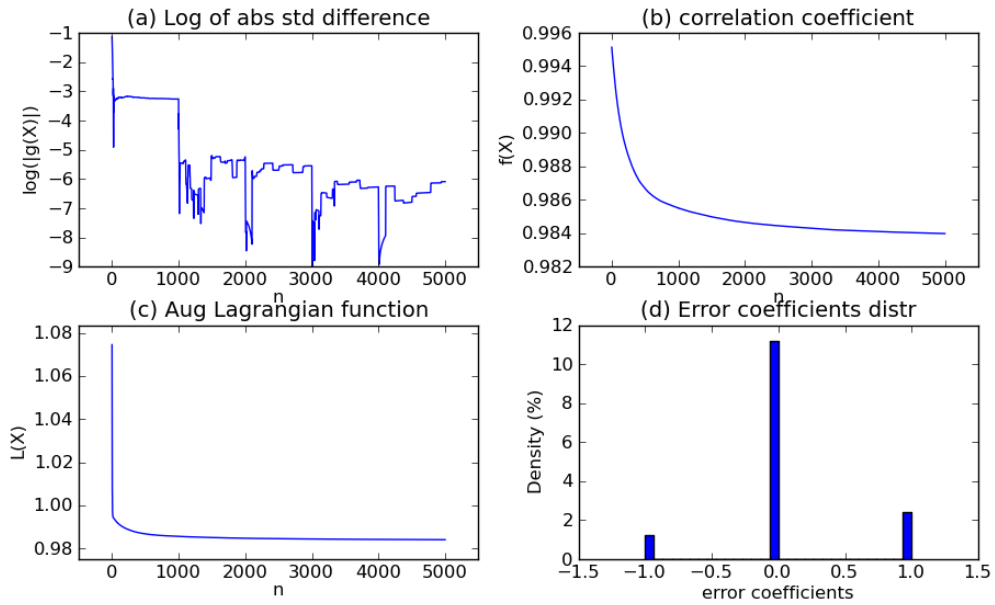

Figure 2.2: Process of the Augmented Lagrangian multiplier method in generating the uncertainty estimates shown in Fig. 2.1. (a) the convergence of the equality constraint function $g(X)$ during 5000 iterations. (b) convergence of the correlation coefficient to be minimized. (c) convergence of the augmented Lagrangian function. (d) distribution of error coefficients ($e_{xi} = f \cdot e_i$) at the end of computation. The three most frequent values for f are -1.0, 0 and 1.0.

covariance with the observation ($Var(\mathbf{O}, \mathbf{E_r}) \simeq 0$), and the latter suggests that although the local error distribution is constrained by its standard deviation $\pm e_i$, the constraint on the variance of the resultant error $Var(\mathbf{E_x})$ is negligible: the variance of $\mathbf{E_x}$ is of similar magnitudes as those of the random UVs (note that minimizing the correlation of $\mathbf{O} + \mathbf{E_x}$ and $\mathbf{O}$ is equivalent to maximizing the variance of $\mathbf{E_x}$). Finally, as there is usually a tightly packed cluster of the random UVs on the Taylor diagram, only three of them are retained in the final plots.

2.3 Results

2.3.1 Long term mean annual cycle of precipitation in 1988-2008

The mean annual cycle of precipitation is computed from monthly ERA-I, JRA-55, GPCP (version 2.2), CRUTS (version 3.1) and HOAPS (version 3.2)

during the time period of overlap (Jan 1988 to Dec 2008). All computations are done using their original resolution (ERA-I: 0.75° × 0.75°, JRA-55: 1.25° × 1.25°, GPCP: 2.5° × 2.5°, CRUTS: 0.5° × 0.5°, HOAPS: 0.5° × 0.5°), except when computation involves data on two different grids, when they are regridded to the lowest resolution (2.5° × 2.5°). GPCP is used as the reference and differences in Jan and July mean precipitation rates are displayed in Fig. 2.3 and 2.4.

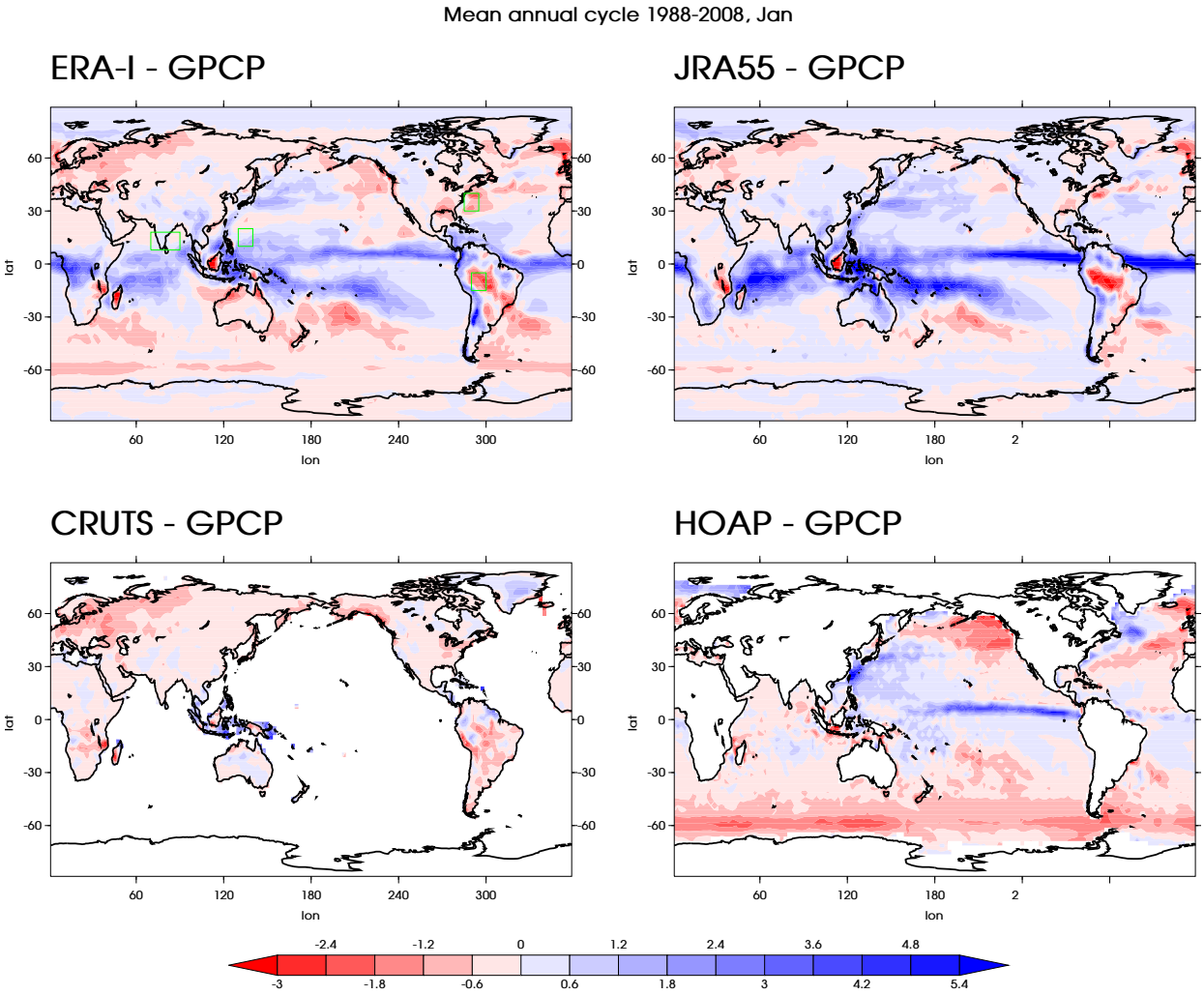

Figure 2.3: Absolute differences of the mean Jan precipitation (mm/day) from 1988 to 2008 between GPCP and (a) ERA-I, (b) JRA-55, (c) CRUTS and (d) HOAPS. Four selected tropical regions are highlighed with green boxes in (a), defining the sample regions of the Warm Pool (10° – 20°N, 130° – 140°E), west Amazon (5° – 15°N, 60° – 70°W), Indian sub-continent (8° – 18°N, 70° – 90°E) and Gulf stream region (30° – 40°N, 65° – 75°W).

Compared with GPCP January precipitation, ERA-I shows a wet bias in the tropical convergence zones (ITCZ, SPCZ, equatorical IO and central Africa), and weak dry biases over the majority of extra-tropical ocean and land, with the exception of a slightly stronger precipatation region in the northern Pacific

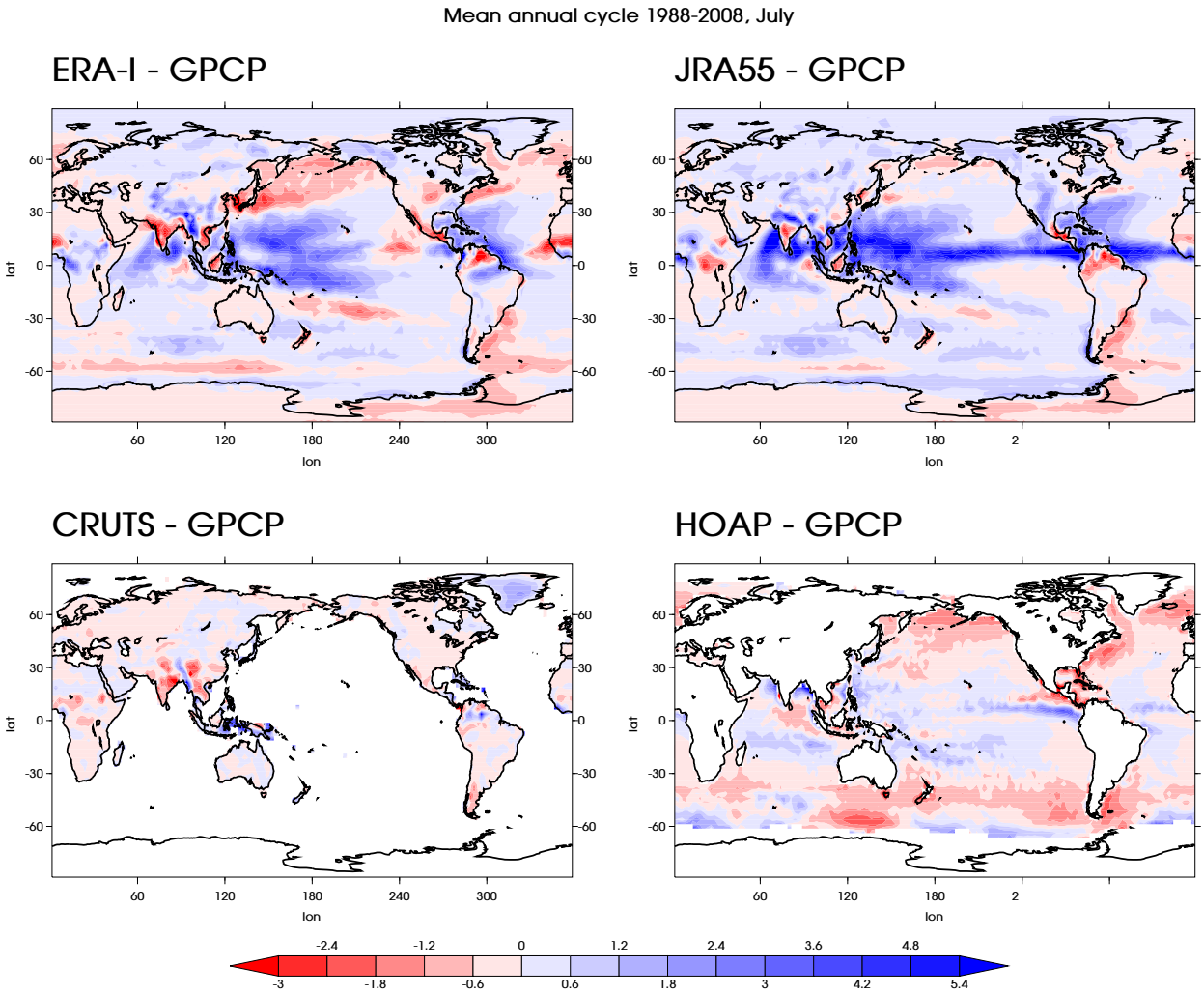

Figure 2.4: As Fig. 2.3 but for July.

storm track. A moderately underestimated rainfall in the Gulf stream region is apparent in ERA-I. The dry biases over extra-tropical land are of comparable magnitudes as the difference between CRUTS and GPCP (Fig. 2.3c). The wet bias found in Congo basin in ERA-I is well-known (*Trenberth et al.*, 2011; *Lorenz and Kunstmann*, 2012) and suggested to be related to a cold bias in its surface temperature analysis (*Lorenz and Kunstmann*, 2012).

JRA-55 mostly shares the similar spatial pattern as ERA-I in January but with larger magnitudes, particularly in the tropics. Continental Australia and southern Africa have more rainfall than in GPCP and ERA-I. The wet bias found in ERA-I central Africa is mostly gone in JRA-55, but the large dry bias over the Amazon is clearly visiable in both reanalyses. This Amazonian dry bias has persisted from their respective predecessors (ERA-40 and JRA-25) (*Bosilovich et al.*, 2008; *Ebita et al.*, 2011; *Kobayashi et al.*, 2015). In the case of JRA-25,

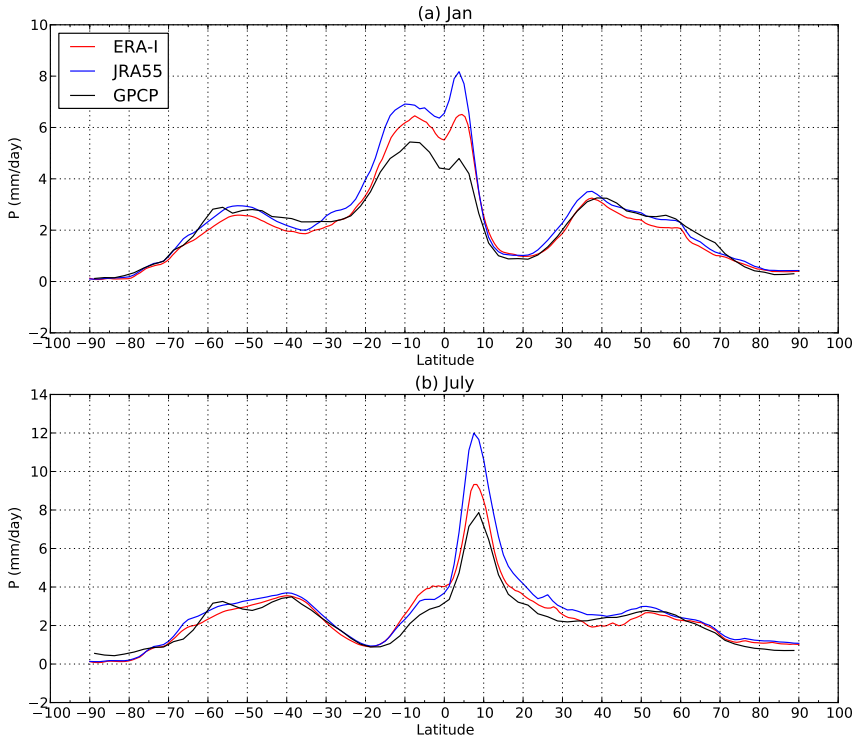

Figure 2.5: Zonal average of long term mean precipitation rates (mm/day) in ERA-I (red), JRA-55 (blue) and GPCP (black), during 1988-2008.

the dry bias was suggested to be the problem of unrealistically high surface pressure. In JRA-55 the observational data from SYNOP stations of surface pressure over Amazon region were entirely excluded, due to their inconsistency with the background fields. A prelimiary evalution by *Ebita et al.* (2011) shows a much improved agreement of Amazon basin precipitation with GPCP (v2.1) in JRA-55 than in JRA-25, during 1980 to 1991, particularly during boreal summer and autumn seasons, but the peak values during boreal winter are still underestimated. Results in Fig. 2.3 (and later in Fig. 2.7) confirm that these biases are largely consistent during the 1990-2010 decades as well. Both ERA-I and CRUTS display some negative biases in Amazon compared with GPCP, but the surface gauge coverage of GPCP and CRUTS is much sparser over the Amazon (except near the Atlantic coast) than other continental regions, thus raising the observational uncertainty.

Over the oceans, HOAPS has higher precipitation over regions with high local variability, including the ITCZ and NH storm track regions, consistent with *Andersson et al.* (2011). Since both HOAPS and GPCP use satellite-based

retrievals to provide oceanic estimations, the observed difference is likely due to the additional Infrared retrievals from GOES and TOVS, and OLR information in the GPCP product. Moreover, HOAPS has been found to have higher mean precipiation rate over the central Pacific region, contrary to other satellite retrievals (*Andersson et al.*, 2011). The co-location of largest wet biases in HOAPS and high precipiation variances will be explored further in the next section.

In July, ERA-I and JRA-55 have in general similar global patterns of biases with respect to GPCP (Fig. 2.4). As in January, JRA-55 has large wet biases over the deep convection regions in the tropics, and the pattern corresponds well with the positive moisture increments (see *Kobayashi et al.* (2015) Fig.11), and therefore is likely to be caused by the spin-down problem of the forecast model that renders a water-leaking atmosphere – a similar problem as in ERA-40 (*Andersson et al.*, 2005; *Bosilovich et al.*, 2008) and ERA-I (*Trenberth et al.*, 2007, 2011).

Over western North America and central Africa, JRA-55 biases are the opposite sign to ERA-I. In the NH, the mid-to-high latitude land is systematically wetter than GPCP and CRUTS for both reanalyses, which seems to be a common problem for reanalyses and is likely related to the increase in summer time convective precipitation (*Lorenz and Kunstmann*, 2012). In the SH, there exists a seasonal north-south shift of a dry bias over the Amazon region in JRA-55. In July the dry bias moves to the north of the basin (Fig. 2.4b, and in Jan it shifts deep into the basin (Fig. 2.3b)). Both reanalyses and CRUTS show some negative biases compared with GPCP over the Indian subcontinent, with ERA-I being the most biased. However, this region of dry bias is surrounded by notable wet biases over the Bay of Bengal, the Indian Ocean and the Arabian Ocean, similar to the land areas in the maritime continent, parts of the Southeast Asian and Madagascar.

The oceanic precipiation in HOAPS shows better agreement with GPCP in boreal summer (Fig. 2.4d), but still has some wet biases of about $4\,mm/day$ over the cold tougue region, accompanied by a dry bias surrounding central America and along the Gulf stream region. Mid-latitude oceanic rainfall in HOAPS is systematically lower than that in GPCP, which relies on SSM/I retrievals for the tropical - subtropical regions but incorporates TOVS inputs in the 40 - 70 latitudinal bands (*Andersson et al.*, 2011; *Klepp et al.*, 2010).

The zonal average plot in Fig. 2.5 reveals that the largest discrepancies among datasets are in the low latitudes. The good agreement shared by both reanalyses and GPCP in the mid-to-high latitudes is compromised in the deep tropics,

following the seasonal shift of the deep convection zones. Overall, JRA-55 has the highest tropical precipitation, followed by ERA-I. This feature is more spread out in boreal winter, covering a meridional range of $15°S - 5°N$, while in summer it is compressed to a narrower band of $5°N - 10°N$.

2.3.2 Precipitation time series for sample regions

To examine the observed discrepancies among datasets in more details, time series of four selected regions are plotted out in Fig. 2.6 - 2.10. Region definitions are listed in Table 2.2, and a rectangular box for each region is shown on Fig. 2.3a.

Table 2.2: Sample region definitions.

Region	Spatial domain	Land/ocean
Warm Pool	$10° - 20°$N, $130° - 140°$E	ocean box
west Amazon	$5° - 15°$N, $60° - 70°$W	land box
Gulf stream	$30° - 40°$N, $65° - 75°$E	ocean box
Indian sub-continent	$8° - 18°$N, $70° - 90°$E	land and ocean

2.3.2.1 Warm pool region

This region is located in the tropical warm pool area, east of the Philippines. It is affected by the Asian monsoon and covered by the ITCZ in boreal summer, therefore serves as a useful measure of the skills in depicting deep tropical convection by the reanalyses. Consistent with previous discussion, both reanalyses appear biased high, with JRA-55 being so to a greater extent (53% more than GPCP on average for JRA-55, and 31% for ERA-I). JRA-55 shows excessive precipitation than other datasets during most of the year (Fig. 2.6b), and its difference peaks in July-Aug, when the ITCZ shifts over this region, enhancing both convection and precipitation frequencies. ERA-I shows good agreement with GPCP and HOAPS in terms of seasonal cycle amplitude (Fig. 2.6b), but the wet season starts earlier in spring and finishes later in winter. All datasets display similar year to year and intra-seasonal variability in general (Fig. 2.6c, d), but JRA-55 and HOAPS have larger variances over different time scales (see also section 2.3.3).

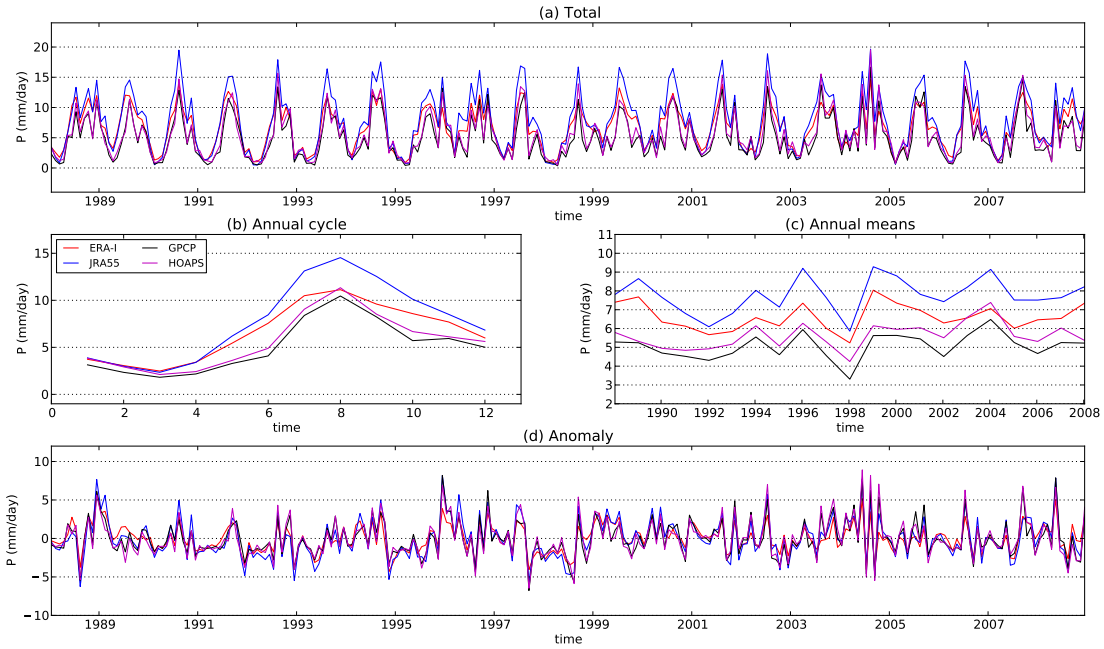

Figure 2.6: Precipitation time series for a sample box over the warm pool in northwest Pacific (10° – 20°N, 130° – 140°E). (a) monthly precipitation time series during 1988-2008. (b) mean annual cycle. (c) annual mean time series. (d) anomalies with respect to the mean annual cycle of each time series.

2.3.2.2 West Amazon

Although improved compared with JRA-25, the JRA-55 still has the lowest mean DJF precipitation over Amazon region (Fig. 2.7b), but is closer to GPCP and CRUTS in JJA. ERA-I shows a weaker seasonal cycle. The poor agreement in year to year (Fig. 2.7c) and intra-seasonal variability (Fig. 2.7d) reflects the large observational uncertainties in this area due to insufficient surface monitoring, which is a shared problem in many other major river basins around the world (*Qian et al.*, 2006; *Biemans et al.*, 2009). In terms of year-to-year variability, ERA-I has the lowest RMS difference (0.32) with GPCP, compared with CRUTS (0.58) and JRA-55 (0.88). The large DJF dry bias in JRA-55 makes its long-term mean precipitation 15% lower than GPCP. Another notable feature is the large year-to-year and intra-seasonal variations in the CRUTS time series (Fig. 2.7c, d). The temporal variance decomposition analysis (section 2.3.3) suggests that this is due to the inclusion of some grid cells with very high, and possibly spurious variances into the time series calculation.

Insufficient data exchanges with the Brazilian network leaves gaps in the Amazon basin, and subsequently introduces large interpolation errors (more on this in Section 2.3.3).

Computations with the Amazon box shifted eastward by 5° longitude (so that it does not include a local maximum in the eddy variances) shows better agreements of CRUTS with others. Similar high variance regions also occur in CRUTS around the circumference of the Amazon basin, in the Himalayas region, maritime continent and Ethiopia (Fig. 2.18d).

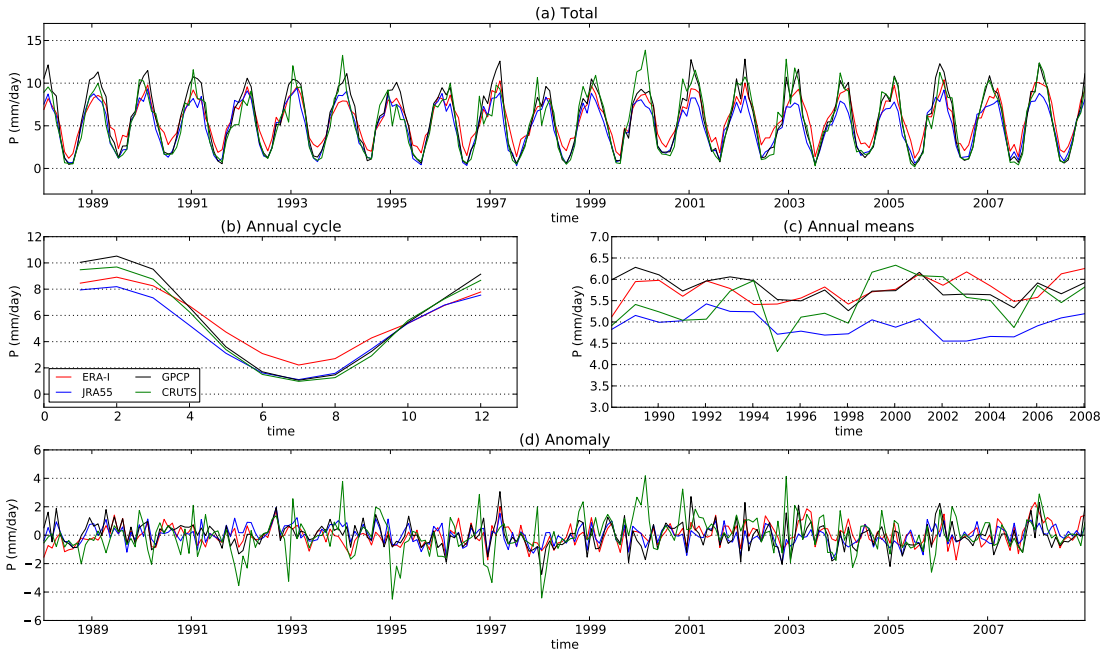

Figure 2.7: Same as Fig. 2.6 but for the west Amazon region.

2.3.2.3 Gulf stream

Precipitation rates over this region feature a semi-annual cycle with alternating high and low values in winter, spring, summer and autumn (*Prat and Nelson*, 2014). This feature can be observed in Fig. 2.8b, but with considerable discrepancies among datasets: HOAPS summer precipitation is so low that the second harmonic of the semi-annual cycle is barely noticable, while JRA-55 is biased wet in summer. Despite discrepancies in the annual cycle, anomaly time series show better agreements among datasets, except that HOAPS features a much higher intra-seasonal variance, which is more visible in Fig. 2.18e.

2.3.2.4 Indian sub-continent

During the summer monsoon season, precipitation in this area has opposite biases over land (dry biases in ERA-I, JRA-55 and CRUTS wrt GPCP, Fig. 2.9b)

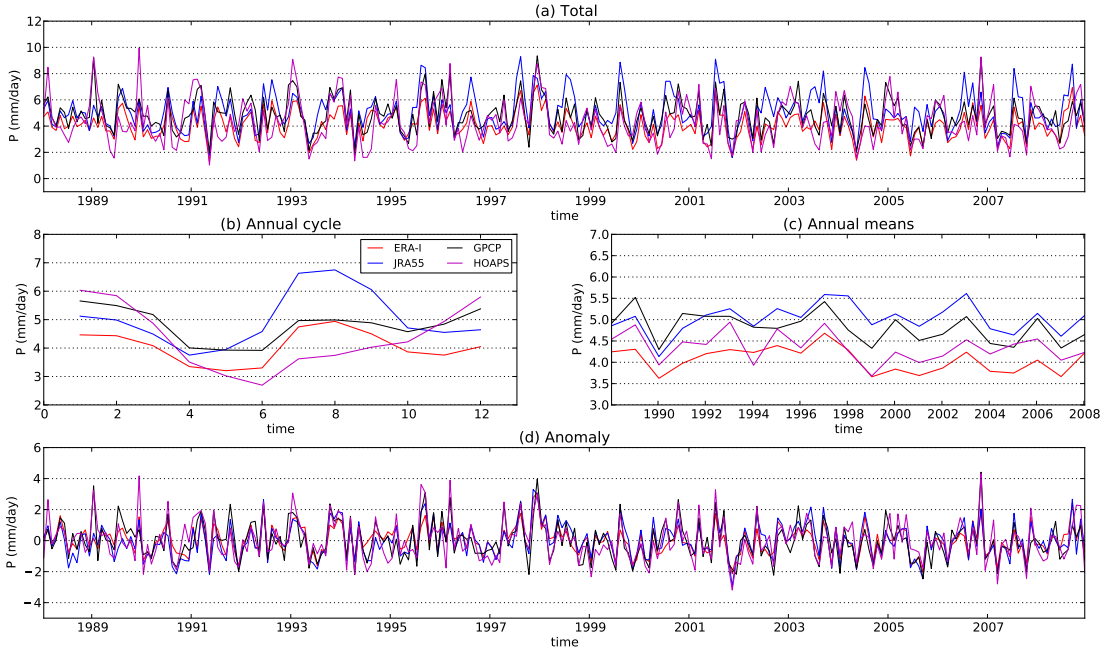

Figure 2.8: Same as Fig. 2.6 but for the Gulf stream region.

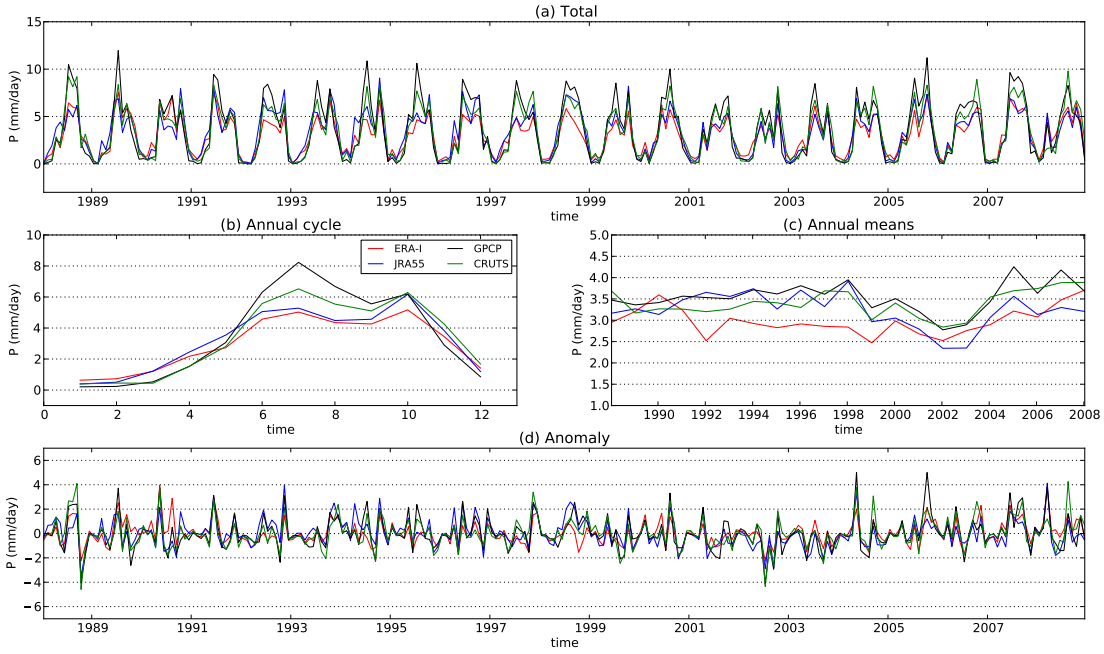

Figure 2.9: Same as Fig. 2.6 but for the Indian subcontinent land areas.

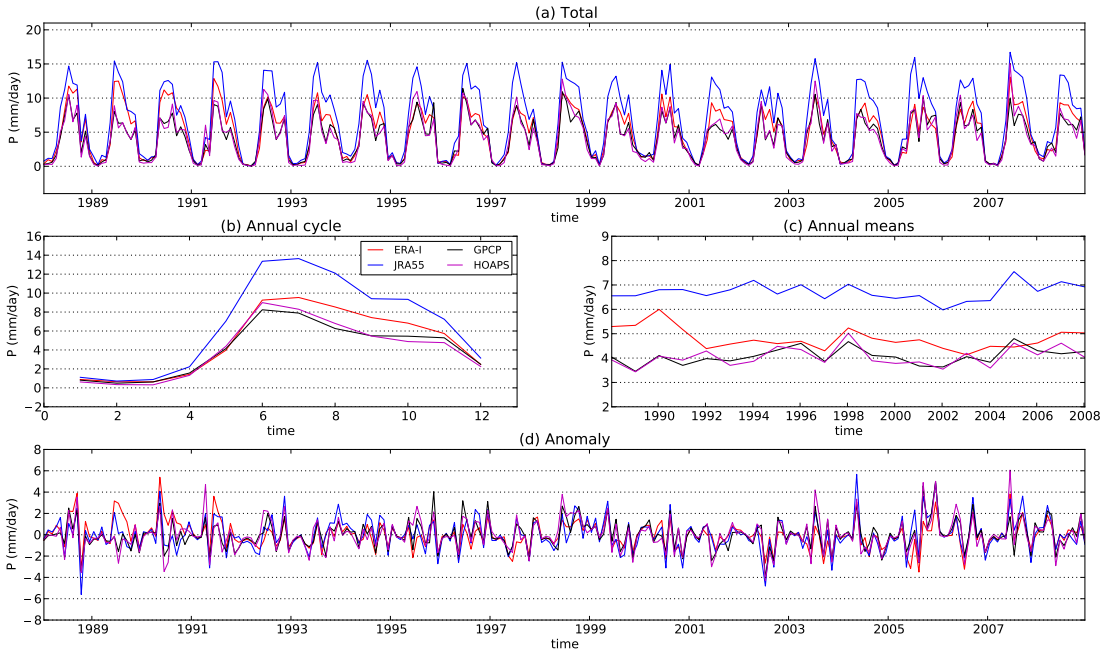

Figure 2.10: Same as Fig. 2.9 but for the surrounding ocean areas.

and over ocean (wet biases in ERA-I, JRA-55 and HOAPS wrt GPCP, Fig. 2.10b). Over ocean, the difference is most prominent in JRA-55, and is part of the leaking tropical atmosphere problem in the forecast model discussed above. Such a systematic bias makes the JRA-55 value 65% higher than GPCP estimates on average (Fig. 2.10c). However, uncertainties in this area in the GPCP estimates are also larger, as represented by the large long-term mean RMS error values over the Bay of Bengal (Fig. 2.11b). An abrupt drop of ERA-I annual mean precipitation in this region occurs around 1992 (Fig. 2.10c). This is likely to be part of a more general problem caused by the drying effect of the 1D+4D-Var rain assimilation scheme which responds to the changing volume of SSM/I radiances from the DMSP satellites (*Dee et al.*, 2011; *Trenberth et al.*, 2011).

Over land, GPCP reports higher values than the other three datasets during June - Oct (Fig. 2.9), when the Indian continent is controlled by the summer monsoon and precipitation rates are enhanced largely by increased frequency of non-showery rains (*Dai*, 2001). Although model-based reanalysis precipitation is generally biased in tropics (*Trenberth and Guillemot*, 1998; *Andersson et al.*, 2011; *Lee and Biasutti*, 2014), few studies have demonstrated such a difference between observations from GPCP and CRUTS, and the large contrast in the sign of the biases over ocean and land. There are relatively big uncertainties in the GPCP July estimations over the Bay of Bengal and along the western coast of the Indian sub-continent, as represented by the 1979-2012 mean July RMS errors

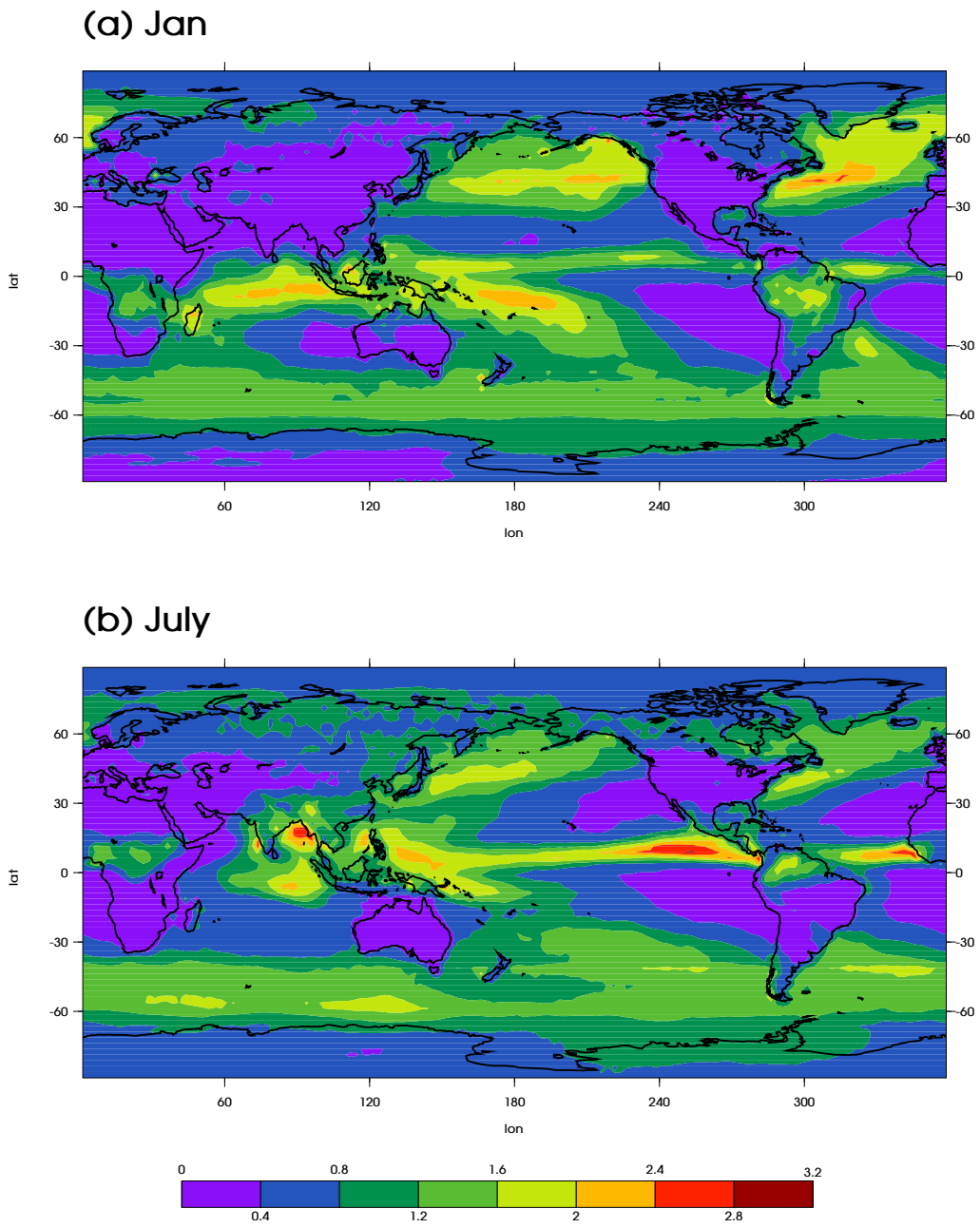

Figure 2.11: Mean RMS error of GPCP precipitation (mm/day) in Jan (a) and July (b), during 1979-2012. The error should be interpreted as dominated by random flucuations.

(Fig. 2.11), but the land errors are not particularly high compared with other tropical regions. On the other hand, although there was a big drop in the station numbers in India available to CRUTS dataset around 1985/86, due to reduced data exchanges after that, there is not enough evidence to imply a drop in the quality of estimation, as interpolation methods attempt to allow for the drop off. Also, the time-means for CRUTS are determined mostly by the 1961-1990 climatology of *New et al.* (1999), based on a much denser network of stations with adjustment for elevation dependence.

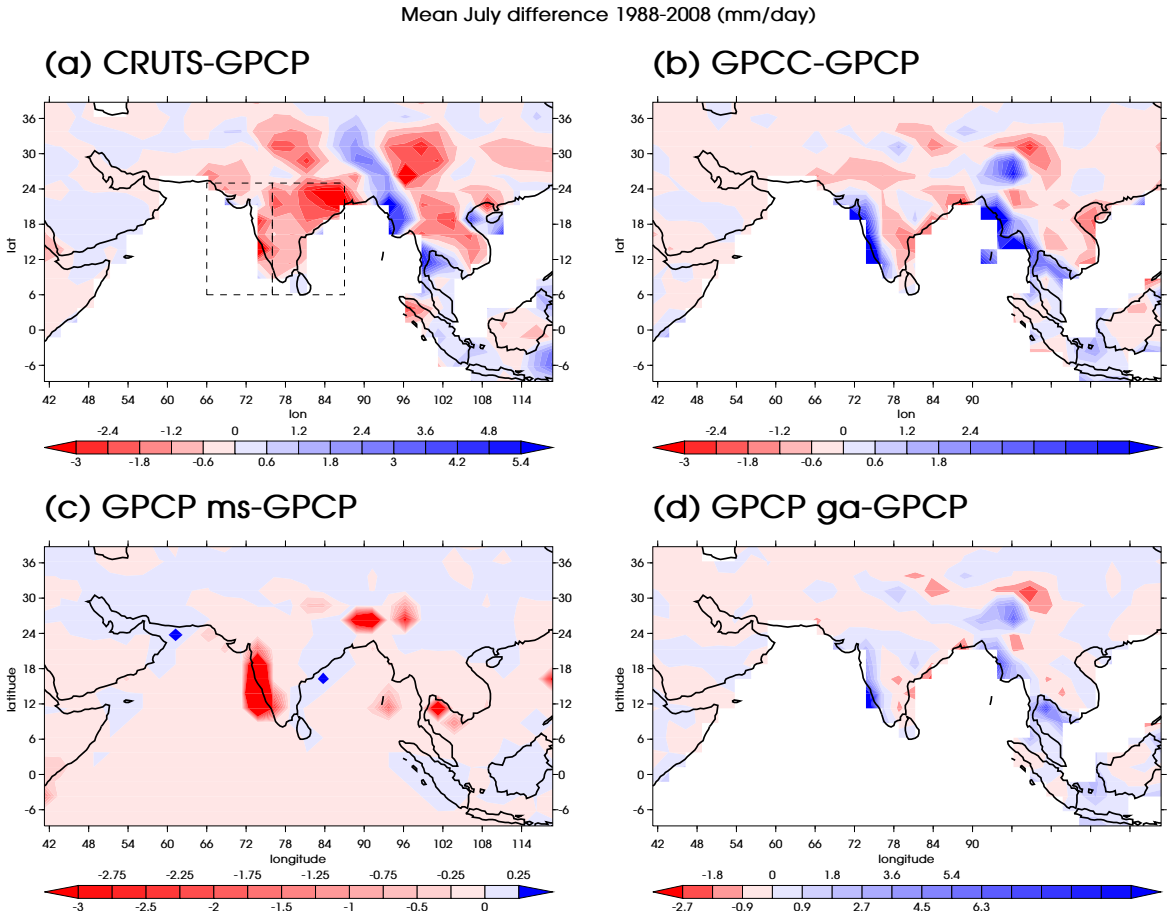

Figure 2.12: Mean July precipitation differences (mm/day) during 1988-2008. (a) difference of CRUTS - GPCP. (b) difference of GPCC - GPCP. (c) difference of GPCP multiple satellite data (GPCP-ms) and GPCP. (d) difference of GPCP gauge data (GPCP-ga) and GPCP. The rectangular region of west/east Indian sub-continent are labelled out in (a).

To diagnose this difference in more detail, the GPCC Full data reanalysis (version 6) data, and two intermediate GPCP products (GPCP-ga and GPCP-ms) during the same time period are compared (Fig. 2.12, 2.14). GPCP-ga (GPCP gauge) and GPCP-ms (GPCP multi-satellite) are the two major components for

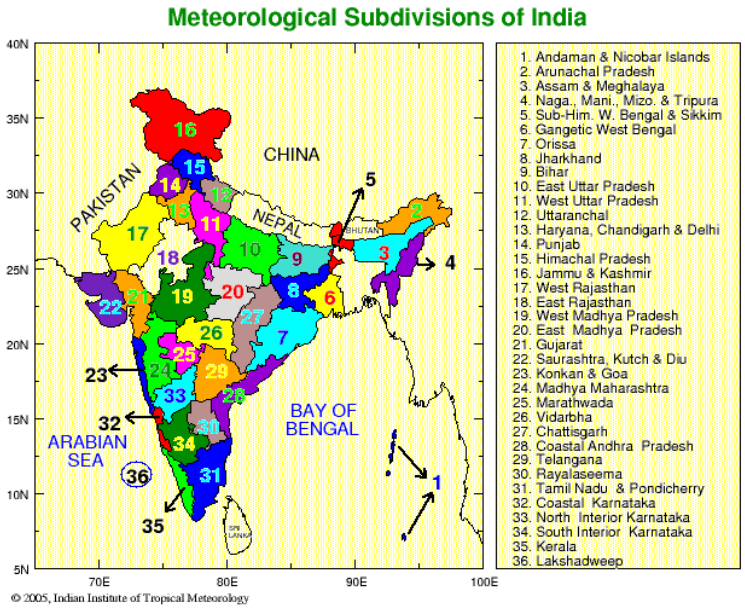

Figure 2.13: Map of the meteorological sub-divisions of India. Figure is from the Indian Institute of Tropical Meteorology.

the combined satellite-gauge product of GPCP. The former is based on version 6 of GPCC Full data reanalysis and v4 of GPCC Monitoring Product, and the latter is a combination of GOES Precipitation Index (satellite IR observations), SSMI (SSMIS) emissions and scatterings, and TOVS IR observations during the SSMI period. The combined satellite-gauge product reflects, subject to some weightings taking into account error variances, both the remote and surface estimations. Therefore some examination of these components could help to trace the source of the observed discrepency.

Fig. 2.12 displays the Indian sub-continent mean July precipitation differences in CRUTS, GPCC, GPCP-ms and GPCP-ga when compared with GPCP. CRUTS is much drier than GPCP (Fig. 2.12a), same as discussed above. GPCC and GPCP-ms have opposite biases wrt GPCP, and since the former forms the basis of the surface source and the latter the remote source for GPCP respectively, the difference reveals the large discrepencies and uncertainties between surface and remote observations, particularly over the western coasts and Ghat regions. The complex topography over this region makes reliable and representative gauge monitoring difficult, and being along the coast line poses extra challenges to satellite observations (*National Research Council*, 2009, chap. 4). Fig. 2.12d shows similar wet anomalies over the western Indian as in GPCC, much as expected.

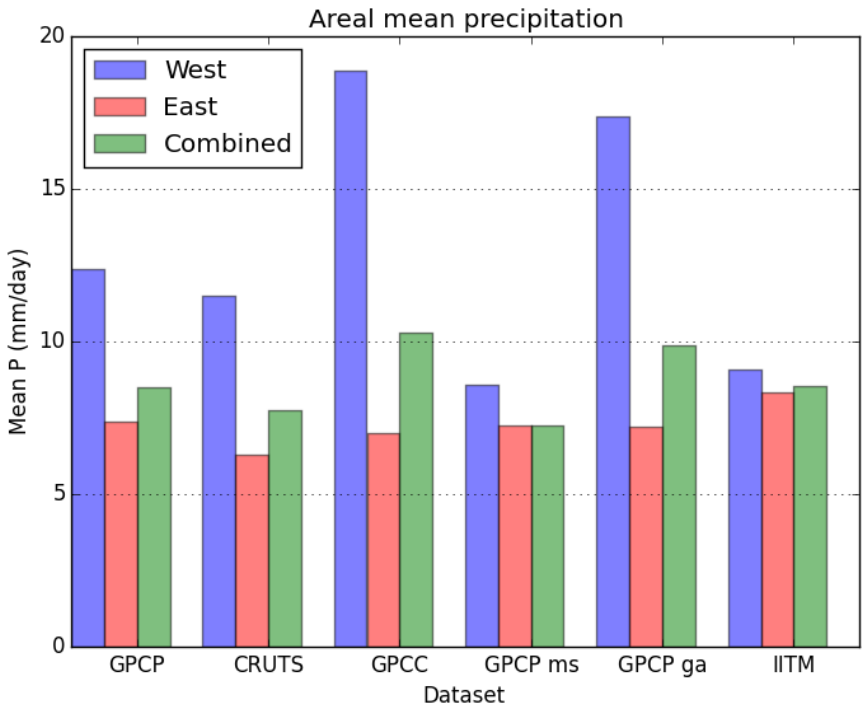

Figure 2.14: Spatial mean of July precipitation (mm/day) over the west (blue), east (red) and the combined (green) region of Indian sub-continent, in different datasets. The west region in IITM is approximated by the areal average over sub-divisions of 21, 22, 23, 24, 32, 33, 34 and 35 (see Fig. 2.13), and the eastern box by sub-divisions of 6, 7, 8, 19, 20, 25, 26, 27, 28, 29, 30 and 31.

Note that some differences are to be expected between the original GPCC data and GPCP-ga, as various corrections are applied to the gauge estimations in GPCP, including wind-induced undercatch, side-wetting and evaporation (*Huffman and Bolvin*, 2011). The gauge undercatch errors are particularly high during winter in the high latitude regions or over mountain ranges where solid-form precipitation dominates (*Lorenz and Kunstmann*, 2012). The Catch Ratio (CR) (catch efficiency of gauge measurements) increases to above 80 % in the low latitudes ($20 - 40°N$) (*Adam*, 2003), but can still be increased by a systematic bias adjustments by $\sim 5 - 10\%$, which is slighted higher than the adjustments following the method of *Legates* (1987). As GPCP adopts the same method of *Legates* (1987) (*Huffman and Bolvin*, 2011), differences of similar magnitude should be expected by the bias correction on a latitudinal band scale.

The Indian sub-continent is further divided into western ($6° - 25°$N, $66° - 76°$E) and eastern ($6° - 25°$N, $76° - 87°$E) sub-regions (as illustrated by dashed boxes in Fig. 2.12a). The western region covers the coastal plains and western Ghats,

where intense monsoon rainfall is observed along a narrow region in summer (*New et al.*, 2002). And the eastern region covers the arid areas on the lee side of the Ghats in the south, and the Chota Nagpur Plateau in the north. The Indian Institute of Tropical Meteorology (IITM) rainfall data (*Sontakke et al.*, 1993) are also included as a reference. This dataset provides monthly mean rainfall estimates over 30 meteorological sub-divisions of Indian (Fig. 2.13), based on a selected network consisting of 306 relatively uniformly distributed stations for which rainfall data are available from 1871. The mean rainfall level in the western box is *approximated* by the areal weighted average over the sub-divisions of 21, 22, 23, 24, 32, 33, 34 and 35 (see Fig. 2.13), and the eastern box by sub-divisions of 6, 7, 8, 19, 20, 25, 26, 27, 28, 29, 30 and 31. Spatial averages of mean July precipitation for both regions and the merged combination are shown in (Fig. 2.14), which shows better agreement among datasets for the eastern region (red), while the western part (blue) contributes most of the overall (green) differences. For the western region, gauge estimates from GPCC are the wettest, closely followed by the GPCP-ga. Multi-satellite (GPCP-ms) estimates are lower by about 54 %, but the combined effect is GPCP being higher than CRUTS by about 1 mm/day. The IITM is slightly higher than the others over the eastern region, possibly due to the approximations in using the sub-divisional averages to represent a rectangular region. However, the western region in IITM is notably lower than GPCC (by about 52 %) and GPCP-ga (by about 48 %).

It is possible to further de-compose and examine the multi-satellite estimates in GPCP into individual contributing sources, as such intermediate products are offerred available on their official website. It is likely that considerable uncertainties and errors exist in both surface and satellite observations over the western region, and further investigations are required to diagnose such differences. On the other hand, good agreements over the eastern region between GPCC gauge and GPCP satellite may suggest a small dry bias in CRUTS.

2.3.3 Temporal variances of precipitation

Precipitation in different regions exhibits different modes of variability and reflects different influences from the key processes that drive precipitation (*Ruane and Roads*, 2007). Therefore correctly representing these frequency characteristics is another requirement for precipitation datasets. In this chapter focus will be placed on time scales from intra-seasonal to inter-annual

using monthly data, while findings based on the diurnal-semidiurnal moisture divergence computed from 6-hourly data (which forms an effective approximation for precipitation) will be discussed in Chapter 3.

Fig. 2.15 compares the temporal standard deviations of different precipitation datasets by showing the ratios of standard deviations. Computation of standard deviations uses 21 years of monthly values, therefore encapsulating variability over intra-seasonal, annual and inter-annual time scales. To decompose contributions from different time scales, variances of the mean annual cycle, annual means (11-month filtered after removing the annual cycle) and the intra-seasonal anomalies (after subtracting the mean annual cycle and annual means) are shown in Fig. 2.16 - 2.18. The contriubtions from cross-term covariances are marginal and therefore not shown.

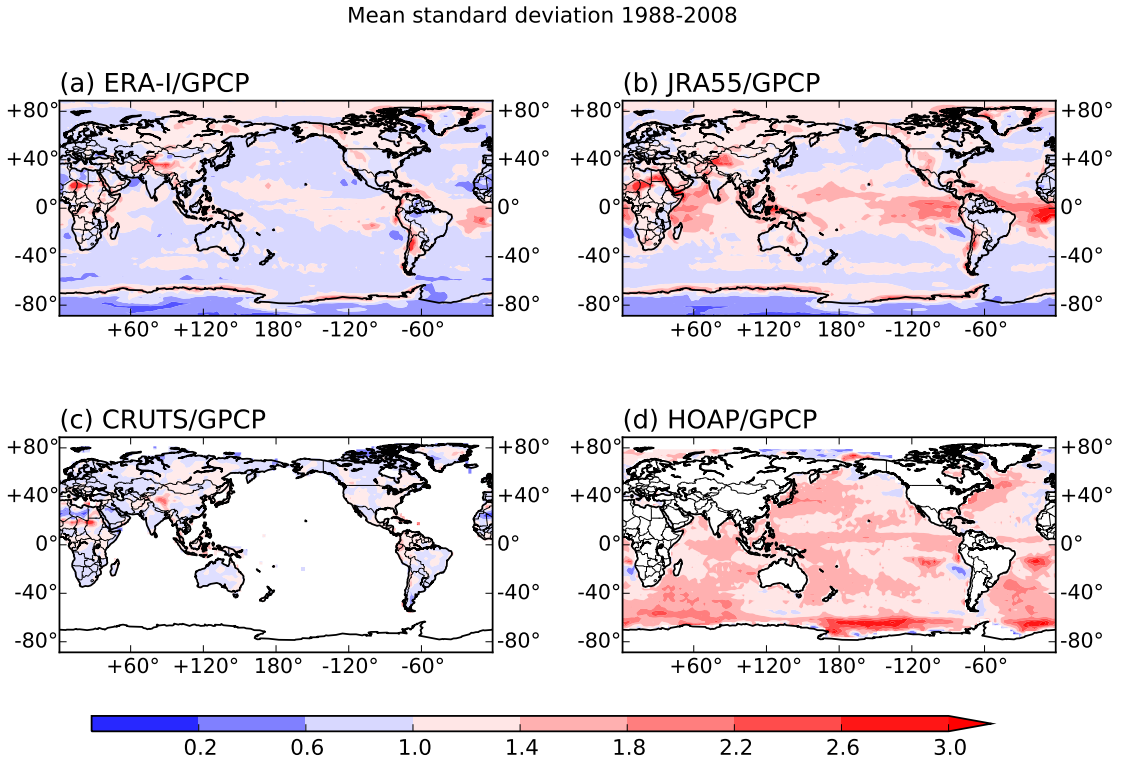

Figure 2.15: Ratios of precipitation temporal standard deviations in (a) ERA-I, (b) JRA-55, (c) CRUTS and (d) HOAPS with respect to that of GPCP. Computation of standard deviations uses 21 years (1988-2008) of monthly values.

ERA-I shows insufficient variability over the Amazon and the Indian subcontinent mainly due to a smaller annual cycle amplitude (Fig. 2.15, Fig. 2.16a, c), consistent with the previous section. Variability over the equatorial Indo-Pacific region is smaller than GPCP (Fig. 2.15a), which could be explained by the less pronounced intra-seasonal variances in ERA-I (Fig. 2.18a,c).

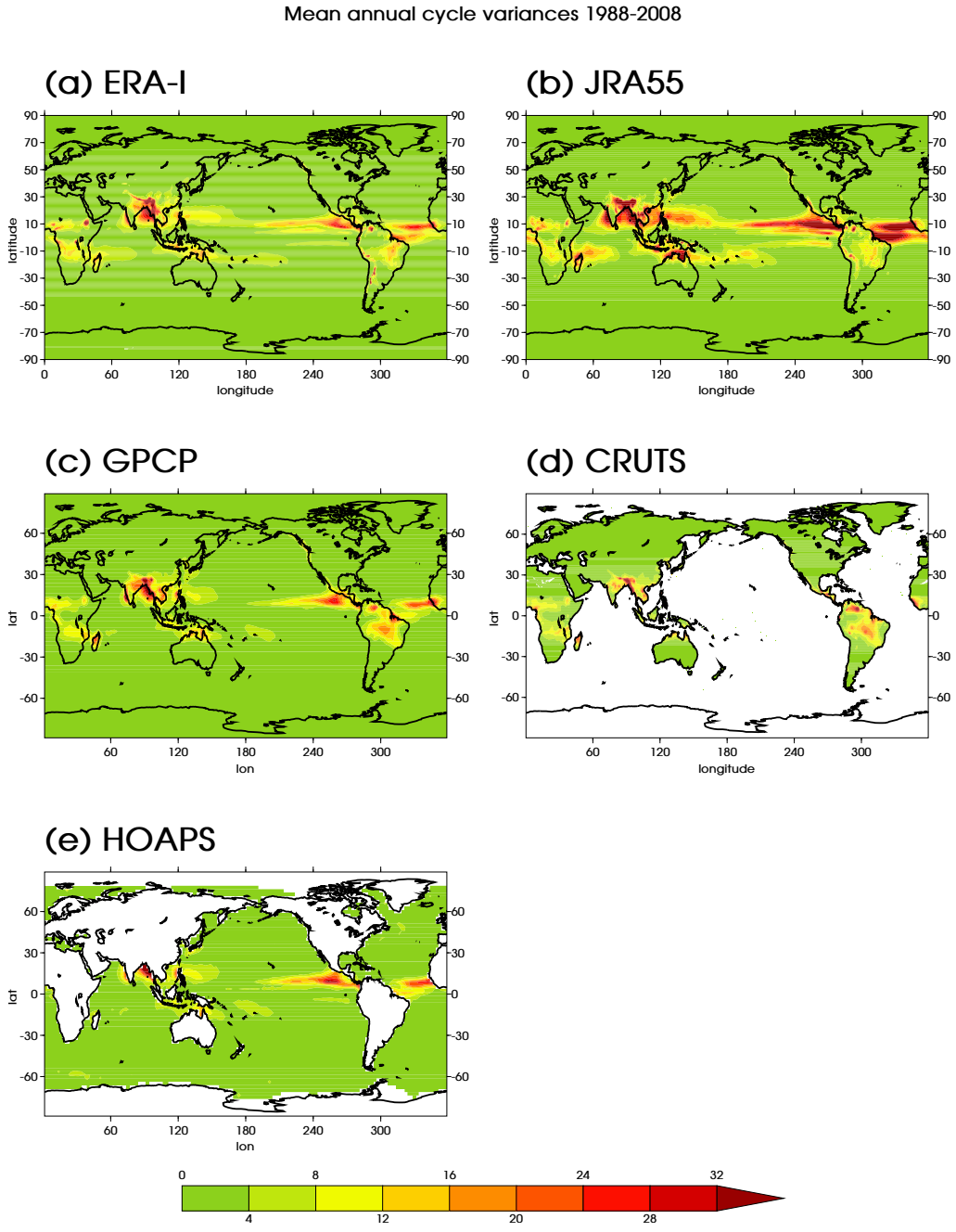

Figure 2.16: Global maps of temporal variances ($(mm/day)^2$) of precipitation associated with mean annual cycle in (a) ERA-I, (b) ERA-55, (c) GPCP, (d) CRUTS and (e) HOAPS.

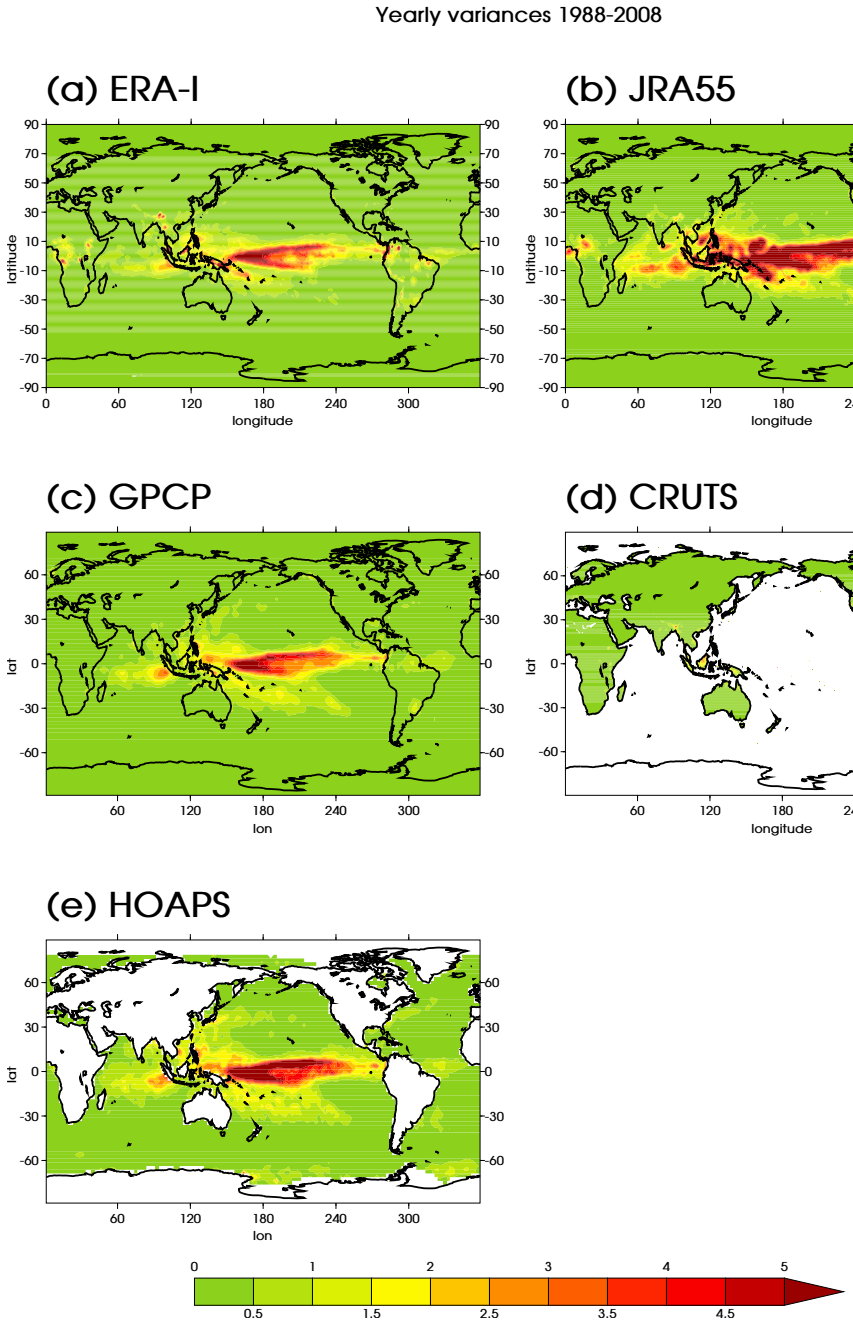

Figure 2.17: Same as Fig. 2.16 but for variances of annual means, therefore relecting year to year variability.

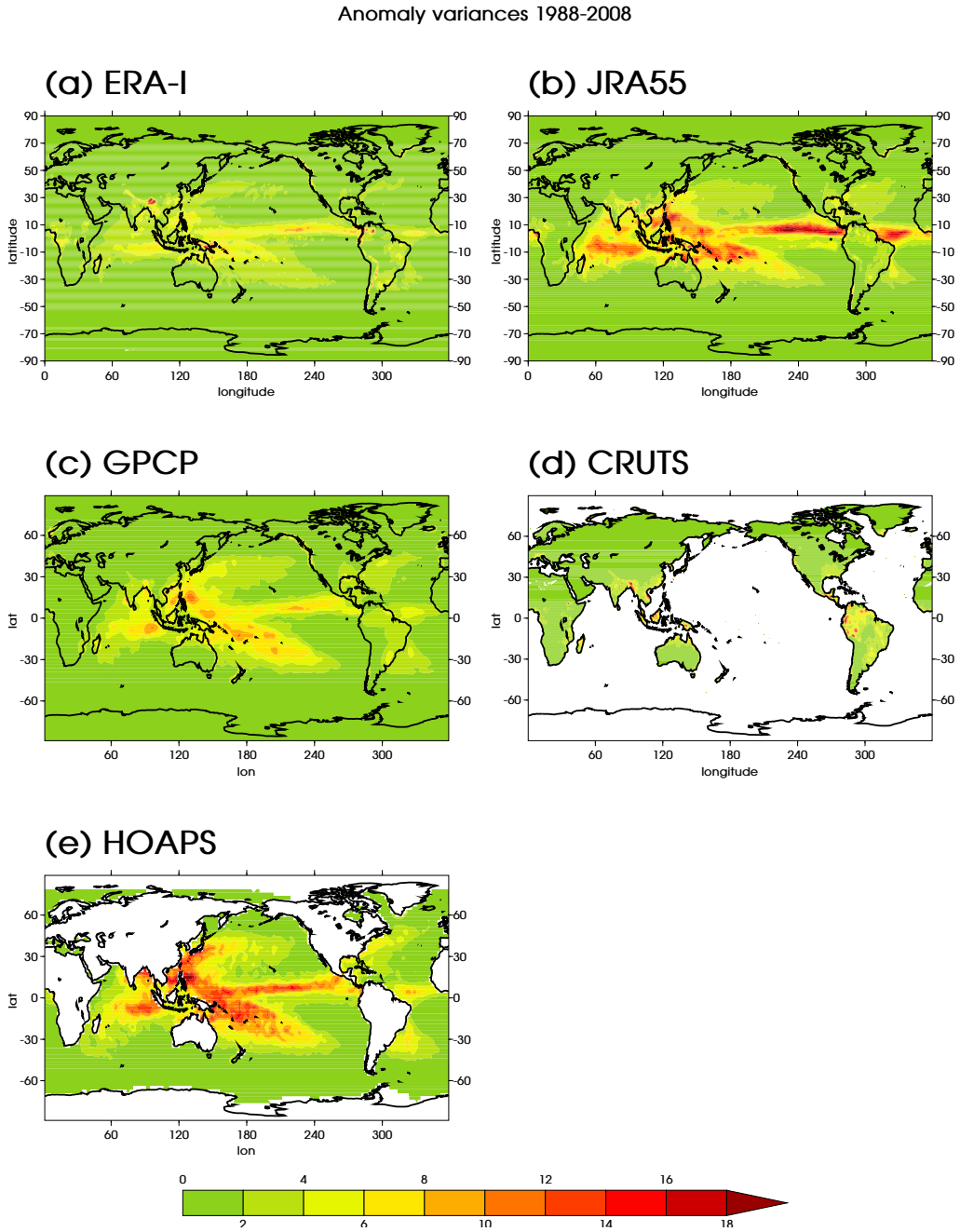

Figure 2.18: Same as Fig. 2.16 but for variances of the intra-seasonal anomalies.

Therefore the impact of MJO cycles on precipitation in ERA-I are likely to be underestimated in magnitudes. Intra-seasonal variances over the Kuroshio current region are also lower than in GPCP.

Variability in JRA-55 is systematically overestimated in the tropical oceans (Fig. 2.15), with considerable contributions from all time scales (Fig. 2.16, 2.17 and 2.18). Variability related to the Asian monsoon, seasonal ITCZ location changes, intra-seasonal MJO and inter-annual ENSO cycles are all notably higher. Similar to ERA-I, the Amazonian variability is underestimated due to the underestimated winter rainfall.

HOAPS shows a higher degree of variability in both tropical and extra-tropical oceans compared with GPCP (Fig. 2.15d). The difference is more pronounced where both the background precipitation rate and variability are high, these regions include the ITCZ, SPCZ, the Warm Pool region and storm track regions in both hemispheres. Unlike JRA-55, the difference mainly stems from the intra-seasonal time scale (Fig. 2.18e). This is partly but not entirely due to the higher resolution of HOAPS: after regridding the $0.5° \times 0.5°$ HOAPS data onto the $2.5° \times 2.5°$ GPCP resolution, the observed difference is reduced but still remains.

As noted during the analysis of precipitation in the west Amazon region, there are some isolated regions with high temporal variance in the CRUTS precipitation. These are particularly prominent in the intra-seasonal variance (Fig. 2.18d). Delaunay triangulation is used to interpolate the station precipitation anomalies onto the CRUTS regular grid (*Harris et al.*, 2014). In areas with sparse observations, station records that have intermittent observations can result in large changes in the triangulation topology, perhaps introducing spurious variance into the grid-cell precipitation. The difference over Maritime continent shown in Fig. 2.15 is partly caused by regridding errors when converting the CRUTS standard deviations to a much lower resolution.

2.3.4 Pattern comparision using Taylor diagrams

To summarize the similarity of the spatio-temporal patterns in these datasets, Taylor diagrams of the precipitation in tropical/extra-tropical land/ocean regions are generated for each season, and the results are shown in Fig. 2.19 - 2.22. GPCP is used as the observational reference, and CRUTS (HOAPS) is used as a second observation to provide information on observational uncertainties

over land (ocean). Note that the observations are not strictly independent and contain shared data sources, therefore the comparisons of GPCP and CRUTS and HOAPS do not encompass all the observational uncertainties, but should be interpreted as a measure of the minimal uncertainty one should expect from a reanalysis dataset (*Bosilovich et al.*, 2008). Uncertainty ranges derived from GPCP error estimates are also displayed on the Taylor diagrams as derived earlier in section 2.2.2.2, and overall biases are illustrated using triangles.

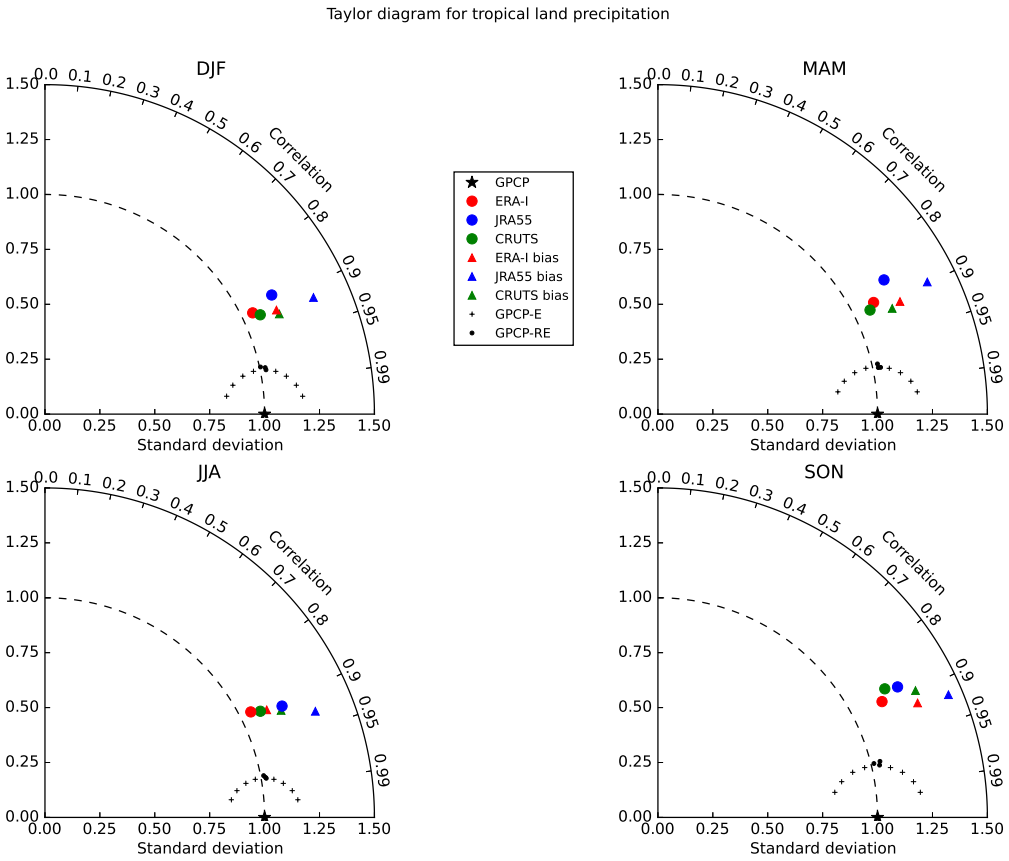

Figure 2.19: Taylor diagrams for the monthly mean precipitation estimates during 1988-2008 over tropical land. GPCP is used as the reference dataset (asterisk), and reanalyses are labelled as solid circles. A second observation-based dataset is included to indicate the observational uncertainty (CRUTS for land in this figure and Fig. 2.21 and HOAPS for ocean in Fig. 2.20 and 2.22). Solid triangles denote the overall biases of the datasets. A bias point located on the right-hand side of the model point indicates positive bias, and left-hand indicates negative. Bias magnitude is measured as the spatail mean difference between a model dataset and the GPCP reference, normalized by the standard deviation of GPCP ($(\bar{\mathbf{M}} - \bar{\mathbf{O}})/\sigma_{\bar{O}}$, see Eq. 2.1). This is represented as the distance between the bias point and the corresonding model point. Observational uncertainties based on GPCP's random error are illustrated by black pluses and dots, and the space they encompass represents the range of uncertainty stemmed from random error perturbations.

For both tropical land (Fig. 2.19) and ocean (Fig. 2.20), ERA-I shows better

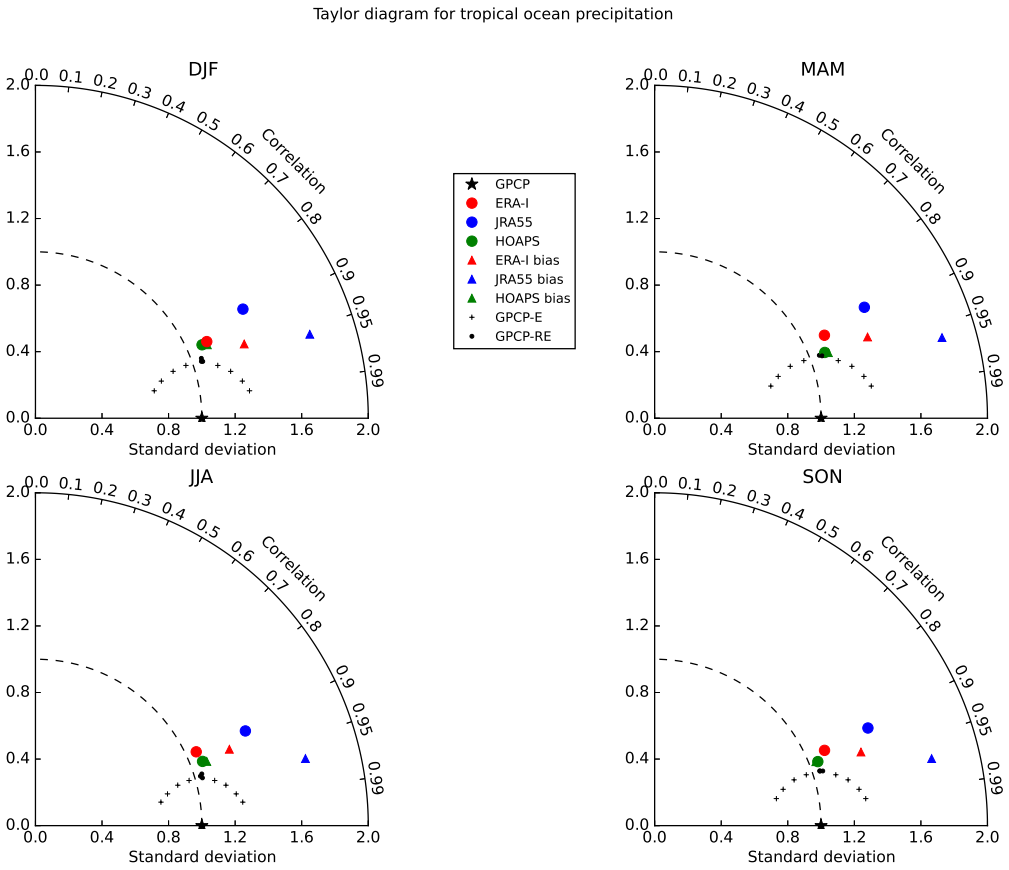

Figure 2.20: Same as Fig. 2.19 but for tropical ocean areas.

agreement with GPCP in both correlation and standard deviation. It is also very close to CRUTS (HOAPS) for all seasons, suggesting comparable quality as those "independent" observations. Consistent with previous discussion, oceanic variability in JRA-55 is overestimated by about 50% for all seasons, and to a lesser extent (20%) over tropical land, but the patterns are still highly correlated. Both reanalyses are biased high in the tropics, with JRA-55's bias being notably higher. And all data points lie outside the uncertainty range of GPCP (except for the oceanic HOAPS in MAM, Fig. 2.20b), suggesting that the differences are significant and are less likely to be caused by errors in GPCP.

Unlike in the tropics, JRA-55 is of comparable quality to ERA-I over extra-tropical land (Fig. 2.21), and out-performs it over extra-tropical ocean (Fig. 2.22). Over extra-tropical land (Fig. 2.21), both ERA-I and CRUTS are dry biased with respect to GPCP in boreal autumn and winter, and this may due to the undercatch corrections applied in GPCP product (*Bosilovich et al.*, 2008). During the rest of the year all datasets are relatively clustered and are aligned along the edge of GPCP uncertainty range, therefore implying

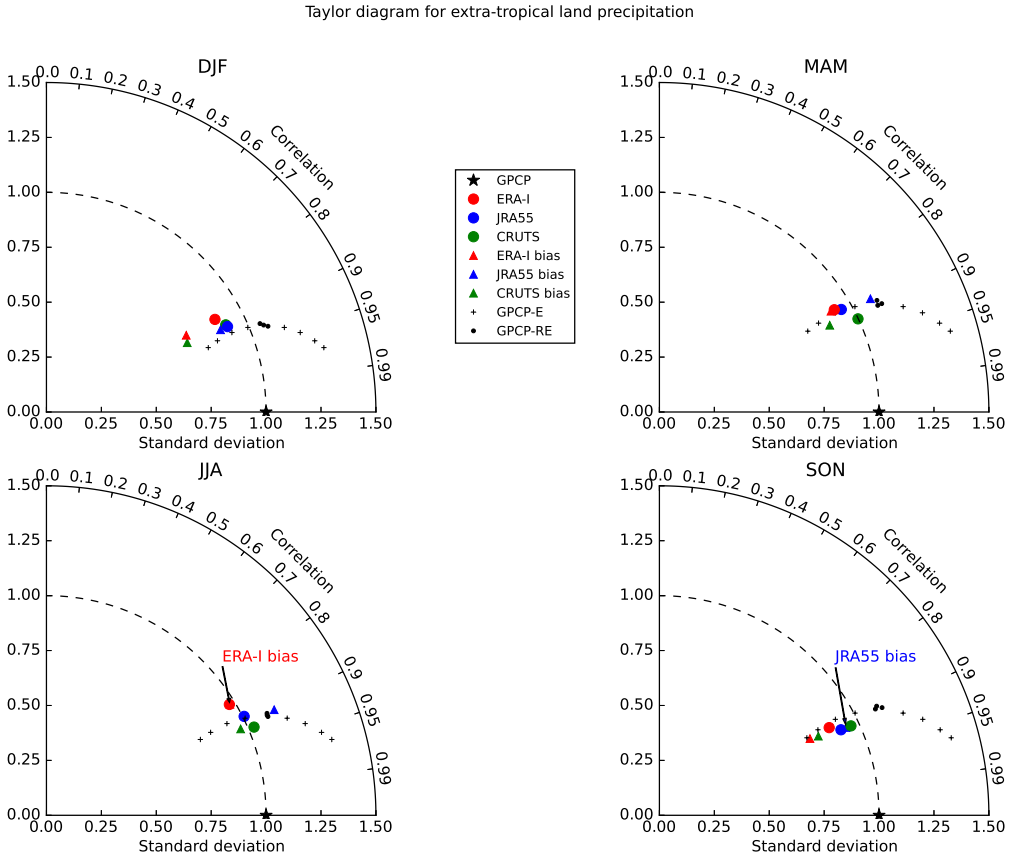

Figure 2.21: Same as Fig. 2.19 but for extra-tropical land areas.

better agreement. Over extra-tropical ocean (Fig. 2.22), JRA-55 matches well with GPCP with little bias, while ERA-I and HOAPS tend to be drier in all seasons. Note that the GPCP errors over extra-tropical ocean are much larger and are mostly distributed over storm track regions in both hemispheres and polarward from about 40° N/S (Fig. 2.11). Satellite observations form the only input data source for oceanic precipitation in GPCP, and SSMI(SSMIS) coverage over the high latitude oceans are limited by the orbit of the DMSP satellites, therefore TOVS(AIRS) retrievals are used to fill up the gaps from about 40° N/S polarward (*Huffman and Bolvin*, 2011). Accompanied with this transition from microwave-based low-to-mid latitude retrieval to IR-based high latitude retrieval, the bias adjustment method for the TOVS estimates also changes (*Andersson et al.*, 2011). Greater uncertainty in these retrievals and methods explain the notable increase in error magnitudes polarward from 40°N/S in GPCP.

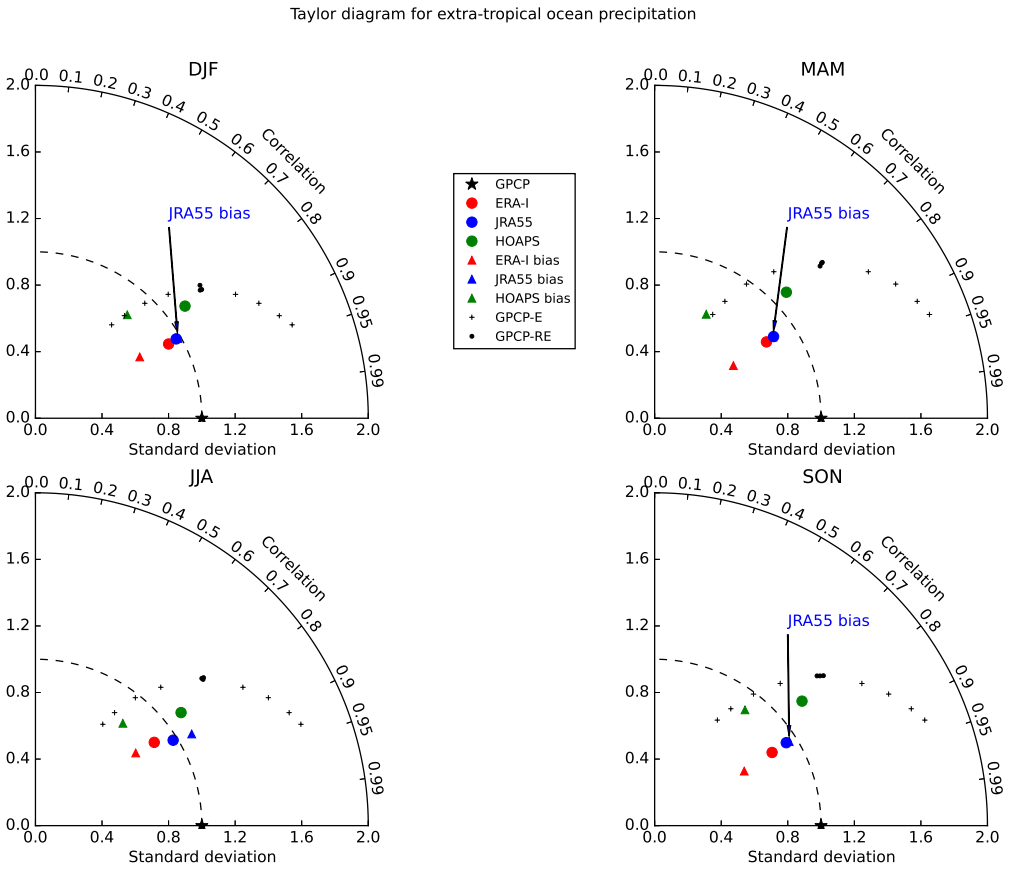

Figure 2.22: Same as Fig. 2.19 but for extra-tropical ocean areas.

2.4 Conclusions and Discussion

This chapter assessed the challenges in providing a reliable global scale precipitation estimate, and reviewed some known problems in the atmospheric reanalyses and observations. Based on knowledge from the literature, ERA-I and GPCP were selected as the best model- and observation-based products to evaluate the newly released JRA-55. Comparison of the long-term mean precipitation rates and variability magnitudes reveals strengths and deficiencies in both ERA-I and JRA-55.

Both ERA-I and JRA-55 tend to over-estimate precipitation in the tropics, particularly for JRA-55 which is biased high by around 4 mm/day. The regions of high biases co-locate with regions of positive humidity analysis increments in JRA-55 (*Kobayashi et al.*, 2015), and is likely to be caused by the spin-down problem of the forecast model that renders a water-leaking atmosphere. ERA-I has the similar problem but to a lesser extent (*Trenberth et al.*, 2007, 2011) . The examination of some selected tropical regions suggests that regional biases in

the mean precipitation are connected to biases in either the strength or phase of the seasonal cycle.

Large discrepancies are observed over the Indian sub-continent among reanalyses and observations. The difference arises from disagreements between surface gauges and satellite measurements. High gauge estimates over the western Ghat regions from GPCC, which is then inherited by GPCP, make large contrast to the satellite retrievals in GPCP and the gauge values from CRUTS.

In the mid-to-high latitudes, JRA-55 out-performs ERA-I in the matches of both spatial patterns and magnitudes of variances, as illustrated in the Taylor diagrams. ERA-I and CRUTS have slightly lower winter precipitation in extra-tropical regions. Both reanalyses overestimate summer time precipitation in mid-to-high latitudes, which is a shared problem among many reanalyses (*Lorenz and Kunstmann*, 2012), and confirms that the deficiency in the representation of convection is still a large source of uncertainties.

Based on the above conclusions, some suggestions could be offered to users in choosing between ERA-I and JRA-55 for precipitation-related studies: for the tropics, caution is needed in using either of them, as they both suffer from a leaking atmosphere problem and systematically over-produce rainfall, but this is particularly pronounced in JRA-55, thus giving some preference to ERA-I. In addition, the Indo-Pacific region in ERA-I has insufficient variability, and the effect of intra-seasonal variability (e.g. MJO cycles) on precipitation is less pronounced than in GPCP, which in turn is less pronounced than JRA-55 and HOAPS. Variability in JRA-55 seems to be overestimated over time scales from intra-seasonal to inter-annual. Over the problematic tropical land regions, like the Amazon and central Africa, the lack of sufficient observations makes a solid validation impossible, and no evidence of improvement has been seen in recent decades. For studies with a mid-to-high latitude focus, the new JRA-55 product serves as good candidate.

We did not analyse precipitation variability over longer time scales, which is an important climate change topic and has significant social implications. However, due to the inherent heteorgeneity of reanalysis products, analysis of long-term or decadal changes requires careful treatments of the data (*Bengtsson et al.*, 2004), or the use of specialized reanalysis that are designated for such purposes (e.g. 20CR reanalysis or the newly produced ERA-20C).

In generating the Taylor diagrams we explored a novel method to address

the observational uncertainties by using the estimated errors of the reference dataset. Such error data provide valuable information and put the variables in an uncertainty context, thus allowing more realistic and objective validations. However, not many studies make full use of such information. One of the earlier efforts is *Janowiak et al.* (1998), which compared NR1 precipitation against GPCP with the random errors of GPCP taken into consideration. The Augmented Lagrangian multiplier method explored here allows such considerations to be incorporated into the highly summative Taylor diagrams. However, some technical details remain to be clarified, for instance should it be proved that the correlation-minimized uncertainty variables are distributed along a strict section arc, and encompass the full range of uncertainties in spite of the locally constrained error distribution, then the Augmented Lagrangian multiplier computation could be replaced by a simpler calculation of the maximum/minimum standard deviation uncertainty variables, plus the average of a few cases with randomly sampled errors (which are all computationally trivial), with the uncertainty range depicted by an arc going through them.

Chapter 3

Evaluation of atmospheric hydrological cycle – evaporation, total precipitable water and the water budget

3.1 Research Background

In the previous chapter, we reviewed the state-of-art global scale precipitation observations and evaluated precipitation in the newly released JRA-55 reanalysis. Significant biases were identified in the latest reanalyses in the rain-rich low latitudes, highlighting the drawbacks in the current numerical models and the uncertainties in the large scale precipitation estimates. However, even greater uncertainties lie in the evaporation/transpiration observations, which are seldom observed directly at a continental/global scale (*Trenberth et al.*, 2011; *Zhang et al.*, 2010). Oceanic evaporation provides 86% of the water to fuel the global hydrological cycle (*Gimeno et al.*, 2010), and local evaporation plays a significant role in supplying the precipitation over a considerable proportion of the land masses (*van der Ent et al.*, 2010). Therefore, a good knowledge of the atmospheric load of water and the evaporation/transpiration would form a solid ground for a reasonable precipitation estimate. Incorrect humidity forcing can potentially lead to biased precipitation simulations in numerical models, and violations of a closed water budget highlight limitations of both observations and models.

This chapter will follow up the discussion of the large scale hydrological cycle and shift the focus to evaporation/evapo-transpiration (E/ET) and total column water (TCW) estimates in observations and reanalyses. After assessing the major ingredients of the atmospheric water budget, we will consider the budget residuals in ERA-I and JRA-55 reanalyses. A clustering analysis is used to classify the atmospheric hydrological cycle over global land into a few regimes, allowing us to associate the budget residuals with contextual characteristics of the hydrological cycle. Results regarding individual budget terms are then used to help trace the origins of the largest residuals, and consequently reveal the causes responsible for the non-negligible residuals in ERA-I and JRA-55.

3.1.1 Land evaporation observations

Land evaporation/transpiration is a central process that links the water, energy and carbon cycles. Globally, recycling of continental ET is responsible for 67 % of rainfall over land (*van der Ent et al.*, 2010) and over 50 % of the solar energy absorbed by land is converted to latent heat through ET (*Jung et al.*, 2010; *Hartmann et al.*, 2013), thus making it an important modulator of the soil moisture, surface temperature and precipitation (*Wang and Dickinson*, 2012; *Jung et al.*, 2010; *Koster et al.*, 2004). Knowledge of large scale ET is important to our understanding of the energy and water cycle changes in a warming climate, and a robust observation of that is essential to the assessment of the prediction of future changes (*Rodell et al.*, 2015).

However, the current estimates of global ET have considerable uncertainties. Long-term annual mean ET has an uncertainty of 50 % among datasets (*Vinukollu et al.*, 2011; *Jiménez et al.*, 2011). This is to a large extent due to the limited spatial representativeness of direct ET measurements (*Wang and Dickinson*, 2012), and various limitations in the large-scale, indirect measurements.

Eddy covariance flux tower sites (e.g. FLUXNET, (*Baldocchi et al.*, 2001)) provides regional scale ET measurements, but their total number around the globe is still quite limited (720 tower locations out of which 464 are active, at the time of writing) and the distribution is irregular and biased towards the mid-latitudes in the NH (see Fig. 2 in *Jung et al.* (2009)), therefore the representativeness of these point-scale in situ measurements is still an open question (*Trenberth et al.*, 2011).

Indirect estimates that benefit from the spatial and temporal coverage of satellite retrievals rely on the quality of the empirical or semiempirical model. The most commonly used models include the Monin-Obukhov similarity theory (MOST) which provides the foundation for many land surface models (LSMs) (*Wang and Dickinson*, 2012), and the Surface Energy Balance System (SEBS) which estimates ET through sensible heat flux estimations (*Vinukollu et al.*, 2011). The Penman-Monteith model and its simplifications such as the Priestley-Taylor model are also widely applied, and various derivations have been developed to better account for vegetation types (*Wang and Dickinson*, 2012; *Vinukollu et al.*, 2011). Both Penman-Monteith and Priestley-Taylor model evaluate Potential Evapo-transpiration (PET), which is closer to the observed evaporation over energy-limited regions such as wetlands. The accuracy of surface temperature and soil moisture observations from remote sensing is often an additional barrier for satellite-based estimates. Other approaches include quantifying the basin or continental scale ET through the surface or atmospheric water budget, and up-scaling of the FLUXNET observations using a machine learning algorithm (*Jung et al.*, 2009, 2010).

The LandFlux-EVAL project is one of the recent efforts to resolve the uncertainties in global ET among various datasets. ET estimates are categorized into four main classes depending on the conceptual framework of the dataset: diagnostic class (that is more observation-based and uses simple empirical models), LSM class, reanalyses class, and AR4 climate model simulations (*Mueller et al.*, 2011). Systematic differences are observed among classes and datasets coming from the same category tend to cluster. A considerable amount of uncertainty is related to models (*Vinukollu et al.*, 2011), but forcings can be critical for the resultant ET patterns, particularly for precipitation and radiation (*Vinukollu et al.*, 2011; *Mueller et al.*, 2011, 2013). Other factors include vegetation types and their representation in models, the stomatal conductance effect and its responses to various atmospheric forcings including a rising CO2 level. Land use change is likely to have an important role in affecting regional ET, but is largely absent in reanalysis products (*Hagemann et al.*, 2005).

Overall, a robust and consistent global scale land ET reference dataset is still lacking. Unlike in the case of precipitation where a good quality reference could be used as a surrogate truth to evaluate a new data product, no such reference exists for ET, instead, one should include an ensemble of multiple datasets spanning a range of categories as the reference (e.g. *Mueller et al.* (2011)). Alternatively, the surface water budget can be used as a physical

constraint on ET, which will transfer the uncertainties in ET onto the estimates of precipitation, surface runoff and soil moisture storage change. On a long-term annual mean time scale when the storage change term is negligible, this transference of uncertainty still pays off and gives a more reliable estimate, particularly in the well gauged basins (*Vinukollu et al.*, 2011). Therefore, we restrict the evaluation of land ET in JRA-55 and ERA-I to long-term annual means and use an inferred ET value by subtracting surface runoff (GRDC-WBM, (*Fekete et al.*, 2000)) from precipitation (GPCC, (*Becker et al.*, 2013)) as the reference.

3.1.2 Ocean evaporation observations

Similar to the land surface, ocean surface water fluxes are estimated with much better spatio-temporal resolution using remotely sensed variables compared with the in situ measurements obtained from ships and buoys that suffer from inherent undersampling. However, lack of in situ data coverage over oceans makes the calibration and validation of satellite-based estimates difficult, and is responsible for the poor performance of reanalyses in their evaporation and precipitation estimates (*Andersson et al.*, 2011; *Bourras*, 2006). Various satellite-based E products are constructed on a set of bulk formulae that relates turbulent flux to meteorological variables such as SST, surface wind, air temperature, humidity and radiation. Among these the vertical distribution of humidity is found to have a large influence on both satellite-based products (*Bourras*, 2006) and reanalyses (*Bosilovich et al.*, 2011; *Kumar et al.*, 2012; *Brown and Kummerow*, 2014). In the tropics where observations from moored buoys are available (e.g. Global Tropical Moored Buoy Array), reanalyses tend to show systematic high biases with respect to OAFlux (*Bosilovich et al.*, 2011), which in turn is slightly overestimated compared with buoy fluxes (*Kumar et al.*, 2012). Outside the tropics, datasets show better agreement with each other, though in situ observations are largely absent.

3.1.3 Total column water observations

There exists a strong relationship between the air temperature (largely relecting underlying SST), total column water (TCW) and precipitation. The water holding capacity of the atmosphere is defined by Clausius-Clapeyron (C-C) function, which predicts a $\sim 7\,\%$ increase in the atmospheric vapour load for

1°C of mean surface temperature rise (*Held and Soden*, 2006). Sufficient vapour is a prerequisite to rainfall, and this thermodynamic relationship between TCW and precipitation is particularly strong in the low latitudes, where large scale mean-flow is the major component of atmospheric circulation (*Trenberth*, 2011). Based on this relationship, the strength of the hydrological cycle can be defined in a reservoir-flux model: a faster increase in TCW rates with respect to the mean precipitation implys slower recycling and longer life time of water (*Held and Soden*, 2006; *Trenberth*, 2011). Unlike evaporation and precipitation, reanalysis TCW estimates are combined observation-model products, and congruences with remotely sensed TCW observations are expected. Therefore, the analysis of TCW in reanalyses will be approached from a combined P-TCW relationship perspective, and results obtained are helpful in explaining the observed P biases in reanalyses.

Section 6.2 introduces the datasets used in this chapter in addition to the two reanalyses ERA-I and JRA-55. The hydrological regime classification using a K-means algorithm is explained in full detail in this section. Section 6.3 presents the evaluation of terrestrial ET, oceanic E and TCW. After which the water budget residuals are analyzed in a hydrological regime framework, and causes of the largest residuals in both reanalyses are examined.

3.2 Data and methods

3.2.1 Evaporation observation data

As discussed in the previous section, a reliable reference dataset for land ET is lacking, so a budget-inferred approach is adopted here. Gridded land precipitation from GPCC (*Becker et al.*, 2013) is used in preference to GPCP due to its higher spatial resolution ($1.0° \times 1.0°$ compared with $2.5° \times 2.5°$). This allows a more accurate measure of mean ET when gridded values are areally integrated over global land. A runoff climatology product GRDC-WBM (*Fekete et al.*, 2000) is obtained from the Global Runoff Data Center (GRDC). This dataset combines streamflow observations with water balance model estimates to give a continuous gridded field of monthly climatological runoff at a resolution of $0.5° \times 0.5°$ (*Fekete et al.*, 2000).

The inferred ET from surface water budget is defined as:

$$ET = P - R - dS \tag{3.1}$$

where P is precipitation, R is surface runoff and dS is the change in local water storage, all represented in mm/day. The storage change term dS can have substantial seasonal variations and may inter-annually change due to human water use (*Wang and Dickinson*, 2012), therefore the assumption of dS being negligible is only valid when taking the long-term annual means (*Wang and Dickinson*, 2012), thus limiting our analysis to only the climatology.

Two oceanic evaporation datasets are used as the observational reference. OAFlux (*Yu et al.*, 2008) provides evaporation estimates over the global open ocean at 1-degree resolution for 1958 - 2012. This product blends surface meteorological variables from multiple sources including satellites and NWP reanalysis products in a variational manner that minimizes the least square fit error at each time step (*Yu et al.*, 2008). Then version 3.0 of the COARE bulk algorithm is applied to compute the evaporation. From an energy-budget point of view, OAFlux was found to close the budget better than other alternatives (*Trenberth et al.*, 2009, 2011). Accompanying the monthly E values, OAFlux also provides an error estimate for each corresponding month at each grid box, thus allowing uncertainty estimation to be carried out. The augmented Lagrangian multiplier method introduced in the previous chapter is applied to this random error, and the resultant uncertainty range is shown on the Taylor diagrams in the comparisons of oceanic E.

HOAPS (v3.2, *Andersson et al.* (2010)) was introduced in the previous chapter to evaluate oceanic precipitation. As it is designed with the principle of using one observation framework (SSM/I only) to derive multiple variables (*Andersson et al.*, 2010), computations involving multiple variables can have better homogeneity and internal consistency. Therefore it is selected here as another observational reference for both E and TCW.

3.2.2 Total column water vapour data

Besides HOAPS, the RSS total precipitable water vapour (TPWV7, available at http://www.remss.com/measurements/atmospheric-water-vapour/) is also obtained to facilitate the comparison of TCW. This dataset provides 1-degree TPW estimates by merging version-7 of the passive RSS microwave geophysical ocean products. TPW values are obtained from SSM/I F08 through F15, SSMIS

F16 and F17, AMSR-E and WindSat radiometers, which have been carefully inter-calibrated at the brightness temperature level, making it suitable for climate studies. Data are available for 1988 - 2012, from which the period 1988 - 2005, when HOAPS data are available, is retrieved for computation.

3.2.3 Moisture divergence

Horizontal moisture divergence is computed following *Trenberth and Guillemot* (1998):

$$\bigtriangledown \cdot \mathbf{Q} = \bigtriangledown \cdot \frac{1}{g} \int_0^{P_s} q\mathbf{v} dp \tag{3.2}$$

Specific humidity (q), horizontal winds ($\mathbf{v}$) and surface pressure (Ps) at 0.75° × 0.75° resolution are obtained from ERA-I for the period of 1979-2012. Horizontal moisture fluxes are computed on each of the 60 sigma levels using 6-hourly data, to capture as much covariance of q and $\mathbf{v}$ as possible. Since the daily and subdaily data from JRA-55 were not released at the time of writing, only pre-diagnosed monthly moisture divergence data were obtained.

3.2.4 Budget residuals

The atmospheric water budget of an air column is defined as:

$$\frac{dS}{dt} = E - P - \bigtriangledown \cdot \mathbf{Q} - R \tag{3.3}$$

where dS/dt is the tendency of water storage, and R is an unphysical residual term that stems from the errors/uncertainties in the measurements of other physical terms, and represents the violation of a closed water budget. Specific to reanalysis, it is the result of the data assimilation scheme which assimilates observations to the forecast fields to form an analysis at the end of each time step, creating a difference between the analysis and forecast fields, thus the name "analysis increment" is given (*Trenberth et al.*, 2011; *Mo and Higgins*, 1996; *Dee et al.*, 2011)

Defined in the above manner, positive residuals suggest that the atmosphere is "flooding", meaning excessive moisture input (E), or insufficient moisture output (P and $\bigtriangledown \cdot \mathbf{Q}$), or a combination of the two. Conversely negative residuals suggest a "leaking" atmosphere: too much water output than input. Unlike

the land surface, atmospheric water storage change is usually 1 - 2 orders of magnitude smaller than other terms on a monthly basis. However it is included in the budget formulation for the sake of stringency.

3.2.5 Hydrological regimes defined by K-means clustering

A K-means clustering is used to classify the global land into six regimes, defined by the characteristics of the overlying atmospheric hydrology. Regions within a regime share more similarities than with locations in a different regime. Then the water budget is computed at a regime level rather than grid-box level, thus overcoming the noisy residual map problem (see Fig. 1 in *Seager and Henderson* (2013)). A link between the quantified residuals and the contextual characteristics of the hydrological cycle is built at the same time, providing more informative results and facilitating tracing of the origins of the residuals (i.e. budget imbalances). The large-scale water budget has been analyzed previously at a continental or hemispheric level (e.g. *Trenberth et al.* (2007)), however, there is no natural relationship between the partitioning of land masses and the classification of their hydrological features. And as will be shown in the results, a single continent may contain multiple hydrological regimes that range from the driest to the wettest climate, and treating them indiscriminately will inevitably lose valuable details and potentially lead to misleading conclusions.

A K-means algorithm is chosen in preference to alternative clustering methods due to its simplicity in formulation and the freedom in choosing a cluster number. Hierarchical clustering has a drawback that the merging and splitting are determined in a "greedy" manner that once a sample is allocated into one group, it has no chance to be re-allocated into a another group in the subsequent process (*Wilks*, 2011, chap. 15).

To perform the clustering, global maps of long-term average E, P, $\bigtriangledown \cdot \mathbf{Q}$ and dS are combined to form the observation set, where each observation is a 4-dimensional real vector $\mathbf{x}$, representing the water fluxes in that grid box. All grid boxes are treated as independent (no area weighting is applied), and the observation matrix $[\mathbf{X}]$ has a dimension of $(N \times 4)$, where N is the number of grid boxes in the dataset.

At any given number of clusters K, a standard K-means clustering seeks to partition the N observations into $K\,(K \leq N)$ sets: $\mathbf{P} = \{P_1, P_2, ..., P_K\}$, so that the

cost function is minimized:

$$I([\mathbf{X}], \chi) = \underset{\mathbf{P}}{\operatorname{argmin}} \sum_{i=1}^{N} \| \mathbf{x_i} - \boldsymbol{\mu}_c^2 \| \tag{3.4}$$

where χ is the allocation function that defines the partitioning:

$$\chi(\mathbf{x_i}) = c \tag{3.5}$$

and $\boldsymbol{\mu_c}$ is the reference vector (cluster center) for $\mathbf{x_i}$.

The cost function defined above is a measure of the within-cluster sum of squares (WCSS). The algorithm converges to a state that optimizes the grouping of observations: the distance (usually measured by Euclidean distance) between any observation $\mathbf{x_i}$ and its reference vector $\boldsymbol{\mu_c}$ is smaller than with any other reference vector. However, the cost function does not always converge towards a global minimum and different initial reference vectors usually lead to convergences at different local minima. Therefore the computation is repeated 10 times starting from randomized initial states, and the one that minimizes the cost function most is selected as the solution.

The number of clusters K is a critical choice made by the user and therefore involves some degrees of subjectiveness. Depending on the specific problem being solved, the influence of this choice differs and different techniques may be used to facilitate the decision making. In some cases a prior knowledge of a correct cluster number exists, or the clustering can be easily visualized. However, in many other cases that involve clustering of high dimensional data, selecting an appropriate cluster number requires some extra work, such as experimenting at different K and choosing through trial-and-error.

To help determine an appropriate K, we applied two information criteria metrics to the clustering results. In addition to the geometric interpretation of the K-means algorithm described above, a probabilistic interpretation based on a Gaussian mixture model also leads to the same formulation (*Dreyfus*, 2005, chap. 7). Based on a few assumptions that simplify the model, the cost function of K-means can be expressed as a function of the log-likelihood (l) of the Gaussian mixture model, and the cluster number K:

$$\ln(I) = \ln(Nn) - \frac{2l}{Nn} - \frac{2\ln(K)}{n} - \ln(2\pi) - 1 \tag{3.6}$$

After training, the maximized log-likelihood is substituted into the formulation of Bayesian Information Criteria (BIC, *Schwarz* (1978)) and Akaike Information Criteria (AIC, *Akaike* (1974)) to compare results at different K:

$$\begin{cases} BIC(k) & = -2l + k \ln N \\ AIC(k) & = -2l + 2k \end{cases} \tag{3.7}$$

In both cases, the first term quantifies the goodness of fit of the model, and the second term penalizes overfitting. Note the difference between k and K: the former is the number of free parameters in the Gaussian mixture model, which equals to $K(n+1)$. In our case the number of dimensions in the observation vector is $n = 4$.

Clustering is performed at K ranging from 1 to 29, and BIC/AIC values at each setup are computed. Both criteria start to converge at $K = 20$ (Fig. 3.1), a number similar to the Köppen-Geiger classification (*Peel et al.*, 2006). The Köppen-Geiger classification is a widely used climate classification system that classifies global land areas into five major schemes combining temperature, precipitation and vegetation types into the classification criteria. Each major scheme is further divided into a number of second level types, which in turn are divided into third level types, resulting in a total of 13 second level types and 22 third level types (*Peel et al.*, 2006). An "elbow" (a transitional point beyond which additional parameters give decreased added value) is observed at $K = 6$, which is then selected as the number of regimes. Clustering using higher numbers ($K = 7$, 8, *and* 10) are also performed, and the results show consistent large scale patterns with the $K = 6$ setup, but adding more regional details, such as some transitional zones between the major regimes. In all cases, the largest fractional residuals are located in broadly the same regions, therefore only the results of $K = 6$ are presented.

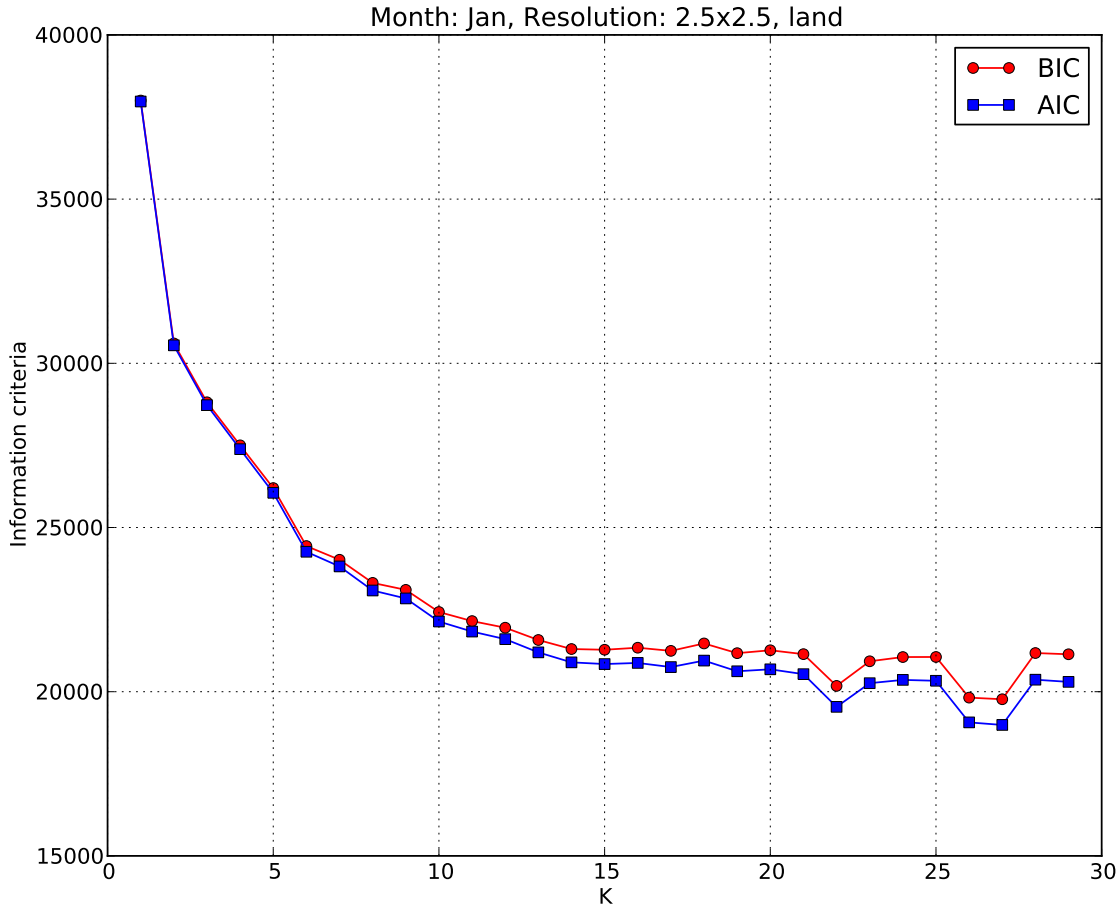

Figure 3.1: Bayesian Information Criteria (BIC) and Akaike Information Criteria (AIC) values of the K-means clustering results for different cluster numbers (K). Observation set is the mean 1979-2012 January ERA-I data with oceans masked out. At each K, clustering is repeated 10 times from which the optimal one is selected as the solution.

3.3 Results

3.3.1 Mean annual ET over land

Global mean annual terrestrial ET during 1979 - 2010 are estimated for ERA-I, JRA-55 and the inferred ET ($P - R$), and the results are represented in mm/yr (area weighted) and $10^3\,km^3/yr$ (areal integrated) to facilitate comparison with literature. Antarctica and Greenland are excluded from computation, and care has been taken to ensure that the land areas in three datasets are consistent ($\sim 130,144,580\,km^2$). The annual averages of global ET are listed in Table 3.1 together with a number of previous estimates.

ERA-I suggests an annual mean ET of 80.0 ± 1.0 $10^3 km^3/yr$ (615.1 ± 7.2 mm/yr), and JRA-55 75.5 ± 0.8 (579.8 ± 6.0). Both fall in the range of

multi-reanalyses ensemble in *Trenberth et al.* (2011) (72 in JRA-25 to 100 in R2), the range of $504 - 664$ mm/yr suggested by *Trenberth et al.* (2009), and the model range estimated by the Global Soil Wetness Project 2 (GSWP-2, $58 - 85$ $10^3 km^3/yr$). However, they are both larger than the surface budget inferred ET (61.9 $10^3 km^3/yr$) and the benchmark product by *Mueller et al.* (2013) (493 mm/yr). Both reanalyses are higher than the *Jung et al.* (2010) estimates (65 ± 3 $10^3 km^3/yr$) by 23% and 16%, respectively.

This overestimation by ERA-I and JRA-55 is consistent with the tendency of reanalyses to overestimate ET compared with other categories of land ET estimates (*Mueller et al.*, 2011, 2013). *Mueller et al.* (2013) found that the ensemble of four reanalyses (ERA-I, MERRA, JRA-25 and CSFR) shows the highest ET estimates ($563\,mm/yr$) compared with the LSM category ($423\,mm/yr$) and the Diagnostic products ($\sim 500\,mm/yr$). The *Jung et al.* (2010) estimates did not take in to account wetlands or inland water bodies including lakes and seas, therefore is likely to be low biased (*Trenberth et al.*, 2011).

Table 3.1: Global land mean annual ET from ERA-I, JRA-55, P-R inferred and a set of previous estimates. The computations in both reanalyses and P-R inferred ET exclude Antarctica and Greenland and the land mask has a total area of $\sim 130,144,580\,km^2$.

Datasets	Global ET mm/yr	$\times 10^3\,km^3/yr$	mm/d	Spatial grid resolution, Temporal extent
ERA-I	615.1 ± 7.2	80.1 ± 0.9	1.69 ± 0.02	0.75 degree, 1979-2010
JRA-55	579.8 ± 6.0	75.5 ± 0.8	1.59 ± 0.02	1.25 degree, 1979-2010
P-R	475.4	61.9	1.3	1.0 degree, 1979-2010
Dirmeyer et al. (2006) GSWP-2 LSMs		58-85		1 degree 1986-1995
Trenberth et al. (2011), reanalyses		72-100		2002-2008
Trenberth et al. (2009), reanalyses	504-664			1985-1989, 2000-2004
Mueller et al. (2013), merged	493			1989-1995, 1989-2005
Jung et al. (2010), FLUXNET upscaling,		65 ± 3		0.5 degree, 1982-2008

3.3.2 Mean evaporation over ocean

Fig. 3.2 compares the oceanic evaporation in ERA-I, JRA-55, HOAPS and OAFlux. Data from their overlapping period (1988 - 2008) are averaged in January and July, and a mutual land-sea mask that combines the grids of dynamic sea ice in HOAPS and OAFlux is used to isolate the valid pixels.

Compared with OAFlux, ERA-I, JRA-55 and HOAPS all show some degrees of overestimation in the tropics. ERA-I has the best overall match with OAFlux, but is higher by $\sim 1\,mm/day$ (around 15 % of the climatology) over the Arabian Sea and the subtropical high areas of the winter hemisphere (Fig. 3.2a,b). Overestimation in JRA-55 is systematic and particularly strong in the tropics for both seasons (Fig. 3.2c,d). This leads to an overall high bias of $1.0\,mm/day$

(1.1 mm/day) in the $30°N - 30°S$ latitudinal band, and 0.7 mm/day (0.8 mm/day) globally in January (July). A high bias with similar magnitude is also found in its predecessor JRA-25 (*Bosilovich et al.*, 2011). Note that precipitation in JRA-55 is also systematically high biased (see Chapter 2), reflecting an overestimated hydrological cycle intensity. HOAPS has alternating positive and negative differences with respect to OAFlux latitudinally, and the patterns correspond well with the differences in the temporal variability of E, as will be shown in the following section.

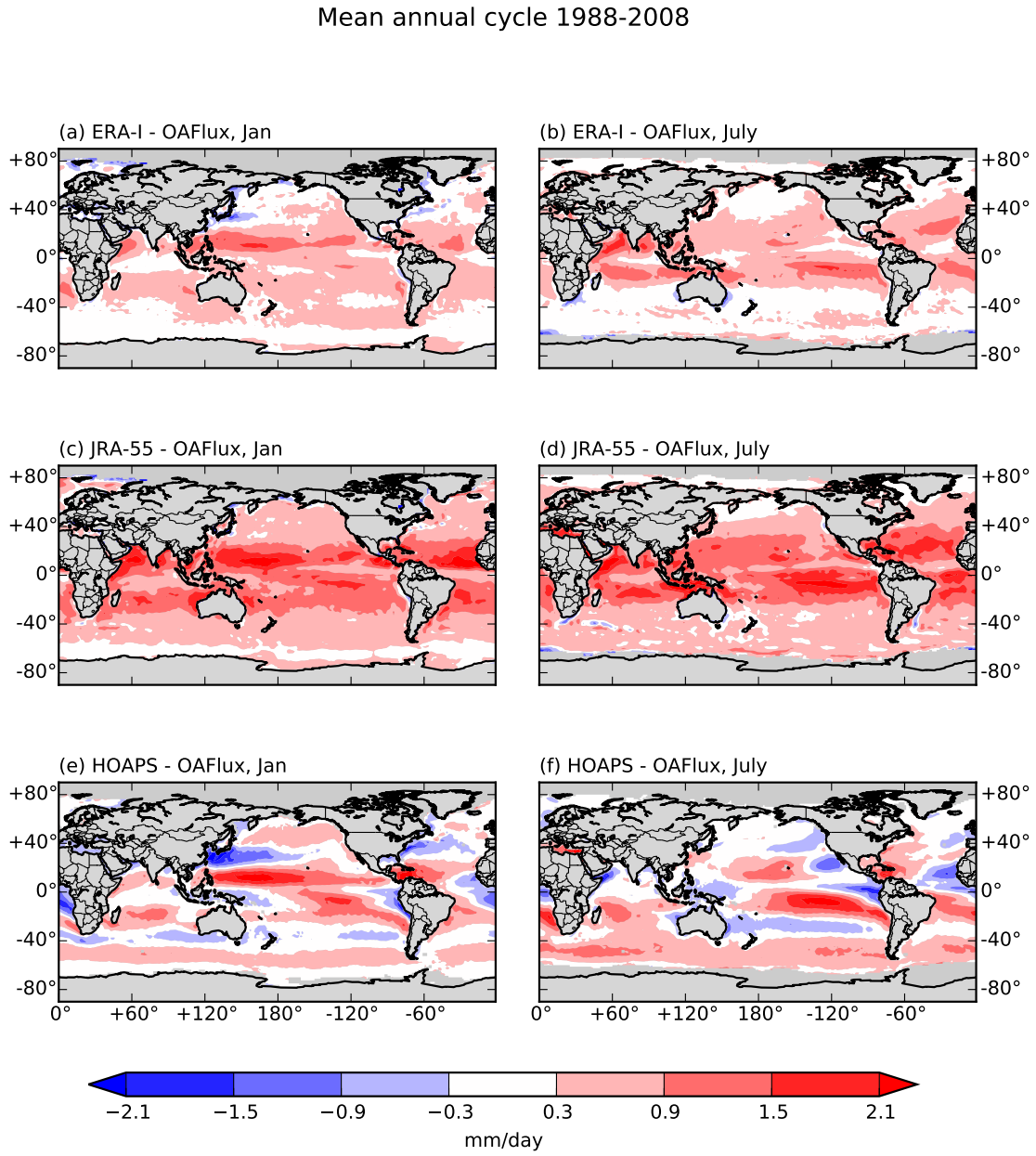

Figure 3.2: Comparisons of the mean January (left column) and July (right column) oceanic evaporation in ERA-I (first row), JRA-55 (second row) and HOAPS (third row) with the OAFlux reference. Data used are from their common time period 1988 - 2008, and unit is mm/day. A mutual mask that combines the grids of dynamic sea ice in HOAPS and OAFlux is used to isolate the valid pixels. Missing areas are plotted in grey.

3.3.3 Temporal variances of oceanic evaporation

Standard deviation is used as a measure of the temporal variability in a dataset, and their differences are shown in Fig. 3.3. Computation of standard deviations uses 21 years of monthly values, therefore consists of contributions from annual cycle, inter-annual and intra-seasonal time scales. These components are later decomposed by computing the variance associated with the mean annual cycle, the year-to-year variance represented by the 11-month filtered anomalies, and the intra-seasonal variance (variance of the anomalies after subtracting the mean annual cycle and the annual means). The component variances are shown in Fig. 3.4 - 3.6.

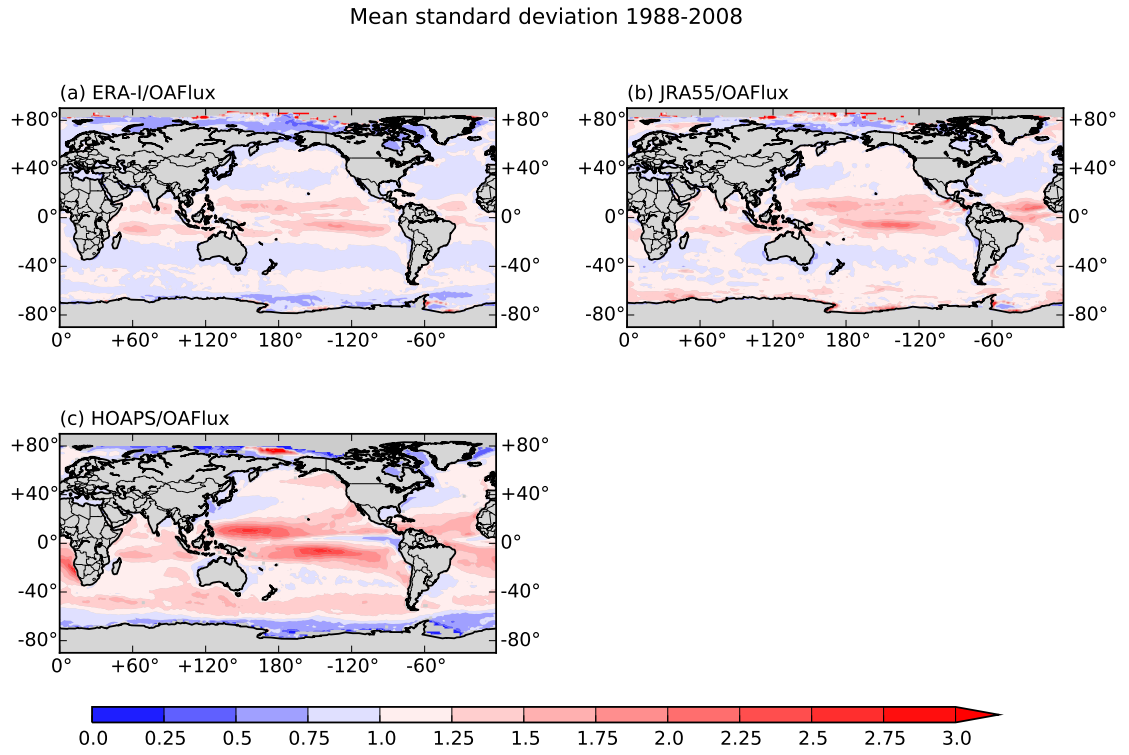

Figure 3.3: Ratios of the evaporation standard deviations of (a) ERA-I, (b) JRA-55 and (c) HOAPS with respect to that of OAFlux. Computation of standard deviations uses 21 years of monthly data during 1988 - 2008.

ERA-I and JRA-55 have comparable standard deviations with OAFlux over most of the ocean (Fig. 3.3a,b), except in the tropics the JRA-55 variability tends to be higher by up to $\sim$ 170 %. Variability over the Kuroshio current and Gulf stream regions shows slight low biases in both reanalyses. Decomposed into components, the observed differences have contributions from the mean annual cycle (Fig. 3.4a,b), inter-annual (Fig. 3.5a,b) and intra-seasonal (Fig. 3.6a,b) time scales.

Greater magnitudes of differences are observed between HOAPS and OAFlux (Fig. 3.3c), with similar spatial patterns as the January mean differences (Fig. 3.2e): higher values of mean *E* correspond to higher degrees of variability over the tropical convergence zones, and lower values of *E* co-locate with lower standard deviations over the Kuroshio current and Gulf stream regions in HOAPS. Similar correspondence can also be identified in the subtropical Pacific in the southern hemisphere (Fig. 3.2f and Fig. 3.3c). The decomposed difference suggest that the lower variability in the Kuroshio current and Gulf stream regions in HOAPS mainly stem from differences in the strength of the annual cycle (Fig. 3.4c), while differences in the tropics arise because HOAPS *E* fluctuates more strongly on intra-seasonal and especially inter-annual time scales (Fig. 3.5c, 3.6c). The notably higher degree of intra-seasonal variability is also observed in HOAPS's *P* estimates (see Chapter 2).

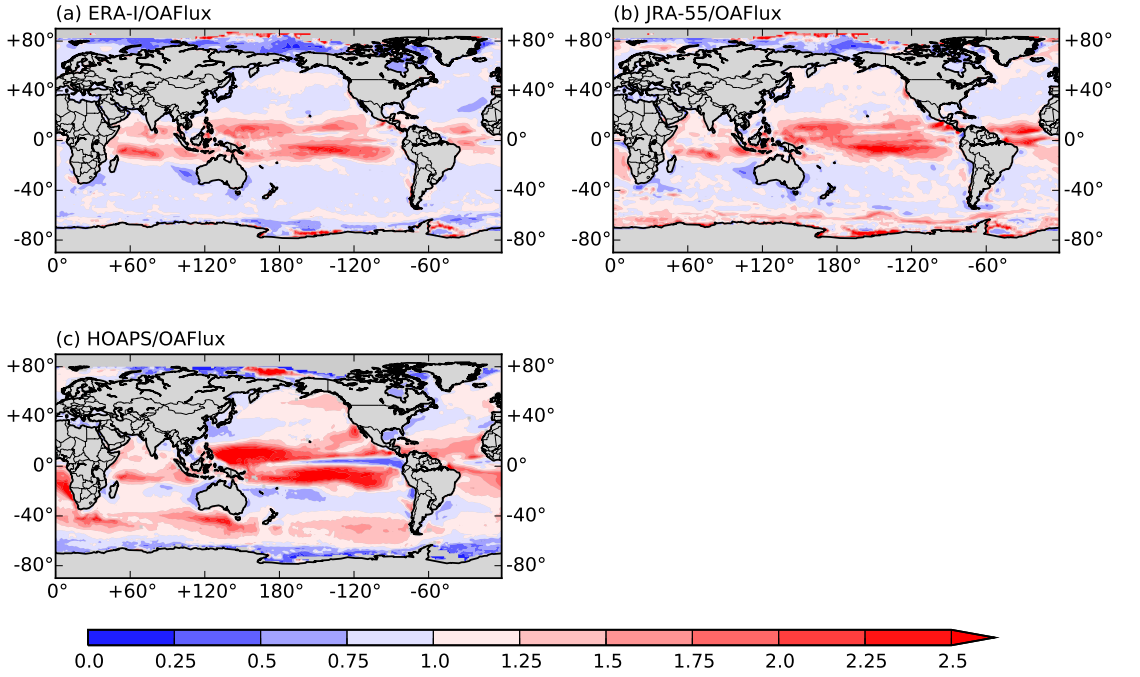

Figure 3.4: Ratios of standard deviations in the annual cycle of oceanic evaporation in (a) ERA-I, (b) JRA-55 and (c) HOAPS with respect to that of OAFlux.

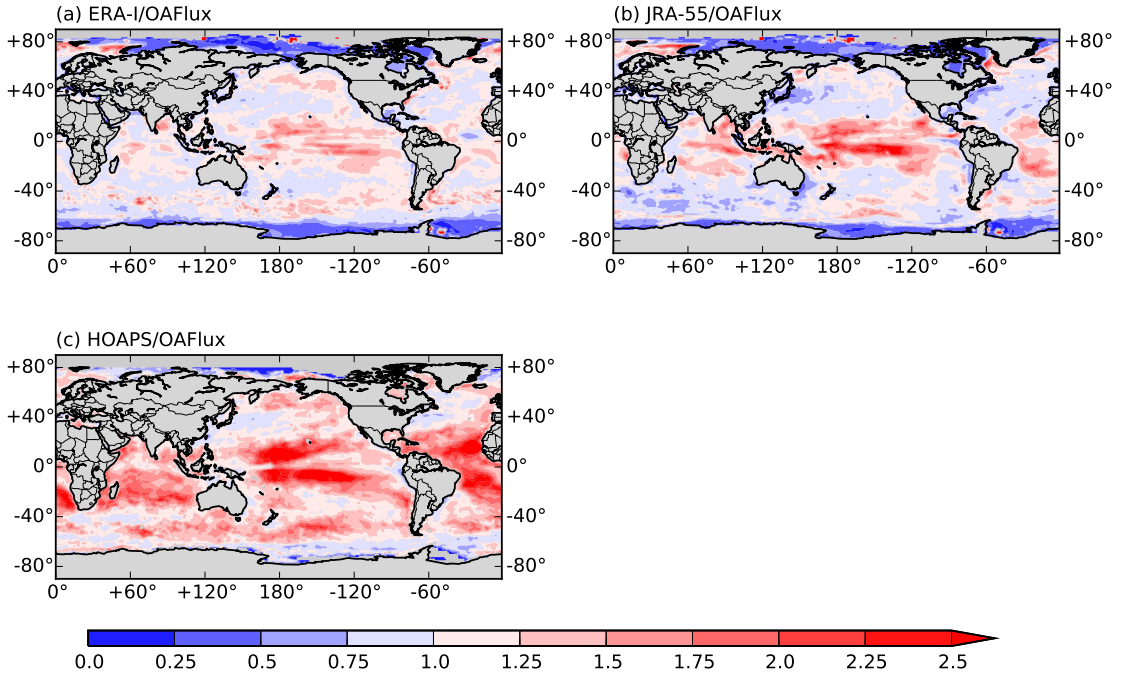

Figure 3.5: Same as Fig. 3.4 but for standard deviations over inter-annual time scales.

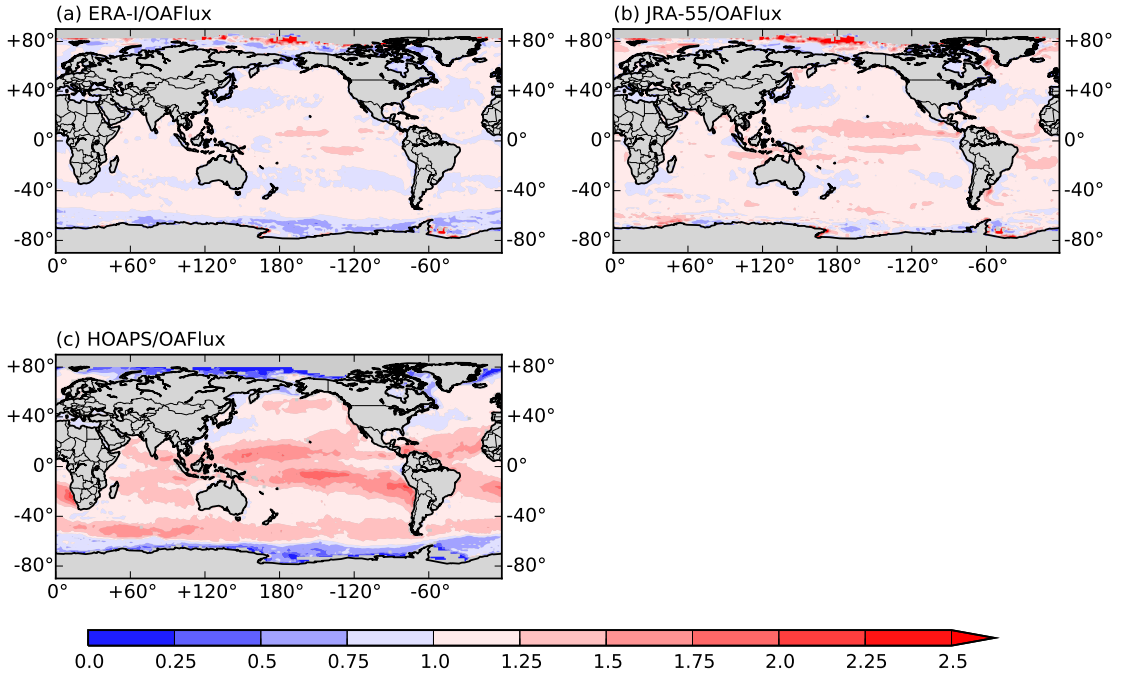

Figure 3.6: Same as Fig. 3.4 but for standard deviations over intra-seasonal time scales.

3.3.4 Oceanic evaporation pattern comparison using Taylor diagrams

Spatio-temporal patterns in datasets are summarized in the Taylor diagrams for tropical/extra-tropical oceans for each season, and the results are shown in Fig. 3.7 and 3.8. OAFlux is used as the observational reference, and HOAPS as a second observation to provide information on observational uncertainties. Uncertainty ranges derived from the OAFlux error estimates are also displayed on the Taylor diagrams (see Chapter 2 for methodology), representing the area on a Taylor diagram where "reality" could reasonably reside, if the OAFlux error estimates are valid. Overall bias of a dataset is shown as a triangle of the corresponding colour.

Over tropical oceans, little difference in performance is observed across seasons (Fig. 3.7). Throughout the year, JRA-55 and HOAPS show very similar correlations and standard deviations, which match the reference slightly less well than ERA-I. All three datasets show positive overall biases in the tropics with the JRA-55 bias being notably stronger, as suggested in Fig. 3.2. Data points all lie outside of the uncertainty range of OAFlux, suggesting the differences are significant.

Comparisons over the extra-tropical ocean show more seasonal variations (Fig. 3.8), which mostly stem from HOAPS. In DJF HOAPS has the best pattern correlation with OAFlux (0.98), and the JJA standard deviation has a close match (0.98). However in MAM and SON the variability in HOAPS is lower by around 21%, and is largely due to lower E strengths associated with the Kuroshio current and Gulf stream (Fig. 3.2e reveals such a difference in January but similar differences are also found in other months). Similar to the tropics, scores for both reanalyses are largely consistent throughout the year with comparable quality. JRA-55 still has the largest positive bias but with a smaller overall magnitude than in the tropics (note the scale difference in the radial axis). Except for HOAPS in DJF season, all data points lie well outside the OAFlux uncertainty range.

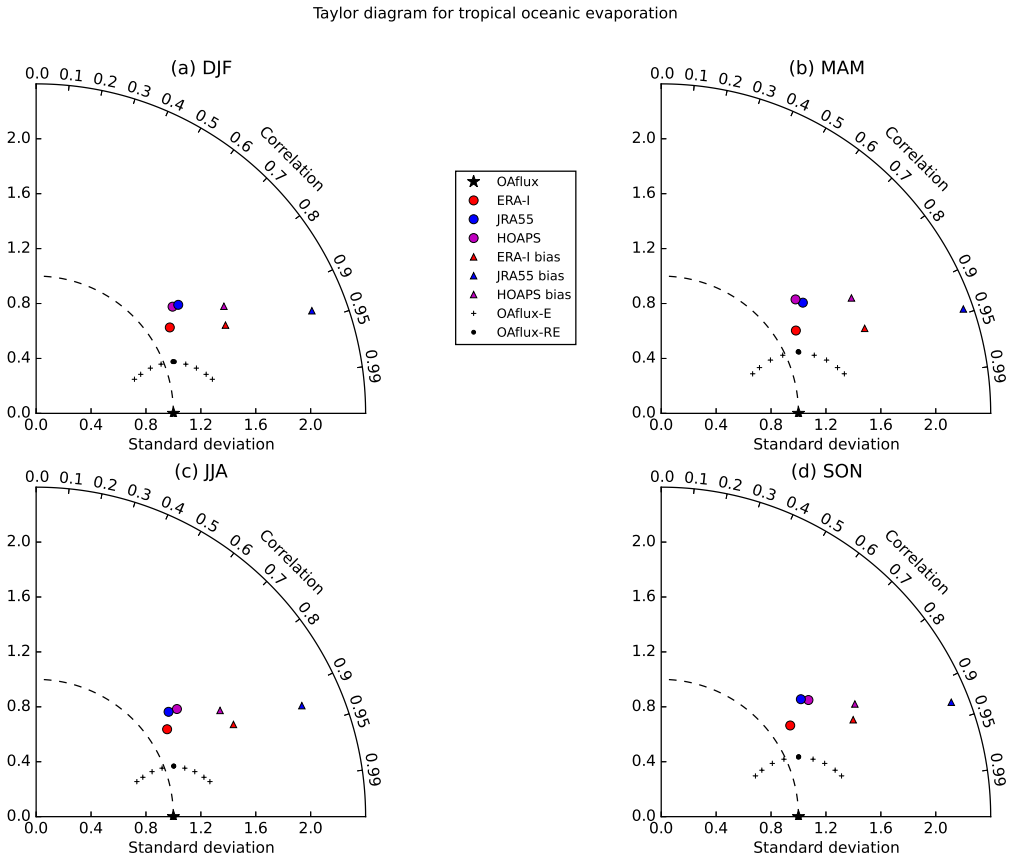

Figure 3.7: Taylor diagrams for the monthly evaporation estimates during 1988-2008 over tropical oceans. OAFlux is used as the reference dataset (asterisk), and reanalyses are labelled as solid circles. HOAPS is included to indicate the observational uncertainty. Solid triangles denote the overall biases of the datasets. A bias point located on the right-hand side of the model point indicates positive bias, and left-hand indicates negative. Bias magnitude is measured as the spatail mean difference between a model dataset and the OAFlux reference, normalized by the standard deviation of OAFlux (See Chapter 2). This is represented as the distance between the bias point and the corresonding model point. Observational uncertainties based on OAFlux's random error are illustrated by black pluses and dots, and the space they encompass represents the range of uncertainty stemming from random error perturbations.

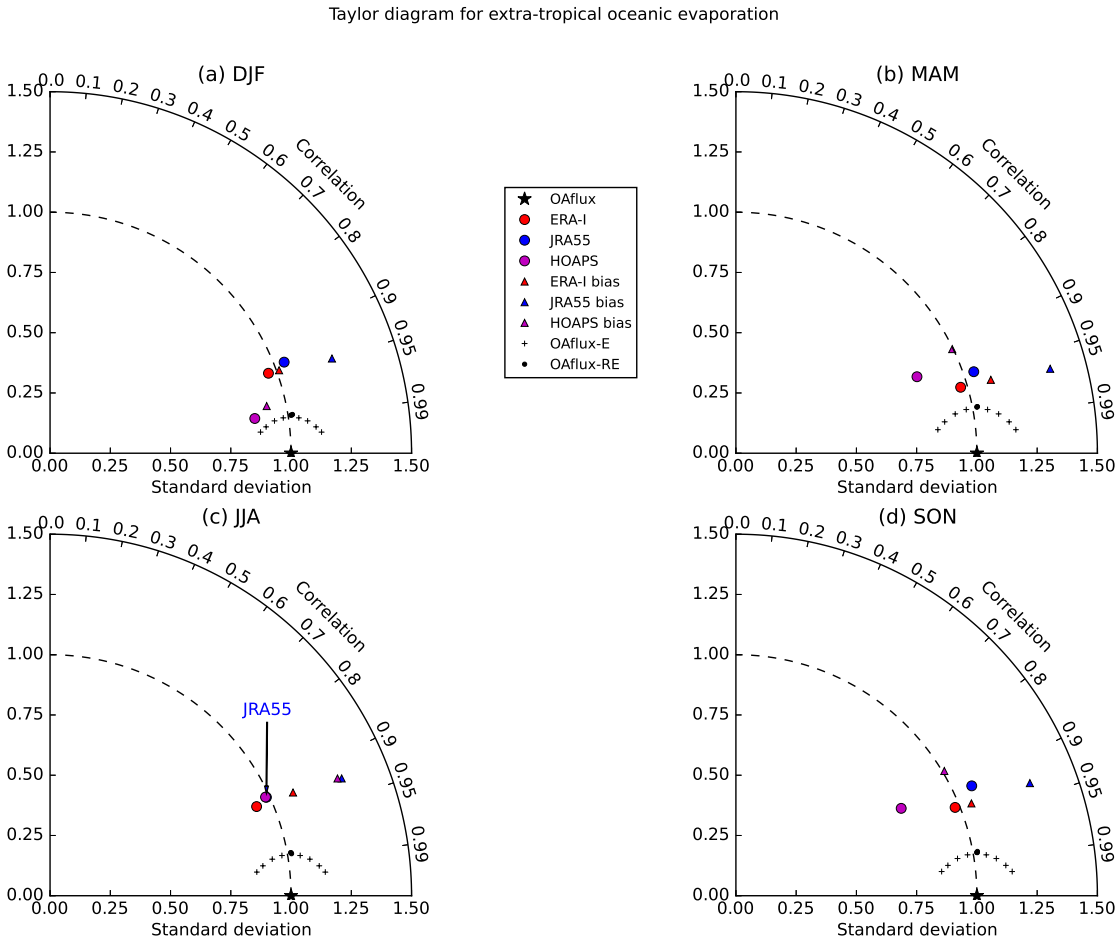

Figure 3.8: Same as Fig. 3.7 but for extra-tropical oceans. Note the scale along the radial axis is different from Fig. 3.7.

3.3.5 Mean total column water

Unlike the type C variables of P and E that are simulated by the reanalysis model, moisture is classified as a type B variable and is influenced by both the model and the assimilated observations (*Kalnay et al.*, 1996; *Kistler et al.*, 2001), therefore is considered as more reliable. Indeed, the differences from HOPAS observations over most of the ocean (Fig. 3.9) are below 10 % of the climatology, even for the tropical convergence zones where both reanalyses show systematic low biases. Pattern comparisons using Taylor diagrams (Fig. 3.10) also confirm the very good matches among datasets. However, in judging whether an observed difference is significant or not, the fractional perspective is only one of the many factors that need to be taken into account, the possible implications for the related broader questions are equally important. TCW provides necessary thermodynamic conditions for precipitation to occur and can also influence precipitation rates under a given circulation field. In the case of reanalysis, an incorrect moisture estimate can bias precipitation simulations, possibly due to assimilation of problematic satellite retrievals (*Bosilovich et al.*, 2011; *Robertson et al.*, 2011). To investigate the possible implications of such observed TCW differences in the water budget, scatter plots of TCW against P are created for ERA-I, JRA-55 and HOAPS. HOAPS is selected as a reference because of its SSM/I framework in deriving TCW and P, thus offering better internal consistency.

The scatter plots (Fig. 3.11) for each dataset are created by spatially averaging monthly TCW and P values over their respective ITCZ, where absolute TCW differences are largest. Computations using a single ITCZ definition (e.g. the ITCZ defined using ERA-I P field) for all three datasets give qualitatively consistent results. The ITCZ region is defined as the tropical ocean where long-term mean P is above 6.0 mm/day. For ERA-I and JRA-55, monthly values from 1979-2012 are used, while for HOAPS the available data cover a shorter period of 1988-2006. As shown in Fig. 3.11, a linear relationship between P and TCW ($P = a + b \times TCW$) is observed for all three datasets, but with varying slopes and intercepts. The slope is a measure of the thermodynamic dependency of P, and the difference between intercepts can be regarded as a systematic P bias. ERA-I shares broadly the same range of TCW variability as HOAPS in January, but with slightly higher values of P (Fig. 3.11a). In July, ERA-I generates comparable levels of P as HOAPS at a lower level of TCW (Fig. 3.11b). More notable differences are exhibited by JRA-55, which maintains a higher level of P

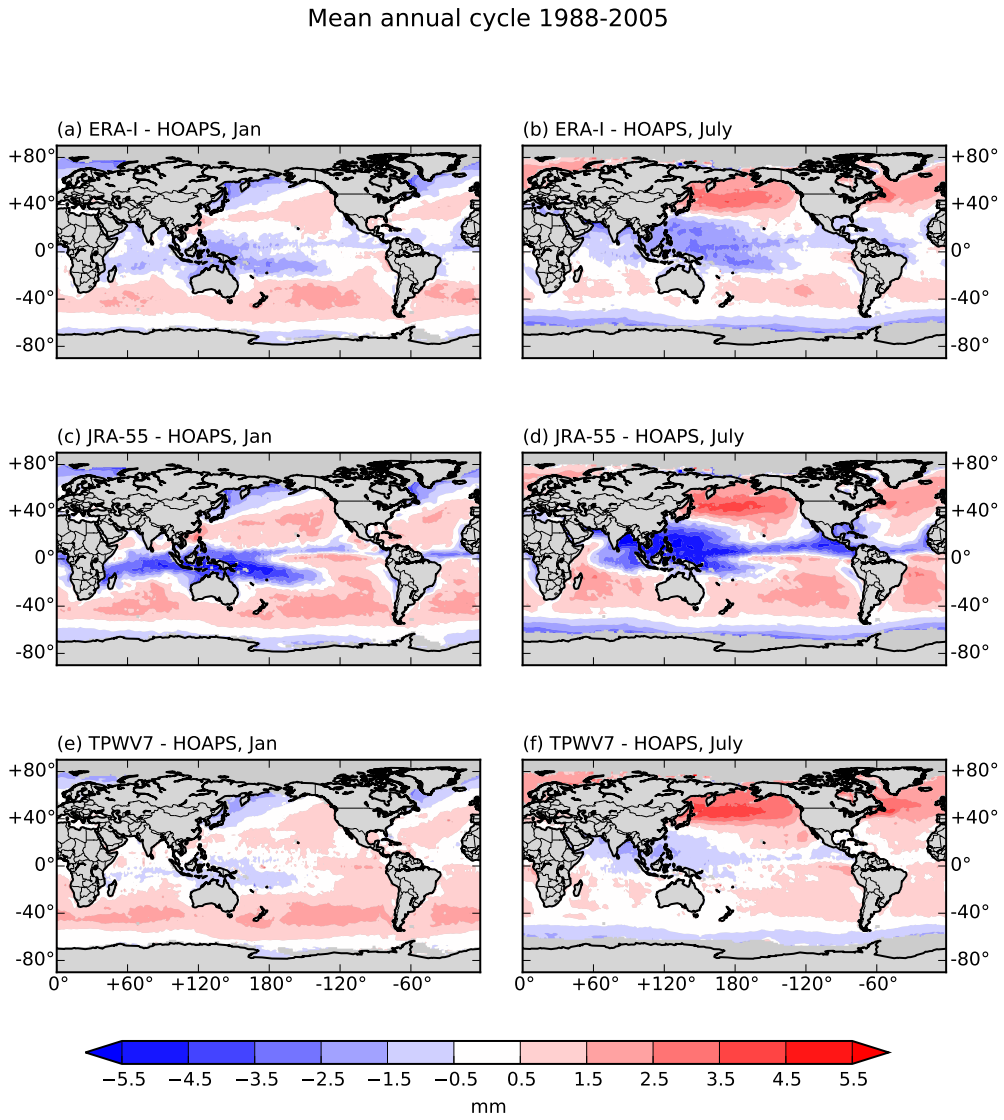

Figure 3.9: Comparisons of the mean January (left column) and July (right column) oceanic total column water (mm) in ERA-I (first row), JRA-55 (second row) and TPWV7 (third row) with the HOAPS reference, for their common time period 1988 - 2005. A mutual mask that combines the grids of dynamic sea ice in HOAPS and TPWV7 is used to isolate the valid pixels.

at an even lower level of TCW in both seasons. In both January and July, JRA-55 shares the same slope as HOAPS ($b = 0.6\,day^{-1}$), therefore the difference in their intercepts ($\delta a = -18.0 + 20.9 = 2.9\,mm/day$) suggests a $2.9\,mm/day$ high bias in JRA-55 at an equivalent TCW level. In both seasons ERA-I has a slightly lower slope ($b_{Jan} = 0.4\,day^{-1}$ and $b_{July} = 0.3\,day^{-1}$), making its bias smaller at higher TCW levels. To examine whether the observed differences are due to the different time period of the reanalyses and the HOAPS data, another computation using the common 1988-2006 period gives qualitatively consistent

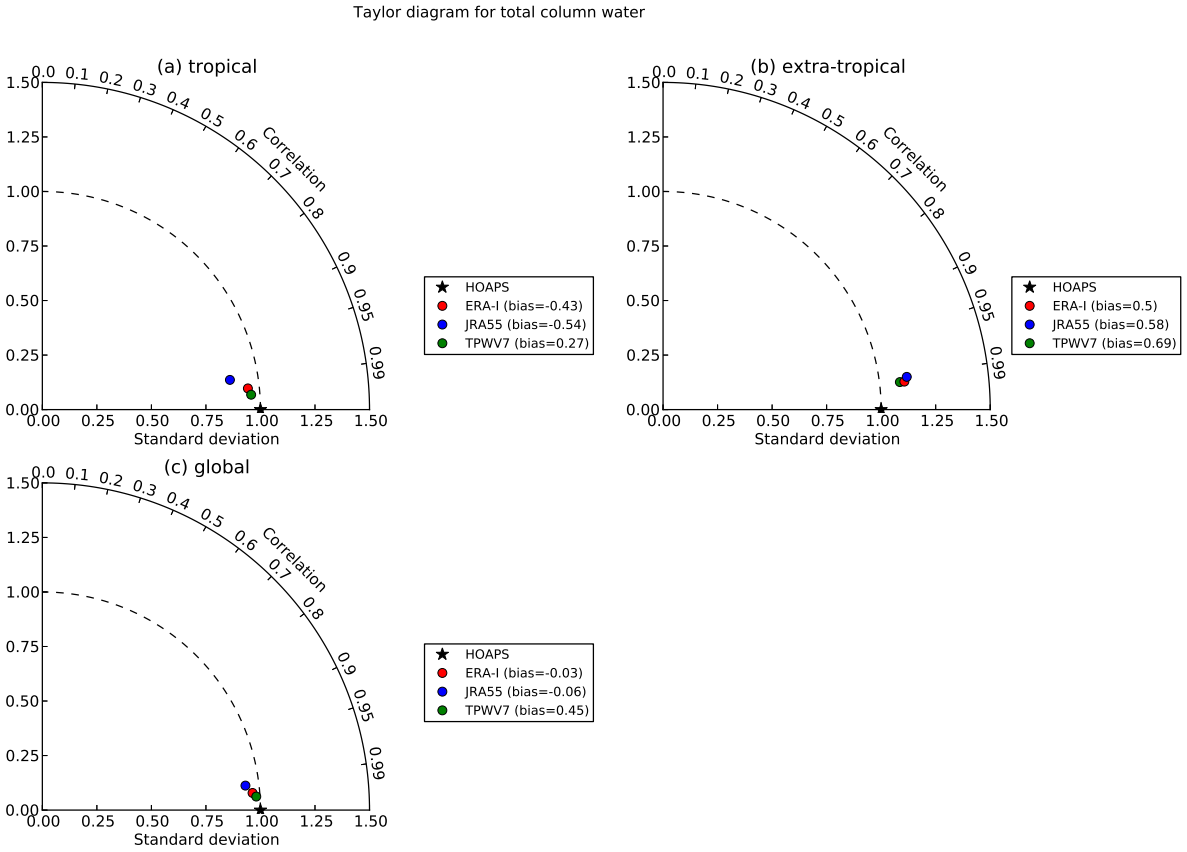

Figure 3.10: Taylor diagrams for the DJF mean total column water estimates during 1988-2005 over (a) tropical, (b) extra-tropical and (c) global oceans. HOAPS is used as the reference dataset (asterisk), and reanalyses are labelled as solid circles. TPWV7 is included to indicate the observational uncertainty. Overall bias of a dataset is labelled in the legend, measured in *mm*. As little seasonality is observed only the DJF results are shown.

results (not shown).

These counter-intuitive low-moisture-high-rainfall results illustrate that problems exist in the reanalysis weather system: either stronger circulation in reanalyses associated with an overestimated hydrological cycle intensity (in particular, the Hadley cell intensity), or a spin-down problem of the forecast model that renders a water-leaking atmosphere. Previous studies (*Andersson et al.*, 2005; *Trenberth et al.*, 2007, 2011; *Kobayashi et al.*, 2015) have shown evidence that support the latter in the cases of ERA-40, ERA-I and JRA-55. However, the reliability of the reanalysis-based estimates of circulation strength is also questionable. The tropical static stabilities in ERA-40 and NECP-I have been found to have a weakening tendency during the past decades, caused by the assimilated top-cool radiosonde profiles that have increasing tropical lapse rate

(*Santer*, 2005; *Mitas and Clement*, 2006). The result of this thermal structure is that circulation is strengthened in order to balance the diabatic heating, which in turn is overestimated in both ERA-40 and NECP-I (represented by the wet biases in P, see Chapter 2). Whether similar problems also exist in ERA-I and JRA-55, and to what extent the internal consistency of the climate system is compromised by the data assimilation scheme and the related long-term hydrological intensity responses are questions that remain unanswered. The TCW-P scatters displayed here show only one aspect of the internal consistency problems in reanalyses.

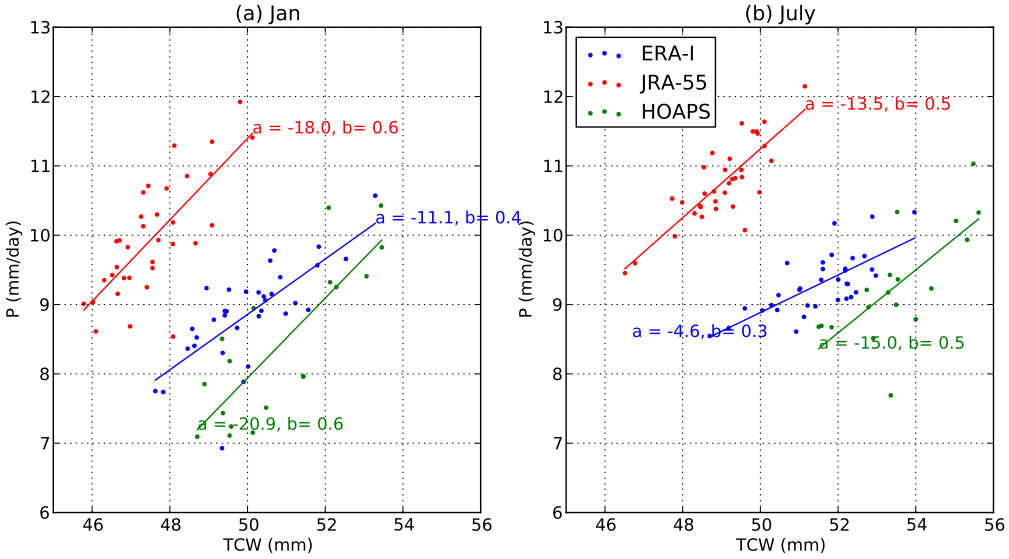

Figure 3.11: Scatter of P verus TCW over the ITCZ region in ERA-I (blue), JRA-55 (red) and HOAPS (green). ITCZ is defined as the tropical ocean area where mean January (a) and July (b) precipitation is above $6.0\,mm/day$. ERA-I and JRA-55 data are from 1979-2012, and HOAPS data period is 1988-2006. A line fitting the scatter (by least squares) of a dataset is shown using the corresponding colour, and the resultant intercept (a) and slope (b) are labelled on the plot.

3.3.6 Water budget and residuals over global land

We have examined two major terms – E and P – in the atmospheric water budget, and covered some basic aspects of the TCW. The time tendency of TCW on a monthly time scale is usually the smallest term. Horizontal divergence of moisture combines dynamic and thermodynamic components of the hydrological cycle, and plays a critical role in the tropical moisture budget (*Trenberth and Guillemot*, 1995, 1998), therefore we will devote the remaining chapters of the thesis to the discussions of its variability over various time

scales. The water budget is rarely closed perfectly in any observational dataset or combinations of them, the violations of this physical constraint highlights problems in the existing estimates, and analysis of the residual can provide insights into the possible causes. In this section the budget residual over global land areas will be studied with a hydrological regime approach.

The atmospheric hydrological cycle over global land as depicted by ERA-I is classified into six regimes using a K-means algorithm. Data are regridded to the native resolution of GPCP ($2.5° \times 2.5°$) to reduce the computational costs and avoid regridding errors in the GPCP values. Observations of E, P, $\bigtriangledown \cdot \mathbf{Q}$ and dS at grid boxes (with Antarctica excluded) are treated as independent samples, and seasonality is addressed by performing a clustering for January, July and the annual mean separately, using the 1979-2012 climatologies. Note that although usually being negligible compared with E or P, the storage change term (dS) may have comparable magnitudes as the residual, therefore it is retained in the budget equation to ensure more accurate quantification of the residual. Nevertheless, the observation data used for the clustering analysis is not normalized, therefore variances of P, E and $\bigtriangledown \cdot \mathbf{Q}$ will dominate that of dS. Moreover, as the budget is usually relatively closed ($E \simeq P + \bigtriangledown \cdot \mathbf{Q}$), the effective number of dimensions in determining the clustering is two, which allows the clustering results to be easily visualised by a 2-D scatter plot.

3.3.7 Hydrological regimes in ERA-I

Fig. 3.12 displays the region definitions of clustering in January, July and the annual mean in ERA-I. Regime numbering is arbitrarily defined by the order of the sorted P values. Similarities with the Köppen-Geiger climate classification (Fig. 3.13) can be readily observed, such as the wettest regime (regime 6) is located with the tropical forest (Af, the Köppen-Geiger notation), tropical monsoon (Am) and tropical savanna (Aw) climate types; the driest regime (regime 1) is found over the desert climate (BW) in north Africa, the Arabian peninsula and the central Australia. Climate types that are characterized by greater seasonal variations are represented by the differences in the January and July regimes: the Asian monsoon region is represented by the second driest regime (regime 2) in January (Fig. 3.12a) and the two wettest regimes (regime 5 and 6) in July (Fig. 3.12b); The tropical savanna in Brazil has more rainfall in boreal winter (regime 5 and 6 in January) than in summer (regime 2 in July). And many of the temperate climate types are identifiable as regimes

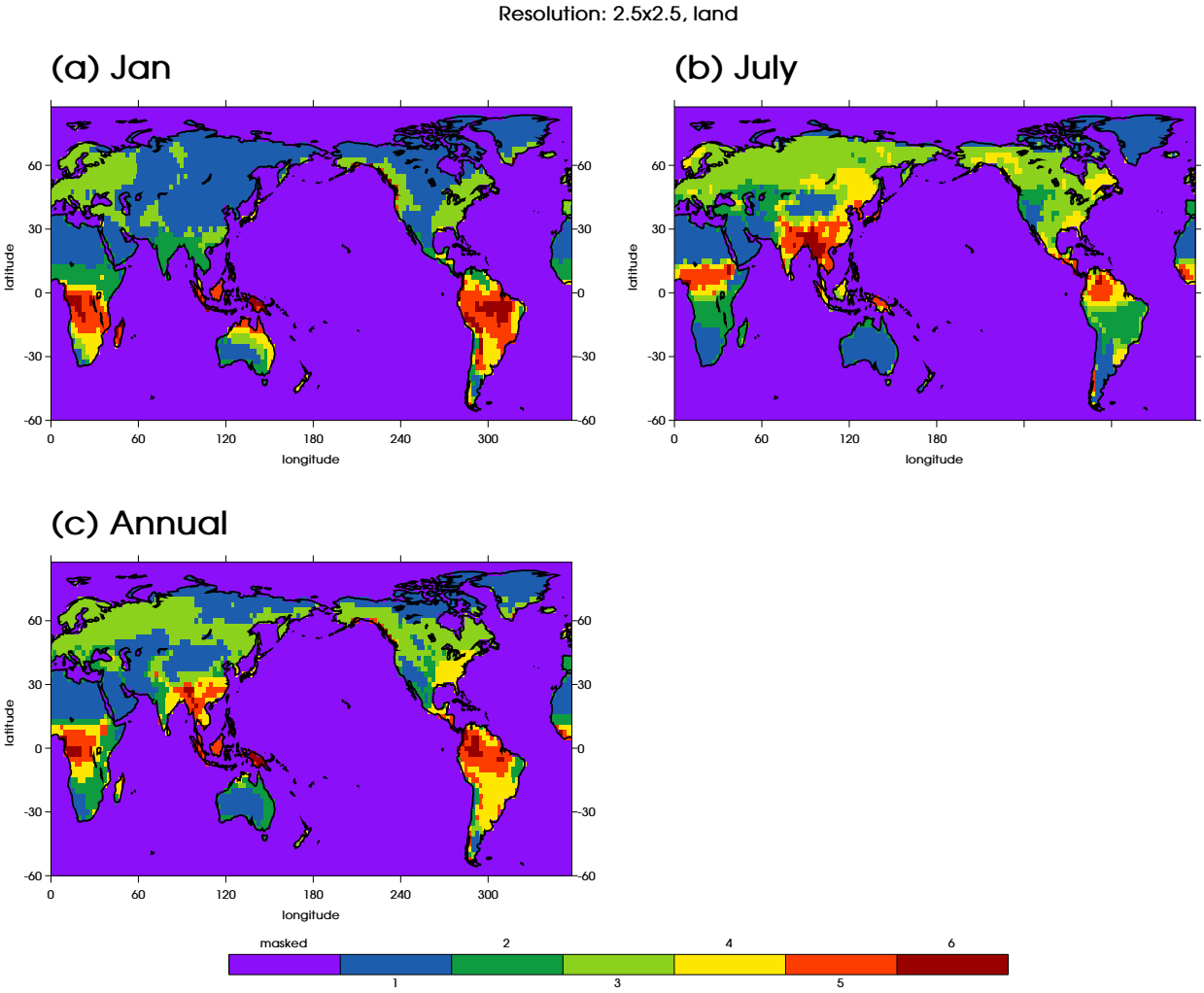

Figure 3.12: Regime definitions of the atmospheric hydrological cycle over global land in ERA-I. Regimes are defined by clustering the hydrological variables using the January (a), July (b) and (c) annual means of the 1979-2012 data.

with intermediate precipitation amounts in the July and annual mean classes (Fig. 3.12b,c).

However, the clusters are distinguished by more than just the precipitation amount, as shown when the cluster centers are visualized on P, E and P, $\bigtriangledown \cdot \mathbf{Q}$ scatter plots (Fig. 3.14). Across global land, there exists a good linear relationship between P and $\bigtriangledown \cdot \mathbf{Q}$ (Fig. 3.14b, d and f). Since the budget equation is strictly linear, a similar linear relationship is expected between P and E, but this is not the case (Fig. 3.14a, c and e). The range of variability in E is much smaller than that of P and $\bigtriangledown \cdot \mathbf{Q}$ (*Trenberth and Guillemot*, 1998; *Mueller et al.*, 2013), so the nonlinear behaviour is not very distinct in the P v.s. $\bigtriangledown \cdot \mathbf{Q}$ scatter plots. A dividing line could be drawn through $P \simeq 3\,mm/day$ that separates

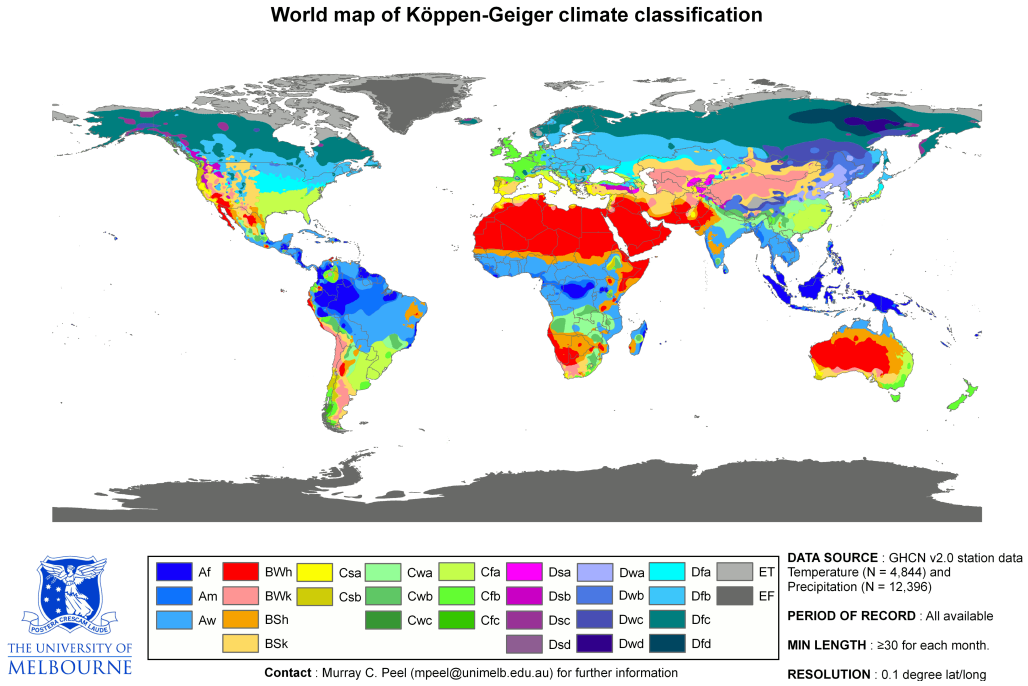

Figure 3.13: Updated world map of the Köppen-Geiger climate classification. From *Peel et al.* (2006).

the global land masses into one group where variability in P is more related to E, and a group where P corresponds more closely to transported moisture than to locally evaporated. The division in the main moisture sources also corresponds to mean rainfall amounts. It should be noted that in the reanalysis system, feedbacks in the hydrological cycle do not function in the same way as in reality: P is simulated by a numerical weather prediction model, and E from a land surface model/scheme, which uses meteorological forcings as inputs. Therefore, there exists a more direct influence of P on the soil moisture and E, but the feedback in the opposite direction is rather indirect: the assimilation of humidity observations in each forecast cycle means the impacts of E on humidity and subsequently P can only be secondary.

The average water budget for each regime is computed and the results are shown in Fig. 3.15 in the form of stacked bars. For each regime, the budget-inferred P is shown as the amount of convergence (cyan) added on top of E (green). P from reanalysis is plotted as a blue pillar, and the P estimates from GPCP (red pillars) are shown as a reference. Note that the difference between the budget-inferred P (left pillar) and the reanalysis P (mid-pillar) is the quantified budget residual. The storage change term dS is too small to show but it is included in the calculation. The resultant residuals (i.e. the ERA-I budget imbalance due to assimilation increments, Eq.3.3) from such calculations

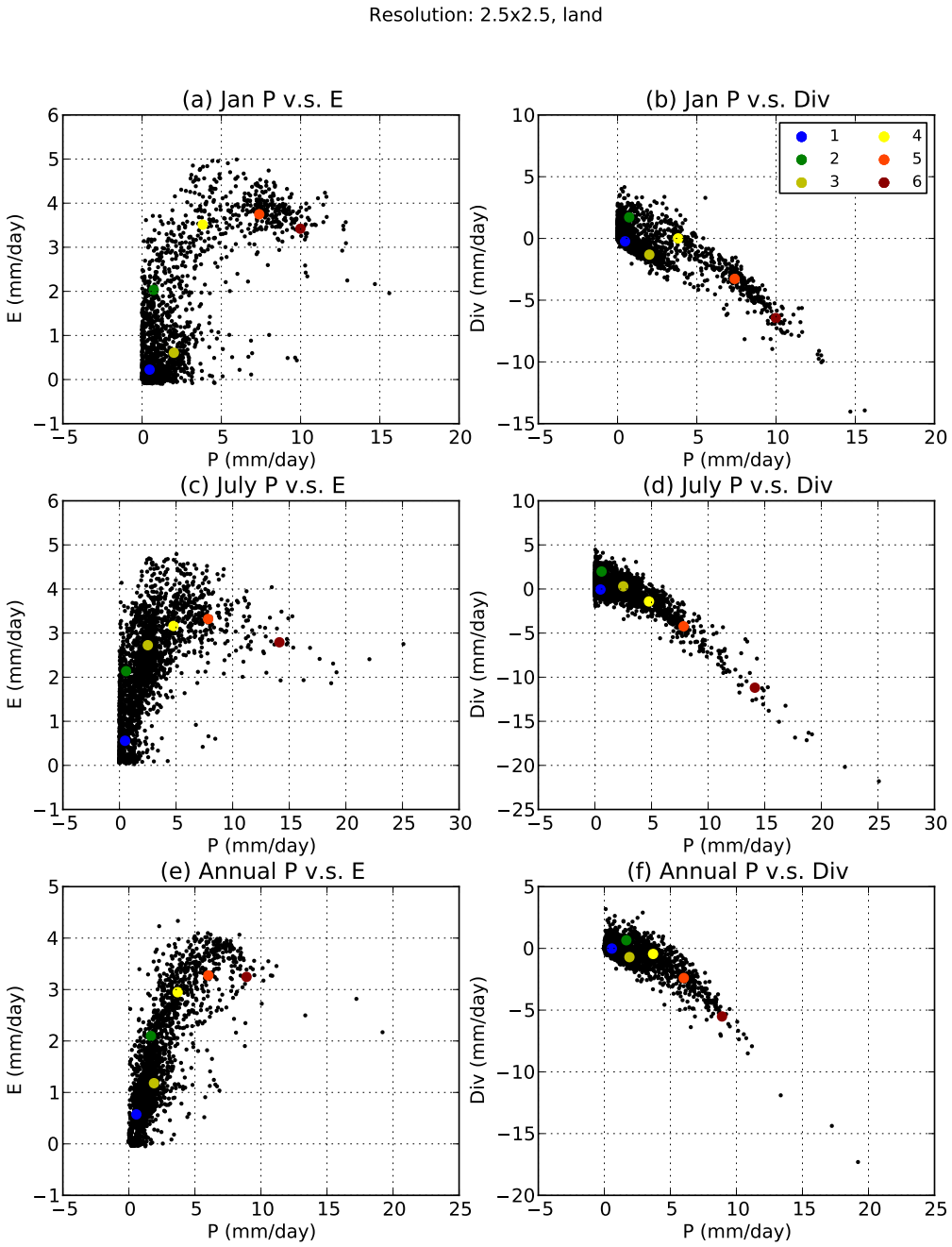

Figure 3.14: Scatter plots of E vs. P (left column) and $\bigtriangledown \cdot \mathbf{Q}$ vs. P (right column) over global land in January (first row), July (second row) and annual mean (third row). Data are the ERA-I 1979-2012 climatologies (with Antarctica excluded). Cluster centers from the K-means clustering are superimposed onto the scatter dots using coloured dots (see key in panel b).

are plotted as the dotted lines onto the y axis on the right, as percentages of the corresponding reanalysis precipitation.

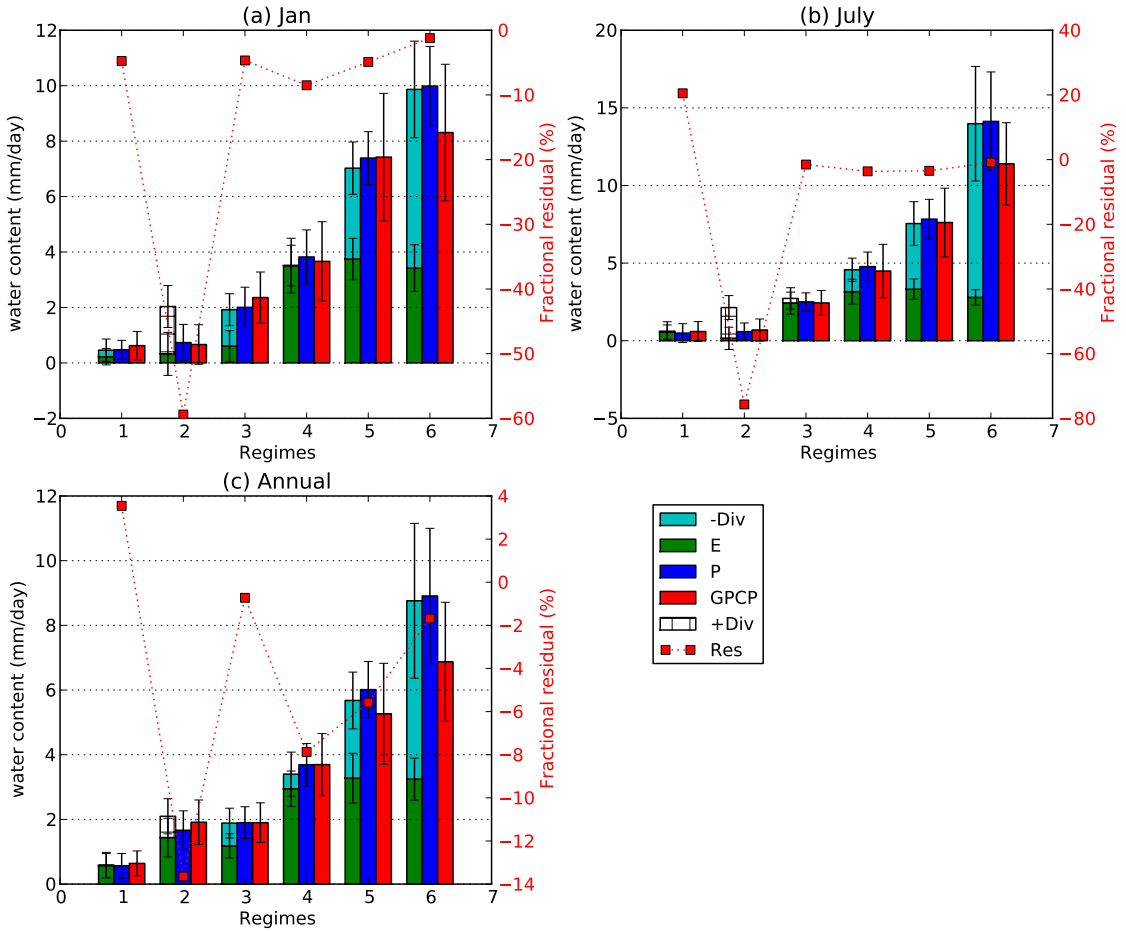

Figure 3.15: Water budget and residuals for the regimes derived from ERA-I in (a) January, (b) July and (c) annual mean. For each regime, the budget-inferred P is shown by the pillar on the left that consists of $\bigtriangledown \cdot \mathbf{Q}$ (cyan) on top of E (green). If $\bigtriangledown \cdot \mathbf{Q}$ is positive (net divegence takes water away), it is plotted as a white bar, coming down from and overwriting the green E bar. P from ERA-I (dark blue) and from GPCP (red) are also plotted. Error bars denote the spatial standard deviations around the regime mean. Fractional residuals (residual divided by mean P, in percentage) are plotted as red squares, using the right-hand y-axis scale.

The regime with highest P (regime 6) has the largest wet bias in ERA-I (Fig. 3.15), which is mostly caused by the wet biases over the Congo and the Amazon basins (see Fig. 1.3 and 1.4 in Chapter 2). Going from the driest (regime 1) to the wettest (regime 6), there is a general tendency of increasing contribution from converged moisture to precipitation, consistent with previous discussions. This can be readily observed by comparing the precipitation constitutions in regime 4, 5 and 6: precipitation in regime 4 is largely dominated by evaporation in both seasons and the annual mean, and the extra rainfall in regime 5 and

6 in addition to regime 4 are mostly contributed by convergence. This is due to the relatively uniform evaporation distributions in tropical Africa and South America, compared with a much narrower band of enhanced moisture convergence following the seasonally shifting ITCZ that co-locates with regime 6 (not shown). In regime 6, converged moisture contributes the majority of total precipitation. Regime 2 in both seasons and the annual mean is the only regime that has significant net moisture divergences over land. In these areas evaporation is the only water supply for precipitation. It is also the regime that shows the largest fractional residuals. Therefore this regime will be examined in more details.

Regime 2 has the largest negative budget imbalance (residuals) when expressed as a percentage of the mean precipitation, with P exceeding $E - \bigtriangledown \cdot \mathbf{Q}$. Since ERA-I P is quite a close match with GPCP P, the large relative residuals in the regime 2 atmospheric water budget are likely to be caused by either low biased E or high biased $\bigtriangledown \cdot \mathbf{Q}$ or a combination of both. Both variables lack a reliable reference dataset, so their temporal variability is examined instead.

Fig. 3.16 shows the time series of the hydrological variables in regime 2, and Table 3.2 lists the correlation coefficients between the absolute residuals and E, P, $\bigtriangledown \cdot \mathbf{Q}$ and dS. Note that the relative residuals, R/P, should not be used for the correlations because dividing by P imparts a relationship with P even where none exists. The correlations with E, P and dS are all trivial or moderate, but are strong and significant with $\bigtriangledown \cdot \mathbf{Q}$. Overestimated divergence is likely to be the cause of the negative residuals. Note that the annual mean divergence in this regime is positive throughout the period 1979-2012 (Fig. 3.16c), which is physically impossible for surface runoff to occur.

Table 3.2: Correlation coefficients between time series of budget residual and E, P $\bigtriangledown \cdot \mathbf{Q}$ and dS. The p value for each coefficient is shown in parentheses, and correlations that are significant at 0.01 level are shown in bold.

	E	P	$\bigtriangledown \cdot \mathbf{Q}$	dS
Jan	0.07 (0.72)	0.09 (0.62)	$-\mathbf{0.84}(<\mathbf{0.01})$	-0.30 (0.08)
July	-0.18 (0.32)	-0.22 (0.21)	$-\mathbf{0.75}(<\mathbf{0.01})$	$-\mathbf{0.42}(\mathbf{0.01})$
Annual	0.40 (0.02)	-0.17 (0.34)	$-\mathbf{0.68}(<\mathbf{0.01})$	0.07 (0.68)

To further substantiate this hypothesis, composites of low-residual (time points when the fractional residual is more than 1 standard deviation above its mean, and therefore closer to zero residual), mid-residual (time points when the fractional residual lies within 1 standard deviations of its mean) and high-residual (fractional residual below -1 standard deviation; note that

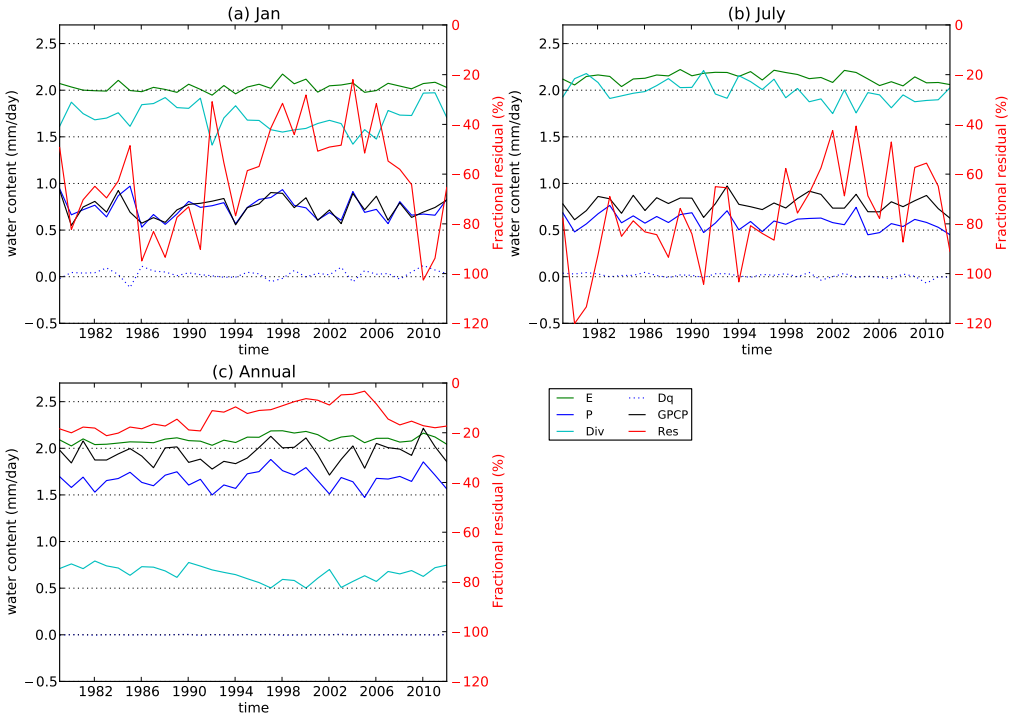

Figure 3.16: Time series of hydrological budget variables averaged spatially over regime 2 in (a) January, (b) July and (c) annual mean. Fractional residuals (i.e. the budget residual as a percentage of the mean precipitation) are plotted onto the y-axis on the right.

residuals are all negative, therefore below -1 standard deviation implies further departures from a closed budget) are defined. Fig. 3.17 shows the anomaly fields of $\bigtriangledown \cdot \mathbf{Q}$, moisture fluxes and 500 hPa geopotential height in the above defined composites. It can be seen that the low-, mid- and high-residual composites correspond to anomalous convergence, neutral and anomalous divergence of moisture over the regime 2 regions of tropical Africa and Asia. The anomalous moisture fluxes are mostly directed on-shore for the convergence case and off-shore otherwise. Associated with this circulation pattern difference, the pressure fields also display distinct distributions: a low pressure system is found to the north of regime 2 over land in the low-residual composite (Fig. 3.17b), and when the circulation is found to be anomalously divergent there is a strong high pressure system taking control over land (Fig. 3.17f).

Similar analyses are also performed for each of the four major land masses that are classified into regime 2 in July (Fig. 3.12b): South Africa, Central Asia, South America and western US. Residuals over western US are not particularly large, neither are they systematically positive or negative. The fractional residuals of regime 2 in July with and without the western US region are $-76.6\,\%$ and

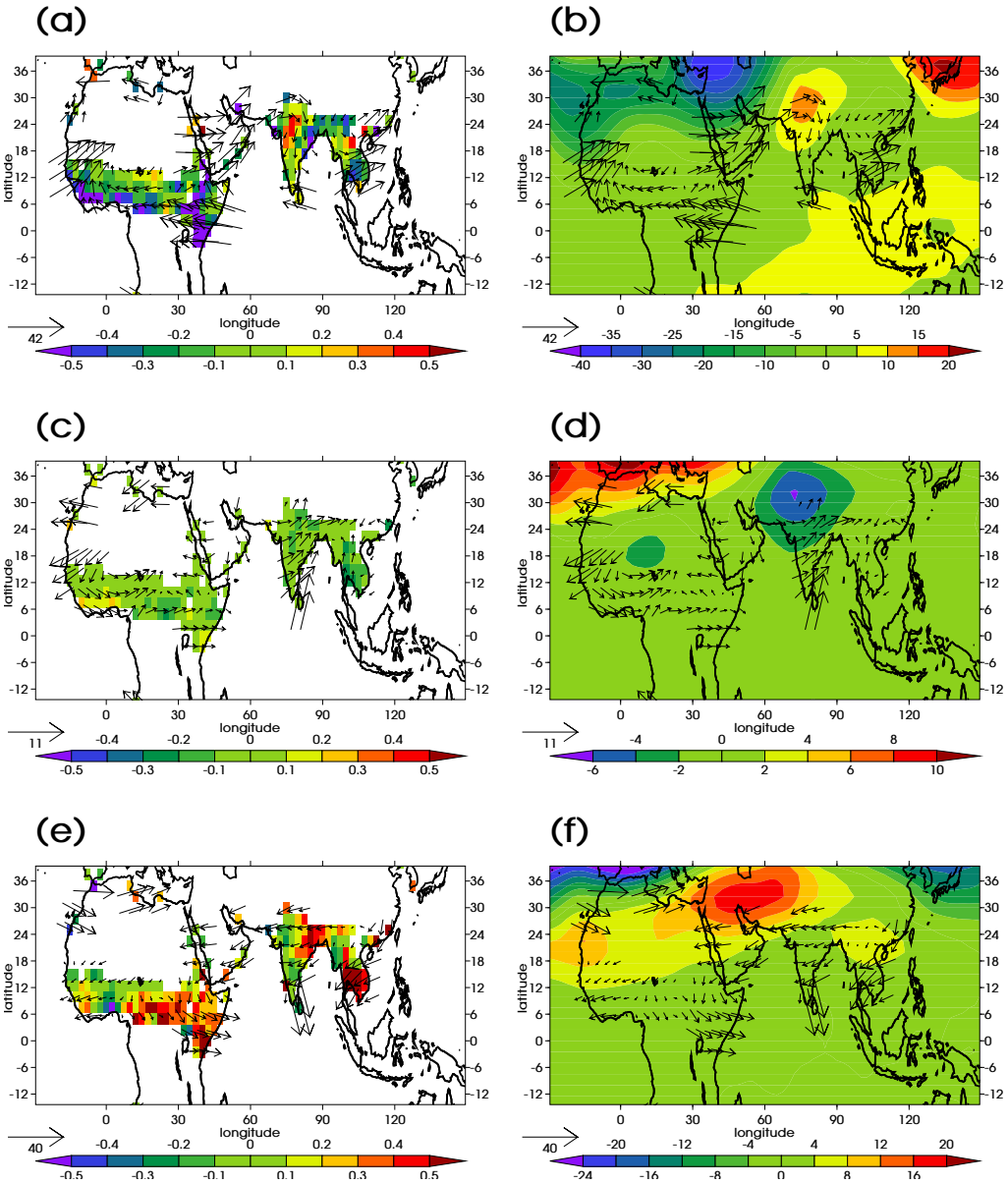

Figure 3.17: Composites of anomalous $\bigtriangledown \cdot \mathbf{Q}$ (coloured grid cells in left column), column integrated moisture fluxes (vectors in both columns) and 500 hPa geopotential height (contours in right column) in 1979-2012 January. The first row shows the low-residual composite, second row mid-residual and third row high-residual composite. $\bigtriangledown \cdot \mathbf{Q}$ is in the unit of mm/day, moisture fluxes in $kg/m/s$, and a scaling vector is shown at the bottom of each plot. For $\bigtriangledown \cdot \mathbf{Q}$ only the land boxes that are classified as regime 2 are plotted.

$-87.9\,\%$, respectively. And the correlation statistics as shown in Table 3.2 change to $-0.16\,(p = 0.37)$ with E, $-0.14\,(p = 0.42)$ with P, $-0.79\,(p < 0.01)$ with $\bigtriangledown \cdot \mathbf{Q}$ and $-0.40\,(p = 0.02)$ with dS, if western US is excluded from the computation. Therefore this region is not included in the subsequent analyses. Correlations with the residual time series (Table 3.3) suggest that for South Africa, Central Asia and South America, moisture divergence is the dominate modulator of residuals.

Composites of $\bigtriangledown \cdot \mathbf{Q}$ and moisture flux anomalies are also created for these regions (Fig. 3.18). Only the low- and high- residual composites are shown for brevity. Consistent with previous findings, low-residual composites are associated with anomalous moisture convergence and high-residual composites associated with anomalous divergence.

Table 3.3: Same as Table 3.2 but for South Africa, South America and Central Asia in July.

	South Africa	South America	Central Asia
E	-0.20 (0.25)	-0.26 (0.14)	-0.07 (0.69)
P	0.05 (0.79)	-0.01 (0.98)	-0.24 (0.18)
$\bigtriangledown \cdot \mathbf{Q}$	$\mathbf{-0.89}(< \mathbf{0.01})$	$\mathbf{-0.69}(< \mathbf{0.01})$	$\mathbf{-0.70}(< \mathbf{0.01})$
dS	0.03 (0.88)	-0.27 (0.12)	0.13 (0.45)

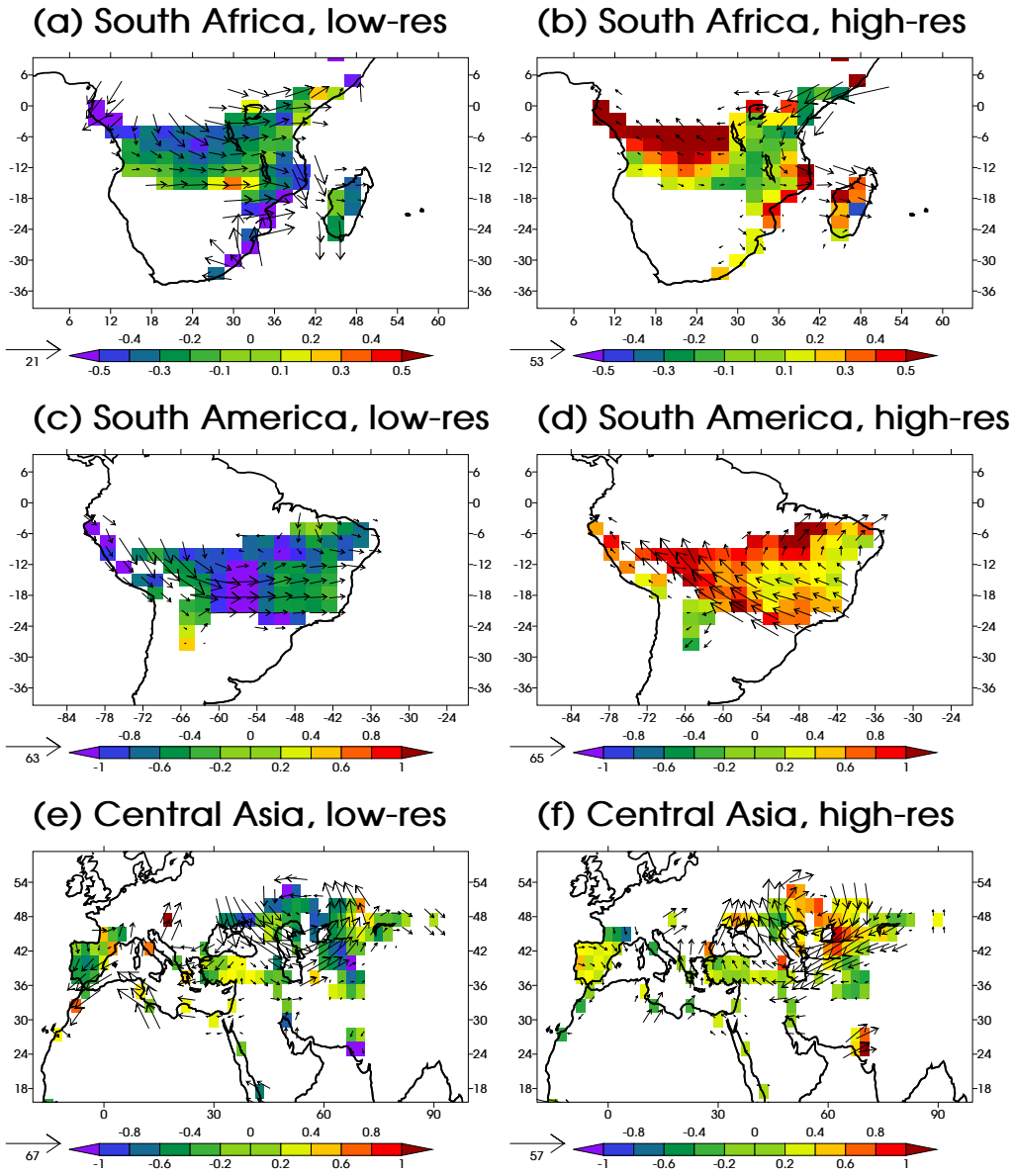

Figure 3.18: Composites of anomalous $\bigtriangledown \cdot \mathbf{Q}$ (coloured grid cells, mm/day) and moisture fluxes (vectors, $kg/m/s$) in South Africa (first row), South America (second row) and Central Asia (third row). Only land boxes that are classified as regime 2 in July are plotted. Left column shows the low-residual composites, and right column the high-residual composites.

3.3.8 Hydrological regimes in JRA-55

Hydrological regimes are also defined using JRA-55 data during the same time period, and the regime definitions and budget bar charts are displayed in Fig. 3.19 and Fig. 3.20, respectively. Notable similarities with the regime definitions in ERA-I can be observed in January and July (Fig. 3.19a,b). Some differences are found in the annual mean definitions, mostly in the Euro-asia and North America continents. The regime level budgets (Fig. 3.20) are also qualitatively consistent with the ERA-I results. Moreover, regime 2 stands out again as the one with the least closed budget in January and July.

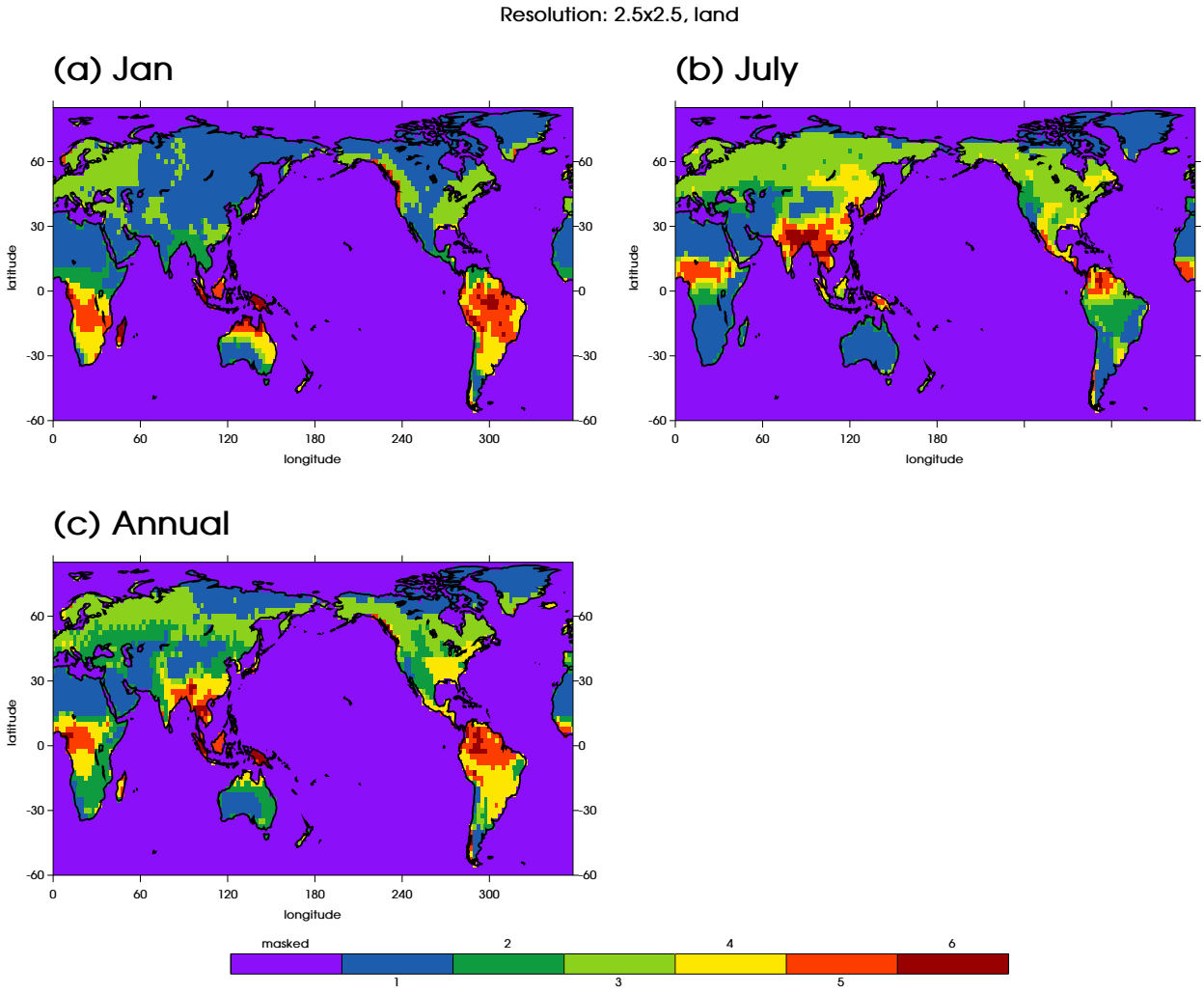

Figure 3.19: Same as Fig. 3.12 but defined by JRA-55.

Fig. 3.21 shows the time series of hydrological budget variables in regime 2 using JRA-55 data. Same as for ERA-I, $\bigtriangledown \cdot \mathbf{Q}$ has the strongest correlation with the budget residual in January (-0.34, $p < 0.05$) and July (-0.65, $p < 0.01$).

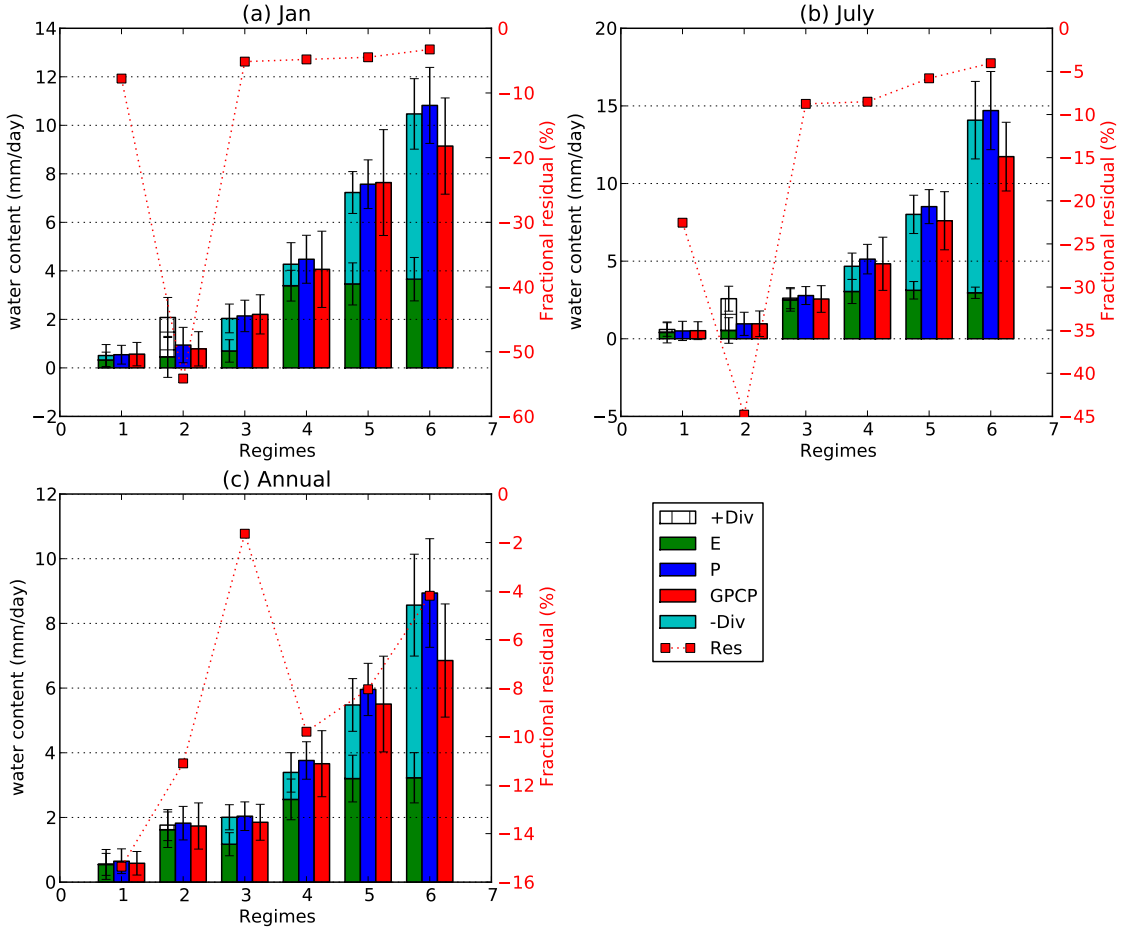

Figure 3.20: Same as Fig. 3.15 but for JRA-55.

The weaker correlation in January is to some extent caused by the high biases in JRA-55 P during 1979-1989 (Fig. 3.21a). For 1990-2012, the correlation with $\bigtriangledown \cdot \mathbf{Q}$ is stronger: -0.74 ($p < 0.01$). For annual means the largest correlation is with P (-0.63, $p < 0.01$), suggesting P as a stronger modulator. However, as the regime definitions are different from those found in ERA-I, the results of annual means can not be directly compared.

Composites of $\bigtriangledown \cdot \mathbf{Q}$ and moisture fluxes (not shown) using the same procedures as in ERA-I are also created for regime 2 in JRA-55, and the results lend further supports to the hypothesis that for regime 2 in the respective season, moisture divergence is closely related to the variation of the budget residual and therefore is likely to be the major cause of it.

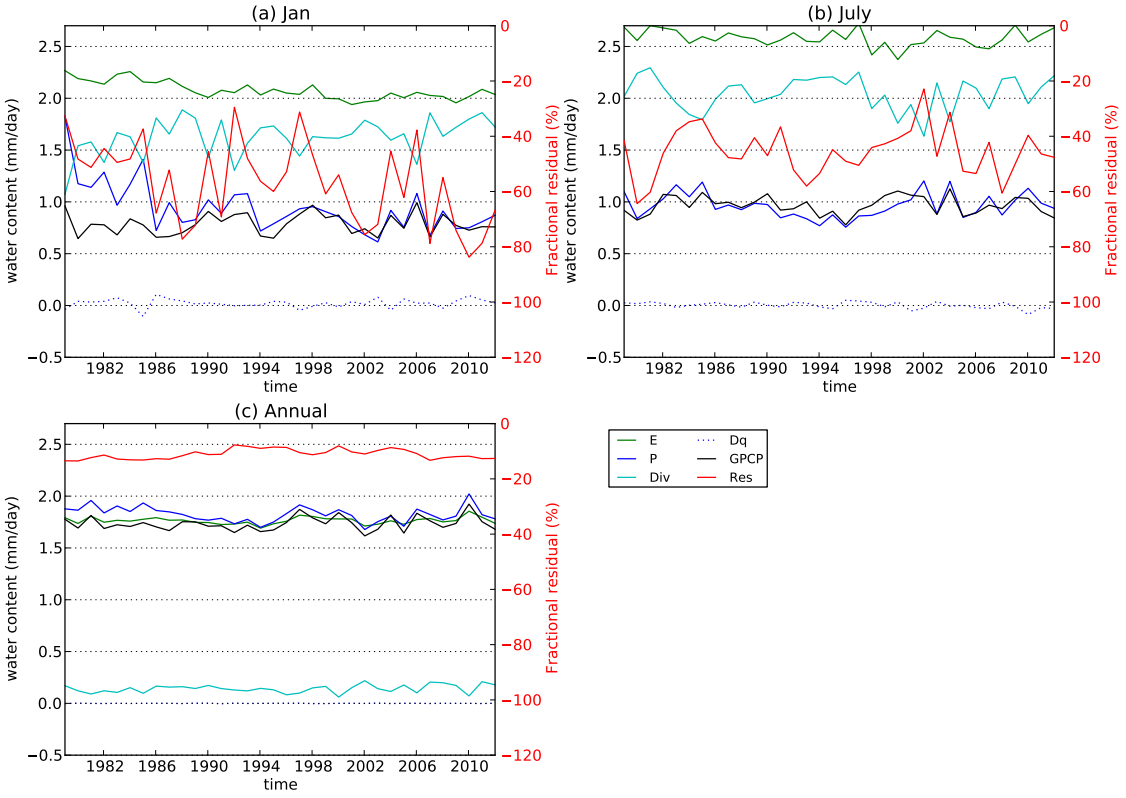

Figure 3.21: Same as Fig. 3.16 but for JRA-55.

3.4 Conclusions and discussion

This chapter completes the assessment of atmospheric hydrological cycle observations by addressing estimations of E and TCW. Greater degrees of uncertainty are expected in the large-scale land surface ET observations, largely due to the inherently limited spatial representativeness of the direct, in situ measurements, and the limitations of the various model-based indirect approaches. A high quality benchmark ET dataset is not available until recently, however, the ET estimates by this benchmark product by *Mueller et al.* (2013) is sensitive to which ensemble members it incorporates, and therefore still bears considerable uncertainties. This lack of a reliable reference for ET limits our assessment to a global annual mean level. Global land ET from ERA-I and JRA-55 falls within, but near the higher end, of the range of estimates from literature, consistent with previous findings (*Mueller et al.*, 2011, 2013).

Oceanic E is examined in more depth. Both reanalyses and HOAPS show some degrees of higher values compared with OAFlux in the tropics, with JRA-55 being the most biased. In terms of spatial patterns, the matches between OAFlux and both reanalyses are satisfactory, and there is little seasonal variation in their

performance. HOAPS shows higher levels of E in the ITCZ compared with OAFlux, and lower values in the Kuroshio current and Gulf stream regions. This pattern corresponds well with the differences in temporal standard deviations. Similar associations between the mean fields and local variability are also observed in its precipitation estimates (*Andersson et al.* (2011), also see Chapter 2).

Since humidity is assimilated into the reanalyses through 4DVAR schemes, good matches were expected among datasets for TCW. The Taylor diagrams confirm this, though systematic differences do exist and the possible implications may not be trivial despite the differences in the tropics being mostly below 10 %. Through the examination of P and TCW relationships in the ITCZ, we confirm that tropical convection in reanalyses is problematic. As they both maintain a higher level of precipitation with a lower level of TCW, the overestimation of P is likely due to the spin-down problem in the reanalysis model that produces high rainfall rates and then rapidly adjusts down (*Andersson et al.*, 2005). Associated with this spin-down is the positive analysis increments in the tropics that bring the humidity level back up to the observations (*Kobayashi et al.*, 2015). However, from a dynamic-thermodynamic decomposition point of view, the interpretation of this low-water-high-rainfall phenomenon is that the circulation and/or hydrological cycle in reanalyses may be too intense. To balance the diabatic heating associated with an overestimated precipitation, the adiabatic cooling that combines the vertical wind and temperature structure needs to be more effective (*Mitas and Clement*, 2006). The temperature profile in reanalyses, particularly the upper-troposphere section, has been questioned (*Santer*, 2005; *Held and Soden*, 2006; *Mitas and Clement*, 2006), rendering the circulation responses uncertain. In fact, intensity in the hydrological cycle context is an ill-defined term. It has been given explicitly or implicitly different interpretations in studies (e.g. *Quan et al.* (2004); *Mitas and Clement* (2005); *Bosilovich et al.* (2005); *Held and Soden* (2006); *Vecchi and Soden* (2007); *Sohn and Park* (2010); *Zhang and Song* (2006); *Zahn and Allan* (2011)), and has subsequently been "measured" through various perspectives using various variables and metrics. This to a certain extent fuels the controversy in the debate over recent decades' hydrological responses (e.g. *Sohn and Park* (2010); *Held and Soden* (2006); *Zahn and Allan* (2011); *Vecchi and Soden* (2007) and the references within). Before the issue of tropical spin-down in reanalyses is solved, conclusions drawn from reanalyses regarding "intensity" responses should be treated with caution.

We analyzed the budget residuals over global land through a hydrological

regime approach. This, on one hand, is because the residual distribution itself is rather noisy (see Fig. 1 in *Seager and Henderson* (2013)), and on the other hand we believe that the budget needs to be closed for a good reason. *Lorenz and Kunstmann* (2012) noticed that in terms of the continental surface water balance, MERRA shows the least residual ($2.6 \times 10^{15}\, kg/yr$) compared to ERA-I ($9.0 \times 10^{15}\, kg/yr$) and CFSR ($19.0 \times 10^{15}\, kg/yr$). That is to some extent the result of the compensation between an overestimated land ET and an underestimated surface runoff. Therefore we seek to use a more informative approach that allows the residuals to be quantified in the context of the local hydrology.

The hydrological regimes defined using ERA-I and JRA-55 show very similar geophysical locations in January and July, and in both cases regime 2 is found to be the one that has the largest fractional budget residuals. This regime features large local E and net divergence of moisture, and co-locates with the regions where the meridional component of the moisture fluxes are strongest (see Fig. 9 in *Trenberth and Guillemot* (1998)), suggesting that the meridional circulation in reanalyses may contain errors. Correlations of the residual time series with other variables suggest that moisture divergence is likely to be the major cause, and subsequent composite analyses lend further support to this hypothesis. Reliable references for land ET and moisture divergence are lacking, and confidences in the P observations are compromised by the sparse gauge distributions in these tropical regions (*Lorenz and Kunstmann*, 2012; *Pan et al.*, 2012; *Bosilovich et al.*, 2008). Therefore a correlation analysis can bypass these difficulties. However, this does not imply that other variables are reliably or correctly estimated in this case. It is possible that ET and P estimates may also contain biases, and certain degrees of error cancellation may occur that help to reduce the residual. As we emphasized, the budget residual is just one aspects of the quality of a dataset, and a closed budget does not necessarily imply correctness in all budget variables.

Chapter 4

Annual and diurnal cycles in horizontal moisture fluxes

4.1 Research background

Vertically integrated moisture fluxes give a picture of the horizontal re-distribution of moisture and energy by the atmospheric circulation, and reflect the modulating effects over different time scales, including large scale climate modes (e.g. ENSO, MJO, NAO), synoptic weather systems and land-ocean interactions and so on. The temporal spectrum of moisture fluxes generally corresponds to variability at different spatial scales, and requires data with a suitable resolution and tailored methods for specific analysis purposes. This chapter will look into the horizontal moisture fluxes using the ERA-I reanalysis, with the flux signals decomposed into different time scales and their interactions. The nature of the reanalysis dataset restricts the range of the time spectrum one could include: the relatively short time span (1979 onwards) and various observation heterogeneity issues (*Trenberth et al.*, 2011; *Bengtsson et al.*, 2004; *Bosilovich et al.*, 2011) make decadal and inter-decadal analysis mostly impossible, and the 6-hourly (forecast period is 12 hourly in ERA-I) temporal resolution places some barriers on analysis of diurnal cycles . These are taken into account in the subsequent analysis and care is taken in distinguishing artifacts of the dataset from the true signals when interpreting the results.

Horizontal winds and humidity are decomposed into three major time scales separately: the mean annual cycle, mean diurnal cycle and the eddy component. The mean annual cycle accounts for the climatological seasonal variations and

therefore forms the backbone of the moisture fluxes. Relative to this backbone component, the mean diurnal cycle explains anomalous moisture transports by variational winds and humidity fields during the course of a day, a relatively small scale feature which is most prominent over complex orography and coastal areas, but also reveals global scale patterns in phase with the diurnal solar heating. These two components are both based on the long-term averages (1979-2012 mean) and reflect the climatological mean behavior. Variations over individual years, seasons and the shifts of diurnal variability as well are represented collectively by the "eddy" component. The term "eddy" is used in a general sense to account for variations that are not accounted for by the mean annual and diurnal cycle components. This chapter will diagnose the annual and diurnal cycles and will then focus on diurnal variability; and two major aspects of the "eddy" component, namely the inter-annual variability in the tropical Pacific and the extreme fluxes associated with tropical cyclones are discussed in more details in Chapter 5 and 6, respectively.

4.1.1 Diurnal and semi-diurnal cycles

Two most fundamental modes of variability of the global climate system are the seasonal and diurnal cycles, both are associated with regular solar heating variations (*Yang and Slingo*, 2001). During the course of a day, Sea Surface Tempearture (SST) warms by the direct daytime solar heating and cools by nighttime radiative cooling. This diurnal variation of the top few meters of ocean has been studied for several decades. *Sverdrup et al.* (1942) and *Roll* (1991) reported the existence of diurnal SST changes based on vessel temperature observations. Later studies using either in situ (e.g. *Bruce and Firing* (1974), *Price et al.* (1987), *Yokoyama and Konda* (1996), *Webster et al.* (1996), *Kawai and Kawamura* (2002), *Matthews et al.* (2014)) or satellite observations (*Deschamps and Frouin* (1984), *Gentemann et al.* (2003), *Stuart-Menteth* (2003), *Sykes et al.* (2011)) confirmed the universality of the diurnal SST cycles. The amplitude of the variation has been found to be around 0.2 - 0.6 K on average, but can reach up to 5 K in extreme cases (*Kawai and Wada*, 2007).

Note that the term "SST" in general refers to the water temperature at the ocean surface, but there is a complex temperature profile in the top few meters and the resultant layers have different correspondences with different measuring instruments and implications on air-sea interactions. For instance, the theoretical temperature at the immediate contact interface between ocean

and air is defined as "interface SST", which is directly relevant to oceanic heat fluxes but can not be measured directly by current techonology (*Kawai and Wada*, 2007). At $\sim 10 - 20\,\mu m$ depth the temperature is "skin SST", which is measured by Infrared satellites. The more penetrating microwave satellite instrument measures "subskin SST", at a depth of $\sim 1\,mm$. What ships and buoys usually measure is the "depth SST" at around $\sim 1\,m$ depth. Diurnal variability exists in all of the above mentioned layers, but with different features (*Kawai and Wada*, 2007). Most reanalysis products use a prescribed SST as the boundary condition (the Climate Forecast System Reanalysis (CFSR) is a partially coupled reanalysis (*Kumar et al.*, 2013)), and in the case of ERA-I, four SST data products are used in succession (*Dee et al.*, 2011), but are all "bulk SST" or "depth SST" measurements (even though satellite retrievals may be assimilated) interpolated onto the model time step. However, as this chapter is mostly concerned with atmospheric mositure fluxes, the "SST" that is most relevant is the "interface SST", or the "skin SST" which is close enough to "interface SST" (*Kawai and Wada*, 2007). In the rest of the chapter we will be using the term "SST" in a general sense to refer to the temperature near the surface. However, it is helpful to note these subtle differences and be aware of possible problems caused by the mis-match of the boundary condition "SST" and the atmospheric responses it forces.

Furthermore, model experiments confirmed that the inclusion of a diurnal solar insolation forcing is responsible for the observed diurnal cycles in SST (*Schiller and Godfrey*, 2003, 2005). The effect is not restricted to the SST itself, but has implications for various atmospheric properties through air-sea interactions, including humidity and surface heat fluxes (*Dai and Trenberth*, 2002, 2004; *Schiller and Godfrey*, 2003, 2005; *Zeng and Dickinson*, 1998; *Yang and Slingo*, 2001). Currently many climate models use a slow varying SST as boundary condition, this lack of diurnal SST forcing has been suggested to be a significant deficiency, which leads to insufficient diurnal variations in air temperature, pressure and precipitation (*Dai and Trenberth*, 2004). Little added value is observed when the day-to-day variation is introduced onto the monthly mean SST values, this missing piece can only be retrieved when temporal resolution below one day is resolved (*Zeng and Dickinson*, 1998).

The difference due to the lack of diurnal cycle in model simulations is most prominent but not restricted to diurnal time scales. For instance, on a regional scale, an SST anomaly due to the exsitence of the diurnal warm layer can reach $0.8\,°C$, with a daily mean of $0.2\,°C$ (*Matthews et al.*, 2014); surface heat fluxes

can increase by the order of $50\,W/m^2$ during the daytime when diurnal SST is incorporated, and the time mean value can be above $10\,W/m^2$ (*Kawai and Wada*, 2007). Neither are negligible for the atmosphere.

In addition to this bottom-up influence through diurnally varying surface temperature forcing, the atmosphere oscillates from the top-down at diurnal and semi-diurnal periods as well. With manifestations in atmospheric pressure, temperature and wind fields, these diurnal/semi-diurnal oscillations are also known as "atmospheric tides" (*Lindzen*, 1967; *Dai and Wang*, 1999; *Deser and Smith*, 1998). Previous studies have documented the existence of this tidal variation in surface wind and pressure fields, particularly over tropical oceans (*Dai and Wang*, 1999; *Deser and Smith*, 1998). Excited by the absorption of solar radiation by ozone and water vapour, the tidal oscillation decreases towards the surface, during which the diurnal component has been largely dampped out, leaving only the semi-diurnal component (*Lindzen*, 1967; *Deser and Smith*, 1998). As the Quasi-biennial Oscillation (QBO) affects this semi-diurnal variation via the ozone concentration, a signature of QBO is imprinted in the surface pressure, forming the basis of QBO reconstruction from SLP data (*Brönnimann et al.*, 2007). Models have been developed to describe the semi-diurnal oscillation of surface pressure, and via the horizontal momentum equations, the surface wind fields (*Deser and Smith*, 1998; *Ueyama and Deser*, 2008).

In regard to the global scale hydrological cycle, much attention has been focused on the diurnal cycle of deep convection and associated precipitation (e.g. *Yang and Slingo* (2001); *Dai et al.* (2007); *McGarry and Reed* (1978); *Janowiak et al.* (1994); *Sui et al.* (1997)), however there have been few studies that combined the diurnal variations in humidity and wind fields to diagnose the moisture flux diurnal cycles and their seasonal differences. This is partly due to the lack of high spatio-temporal resolution observations in water vapour and winds. *Tian et al.* (2004) used combined water vapour and window radiances from multiple satellites to analyse the upper troposphere humidity (UTH) diurnal cycles, and documented a certain phase lag between the UTH, high clouds and deep convection diurnal cycles. However this has limited implications in terms of large scale moisture transports, due to the low levels of humidity in this section of the troposphere. *Dai and Trenberth* (2002) provided evidence for the diurnal variations in precipitable water (PW) over continental North America. The GPS, ground-based microwave radiometer and radiosondes observations give largely consistent results in the diurnal PW cycles, and the vertical profile created from radiosondes illustrates the vertical differences in the diurnal amplitudes and

phases. In particular, a clear distinction between the boundary layer and the free troposphere was identified.

Inspired by these early efforts, this chapter attempts to extend the analysis to cover the global scale mid-to-lower troposphere where the majority of moisture transports reside, and highlight the seasonal evolutions of diurnal cycles. To overcome the low temporal sampling deficiency of the reanalysis data, we modified the conventional approach in diurnal cycle studies, which is to obtain the seasonal means of some sub-daily data then use harmonic analysis to describe the diurnal cycles. Instead we computed the annual cycle harmonics of the synoptic hours and obtained the diurnal cycles from the differences among them. Some information of the diurnal cycle is inevitably lost, but we still retrieve a robust diurnal signal that is embedded in the annual cycles and a smooth seasonal evolution can be easily visualized. Section 4.2 explains the method in detail, and the diurnal moisture fluxes due to variability in humidity and the atmospheric tides are shown in Section 4.3.2 - 4.3.5.

4.2 Data and Methods

4.2.1 Mean annual cycle of winds and humidity

ERA-Interim (ERA-I) 6-hourly specific humidity (q) and horizontal winds (u, v) on model levels 31-60 ($\sim 230\,hPa$ to surface) are used to compute the column moisture fluxes. At each level, the 6-hourly annual cycles of u, v and q are computed by averaging across 34 years (1979-2012), and the resultant time series are fitted by a harmonic analysis (mean plus first 3 harmonics) at each of the synoptic hours *separately* at 00, 06, 12 and 18 UTC:

$$\begin{cases} X_{a00} &= \mu_{00} + \sum_{j=1}^{3} S_{j00} \\ X_{a06} &= \mu_{06} + \sum_{j=1}^{3} S_{j06} \\ X_{a12} &= \mu_{12} + \sum_{j=1}^{3} S_{j12} \\ X_{a18} &= \mu_{18} + \sum_{j=1}^{3} S_{j18} \end{cases} \tag{4.1}$$

where X stands for u, v or q. Subscript a denotes annual cycle, μ is the mean at a synoptic hour, and the jth harmonic at the same synoptic hour is represented by S_j. Note that although termed as "annual cycle", the inclusion of up to the third harmonic implies that semi-annual cycle variability is also captured.

The means of the above harmonics across synoptic hours are equivalently the harmonics of the daily means, and are repeated four times to give the "mean annual cycle" time series: u_a, v_a and q_a, each of which has a length of $365 \times 4 = 1460$ (29th Februray in leap years are deleted):

$$X_a = \frac{X_{a00} + X_{a06} + X_{a12} + X_{a18}}{4} \tag{4.2}$$

4.2.2 Mean diurnal cycle of winds and humidity

The deviations of each synoptic harmonic with respect to the "mean annual cycle" are defined as the "mean diurnal cycle":

$$\begin{cases} X_{d00} &= X_{a00} - X_a \\ X_{d06} &= X_{a06} - X_a \\ X_{d12} &= X_{a12} - X_a \\ X_{d18} &= X_{a18} - X_a \end{cases} \tag{4.3}$$

These are "zipped" together in days to a form a time series X_d, with a length of 1460. Note that the diurnal cycle defined in this manner represents the systematic differences across synoptic hours that are embedded in their mean annual cycles. As the mean annual cycle only up to the third harmonic has been retained, the observed diurnal differences are likely to be underestimated, both due to the 6-hourly sampling of ERA-I and to the loss of higher order harmonics. However, for the same reason any observed diurnal variation is robust, and previous studies have confirmed that the four-times-daily sampling frequency is able to reveal diurnal cycles (*Sykes et al.*, 2011).

4.2.3 Eddy component of winds and humidity

The "eddy" components are defined as the residual:

$$X_e = X - X_a - X_d \tag{4.4}$$

Note that the "eddies" defined above are distinct from "anomalies" in that their time averages are not zero definite, as both X_a and X_d are fitted harmonics:

$$\overline{X_e} = \overline{X - X_a - X_d} = \overline{X} - X_a - X_d \neq 0 \tag{4.5}$$

Fig. 4.1 illustrates the definitions of mean annual cycle, mean diurnal cycle and eddy meridional wind components for a sample grid box (located at $5°N$, $120°E$). Note that the mean diurnal cycle varies in both amplitude and phase through the year, and the mean annual cycle has step-wise changes across days.

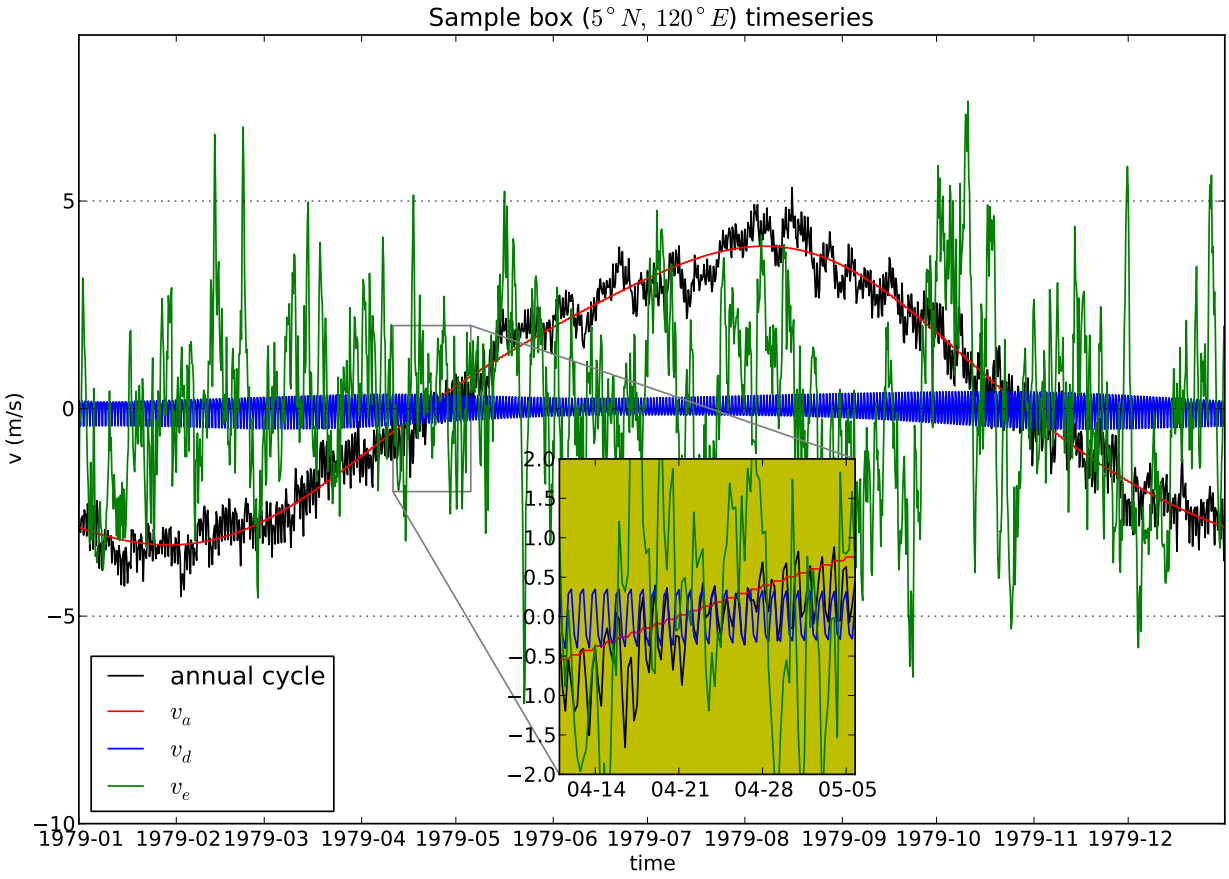

Figure 4.1: The diagnosis of annual cycle, diurnal cycle and eddy components illustrated using the timeseries of meridional wind ($v\,m/s$) at sigma level 60, $5°N$, $120°E$. The mean annual cycle (red; v_a) is obtained by separate harmonic analysis (Eq. 4.1) at each of the four synoptic hours of the 34-year average (black; here shown with the four synoptic hours concatenated into a single timeseries through the climatological year). The mean of the four annual cycles (Eq.4.2) is repeated at the four synoptic hours in each day resulting in small step changes between days (more easily seen in the inset plot). The mean diurnal cycle (blue, v_d) is given by the deviation of each of the four annual harmonics (fitted to the data from the four synoptic hours) from their mean (Eq. 4.3). The eddy wind (green; v_e) is the residual from an individual year's data and these 1979-2012 climatological cycles (Eq.4.4), shown here for one example year (1979).

4.2.4 Moisture fluxes by cross terms in winds and humidity

Interactions between wind and humidity fields over the three time scales give rise to a mean moisture flux that can be represented by 9 terms, the product of 3 terms for wind and 3 terms for humidity:

$$\begin{aligned}\overline{Vq} &= \overline{(V_a + V_d + V_e)(q_a + q_d + q_e)} \\ &= (\overline{V_a q_a + V_a q_d + V_a q_e + V_d q_a + V_d q_d + V_d q_e + V_e q_a + V_e q_d + V_e q_e})\end{aligned} \tag{4.6}$$

The last term $\overline{V_e q_e}$ is the eddy covariance. The cross terms in (4.6) represent interactions across time scales, e.g. $\overline{V_a q_d}$ is the flux resulting from diurnally varying humidity advected by the background mean flow, and $\overline{V_e q_a}$ is the flux created by eddy wind scaled by the mean humidity. When taking a time average (across 34 years), these cross terms, including the covariance term, are not zero definite, as explained above. Furthermore, when these fluxes are vertically integrated, a third term (surface pressure) is introduced into the computation:

$$F = \int_{P_{31}}^{P_{60}} \frac{Vq}{g} dP = \frac{\sum_{i=31}^{60} V_i q_i \Delta P_i}{g} \tag{4.7}$$

The computation is done using model level data, therefore the pressure increment term in (4.7) is:

$$\Delta P_i = \Delta A_i + \Delta B_i P_s \tag{4.8}$$

where A_i and B_i are level dependent constants that define the terrain following sigma levels in ERA-I. Equation (4.7) implies that the vertically integrated horizontal moisture flux is a combination of the mass of the atmospheric column (equivalently surface pressure), the humidity load (specific humidity measured in kg/kg) and the wind speeds.

Integrations that involve only the "mean annual cycle" and/or "mean diurnal cycle" in wind and humidity are annual cycles in nature, therefore the 34-year mean annual cycle of surface pressure is used in the vertical integration. Computations that involve "eddy" component are performed for each individual year, using the surface pressure of the corresponding year. The covariances with surface pressure also imply that the time averages (across 34

years) of the following cross terms are not zero definite:

$$\begin{cases} \overline{V_a q_e P_{si}} &= \overline{V_a} \cdot \overline{q_e P_{si}} = \overline{V_a} \cdot \overline{q_e \cdot (\overline{P_s} + P'_{si})} \neq 0 \\ \overline{V_d q_e P_{si}} &= \overline{V_d} \cdot \overline{q_e P_{si}} = \overline{V_d} \cdot \overline{q_e \cdot (\overline{P_s} + P'_{si})} \neq 0 \\ \overline{V_e q_a P_{si}} &= \overline{q_a} \cdot \overline{V_e P_{si}} = \overline{q_a} \cdot \overline{V_e \cdot (\overline{P_s} + P'_{si})} \neq 0 \\ \overline{V_e q_d P_{si}} &= \overline{q_d} \cdot \overline{V_e P_{si}} = \overline{q_d} \cdot \overline{V_e \cdot (\overline{P_s} + P'_{si})} \neq 0 \end{cases} \tag{4.9}$$

where P_{si} is the surface pressure in the ith year, $\overline{P_s}$ the 34-year average and P'_{si} the ith year's anomaly.

The 9 terms of 34-year averages shown in Eq. 4.6 can be further averaged into calendar months to give an integrated view of the different scale interactions in generating temporally coherent moisture fluxes. Hereafter we will be using overbars $\overline{X}$ to denote averages across 34 years, and angle braces $< >$ to denote monthly means, e.g. the January mean of $\overline{V_a q_d P_s}$ is $< \overline{V_a q_d P_s} >_{Jan}$.

Note that $< \overline{V_a q_d} >= 0$, as in any given day the sum of q_{d00}, q_{d06}, q_{d12} and q_{d18} is zero by definition (Eq. 4.2, 4.3). However, the inclusion of the pressure term incorporates interactions between diurnally varying q_d and P_s and gives rise to non-zero values in $< \overline{V_a q_d P_s} >$. Similarly, the non-zero values in $< \overline{V_d q_a P_s} >$ are due to the interactions between V_d and P_s. The reader will be reminded what a specific term truly represents in the subsequent discussions, and Table 4.1 gives a summary of the flux components and their interpretations.

Table 4.1: Notations and interpretations for the terms in the temporal break down of horizontal moisture fluxes. When zonal fluxes are discussed, V is replaced by U.

Notation	Derivation	Meaning
$V_a q_a P_{sa}$	$\overline{V_a q_a P_s} = \overline{V_a} \cdot \overline{q_a} \cdot \overline{P_s} = V_a q_a P_{sa}$	Product of "mean annual cycles" in wind V_a, humidity q_a and the annual cycle of surface pressure P_{sa}
$V_a q_d P_{sa}$	$\overline{V_a q_d P_s} = \overline{V_a} \cdot \overline{q_d} \cdot \overline{P_s} = V_a q_d P_{sa}$	Diurnally varying humidity q and surface pressure P_s advected by mean background winds V_a
$V_a \cdot \overline{q_e P_s}$	$\overline{V_a q_e P_s} = V_a \cdot \overline{q_e P_s}$	Eddy humidity q_e advected by mean background winds V_a
$V_d q_a P_{sa}$	$\overline{V_d q_a P_s} = \overline{V_d} \cdot \overline{q_a} \cdot \overline{P_s} = V_d q_a P_{sa}$	Diurnally varying wind V_d and P_s scaled by mean background humidity q_a
$V_d q_d P_{sa}$	$\overline{V_d q_d P_s} = \overline{V_d} \cdot \overline{q_d} \cdot \overline{P_s} = V_d q_d P_{sa}$	Covariance in the diurnally varing wind V_d, humidity q_d and surface pressure P_s
$V_d \cdot \overline{q_e P_s}$	$\overline{V_d q_e P_s} = V_d \cdot \overline{q_e P_s}$	Eddy humidity q_e advected by diurnally varying winds V_d
$q_a \cdot \overline{V_e P_s}$	$\overline{V_e q_a P_s} = q_a \cdot \overline{V_e P_s}$	Eddy wind V_e scaled by mean background humidity q_a
$q_d \cdot \overline{V_e P_s}$	$\overline{V_e q_d P_s} = q_d \cdot \overline{V_e P_s}$	Eddy wind V_e scaled by diurnally varying humidity q_d
$\overline{V_e q_e P_s}$	/	Covariance in Eddy wind V_e and humidity q_e
$< X >$	/	Calendar-month mean of the term X

4.3 Results

4.3.1 Monthly mean moisture fluxes

Horizontal moisture fluxes integrated through the mid-to-low troposphere are decomposed into time scales of mean annual cycle, mean diurnal cycle, eddy covariance and interaction components, as described in the previous section. The resultant 9 combinations are averaged across January and July (Fig. 4.2 - Fig. 4.5) to illustrate the contributions from different time scales and scale interactions in generating temporally coherent fluxes.

As the mean annual cycle consists of the mean and the seasonal harmonics, it is not surprisingly the largest contributor to both zonal and meridional fluxes in both seasons (subplot (a) in Fig. 4.2 - 4.5). The mean January zonal fluxes, or more precisely the January mean of the fitted annual cycle, generally follow the lower tropospheric zonal wind: easterly trades in the tropics and westerlies in mid-latitudes (Fig. 4.2a and 4.3a). The SH mid-latitude zonal fluxes are stronger in summer (January), weakening and shifting equatorward in winter (July), while in the NH there is a contrast between ocean basins: the North Pacific westerly fluxes are stronger in winter and the North Atlantic westerly fluxes

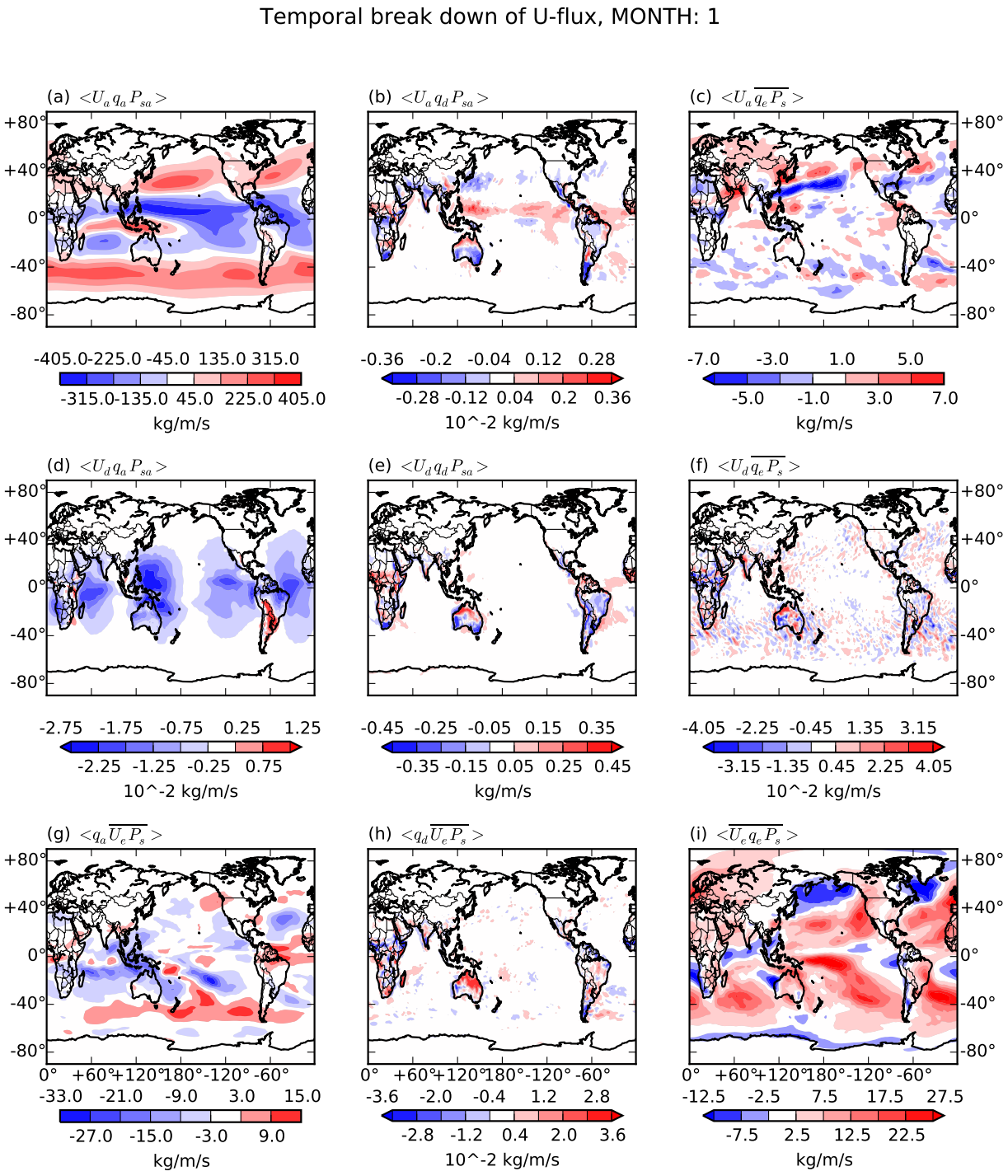

Figure 4.2: January mean zonal column moisture fluxes ($kg\,m^{-1}s^{-1}$) decomposed into different time scales and their interaction terms. From the top to bottom row, wind components are mean annual cycle, mean diurnal cycle and eddy component, respectively. From the left to right column, humidity components is the mean annual cycle, mean diurnal cycle and eddy component, respectively. For example, (a) shows the integrated flux by mean January zonal wind and mean January specific humidity, and (e) is the combination of mean diurnal wind and mean diurnal humidity. For detailed explanation see the Data and Methods section and Table 4.1. Note that subplot b, d, f, h are scaled up by 10^2 for easier labelling.

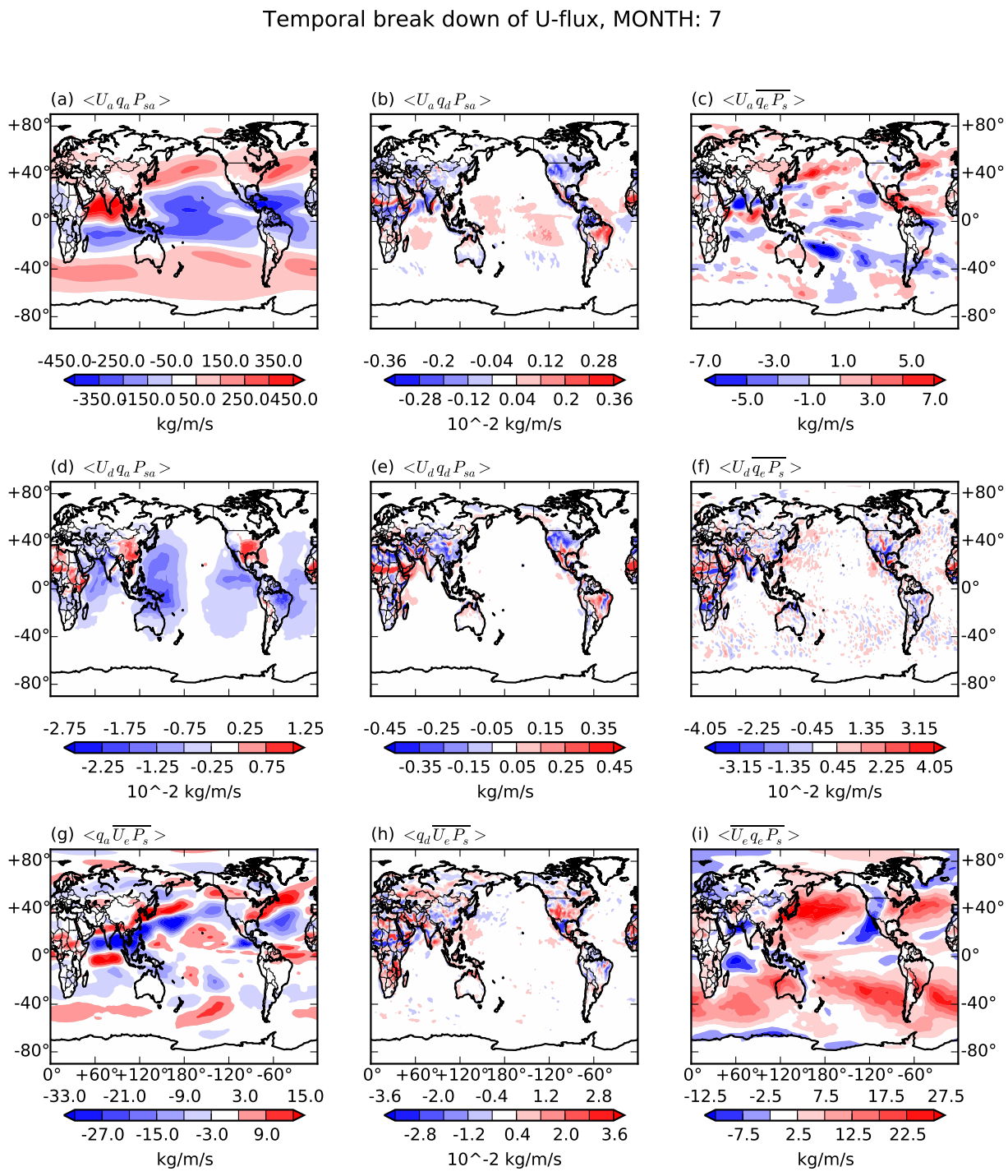

Figure 4.3: Same as Fig. 4.2 but for July averages.

are slightly stronger in summer. The annual cycle reverses the direction of the zonal moisture fluxes in the equatorial and North Indian Ocean, linked to the monsoonal circulations. The meridional moisture fluxes (Fig. 4.4a and 4.5a) are weaker overall, and reveal the transport around the subtropical high and subpolar low pressures of the ocean basins, especially prominent in the summer hemisphere, and poleward transport in the NH storm track regions during the winter. Monsoonal changes are again promiment over the Indian ocean and the Euroasian land mass, and seasonal variations can be observed over the tropical convergence zones.

Eddy covariance terms (subplot (i) in Fig. 4.2 - 4.5) constitute the second largest contributor to horizontal fluxes. Storm track regions in both hemispheres are highlighted in these terms, where mid-latitude cyclones and depressions play an important role in the poleward transport of moisture and heat. Zonal fluxes are mostly eastwards with some notable exceptions, such as the far northern Pacific and NW Atlantic where the eddy covariance transports moisture westwards in Jan. Meridional fluxes are nearly all poleward and associated with the mid-latitude storm-tracks. They play almost no role in meridional transport of moisture in the South Asian summer monsoon.

Non-negligible fluxes are also seen in interaction terms that involve the mean annual cycle and eddy components. For instance $< q_a \cdot \overline{V_e P_s} >$ (subplot (g) in Fig. 4.2 - 4.5) accounts for the fluxes of eddy wind scaled by mean background humidity, and is of the same order of magnitude as the eddy covariance term. A shearing zone in the zonal flux (Fig. 4.2g, 4.3g) is observed in the mid-latitude of the summer hemisphere, and a series of wave-like patterns can be seen in the meridional flux in the mid-latitudes in both hemispheres (Fig. 4.4g, 4.5g). The $< V_a \cdot \overline{q_e P_s} >$ term (subplot (c) in Fig. 4.2 - 4.5) also shows some regional variations with a smaller magnitude. Patterns embedded in these terms consist of interactions between wind, humidity and surface pressure across multiple time scales, detailed analysis of which goes beyond the scope of this chapter.

Terms that involve the mean diurnal cycle in either wind or humidity ($< V_a q_d P_{sa} >$, $< V_d q_a P_{sa} >$, $< V_d q_d P_{sa} >$, $< V_d \cdot \overline{q_e P_{sa}} >$ and $< q_d \cdot \overline{V_e P_{sa}} >$, see the mid row and column in Fig. 4.2 - 4.5) are all negligible in terms of monthly mean fluxes. The largest of these ($< V_d q_d P_{sa} >$) only accounts for a few tenths of $kg\, m^{-1}\, s^{-1}$ of moisture transport and is largely confined to some tropical regions with complex orography or along the coasts. And the other terms are two orders of magnitude smaller (note that all these terms except $< V_d q_d P_{sa} >$

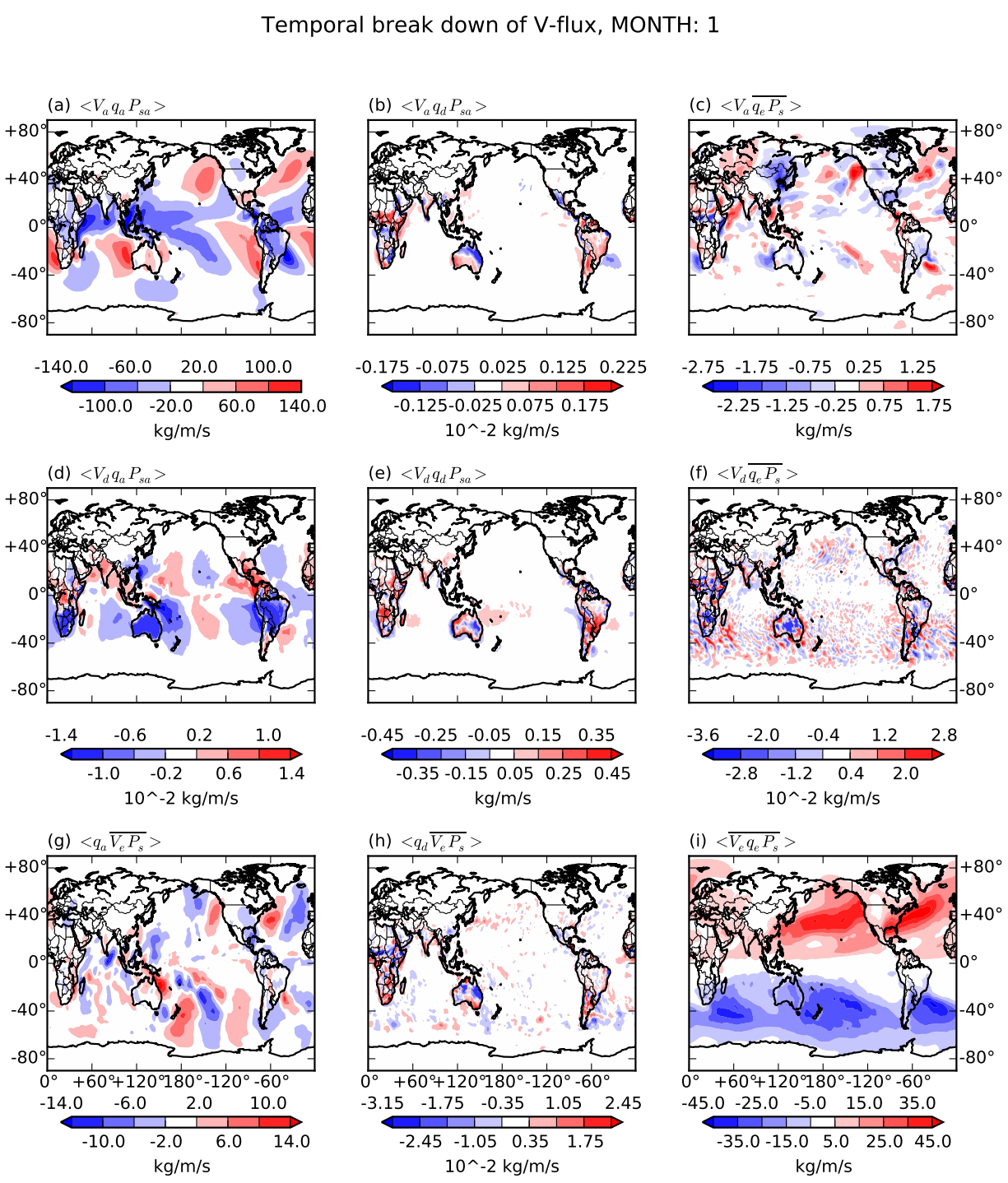

Figure 4.4: Same as Fig. 4.2 but for January mean meridional moisture flux.

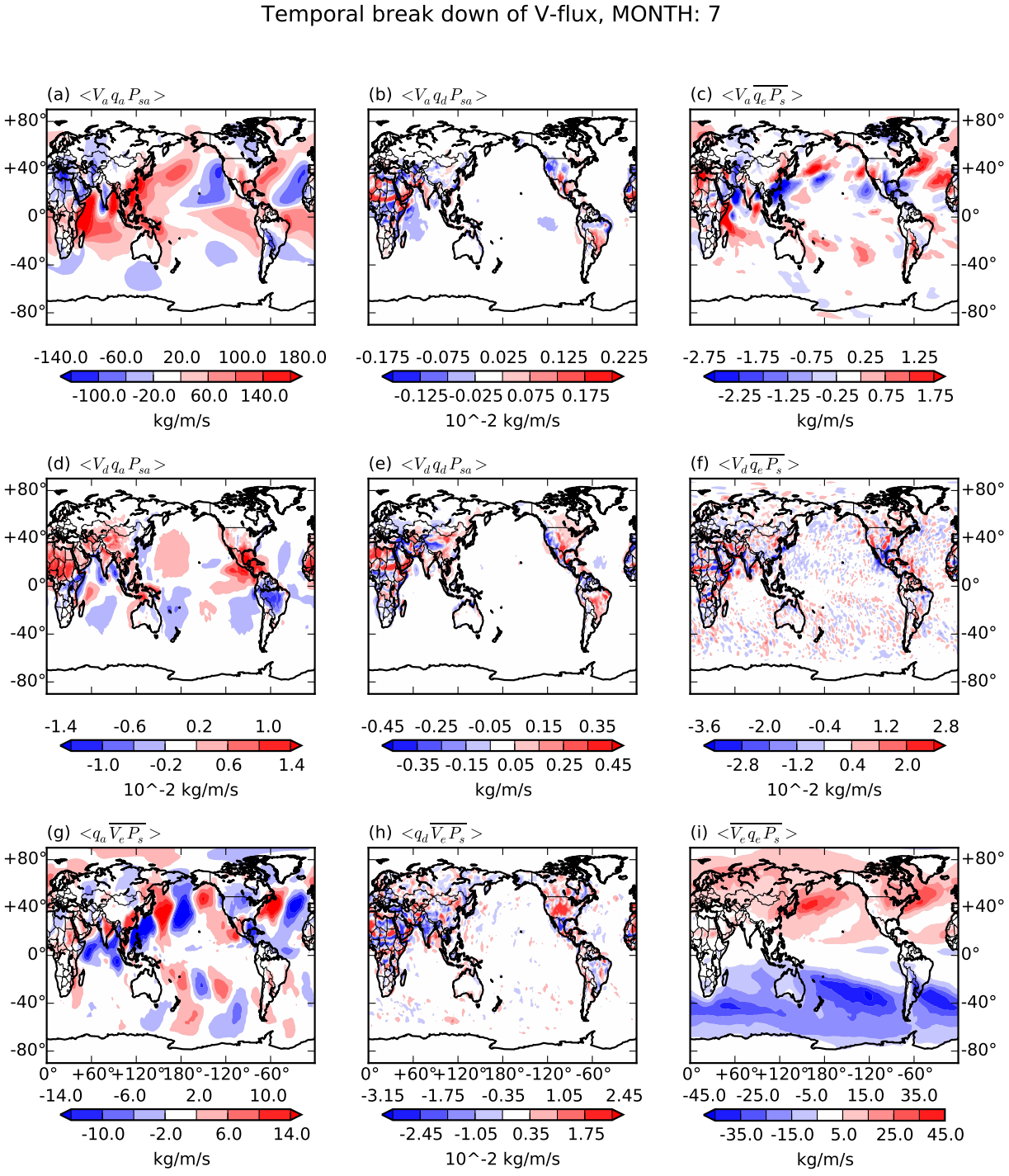

Figure 4.5: Same as Fig. 4.2 but for July mean meridional moisture flux.

have been scaled by 100 relative to the other terms in Fig. 4.2 - 4.5). This implies limited net effect of diurnal variations in generating temporally coherent mositure fluxes, however, as explained in the previous section, the diurnal cycles obtained from fitted harmonics are likely to be underestimated. When averaged across a month, the short-term fluxes created by interactions between q and P_s ($V_a q_d P_{sa}$, see Table 4.1), or between V and P_s ($V_d q_a P_{sa}$) are largely cancelled out. In other words, the daytime increase of moisture load is roughly balanced by nighttime decrease, or a roughly equal amount of moisture is transported by the wind in one direction as in the opposite direction at the end of a day. Systematic convergence/divergence during a fixed period of a day is required for a notable net effect to accumulate. This explains the coastal and complex terrain maxima/minima observed in diurnal-involved combinations, and is indicative of the land-see-breeze and mountain-valley-breeze effects.

Although being negligible in terms of time-accumulated *net* effects, diurnal variations can be significant or have well organized spatial patterns. The latter can be observed in the $< V_d q_a P_{sa} >$ component, where four evenly spaced troughs are found along the equator in the zonal flux (Fig. 4.2d, 4.3d), and similar wave-patterns with some cross-equator asymmetric features can be seen in the meridional component (Fig. 4.4d, 4.5d). These are the result of atmospheric tidal oscillations and aliasing in the 6-hourly ERA-I data, explained further in the following sections.

4.3.2 Diurnal cycles of Total Column Water and zonal moisture flux–spatial patterns

To examine the diurnal variability in horizontal moisture fluxes due to the humidity changes, the mean diurnal cycles of $U_a q_d P_{sa}$ are created by averaging the four synoptic hours across DJF and JJA, respectively. The results are shown in Fig. 4.6. In the tropics, a westward propagating maximum/minimum along the equator completes a cycle in a day. In the mid-latitude the direction of the flux anomaly is not always consistent with the tropical counterparts within the same longitudinal band, e.g. at 06 UTC in DJF the Kuroshino current region has westerly flux anomalies, opposite to the equatorial easterlies (Fig. 4.6).

Note that in $U_a q_d P_{sa}$ the zonal wind is kept constant (at the daily mean) during a day, therefore the resultant flux reveals diurnal interactions between q and P_{sa}. However, sea level pressure has been found to have a much stronger

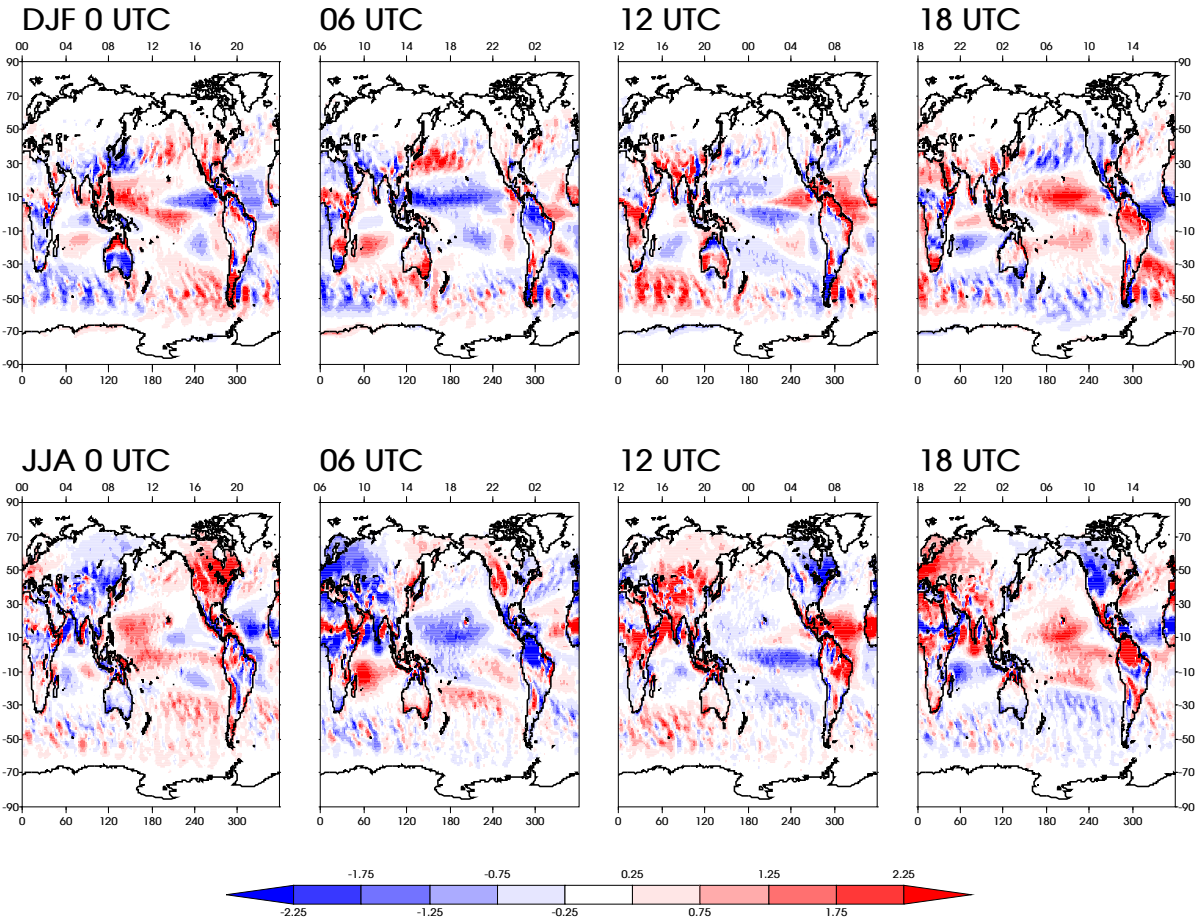

Figure 4.6: Mean diurnal cycle of zonal moisture flux by the term ($U_a q_d P_{sa}$, $kgm^{-1}s^{-1}$). Top row shows the mean synoptic averages in the DJF season, and bottom row the JJA season. The four columns correspond to UTC hour 00, 06, 12 and 18, respectively, and the local solar time is labelled at the top x-axis.

semi-diurnal cycle, as the diurnal modes are largely trapped near the level of forcing (top troposphere-stratosphere) (*Lindzen*, 1967; *Deser and Smith*, 1998). Taking into account the 6-hourly sampling frequency of ERA-I, the variation of P_{sa} between the four synoptic hours is relatively small. Therefore the diurnal cycle observed in zonal flux $U_a q_d P_{sa}$ is attributed to the diurnal cycle in the humidity field, and this will be verified in the following.

Fig. 4.7 shows the diurnal cycle of TCW as represented by q_d. The diurnal deviations from their daily means are vertically integrated, and DJF/JJA averages are computed at the synoptic hours. Comparing with Fig. 4.6, the patterns in TCW and zonal flux are largely consistent, but with opposite signs in the tropics. This is because the direction of mean background flow is mostly easterlies (negative) in the tropics and westerlies (positive) outside. Some

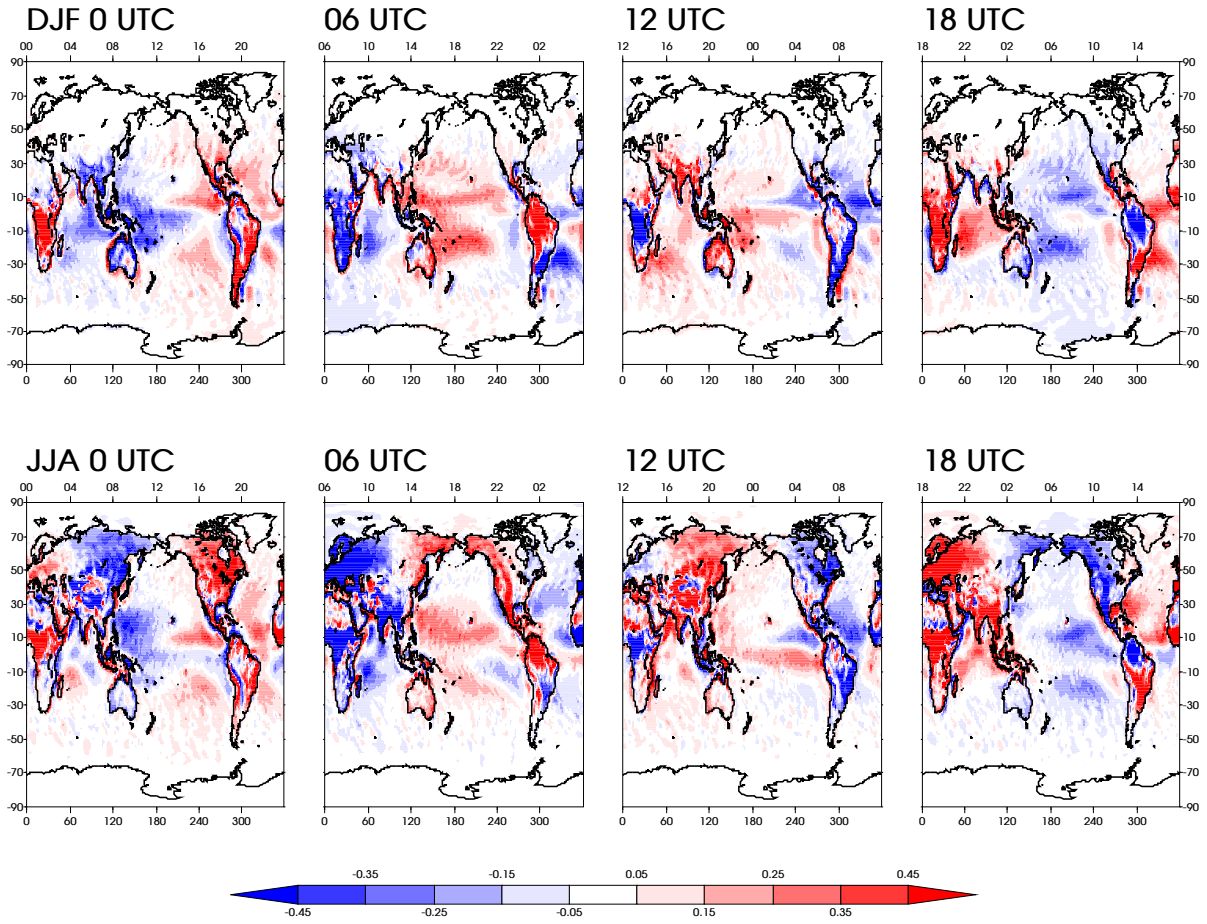

Figure 4.7: Same as Fig. 4.6 but for TCW (mm).

meridional banding features can be observed, particularly in mid-latitude lands where the zonal gradients are smaller (e.g. at 00 UTC in JJA). This clear zonal transition is replaced with irregular patterns in the tropics, where positive and negative TCW regions tend to "wedge" into each other. This indicates different mechanisms responsible for creating the observed diurnal cycle, and for the tropics, it is likely that the shaping of the background convection areas (shape and location of the warm pool and seasonally varying ITCZ and SPCZ) and the zonal thermocline gradient are related.

The meridional averages of the TCW diurnal cycle (Fig. 4.8) are consistent across all four seasons: the local maximum in TCW occurs in the local late afternoon-evening ($\sim$ 1800-2100, i.e. longitudes (degree East) 270 - 315 at 00 UTC, longitudes 180 - 225 at 06 UTC, longitudes 90 - 135 at 12 UTC, and longitudes 0 - 45 at 18 UTC) and minimum in the local morning ($\sim$ 0700-1000, i.e. longitudes 105 - 150 at 00 UTC, longitudes 15 - 60 at 06 UTC, longitudes 285 - 330 at 12 UTC, and longitudes 195 - 240 at 18 UTC). This evening maximum

is about 2-3 hours later than the surface temperature maxima in the afternoon (*Gentemann et al.*, 2003; *Sykes et al.*, 2011; *Deser and Smith*, 1998; *Sui et al.*, 1997), but is in phase with the continental convection maximum (*Yang and Slingo*, 2001; *Dai and Trenberth*, 2002). Correlations between the 6-hourly TCW and $U_a q_d P_{sa}$ diurnal timeseries further validate the attribution to the TCW diurnal cycle, by displaying significant ($p < 0.01$) coefficients all over the globe (not shown), with negative sign within tropics and positive outside.

The same TCW diurnal cycle is also advected by mean meridional winds. However, as the main horizontal winds (and subsequently the moisture transports) are east-west and a strong meridional component only exists in some regions with a much less zonally symmetric distribution (Fig. 4.4a, 4.5a; see also *Trenberth and Guillemot* (1998)), the resultant diurnal variation in $V_a q_d P_{sa}$ is much weaker (about one order of magnitude smaller) than the zonal counterpart and only the zonal component is shown.

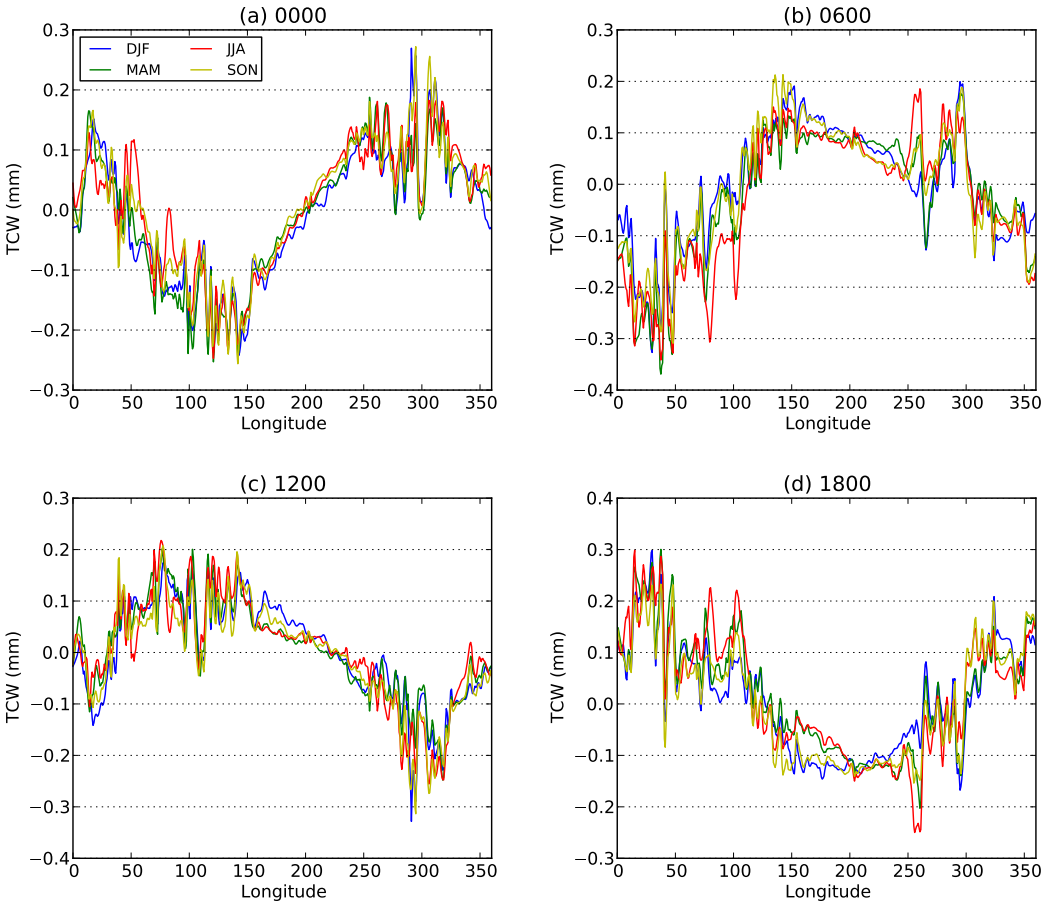

Figure 4.8: Meridional means of TCW (mm) diurnal anomalies at (a) 00 UTC, (b) 06 UTC, (c) 12 UTC and (d) 18 UTC. Seasonal averages are represented in blue for DJF, green for MAM, red for JJA and yellow for SON.

4.3.3 Diurnal cycles of TCW and zonal moisture flux–seasonal evolution

As well as varying spatially, the diurnal cycles of TCW and zonal moisture flux vary over the course of the year. This seasonal evolution of diurnal variability is examined in four regions selected as case studies. The region definitions are listed in Table 4.2 , and the seasonal evolutions in TCW and zonal flux diurnal cycles are shown in Fig. 4.9 and 4.10.

The mean diurnal cycles computed from annual cycle harmonics allow seasonal evolutions of the diurnal cycle to be visualized. As the two oceanic boxes are both located in the deep tropics, it is not surprising to see largely consistent diurnal cycle amplitudes in TCW throughout the year (Fig. 4.9a,b). When

Table 4.2: Region definitions for diurnal cycle case studies.

Region name	Geological boundaries
Cold tongue	$-2.5°S - 2.5°N$, $100 - 105°W$
Warm pool	$3 - 8°N$, $145 - 150°E$
North America	$35 - 40°N$, $100 - 105°W$
North China	$45 - 50°N$, $115 - 120°E$

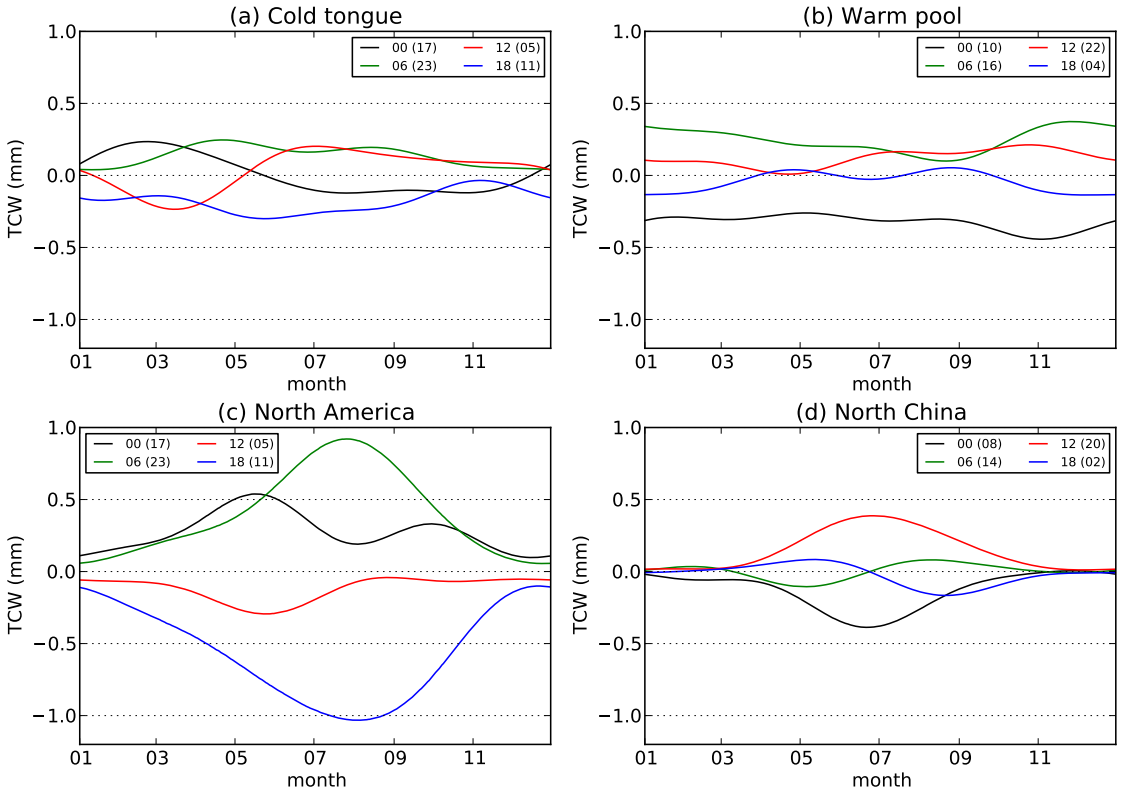

Figure 4.9: Seasonal evolutions of mean diurnal cycles in TCW (mm) in (a) Cold tongue, (b) Warm pool, (c) North America and (d) North China. Each region is a 5 by 5 degree rectangular box (Table 4.2). The four synoptic hours are represented by black for 00 UTC, green for 06 UTC, red for 12 UTC and blue for 18 UTC. The corresponding local solar time is labelled in parentheses following their UTC time legend.

multiplied by the wind to obtain the zonal flux, the warm pool has reduced diurnal amplitudes during boreal summer (Fig. 4.10b). Both of the land boxes are in Northern Hemisphere (NH) and experience greater diurnal amplitudes in boreal summer, and in winter the diurnal cycle nearly disappears (Fig. 4.9c,d, Fig. 4.10c,d), consistent with what is shown in Fig. 4.6 and 4.7. This is likely due to the limited water holding capacity and variability in winter, as the Clausius Clapeyron equation is non-linear with respect to air temperature.

As shown in Fig. 4.9 and 4.10, the diurnal cycle phase (order of the four lines in any given day) in TCW is generally opposite to that in $U_a q_d P_{sa}$ for the two

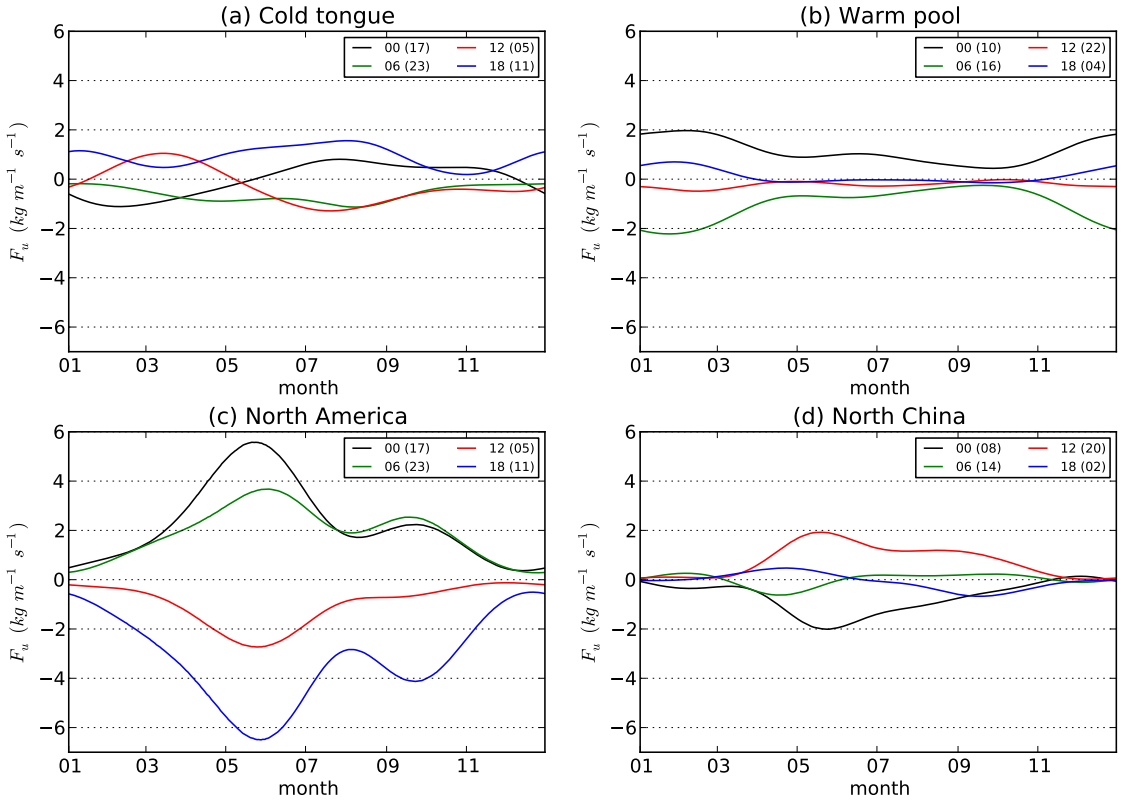

Figure 4.10: Same as Fig. 4.9 but for zonal moisture flux $U_a q_d P_{sa}$, $kg\,m^{-1}\,s^{-1}$.

oceanic boxes (cold tongue and warm pool), and congruous for the two land boxes (North America and North China). This is due to the low- and mid-latitude mean zonal wind direction difference noted above. Besides, any line crossing can be regarded as a change in the diurnal cycle phase, particularly those that involve a change in the peak/trough times. Such changes can be seen in the cold tongue case, where the the maximum TCW occurs around 1700 LST during Jan to mid-March, and changes to midnight-early-morning (2300 - 0500 LST) afterwards (Fig. 4.9a). Such phase changes are less frequent in the other three regions, for instance the warm pool has fairly "parallel" synoptic lines through the year (Fig. 4.9b, 4.10b); and in North China the maximum (minimum) TCW/flux tends to occur in the evening (morning), whenever there is a notable diurnal cycle (Fig. 4.9d, 4.10d).

4.3.4 Diurnal cycles of TCW – vertical structure

In the previous sections, TCW was found to have a diurnal cycle that usually peaks in the local late afternoon - evening. This timing of daily maximum is not inconsistent with the surface Evaporation/Evapo-transpiration

(E/ET) responses to daytime radiative forcing. However, this latent heat enhancement is likely to be confined to the boundary layer, and horizontal convergence/divergence can influence TCW in the free troposphere. Previously *Dai and Trenberth* (2002) documented such a difference based on radiosondes at a North America site. The relationship between TCW and precipitation is complex and they can be correlated positively, negatively or trivially (*Dai and Trenberth*, 2002). As an exporting flux, precipitation outputs freshwater from the atmosphere to the ground, however, re-evaporation of falling precipitation may serve as an input flux to the lower boundary layer humidity. Besides, the water source for precipitation is usually provided through low-level moisture convergence from a much larger area than the actual precipitating region (*Dai and Trenberth*, 2002; *Trenberth et al.*, 2003), and usually the efficiency of rainfall in drying the air column is only about 30 % (*Trenberth et al.*, 2003). Therefore at the intra-day time scale, precipitation can show a positive correlation with TCW. Additionaly, the analysis increment issue in reanalysis data (*Trenberth et al.*, 2007; *Bosilovich et al.*, 2011) prevents a budget analysis at this time scale. Therefore we will focus on E/ET and horizonal divergence here.

To examine the vertical structure of TCW diurnal cycle, diurnal anomalies of specific humidity (q_d) and horizontal wind divergence (δ) from the same case study regions are computed at each vertical level (Fig. 4.11 and 4.12). The humidity profiles exhibit complicated vertical diurnal structures, and the vertically integrated anomaly is not always consistent with the boundary layer responses. For instance in the North America case at UTC 00 (17 LST) in JJA (Fig. 4.11a), the boundary layer negative anomalies are compensated by the mid-troposphere (900 - 500 hPa) positives, and the overall effect is positive TCW anomaly with respect to the daily mean (see Fig. 4.7 and 4.9c). Similar diagnosis holds for the North China case at UTC 12 (20 LST) in JJA (Fig. 4.11g).

This inconsistency suggests that boundary layer thermodynamic response to daytime heating alone can not explain the observed TCW diurnal cycle, and horizontal divergence/convergence needs to be incorporated. This mechanism can be readily observed in the North China case, where the JJA humidity is negatively correlated with divergence (Fig. 4.11e-h). A similar relationship also exists in the North America case, but with some vertical misalignments between the δ and q_d profiles. At UTC 18 in this region, negative q_d co-locates with convergence anomalies in the mid-troposphere (Fig. 4.11d), possibly due to the net export of moisture to the anomalous divergences above and below it.

Note the seasonal difference in diurnal humidity amplitudes is also revealed

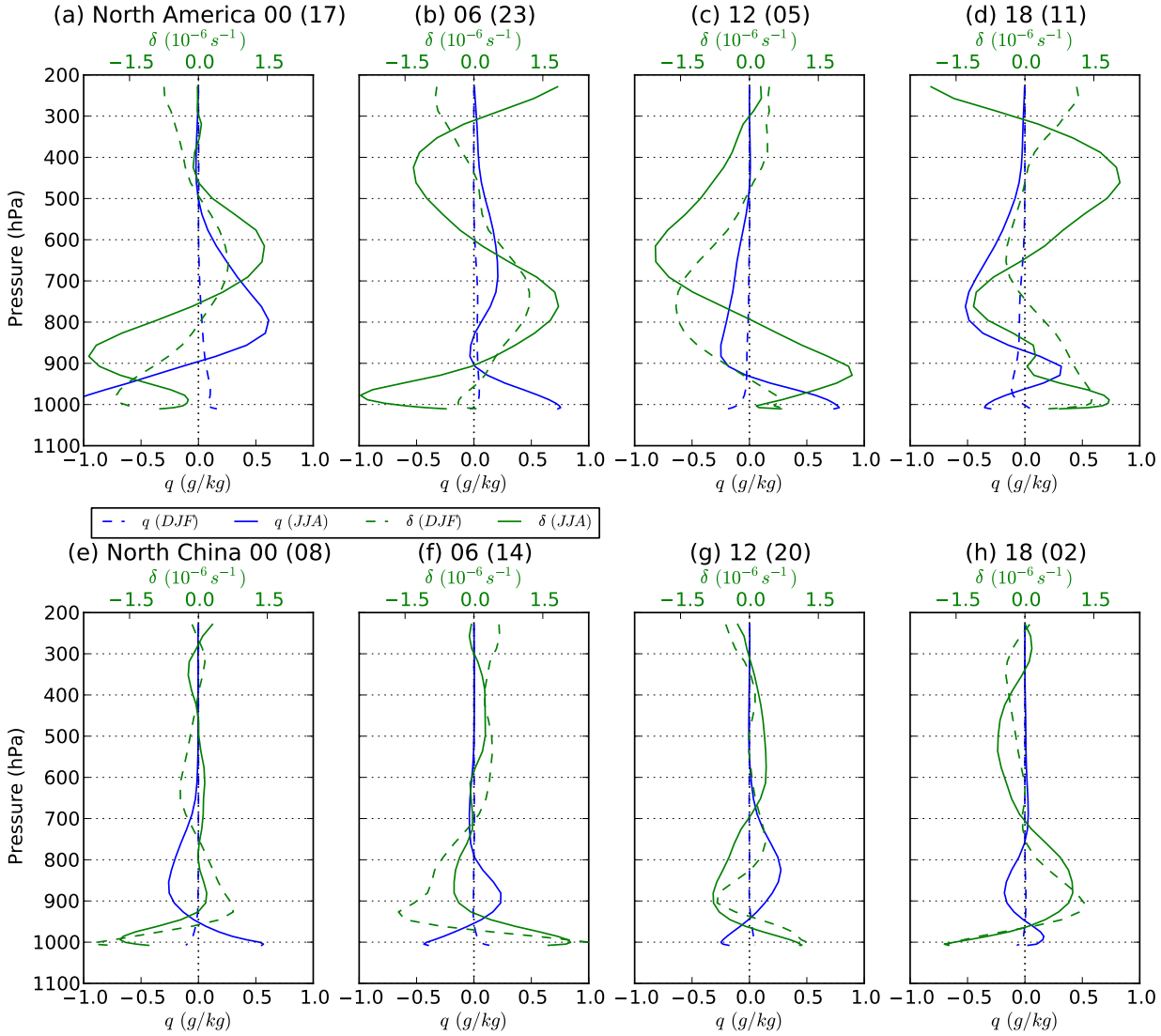

Figure 4.11: Vertical profiles of diurnal anomalies in humidity (q, g/kg) and horizontal wind divergence (δ, $10^{-6}s^{-1}$). Top row shows the mean profile in the North America case study (Table 4.2), and bottom row the North China case study. Columns are the UTC hour 00, 06, 12 and 18, respectively, each with LST hour in parentheses in each panel. q_d profiles are plotted in blue onto the bottom x-axis, and δ in green onto the top x-axis. Both use solid lines for JJA season and dash lines for DJF.

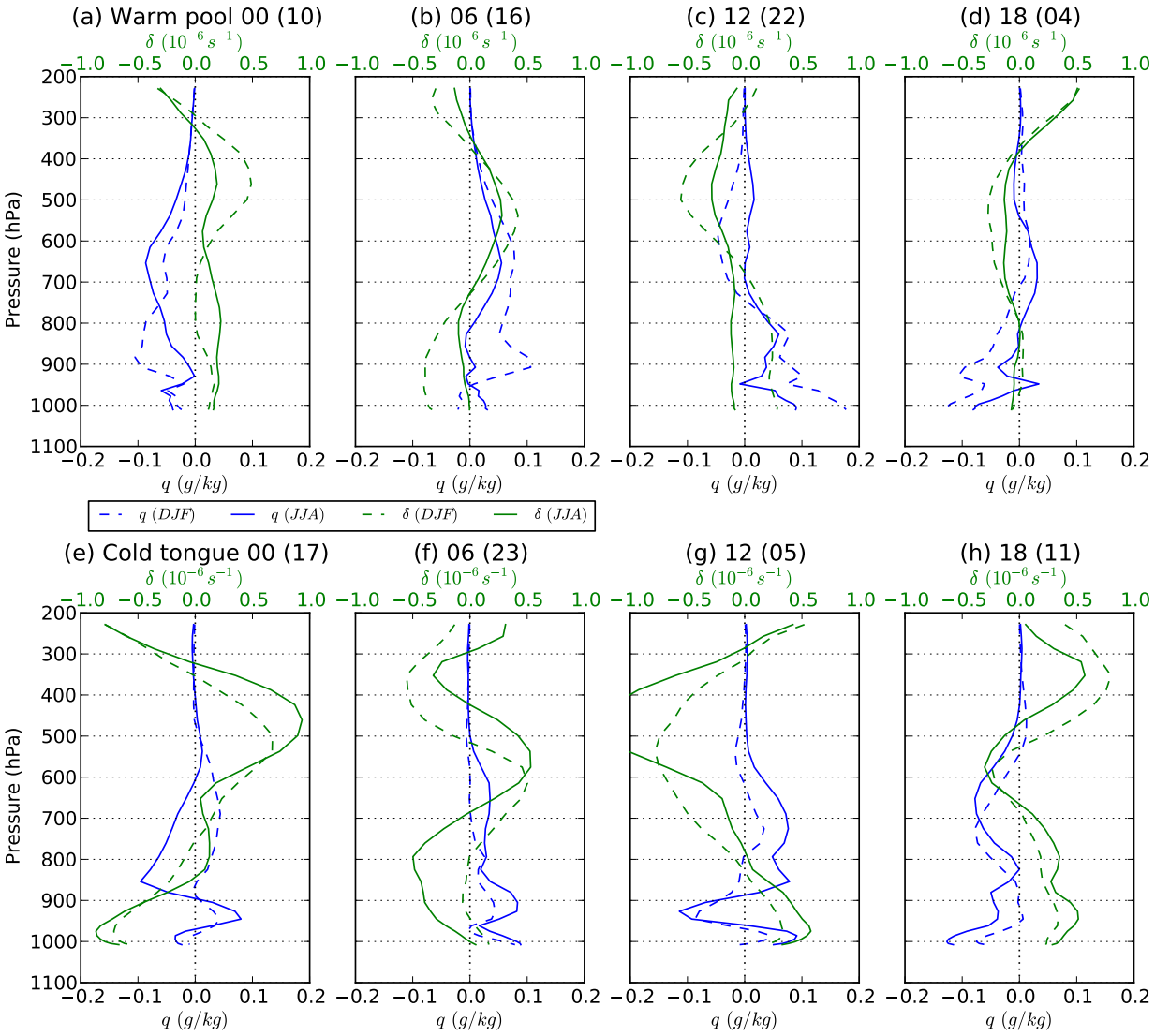

Figure 4.12: Same as in Fig. 4.11 but for the cold tongue and warm pool regions.

in the profiles for the two land boxes, consistent with previous sections. The winter diurnal cycle damping occurs to humidity but not to the divergence field, consistent with the reduced vapour holding capacity effect by the Clausius-Clapeyron relationship.

Horizontal divergence seems to be a contributing factor to the vertical humidity distribution in the two oceanic boxes, but can not account for the variations very well. In the warm pool box, morning (10 LST) divergence anomalies extend throughout the troposphere, associated with anomalous descending motion and negative humidity anomalies (Fig. 4.12a). This morning-time stable tropospheric condition and reduction in humidity are also reported by *Sui et al.* (1997). In the afternoon (16 LST), a low-level convergence anomaly develops below 700 hPa,

and a mid-level divergence anomaly between 700 - 400 hPa (Fig. 4.12b). With the help of an enhanced afternoon moisture flux, this pattern produces positive q anomalies up to $\sim 400hPa$, which is also consistent with *Sui et al.* (1997) (see their Fig. 7b).

In the evening (22 LST), anomalous convergence is found throughout the troposphere together with positive q anomalies in JJA (Fig. 4.12c), however the variation in DJF needs further explanations. In the early morning (04 LST), an anomalous convergence layer develops in the mid-troposphere between 700 - 400 hPa, underneath an anomalous divergence layer above 400 hPa (Fig. 4.12d). This pattern induces an anomalous ascending motion sitting on top of a descending motion, similar to the case in North America at 11 LST (Fig. 4.11d). This low-level nocturnal subsidence is consistent with the negative humidity anomalies below 800 hPa. Boundary layer latent heating is also low at this time of day.

The cold tongue box exhibits more complex behaviors. In the afternoon and at midnight (17 - 23 LST), a low-level-convergence-mid-level-divergence structure may explain the observed humidity increases in the mid-low troposphere in DJF (Fig. 4.11e,f), however the JJA humidity profile at 17 LST has a fast drop between 900 - 600 hPa that can not be explained by this argument. During the early morning to noon (05 - 11 LST), the divergence profiles are largely reversed with respect to 17 and 23 LST, and the resultant subsidence decreases low-level humidity (Fig. 4.11g,h).

4.3.5 Atmospheric tides in surface pressure, winds and moisture fluxes

The previous sections analyzed the diurnal variations in zonal moisture fluxes that stem from the humidity changes, which was found to be related to diurnal variations in divergence. Previous studies have identified diurnal and semi-diurnal fluctuations in sea level pressure and wind fields, both of which affect the column moisture flux (see Eq. 4.7), and the effect of their interactions is represented in $V_d q_a P_{sa}$ (see Table 4.1).

Haurwitz and Cowley (1973) put forward a simple model to describe the semi-diurnal cycle in SLP in the tropics:

$$P = 1.05 \cdot cos^3(\theta) \cdot sin(2t + 159°) \tag{4.10}$$

Where 1.05 is the estimated amplitude in hPa, θ is latitude, t is the local time expressed in longitudinal degrees, and the estimated phase shift 159° corresponds to a maximum at 0942 and another at 2142 LST (*Haurwitz and Cowley*, 1973; *Deser and Smith*, 1998). They also showed that the phase and amplitude of this semi-diurnal pressure wave are relatively uniform within 20° of the equator. Using this pressure distribution pattern as the accelerating force for the horizontal winds ($\delta u/\delta t = -1/\rho(\delta P/\delta x)$, $\delta v/\delta t = -1/\rho(\delta P/\delta y + fu)$), *Deser and Smith* (1998) computed the resultant zonal and meridional wind diurnal cycles and validated the model against observations. According to this formulation, the zonal wind is out of phase with the pressure field, while the meridional wind is in quadrature with the pressure field. Therefore, the product of U_d and P_s (reflecting the interactions between U_d and P_s in $U_d q_a P_{sa}$) will be a wave pattern that has four zonal troughs and is negative everywhere; and the product of V_d and P_s is a wave pattern that has doubled frequency (quadrant diurnal cycle), with opposite signs across the equator. Both of the two waves ($U_d \cdot P_s$ and $V_d \cdot P_s$) propagate westward, and when scaled by the mean background humidity load (q_a), create a series of "moisture pulses" that circulate around the earth.

To verify the theory, we created composites of UTC 00 and 12 averages for the mean diurnal anomalies in surface pressure (P_{sd}) and horizontal winds (V_d) in January (Fig. 4.13). Note that by definition the average of UTC 06+18 will be the exact opposite of the 00+12 average (Eq. 4.3), and UTC 00 and 12 are sampling the same phase location on the semi-diurnal wave. Fig. 4.13a shows the semi-diurnal surface pressure anomalies at UTC 00 and 12. Consistent with previous discussion, two wave cycles are found and the amplitude has a comparable magnitude ($\sim 1.2\,hPa$). The signal is strongest along the equator and decreases towards the poles, as shown in the map as well as the zonal mean curves (Fig. 4.13b). The tropical band ($30°S - 30°N$) can be closely approximated by a fitted sinusoidal wave. Zonal wind at sigma level 56 (approximately 990 hPa) has a similar zonal pattern as surface pressure but in opposite phase (Fig. 4.13c,d), and the mean amplitude in the tropics is $0.27\,m/s$. The product of U_d and P_{sd} will be negative everywhere, as is shown in Fig. 4.13g, in which the four troughs in the low latitudes migrate westward and complete two circles in a day. Taking into account the four-times-daily sampling rate of ERA-I, this specific phase is sampled repeatedly for every 6-hour time step, which explains why it is not averaged out in the monthly mean plot (Fig. 4.2d and 4.3d).

Consistent with the theory, the meridional wind (V_d at sigma level 56) is in

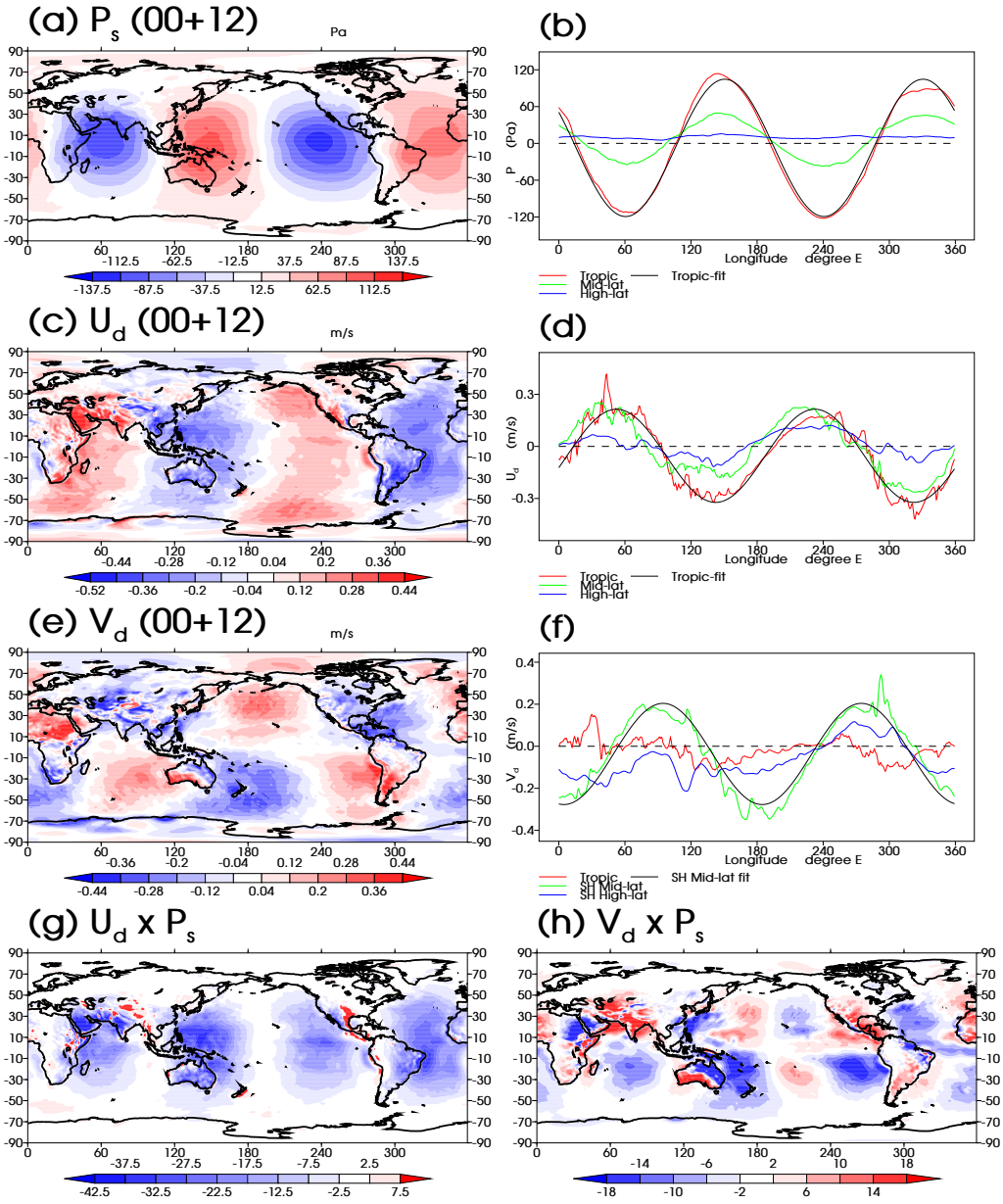

Figure 4.13: Mean diurnal anomalies in surface pressure, horizontal winds and their products. (a) shows the mean diurnal anomalies of surface pressure (P_{sd}) as the average of UTC 00 and 12. (c) and (e) are the same as (a) but for the diurnal zonal and meridional wind, respectively, both at sigma level 56 (approximately 990 hPa). Note that by definition the average of UTC 06 + 18 is the exact opposite of 00 + 12, and 00 and 12 are both sampling the same phase location on the semi-diurnal wave. Subplot (b), (d) and (f) show the meridional means of P_{sd}, U_d and V_d, respectively. Three meridional bands are created: tropic ($30°S - 30°N$, in red), mid-lat ($30 - 60N/S$, in green) and high-lat ($60 - 90N/S$, in blue). Note that for the meridional wind, only the southern hemisphere bands are computed. For the tropic band in (b) and (d), and the SH mid-lat band in (f), a fitted sine wave is plotted in black. (g) shows the product of U_d and P_{sd}, and (h) the product of V_d and P_{sd}.

quadrature with the pressure semi-diurnal pattern, and asymmetric about the equator (Fig. 4.13e). The wave pattern is more evident in the mid-latitudes, and has a similar amplitude as the tropical zonal wind (Fig. 4.13f). When multiplied by P_{sd}, this creates a quadrant diurnal cycle in the meridional mass fluxes in each hemisphere (Fig. 4.13h). The sign asymmetry about the equator implies alternating convergences/divergences along the equator due to these semi-diurnal tidal oscillations (see also *Deser and Smith* (1998)). Again due to the aliasing effect of 6-hourly sampling, only one phase can be sampled by ERA-I, which is retained after a monthly mean average (Fig. 4.4d and 4.5d).

4.4 Conclusions and discussion

We have analyzed some basic aspects of the two major modes in horizontal moisture fluxes related to regular solar heating variation: the mean annual and mean diurnal cycles. The conventional method was modified to cater for the temporal resolution of reanalysis data, thus allowing the mean diurnal cycle to be constructed in association with the mean annual cycle. Interaction across time scales and seasonal evolutions of the diurnal cycle can then be analyzed.

The mean annual (which here includes the annual mean as well as the seasonal variation) cycle forms the majority of observed horizontal moisture fluxes, and reflects the large scale tropic-to-pole humidity gradient and the lower tropospheric wind field. In addition to this backbone component, eddy covariances (which here include all variations and time scales that are not captured by the diurnal and annual cycles and the annual mean) play an important role in re-distributing moisture and energy, especially in the form of mid-latitude cyclones. In comparison, the net effect of diurnal variability is much smaller. Notable net convergence/divergence due to diurnal covariance in humidity and wind only exists either in some tropical regions with complex orography or land-sea contrasts.

Although the net transport by the diurnal cycle is small, it exhibits coherent patterns in space, in the vertical profile and over the course of the year, which deserve physical explanation. Also, although the net transport is small, the movement of moisture backwards and forwards over the course of the diurnal cycle is significantly larger. Therefore, we devoted effort to the analysis of diurnal/semi-diurnal cycles. Specific humidity in the mid-to-low troposphere was found to have a diurnal cycle that tends to peak in the late

afternoon-evening (1800 - 2100 LST), and reach its minimum in the morning (0700 - 1000 LST). This timing of local maximum is about 2-3 hours later than the surface temperature maximum in the afternoon, and in phase with the continental convection maximum (*Yang and Slingo*, 2001; *Dai and Trenberth*, 2002). It is not inconsistent with the boundary layer thermodynamic response to daytime heating. The TCW diurnal amplitude (peak-to-peak) is about $0.4\,mm$ (Fig. 4.8). A previous study has reported an average daytime increase (by diurnal SST forcing) in latent heat flux by $10-20\,W/m^2$ (*Schiller and Godfrey*, 2005). Coverting this latent heat into equivalent vapour (by assuming a mean surface temperature of 15°C), and integrating over 12 hours, the resultant increase in water vapour is $0.2-0.4\,mm$, consistent with the TCW results found here.

However, this scale analysis is only valid over the ocean where evaporation is energy-limited, and the enhanced E/ET effect is largely confined in the boundary layer. The vertical profiles of the selected case study regions further validate this: TCW diurnal anomalies are not always consistent with the boundary layer response, and the horizontal wind divergence seems to be better correlated (negatively) with humidity variations. This is particularly true for the two land boxes. However, the same argument cannot explain the two oceanic cases very well, and a satisfactory mechanism for the TCW diurnal cycle cannot be provided by the evidence at hand, for a number of reasons.

Firstly, the low sampling frequency in reanalysis data inhibits accurate depiction of the diurnal cycle. Four-times-daily sampling was confirmed to be capable of retrieving a diurnal signal, but subject to considerable accuracy losses (*Sykes et al.*, 2011). In addition, the method of defining diurnal cycles from annual cycle harmonics introduces some extra deficiencies, due to the loss of higher order harmonics. Besides, diurnal cycles can exhibit significant inter-annual variability (*Deser and Smith*, 1998), which is averaged out during the data processing stage. The recent update of the Modern Era Retrospective-analysis for Research and Analysis (MERRA) reanalysis to MERRA-2 introduces new data at hourly resolution, making it a promising condidate for diurnal cycle studies.

Secondly, the meridional wave structure in the TCW diurnal cycle (Fig. 4.7) is less well defined than in the surface pressure field (Fig. 4.13a), even over open oceans which are free from terrain effects. In the tropics, positive/negative TCW anomaly centers tend to "wedge" into each other zonally, rather than displaying a meridionally uniform transition. A possible hypothesis is the zonal

difference in the thermocline depth that shoals to the east/west of the warm pool. SST (and mixed layer temperature) with a shallower thermocline is more sensitive to solar heating/cooling, and consequently so are the induced latent fluxes and atmospheric motions. *Clayson and Weitlich* (2005, 2007) documented a local maximum in SST diurnal amplitude over the cold tongue region, and this pattern disappeared in the mature phase of the 1997/98 El Niño event, which is one of the extreme El Niños that feature extreme warming over the eastern Pacific and a distinct pattern of moisture divergence as a response (Chapter 5). This zonal thermocline slope may explain the observed "wedge" features: deeper water warms up more slowly in the morning (negatives wedge to the east, Fig. 4.7a) and cools down more slowly (positives retreat to the west, Fig. 4.7b). The equator versus off-equator cloud cover difference may also have some influence, but further evidence would be needed to validate this.

Lastly, although the diurnal cycle in SST has been documented for decades, much still remains unknown about the impacts on the atmosphere (*Kawai and Wada*, 2007). Enhanced oceanic convective activity has been found to have an early morning maximum (*Yang and Slingo*, 2001; *Kawai and Wada*, 2007; *Sui et al.*, 1997), however, other studies also documented a secondary afternoon maximum (*McGarry and Reed*, 1978; *Augustine*, 1984; *Janowiak et al.*, 1994; *Sui et al.*, 1997; *Fu et al.*, 1990). In addition to data and methods differences that could possibly lead to these different findings, it has been suggested they are related to the large-scale circulation conditions (e.g. disturbed versus undisturbed) and intraseasonal variability (e.g. MJO) (*Sui et al.*, 1997; *Yang and Slingo*, 2001). However, differences across these time scales are likely removed in the construction of diurnal cycle time series, by firstly averaging over 34 years and then retaining the annual cycle harmonics. A mechanism that is valid in both disturbed and undisturbed conditions is required for the observed TCW diurnal cycle, which may be considered as a baseline diurnal cycle that is independent of the intraseasonal circulation changes. Thermodynamic responses in the boundary layer and free troposphere divergence/convergence are contributing factors to this mechanism.

Results represented in this chapter also illustrate that diurnal cycles can exhibit significant seasonal-intraseasonal variations in amplitude and/or phase. Continental regions in temperate climates have larger TCW diurnal variations in summer than in winter, due to the non-linear Clausius-Clapeyron function. Diurnal cycle phase may change multiple times over the seasons, as seen in the cold tongue case study. A phase change count analysis (recording the number

of line-crossings among the four synoptic hours during a year, as in Fig. 4.9, then filtering out the cases where diurnal amplitude can not be sampled by the 6-hourly data) can be used to produce a map of phase change statistics (not shown here), and suggests that some regions experience frequent diurnal phase changes. Future studies that follow the conventional approach in constructing the diurnal timeseries need to be cautious that averaging across a season may introduce a loss in this information.

The classical atmospheric tidal theory predicts a strong semi-diurnal cycle in surface pressure, and through horizontal momentum equations, the winds. The 6-hourly data are not capable of retrieving the semi-diurnal cycle, however, after translating the march in time to a march in longitude, we are able to verify the reanalysis against the predictions from theory. The diurnal/semi-diurnal cycles in pressure and winds match well with previous studies and the atmospheric tidal theory. The interaction between zonal wind and surface pressure is a westward air mass flux anomaly that propagates around the Earth twice daily, and when scaled by the background humidity load, it creates a "moisture pulse". The interaction between meridional wind and surface pressure gives rise to a pattern with alternating divergence/convergence along the equator. A diurnally oscillating meridional overturning circulation was proposed in regard to the observed equatorial divergence pattern (*Deser and Smith*, 1998; *Ueyama and Deser*, 2008), but the possible relationship with a morning maximum in precipitation remains to be explored.

Chapter 5

Different Atmospheric Moisture Divergence Responses to Extreme and Moderate El Niños

The contents of this chapter have been published in the journal Climate Dynamics (*Xu et al.*, 2015).

5.1 Introduction

Globally around 60 % of the terrestrial precipitation directly originates from moisture transported from the ocean (*Trenberth et al.*, 2007; *Gimeno et al.*, 2012). The variability of the oceanic water supply greatly influences water availability for all regions. Excessive transports are usually major causes for extreme weather and flood events (*Knippertz and Wernli*, 2010; *Galarneau et al.*, 2010; *Chang et al.*, 2012; *Knippertz et al.*, 2013), while interrupted transports can lead to droughts and subsequent socioeconomic stresses (*Cai et al.*, 2012, 2014). Hence, a clear understanding of the mechanisms that force observed changes to the hydrological cycle is of major importance.

Most of the major oceanic source regions of atmospheric moisture are confined to the tropics and subtropics, where the high sea surface temperature (SST) and anticyclonic circulations provide favorable conditions for evaporation to occur under clear sky conditions. The surplus evaporation (E) over precipitation (P) provides a useful estimate of the net water input to the atmosphere (E - P). However, large scale estimates of this flux are largely limited to reanalysis

datasets, which suffer from model biases and data inhomogeneity issues (*Hegerl et al.*, 2015; *Wang and Dickinson*, 2012; *Trenberth et al.*, 2007, 2011). Evaporation from reanalysis is not constrained by precipitation and radiation (*Hartmann et al.*, 2013), spurious trends and biases can be introduced by changing satellite observations (e.g. *Bosilovich et al.*, 2005; *Robertson et al.*, 2011), which also contribute considerably to budget errors over land (*Pan et al.*, 2012). Similarly, precipitation from reanalysis also depends strongly on the parameterization schemes adopted by a specific model (i.e. it is a "type C" variable: *Kistler et al.*, 2001; *Kalnay et al.*, 1996). Moreover, E and P computed oceanic freshwater fluxes show poorer performance in closing the water budget, compared with atmospheric moisture fluxes derived values (*Rodríguez et al.*, 2011).

Therefore, like many studies (e.g. *Trenberth and Guillemot*, 1998; *Trenberth and Stepaniak*, 2001) we use the moisture divergence fields computed from "type B" variables (i.e. ones that are more dependent on assimilated observations and less dependent on model parameterizations) to balance the water budget. This indirect approach is more reliable and consistent among observations (*Trenberth*, 1997a; *Parker et al.*, 2000; *Roads*, 2003; *Gimeno et al.*, 2012). Moreover, it is the large-scale convergence rather than locally enhanced evaporation that controls the precipitation patterns in the tropics (*Mo and Higgins*, 1996; *Soden*, 2000; *Su and Neelin*, 2002; *Trenberth et al.*, 2003; *Zahn and Allan*, 2011), and analysis of the moisture divergence provides insights into the major modes of precipitation variability, as well as the moisture sources themselves.

On interannual time scales, large-scale atmospheric variability is closely associated with the El Niño Southern Oscillation (ENSO). Associated with the altered Walker circulation (*Bjerknes*, 1966, 1969) and strengthened and shifted Hadley cell (*Oort and Yienger*, 1996; *Quan et al.*, 2004; *Hu and Fu*, 2007; *Wang*, 2002) the atmospheric hydrological cycle is also reorganized. Recently, there have been investigations of different types of ENSO events and their corresponding mechanisms and impacts (*Capotondi et al.*, 2015). Most of them take the SST anomaly (SSTA) patterns as the starting point, and emphasize the different zonal SSTA structures (*Larkin*, 2005a,b; *Ashok et al.*, 2007; *Kao and Yu*, 2009; *Kug et al.*, 2009; *Fu et al.*, 1986; *Trenberth and Stepaniak*, 2001; *Trenberth and Smith*, 2006; *Giese and Ray*, 2011; *Capotondi*, 2013). Although each uses a different index definition and separation criterion, and gives different names to the El Niño types and emphasizes somewhat different aspects of these events, it appears that there is some correspondence bewteen these parallel studies:

- the "1972 type ENSO" in *Fu et al.* (1986), the "conventional El Niño" in

Larkin (2005a) and *Ashok et al.* (2007), the "Eastern Pacific (EP) type ENSO" in *Kao and Yu* (2009) and *Yu and Kao* (2007), and the "Cold Tongue (CT) El Niño" in *Kug et al.* (2009), all refer to those events associated with anomalously warm SSTs over the eastern equatorial Pacific;

- the "1963 type ENSO", the "dateline El Niño" and "El Niño Modoki", the "Central Pacific (CP) type ENSO", and the "Warm Pool (WP) El Niño" in the aforementioned studies define the counterpart with its warming centered closer to the central equatorial Pacific.

The events identified by these studies are generally consistent when their data periods overlap (see Fig. 1 in *Singh et al.* (2011) for a summary), suggesting that these diverse interpretations all point to essentially the same phenomena (*Kug et al.*, 2009). Studies starting from spatial patterns in other variables find a similar east-central contrast in the El Niño categorizations: surface salinity (*Singh et al.*, 2011), the first occurrence of significant SSTA (*Xu and Chan*, 2001; *Kao and Yu*, 2009), sea level anomalies (*Bosc and Delcroix*, 2008) and outgoing longwave radiation (OLR) in the equatorial Pacific (*Chiodi and Harrison*, 2010).

Empirical Orthogonal Function (EOF) analysis is a commonly used technique in studies that describe ENSO. However the orthogonality constraint on the resultant patterns and time-series means that they do not necessarily have direct physical interpretations. This sometimes hampers the ability of this technique to capture non-linear features embedded in the data, particularly when there is a relative spread of variances across multiple EOFs all related to the same forcing. Previous studies suggest that a complete description of different characters and evolutionary features of El Niños cannot be captured fully by a single index, and a second mode reflecting the zonal SST contrast is a necessary complement (*Trenberth and Stepaniak*, 2001; *Trenberth and Smith*, 2006; *Kao and Yu*, 2009). These complementary modes broadly correspond to the two flavours of El Niños, but have serious deficiencies when considering individual events (*Johnson*, 2013). In such cases additional efforts and other techniques, like regression analyses, are required to enable a clear interpretation of the EOF results.

Similar to EOF analysis, Self-Organizing Maps (SOM) is a powerful dimension reduction tool, but is free from orthogonality constraint. Introduced into the geography community in the 1990s, it has been more commonly used for determining synoptic circulation patterns and downscaling (*Hewitson and Crane*, 1994, 2002; *Crane and Hewitson*, 1998; *Reusch et al.*, 2007; *Verdon-Kidd and Kiem*,

2009; *Verdon-Kidd et al.*, 2014). Here, we explore its potential applications in large scale climatic analysis. In this study, we first use conventional EOF-correlation analysis to illustrate how the tropical atmospheric moisture circulation responds to different flavors of El Niños. Then, noting that the different types of El Niños are associated with different patterns of anomalous moisture divergence which may not be orthogonal, but EOF analysis imposes orthogonality, we obtain a new perspective from a neural network algorithm (SOM). More details on the SOM algorithm are described in Section 5.2, including data preprocessing procedures, and the El Niño phase separation method. Sections 5.3.1, 5.3.2 and 5.3.3 show the distinct moisture divergence responses to extreme and moderate El Niños, which is validated by the SOM results described in Section 5.3.4. A summary and discussion is given in Section 5.4.

5.2 Methods and Data

5.2.1 Moisture divergence

In this study we use the ERA-Interim (ERA-I) reanalysis data (*Dee et al.*, 2011) , a third generation atmospheric reanalysis product (*Trenberth et al.*, 2011). ERA-I has some major improvements over its predecessor (ERA-40) in hydrological components (*Trenberth et al.*, 2011), and outperforms NCEP I, II and MERRA in depicting the global ocean-land moisture transports (*Trenberth et al.*, 2011). The near surface fields in ERA-I are better correlated with buoy observations (implying more faithful air-sea water fluxes) compared to NCEP products (*Kumar et al.*, 2012). And it represents the latest and best reanalysis for reproducing and interpreting the atmospheric branch of the hydrological cycle (*Trenberth et al.*, 2011; *Lorenz and Kunstmann*, 2012).

Horizontal moisture divergence was computed following *Trenberth and Guillemot* (1998):

$$\bigtriangledown \cdot \vec{Q} = \bigtriangledown \cdot \frac{1}{g} \int_0^{P_s} q\vec{v} dp \tag{5.1}$$

Specific humidity (q), horizontal winds ($\vec{v}$) and surface pressure (P_s) were obtained from ERA-I for the period of 1st January 1979 to 31st December 2012. Horizontal moisture fluxes were computed on each of the 60 sigma levels using 6-hourly data, to capture as much covariance of q and $\vec{v}$ as possible. The

original full resolution ($0.75° \times 0.75°$) divergence anomaly (with respect to the 34-year mean annual cycle) was temporally averaged into calendar months, and spatially filtered to a lower $3° \times 3°$ resolution, before passing into the EOF analysis.

5.2.2 ENSO events and phase separation

ERA-I SST data during the same time period were used to compute the Niño 3.4 index (*Trenberth*, 1997b). After filtering with a 5-month running mean to remove intra-seasonal variability, the time-series was normalized by its standard deviation. El Niño (La Niña) events are determined by the criterion that the Niño 3.4 index exceeds $+0.75\,\sigma$ $(-0.75\,\sigma)$ for at least six consecutive months. If this criterion is met, the beginning of the event is defined as the first month that exceeded $\pm 0.75\,\sigma$.

Tracking the evolution of El Niño events through a sequence of phases could be achieved by defining phases according to either their calendar months or their timing relative to the magnitude of the SSTA. Using Niño 3.4 SSTA as the index, *Xu and Chan* (2001) suggested a 3-month delay in the onset time of "Summer" type El Niños compared with "Spring" type El Niños, which also show distinct warming structures. Considering this time shift in the evolutionary pathways, the calendar-month approach (e.g. using Aug-Oct as the starting phase for both types) might end up comparing events at different evolution stages, particularly for the pre-mature phases.

Therefore, taking into account the irregularity of El Niño events, we defined a relative-amplitude-based method to split each event into five evolutionary phases:

1. "Pre-event" phase: three preceding months before the Niño 3.4 index reaches the El Niño criterion (defined above);
2. "Starting" phase: from the beginning of an event to the time when the Niño 3.4 index rises 70 % of the way up to its maximum (See Appendix for an illustration);
3. "Peak" phase: the phase in between the "Starting" and the "Decaying" phases;
4. "Decaying" phase: from the time when the Niño 3.4 index drops 30 % from its maximum value to the El Niño criterion, until the end of the event;

5. the "Post-event" phase: three subsequent months after the Niño 3.4 index drops below the El Niño criterion.

The Niño 3.4 index experiences fastest changes during "Starting" and "Decaying" phases (whereby we assume swift changes in the overlying atmosphere, which is proved to be the case later). As monthly mean Niño 3.4 SST is used, linear interpolation was used to estimate the timing of the phases more precisely (i.e. in days). The same interpolating factors are later applied to other variables (e.g. moisture divergence) in creating the phase composites. More details are given in the Appendix.

Unlike other El Niños that have a single maximum in the Niño 3.4 time-series, the 1986/87 case features a dual peak, with its first peak occurring in January 1987 and the second, larger, peak in August 1987. In the phase separation procedure described above, only the second peak was identified as the maximum, and the presence of the first peak was not accounted for. However, computations with the 1986/87 event excluded give very similar results, and suggest that the major conclusions are insensitive to its inclusion.

5.2.3 Self-organizing maps

SOM is a type of neural network algorithm that introduces a specified number of neurons into the spatio-temporal space of the input dataset, and through an iterative, unsupervised learning process, locates these neurons in such a way that they collectively represent the data values within the entire data space, but individually represent local variability (*Kohonen*, 1990; *Hulle*, 2012). Unlike EOF analysis, there are no linear or orthogonal constraints, and the neuron distribution is determined solely by the distribution of the input data. These characteristics allow SOM to represent the dimensions of the input variables along which the variance in the sequence of inputs is most pronounced (*Cavazos*, 1999; *Liu et al.*, 2006).

In addition to positioning the neurons within the multi-dimensional data space, the neurons are themselves laid out in a "map" that topologically links them so that neighbouring neurons tend to be more similar than non-neighbouring neurons. This map is most commonly a 2D grid with a hexagonal or rectangular layout that determines how many neighbours each neuron has (*Hulle*, 2012), though other options are possible. The topological links between neighbours facilitates examination of evolutionary paths of a physical phenomenon across

the map's neurons, as well as effectively visualizing high-dimensional data and serving as an alternative classification method, as will be shown in the results section.

Even if it is non-linear, the transition from extreme El Niño states to strong La Niña states is nevertheless a continuum and we can represent this using SOM with a simplified 1D map. Thus, each neuron is topologically related only to its immediate neighbours in the 1D array of neurons (of course, each neuron still represents a location in the multi-dimensional data space). A description of the initialization and training formulation to obtain the SOM is given in the Appendix.

The size of the SOM array is usually an arbitrary choice made by the user. Analogous to other statistical methods, there is a trade-off between the degree of generalization, the amount of detail to represent, and the capacity of the available data sample to adequately represent the variance and distribution of the data. Therefore some trial and error experiments are usually recommended to determine an appropriate SOM size. In this case, a 1D array with five neurons gives results that can be easily related to ENSO variability. Using seven neurons (not shown) yields similar patterns with large differences only occurring in the neutral and moderate ENSO states, where the influence of other climate variability is relatively larger. This is consistent with *Johnson* (2013), who suggested that no more than nine SOM neurons could be distinguished in patterns of equatorial Pacific SSTA.

5.3 Results

5.3.1 El Niño - La Niña transitions

The two leading EOFs of the moisture divergence anomalies field are found to be ENSO-related, and they explain 15 % and 11 % of total variance, respectively. Fig. 5.1 displays the patterns and principal components of EOF #1 and #2, together with the climatological average moisture divergence (negative values indicate moisture convergence or $P > E$).

The first EOF (Fig. 5.1a) features a westward-pointing horseshoe structure over the tropical Pacific region that is in good agreement with the typical ENSO SSTA pattern. Anomalous convergence collocates with the warm SST anomalies during the mature phase of an El Niño, and the encompassing

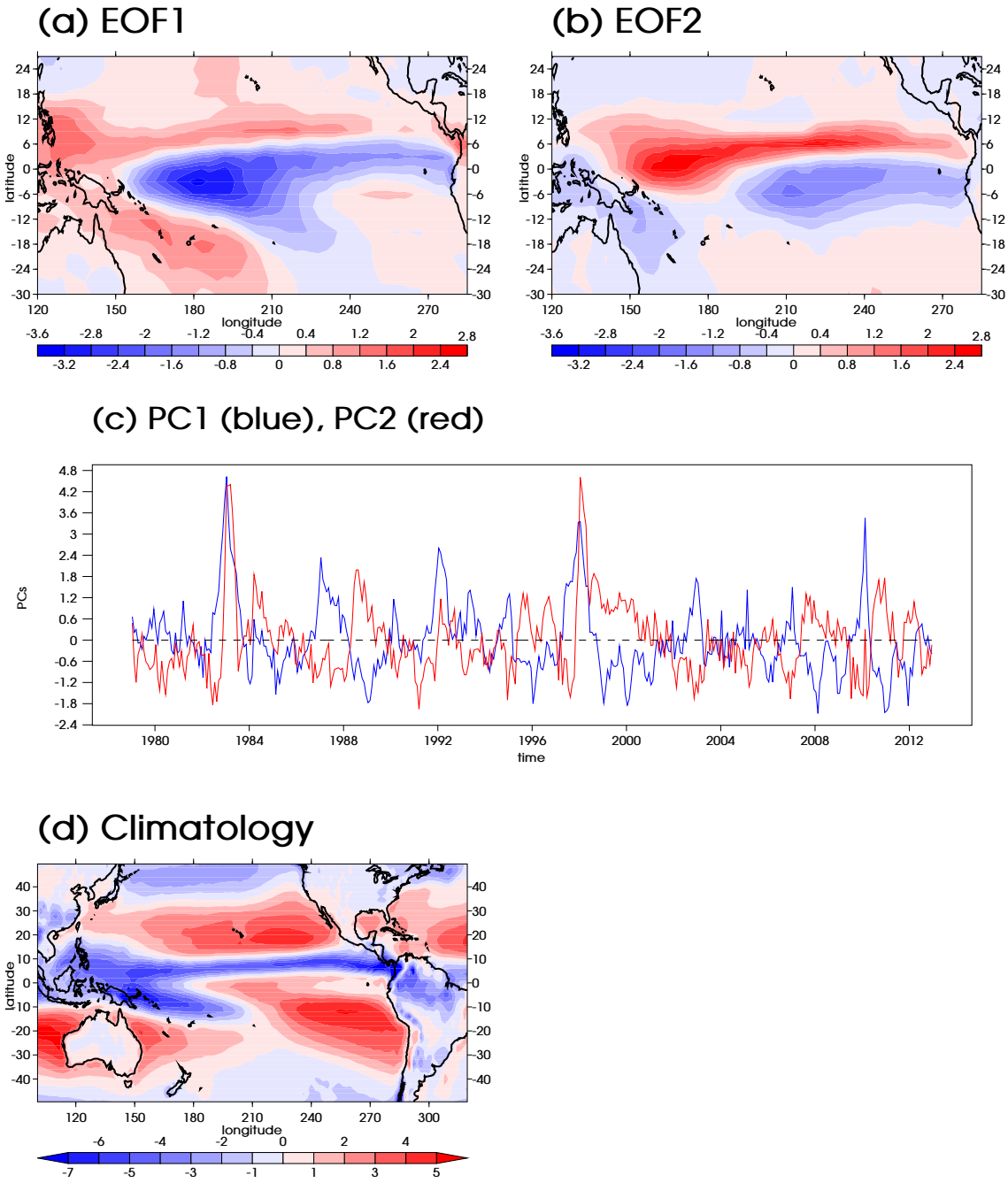

Figure 5.1: Subplots (a) and (b) show the EOF#1 and EOF#2 of tropical Pacific moisture divergence (mm/day), respectively. (c) shows their principle component time-series (PC#1 in blue and PC#2 in red). (d) is the climatological mean moisture divergence (1979-2012).

divergent anomalies corresponds to the negative SSTAs over the warm pool and South Pacific Convergence Zone (SPCZ). This suggests the influences of thermally driven circulation changes on the moisture divergence patterns, and the climatological convergence/divergence regions (Fig. 5.1d) are shifted eastward following the zonal movement of warm SST. Significant correlations ($p < 0.01$) with Niño 4 ($r = 0.68$), Niño 3.4 ($r = 0.85$), Niño 3 ($r = 0.85$) and Niño 1+2 ($r = 0.70$) indices lend further support to the ENSO attribution. All warm events can be easily recognized in the PC#1 time-series (Fig. 5.1c), except the 1994/95 event (which is also the weakest judging by the Niño 3.4 amplitude; not shown).

Although this horseshoe-like spatial pattern of EOF#1 resembles that in the EOF#2 of *Ashok et al.* (2007), from which they diagnosed the "El Niño Modoki", the correlation between PC#1 and the El Niño Modoki Index is not particularly high ($r = 0.31, p < 0.01$). This is partly due to the different fields used in *Ashok et al.* (2007) (SST) and in this study (moisture divergence), and the non-linear responses of atmospheric circulation to the surface forcing. Therefore this pattern does not effectively distinguish Modoki-associated moisture divergence fields from other warm events, but rather represents the broad structure of ENSO cycles in general.

The second EOF pattern (Fig. 5.1b) features a southwest-northeast dipole mode over the western Pacific (west of the dateline), and a north-south gradient over the eastern Pacific similar to that found in EOF#1 but shifted 6° equatorward. The PC#2 time-series (Fig. 5.1c) shows more month-to-month variability than PC#1, but some ENSO signatures are still recognizable, with the 1982/83 and 1997/98 El Niño cases being most prominent, similar to the Eastern Pacific index time-series in *Kao and Yu* (2009). A closer look at the two spikes reveals that during these two events they lag their PC#1 counterparts by about one season, but experience fast changes, suggesting a quick restructuring of the moisture circulation patterns.

Besides greater warming magnitudes, these two warm events (1982/83 and 1997/98) differ from the others from a number of additional perspectives (see next section). It has previously been noted that two leading EOFs are required to describe different evolutions of ENSO events (*Trenberth and Stepaniak*, 2001; *Kao and Yu*, 2009). Therefore we also attribute EOF#2 to ENSO, representing the non-linear responses not captured by EOF#1. This non-linearity is illustrated by the outlying dots in the scatter plot of PC#2 against Niño 3.4 (Fig. 5.2). In general, PC#2 and Niño 3.4 are negatively correlated. However, the 1982/83

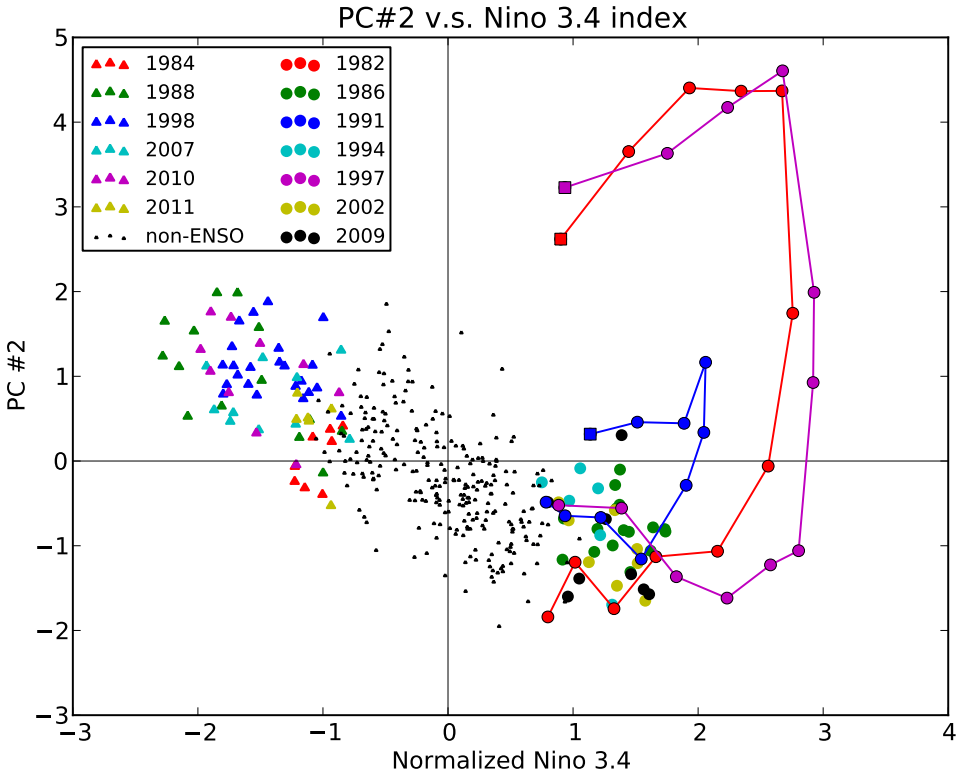

Figure 5.2: Scatter plot of PC#2 against Niño 3.4 index with all El Niño (circles) and La Niña (triangles) events color coded. Non-ENSO months are denoted by small black dots. Evolutionary pathways of the 1982/83 (red), 1991/92 (blue) and 1997/98 (purple) El Niño events are illustrated by solid lines, with the final month being represented with a solid square.

and 1997/98 events, and to a lesser extent the 1991/92 case, contaminate this negative correlation and make the otherwise strong correlation rather poor ($r = -0.3, p < 0.01$). Not all of the months during these three warm cases are outliers, therefore to reveal the evolutionary paths of these exceptional events, we linked the points of these events in a chronological order. Consistent for all three of them, as the El Niño event emerges and rises in amplitude (Niño 3.4 increasing), PC#2 decreases, following the linear path defined by the negative relationship. When Niño 3.4 approaches its maximum value, PC#2 swiftly deviates away from the negative relationship and becomes strongly positive. During this period (which will be shown to be the peak-to-decaying phases), there is no further rise in the SST amplitude, yet the moisture divergence field experiences fast changes. Subsequently, both Niño 3.4 and PC#2 decrease towards zero.

A scatter plot of PC#1 against PC#2 summarizes the complete El Niño-La Niña

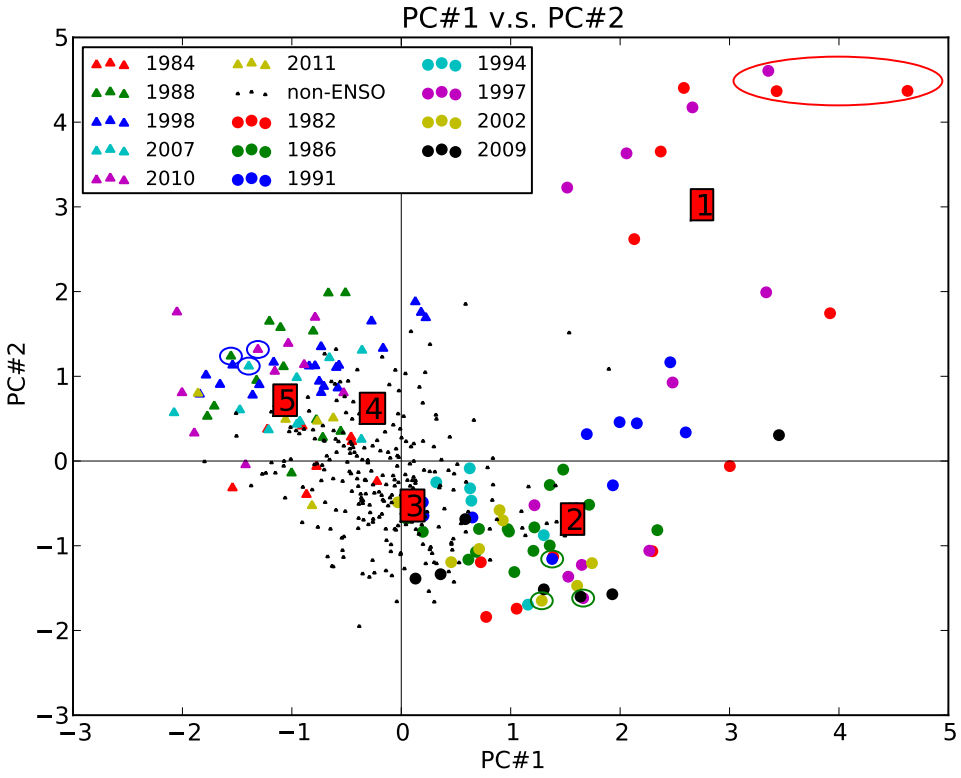

Figure 5.3: Scatter plot of PC#1 and PC#2 with all El Niño (circles) and La Niña (triangles) events color coded. Non-ENSO months are denoted by small black dots. Data points for the extreme El Niño group (consists of the months of 1983-1, 1983-2 and 1998-1) are enclosed by a red ellipse; the moderate El Niño group (consists of 1991-11, 1997-8, 2002-11) by green circles, and the La Niña group (consists of 1988-12, 2007-12, 2010-11) by blue circles. Square-boxed numbers show the locations of the five SOM neurons in PC#1, PC#2 space, i.e. regressed onto EOF#1 and EOF#2 using least squares fit.

response (Fig. 5.3). Two linear relationships are required to fully capture the moisture divergence responses to ENSO effects:

1. The negative La Niña-neutral-moderate El Niño correlation ($r = -0.46, p < 0.01$);
2. The positive moderate-extreme El Niño correlation ($r = 0.64, p < 0.01$);

Although both are statistically significant, these two linear relationships represent very different time subsets (97 % and 3 % of the data, respectively). Despite extreme El Niños only constituting around 3 % of the total time (14 out of 408 months exceeding 2σ in Niño 3.4), both PC#1 and PC#2 show high positive values, and the associated reorganization of atmospheric convection and related global disruptions (*Cai et al.*, 2014), mean that special attention to

these extreme cases is well deserved.

Three groups of nearby points are circled in Fig. 5.3 to represent typical patterns for extreme El Niño state (1983-1, 1983-2, 1998-1), moderate El Niño state (1991-11, 1997-8, 2002-11) and strong La Niña state (1988-12, 2007-12, 2010-11), respectively. Other states can be approximated by the linear relationships defined above. The composite for each group was generated by averaging the linear combinations of EOF#1 and #2 from the corresponding months, and the results are shown in Fig. 5.4. The spatial pattern of the strong La Niña composite (Fig. 5.4a) is similar to that of EOF#1, and the moderate El Niño composite (Fig. 5.4c) but with opposite sign. This is a result of both PC#1 and PC#2 switching sign but remaining approximately the same magnitude (Fig. 5.3). The extreme El Niño group (Fig. 5.4e) displays distinct spatial patterns and stronger magnitudes (note the different color scale). Both the maximum convergence and divergence in the extreme El Niño composite reach 13.0 mm/day or above, which is more than twice the December to Feburary (DJF) climatology (not shown). A zonally elongated convergence band occurs over the eastern Pacific, which co-locates with enhanced precipitation anomalies (*Kug et al.*, 2009; *Cai et al.*, 2012). The climatological SPCZ swings equatorward by a larger amount than during moderate El Niños (the zonal SPCZ feature will be discussed in the next section). A sharp meridional gradient covers the entire tropical Pacific. This is suggested to be the response to the weakened meridional SST contrast over the eastern Pacific (*Cai et al.*, 2014), and the descent anomalies to the north of the equator, mostly caused by dry advection (*Su and Neelin*, 2002). Lastly, the NH branch of the Hadley cell intensifies in both the ascending and descending branches and shifts equatorward by a larger magnitude (*Hu and Fu*, 2007; *Quan et al.*, 2004).

These expressions in the space defined by EOFs #1 and #2 of the anomalous moisture divergence during these three event composites are a good representation of the anomaly fields in the full dimensional space (compare Fig. 5.4a,c,e with Fig. 5.4b,d,f). This is especially so for the strong La Niña and extreme El Niño composites, while the moderate El Niño composite (Fig. 5.4d) shows moisture divergence anomaly features in the South Pacific that are not represented by only EOFs #1 and #2 (Fig. 5.4c). Note that some anomalous features are expected when using a composite formed from only three monthly fields.

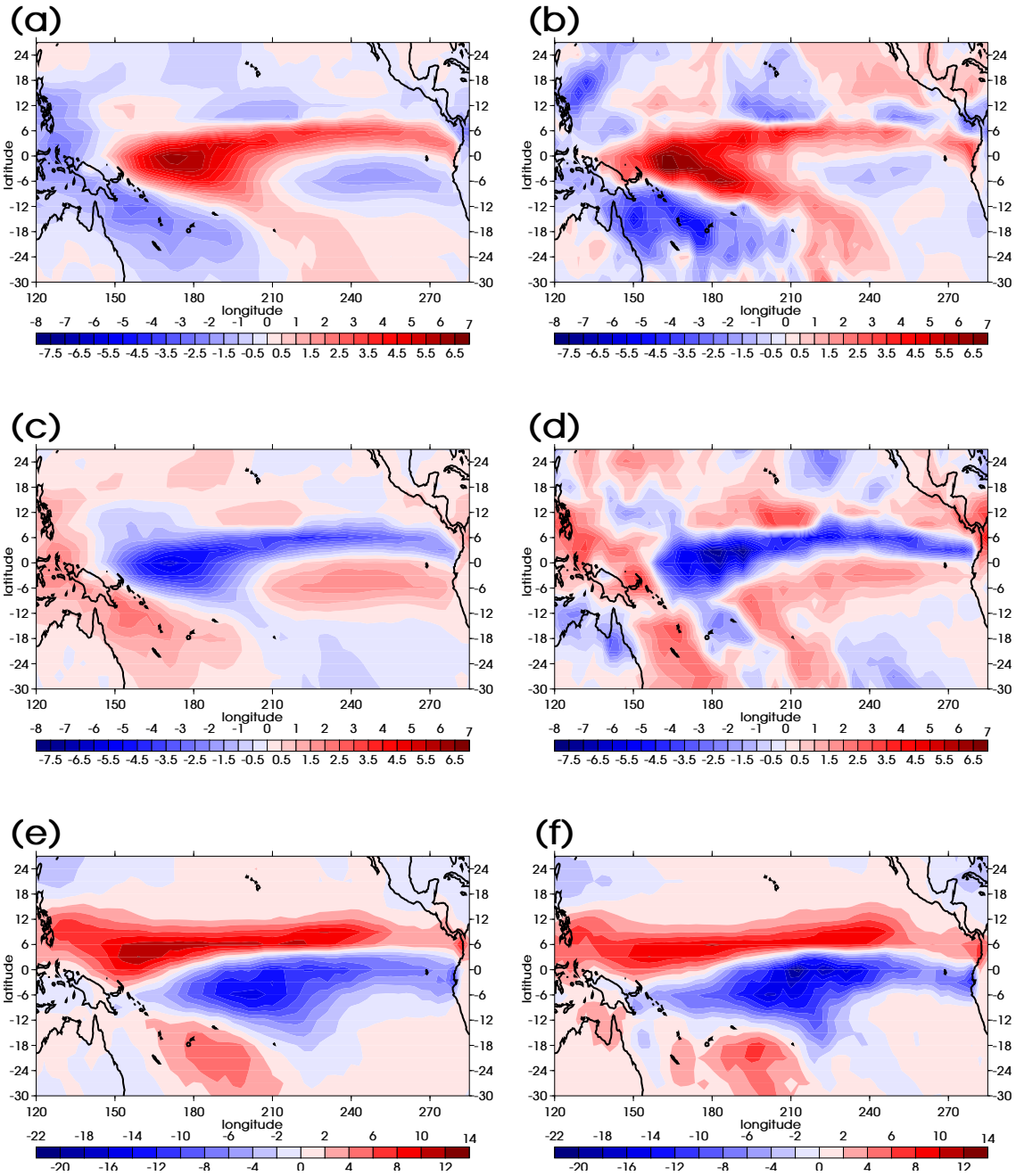

Figure 5.4: Composites of moisture divergence anomaly fields (mm/day) for (a,b) La Niña group. (c,d) moderate El Niño group and (e,f) extreme El Niño group, reconstructed from only EOF#1 and EOF#2 (a,c,e) compared with composites of the actual fields during the same calendar months.

5.3.2 El Niño classification

Given the unusualness of the three warm events, it is justified to make the following El Niño classification from a moisture divergence perspective:

1. Extreme El Niño: represented by 1982/83, 1991/92 and 1997/98 cases;
2. Moderate El Niño: represented by 1986/87, 1994/95, 2002/03 and 2009/10 cases.

The 1982/83 and 1997/98 events have been found to be exceptional in various El Niño classification studies, either from an SSTA zonal contrast point of view (*Kug et al.*, 2009; *Kao and Yu*, 2009; *Larkin*, 2005a,b; *Giese and Ray*, 2011), or by the SSTA onset timing differences (*Xu and Chan*, 2001), or using variables other than SST (*Singh et al.*, 2011; *Chiodi and Harrison*, 2010). The results presented above suggest distinct features from a moisture divergence perspective, and therefore differentiates El Niños on a new dimension.

Unlike the unambiguity in the 1982/83 and 1997/98 cases, the 1991/92 event falls into different groups in different studies: *Kug et al.* (2009) classified it into the "Mix group" (mix of Cold Tongue and Warm Pool El Niño), and in *Kao and Yu* (2009) and *Singh et al.* (2011) it was grouped into the EP category. Similarly in the case of moisture divergence responses it diverges from the linear transitions between La Niña and moderate El Niños, but not as much as the other two extreme events (Fig. 5.2).

To examine the relationship between different El Niño responses to the SSTA zonal structure, we also created scatter plots of PC#2 against Niño 4 ($5°S - 5°N$, $160°E - 150°W$), Niño 3 ($5°S - 5°N; 150°W - 90°W$) and Niño 1+2 ($0 - 10°S, 80 - 90°W$) indices (not shown). The negative correlation among non-El Niño and moderate El Niño points becomes weaker as the index moves from west to east. This suggests better correspondence between the moderate ENSO cycle and central-western Pacific SST variations, while extreme El Niños are more related to the east-west SSTA contrast. Moreover, *Kao and Yu* (2009) and *Capotondi* (2013) also found consistent east-west differences in the subsurface temperature structures associated with the two types of El Niños. Zonal SST gradient, ocean heat content propagation and the thermocline feedback are key to explaining the observed differences in the atmospheric circulation, moisture divergence and subsequently precipitation responses.

5.3.3 El Niño phase comparison

To examine the El Niño differences in more detail, each event is broken into five evolutionary phases according to their relative Niño 3.4 amplitudes, and the phase composites for extreme and moderate El Niños are shown in Fig. 5.5 and Fig. 5.6, respectively.

"Pre-event" and "Post-event" are both 3 months in duration by definition. With the dual-peaked 1986/87 case excluded, "Starting" phase has an average duration of 2.9 months, "Peak" phase around 4.0 months and "Decaying" phase 1.7 months. Therefore an El Niño would typically experience fast SSTA changes in central Pacific within one season, then meander for a slightly longer time in its "Peak" phase, followed by an even faster drop in SSTA in the "Decaying" phase.

Although their onset timings and overall durations differ, the "Peak" phases always occur during the Nov-Dec-Jan season (with the dual-peaked 1986/87 case being exceptional, where the second peak started in July-Aug of 1987). This has been suggested to be the result of a phase-locking mechanism with the seasonal SST cycle (*Xu and Chan*, 2001; see also Fig. 4 in *Wang*, 2002), and such a feature would help eliminate the obstacles in inter-comparing the amplitude-based approach and calendar-month-based approach, and promises relationships being made with results from other studies.

Notable differences between moisture divergence anomalies associated with the extreme and moderate groups start to emerge in the "Starting" phase (Fig. 5.5 b, 5.6b), reach a maximum in "Decaying" phase (Fig. 5.5d, 5.6d), and persist into the "Post-event" phase (Fig. 5.5 e, 5.6e). In addition to anomalies that are both larger and have a maximum convergence anomaly further east in the extreme El Niño composite, an important new finding is that the extension of the anomalous moisture convergence to the eastern Pacific moves on to the equator during the peak and decaying phases (Fig. 5.6c,d), whereas it stays north of the equator throughout moderate El Niños (Fig. 5.5). Shoaling of the thermocline and the resultant influence on SST is very sensitive to the latitude of the anomalous moisture convergence and its associated wind stress. This latitudinal difference and the stronger westerly wind anomalies that accompany it may contribute to the extension of SSTA further into the eastern Pacific during extreme El Niños. The anomalous convergence also exists in balance with a more zonally symmetric Southern Hemisphere (SH) surface pressure field and stronger southerlies east of the dateline in the peak and decaying phases,

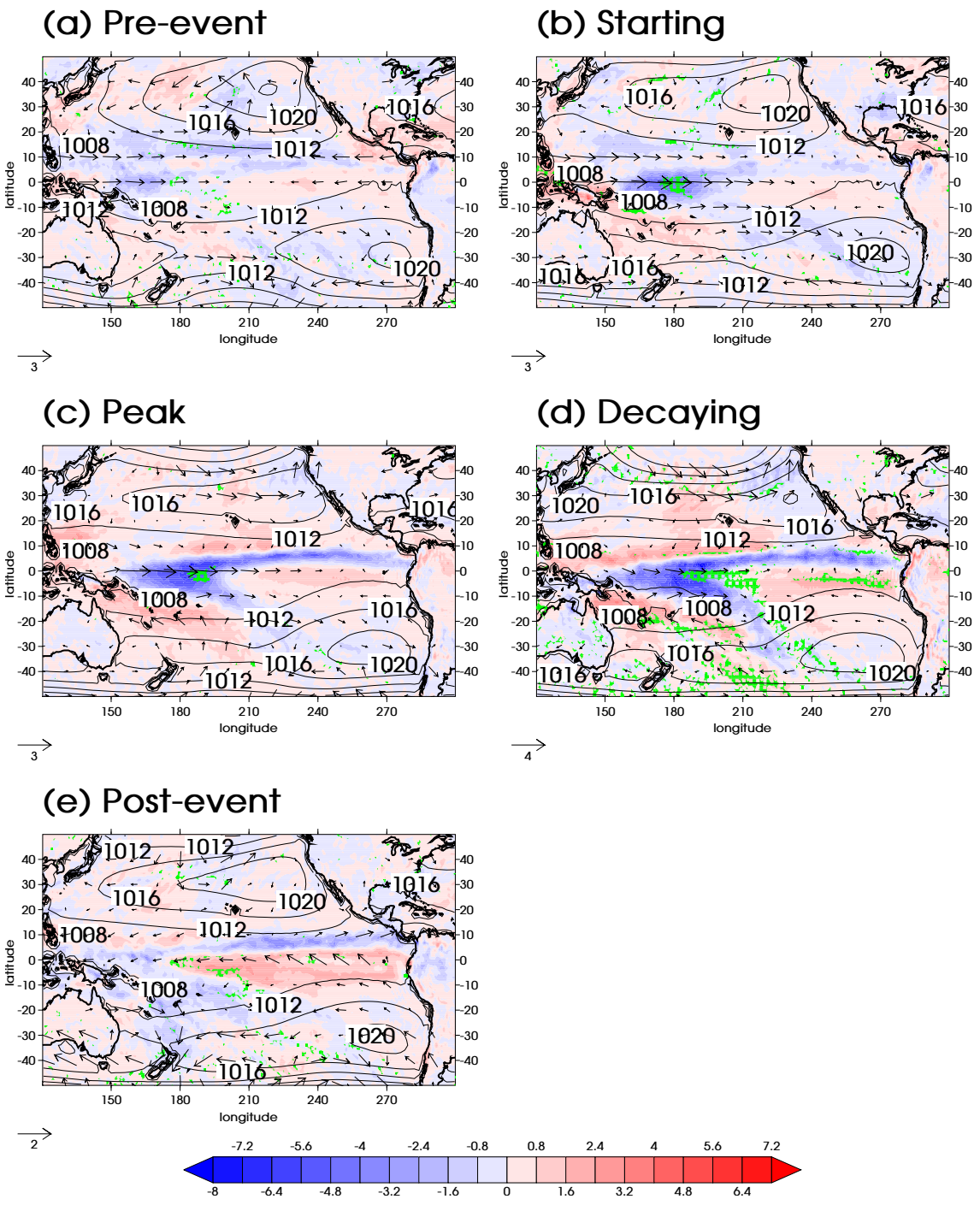

Figure 5.5: Phase composites of moisture divergence anomalies (mm/day) for moderate El Niños in (a) "Pre-event" phase, (b) "Starting" phase, (c) "Peak" phase, (d) "Decaying" phase and (e) "Post-event phase. Green hatch overlay denotes areas where the anomaly reverses the sign of the climatology. Surface pressure composite fields are plotted as contour lines with a contour interval of $4\,hPa$, and $850\,hPa$ horizontal wind anomalies (m/s) are plotted as vectors.

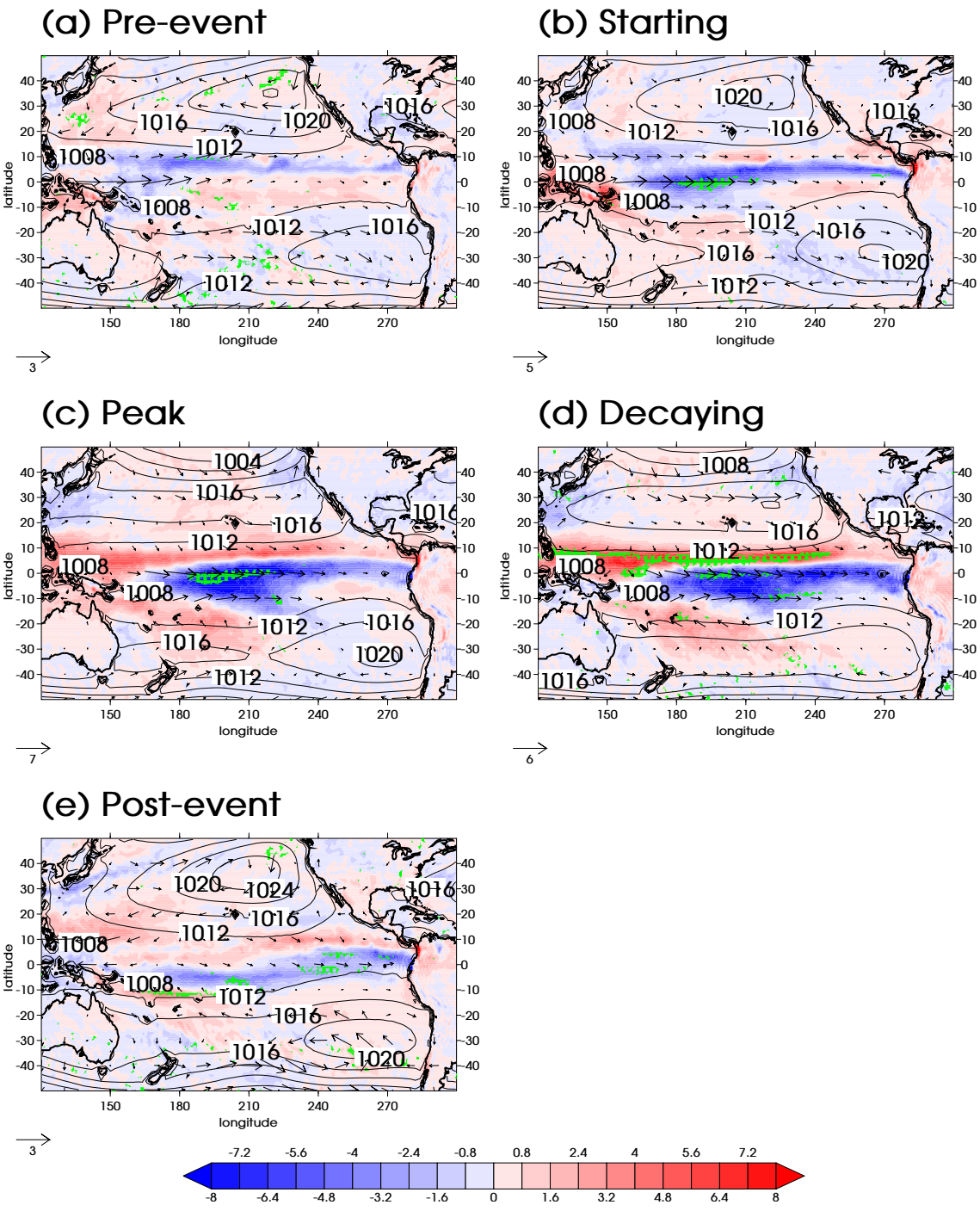

Figure 5.6: Same as Fig. 5.5 but for extreme El Niños.

displacing the SPCZ to a more zonal orientation (see *Cai et al.* 2012).

In contrast, easterly anomalies occur over the equatorial eastern Pacific during a moderate El Niño. Together with the off-equator position of the moisture convergence anomaly, these act to confine surface warming to the central and western Pacific, and deep convection does not occur in the east (consistent with smaller OLR reductions, *Chiodi and Harrison* 2010).

To the north of the equator, northwesterly anomalies are stronger in the extreme El Niños. Associated with a more compact NH Hadley cell, this dry advection helps maintain the sharp meridional gradient in the moisture divergence field (*Su and Neelin*, 2002), which is strong enough to reverse the climatology (indicated by the green hatching in Fig. 5.6) in the "Decaying" phase. Moreover, such a peak-to-decaying phase differentiation is not confined to the moisture divergences observed here: the pattern correlations of SSTA from CT El Niños and WP El Niños in corresponding phases (calendar-month-based) were strongly positive during the peak phases of these two types of El Niños, but swiftly become negative one season later (*Kug et al.*, 2009). Similar results were also found for precipitation and pressure velocity fields (*Kug et al.*, 2009).

5.3.4 SOM analysis

Although two EOFs capture much of the time-varying ENSO signal, their physical interpretation is hampered by their lack of independence. Both the EOFs and the PC time-series are constrained, by definition, to be orthogonal, but that does not mean that they are unrelated. This can be seen in Fig. 5.3, where despite an overall zero correlation between PC#1 and PC#2, a non-linear relationship clearly exists between the two PC time-series. Furthermore, the pattern of EOF#2 will have been constrained so that (a) it is orthogonal to EOF#1; and (b) it has the precise characteristics such that the projection of moisture divergence onto it during the few extreme El Niño months when there is a positive relationship with PC#1 exactly counterbalances the projections during all the other months when there is a negative relationship with PC#1, so that the overall correlation with PC#1 is zero. It is unlikely that EOF#2 will have been unaffected by these constraints, and some ENSO-related information would likely have been spread into higher order EOFs as a result.

This provides the motivation for our SOM analysis of the same moisture divergence field, to explore its utility in easily capturing this non-linear

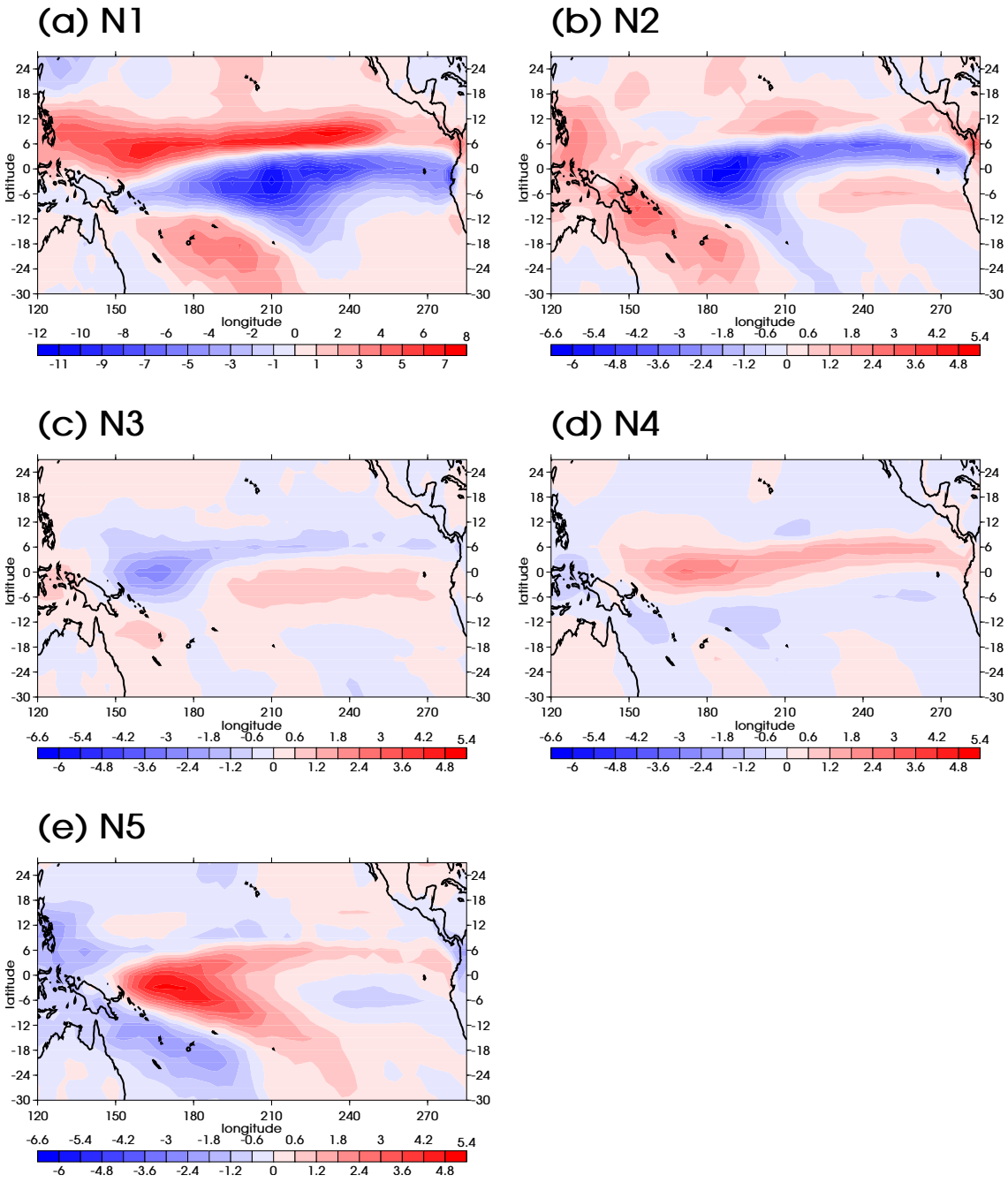

Figure 5.7: Self-Organizing Map (SOM) neurons on moisture divergence anomalies (mm/day); (a) to (e) are SOM neurons 1 to 5. Note that (a) uses a different color scale than others.

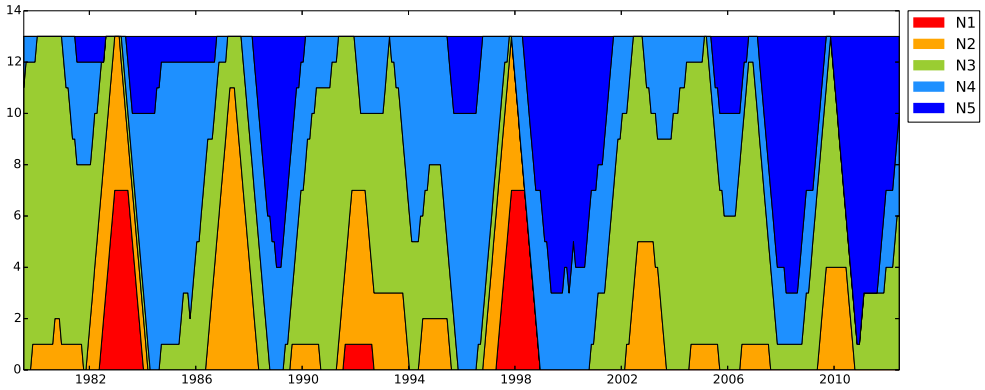

Figure 5.8: Stacked time-series of SOM training sample counts, defined as the number of training samples allocated to each neuron in each sliding 13-month time window.

behaviour. By quantifying the distances between a carefully chosen number of SOM neurons, an equivalent El Niño classification is also achieved.

Fig. 5.7 displays the five SOM neurons we obtained. The 1st neuron (Fig. 5.7a) shows a good agreement with the extreme El Niño group composite in Fig. 5.4e, both in terms of spatial patterns and the anomaly strengths. The 2nd (Fig. 5.7b) and 5th (Fig. 5.7e) neurons resemble the moderate El Niño group (Fig. 5.4c) and the La Niña group (Fig. 5.4a), respectively. Moving from neuron-1 to neuron-5, one observes a gradual transition of the moisture divergence field, therefore the remaining two neurons (neuron-3 and -4) could be expected to represent the neutral and weak La Niña ENSO states.

This attribution is substantiated by the locations of each neuron in the space defined by EOFs #1 and #2, by least squares estimation of the PC#1 and PC#2 coefficients that best replicate each neuron (shown by the red numbered squares in Fig. 5.3). The sequence of neurons follows the pathway defined by the two correlations. Fig. 5.8 shows the number of months in each sliding 13-month window allocated to each neuron. The allocation is based upon selecting the closest neuron, in a Euclidean distance sense, to each monthly field. The time-series of neuron-1 displays non-zero values only during the 1982/83 and 1997/98 El Niños, and for a shorter period in the 1991/92 case. The La Niña neuron (neuron-5) shows good correspondence with La Niña years (1983/84, 1988/89, 1999/2000/2001, 2007/08 and 2010/11). Neuron-2 becomes active either during a moderate El Niño (1986/87, 1994/95, 2002/03 and 2009/10) or in the early phase of an extreme El Niño (1982/83 and 1997/98). The rest of the time period is mostly represented by neutral and weak La Niña neurons (-3

Table 5.1: Inter-neuron distances and the means and standard deviations of intra-group distances (mm/day). Distance (d) is defined as the geometrical distance in the multi-dimensional space, and is related to the root mean square difference (RMS) by $d = \sqrt{N} \times RMS$, where $N = 1120$ is the number of grid boxes in data. Distance between neuron i and j is denoted by the matrix element at row i, column j. The mean and standard deviation of the distances between all training samples and the neuron they are allocated to are listed in the "Mean" and "SD" columns, respectively. Column "Size" shows the size of each group (i.e. number of months).

Neuron	1	2	3	4	5	Mean	SD	Size
1	0	97.6	112.8	105.2	120.6	84.7	7.5	15
2		0	46.1	62.3	81.2	71.4	11.0	50
3			0	31.8	47.6	60.7	7.4	157
4				0	32.4	58.7	7.9	111
5					0	62.6	7.7	75

Table 5.2: Correlation matrix between the 5 SOM neurons. Correlation between neuron i and j is denoted by the matrix element at row i and column j. Note that all correlations are significant at 0.01 level except for the one denoted by asterix ($p = 0.33$).

Neuron	1	2	3	4	5
1	1	0.34	-0.51	-0.03^*	-0.34
2		1	0.29	-0.70	-0.82
3			1	-0.61	-0.48
4				1	0.48
5					1

and -4). Instead of the discrete and selection-exclusive sample counting method used here, one could also use a spatially weighted correlation time-series to reveal more subtle features in the temporal variations of each neuron.

To validate the El Niño classifications, we computed inter-neuron distances (Table 5.1), defined as the Euclidean distance between every two neuron pair, and the mean and standard deviation of intra-group distances. Intra-group distances refer to the distances between all training samples and the neuron they are allocated to. The average and standard deviation of the intra-group distances serve as a measure of how closely the training samples are clustering around the neuron (though note that the distances cannot simply be averaged or summed to represent distances across multiple groups because the distances will be based on different directions in the high dimensional space).

As is shown in Table 5.1, the extreme El Niño neuron (N1) shows increasingly larger distances from the moderate El Niño (97.6, N2), neutral (112.8, N3), weak

La Niña (105.2, N4) and strong La Niña (120.6, N5) neurons. The separation (97.6) between extreme and moderate El Niño neurons is larger than the direct distance from moderate El Niño to strong La Niña (81.2 from N2 to N5). Table 5.2 shows the pattern correlations between the neurons, thus removing the effects of magnitudes in constituting the inter-neuron distances. The moderate El Niño neuron (N2) has a much better (but opposite) pattern match with La Niña neurons (N4 and N5), than with the extreme El Niño neuron (N1). Therefore the distinction bewteen extreme and moderate El Niños suggested by the SOM analysis is justified. On the other hand, differences between moderate El Niño and neutral (46.1 from N2 to N3) is much smaller, which is consistent with the relatively clustered data distribution in EOF #1, #2 space (Fig. 5.3).

5.4 Conclusions and Discussion

We have used EOF and SOM analyses to characterize the spatial patterns of inter-annual variability in the atmospheric moisture divergence over the tropical Pacific, a key component of the hydrological cycle that is linked directly to anomalies in the surface water balance ($E - P$). This variability is of course dominated by ENSO influences, with the moisture divergence shifting eastwards to follow the eastward shift of the warmest equatorial SST during moderate El Niños, accompanied by an equatorward rotation of the SPCZ. The moisture divergence anomalies associated with La Niña events have similar spatial patterns and magnitudes as moderate El Niños, but with opposite sign. Our analysis finds, however, that the moisture divergence patterns during extreme El Niño events are not simply a strengthening of the moderate El Niño pattern but exhibit distinct characteristics: the tropical convergence centre moves much further east, the NH Hadley Cell is more compact and the SPCZ swings further towards the equator. These differences from moderate El Niño behaviour are particularly apparent from the peak of the event through the decaying phase, which is consistent with previous studies using other climate variables (*Kug et al.*, 2009; *Xu and Chan*, 2001).

This complex behaviour is evident in the EOF results, with a clear non-linear relationship found between the leading two PC time-series even though they are constrained by EOF analysis to have no linear dependence. This motivated our use of the SOM technique, which is not constrained by the spatial and temporal orthogonality requirements of EOF decomposition. The SOM analysis

simplifies the non-linear relationship between two EOF patterns into a simple sequence of five patterns (SOM neurons) representing the range of states from La Niña to extreme El Niño. SOM neuron count time-series and inter-neuron distance/correlation statistics further validate the classification of extreme and moderate El Niños.

Our findings have a number of implications. First, a single index such as Niño 3.4 is insufficient to measure the range of atmospheric moisture divergence responses to ENSO, consistent with the prior findings for other variables (*Trenberth and Stepaniak*, 2001; *Trenberth and Smith*, 2006; *Chiodi and Harrison*, 2010; *Kao and Yu*, 2009). An index is required to represent the SST zonal contrast that distinguishes different types of El Niño, and is likely to be the key factor that causes differences in moisture divergence patterns. Our results suggest that alternatives to the conventional EOF method that are free from orthogonal constraints, such as SOM, deserve more attention when determining additional ENSO indices.

Second, analyses of ENSO behaviour need to consider more ENSO classes than the basic La Niña, neutral and El Niño classification. Our analysis of atmospheric moisture divergence demonstrates that this distinction is present in the atmospheric branch of the hydrological cycle too, providing a new perspective to the existing literature, and confirms the coupled ocean-atmosphere signature of this ENSO difference that is not necessarily implied by the SST-based analyses. The consistency with SST-based studies is not a coincidence. The sensitivity of ocean temperature and atmospheric convection is reversed between the central and eastern Pacific: central Pacific SSTAs are much more effective at inducing anomalous convection than their eastern counterpart, due to the warmer background SSTs (*Kug et al.*, 2009; *Hoerling et al.*, 1997; *Capotondi et al.*, 2015), while subsurface temperature below the mixed layer has a stronger response to the thermocline changes over the eastern Pacific (*Capotondi et al.*, 2015). Therefore once the warm SST anomalies develop over the eastern Pacific or get advected from the west in an extreme El Niño, possibly modulated by the seasonality of Kelvin wave propagation (*Harrison and Schopf*, 1984), or a proper timing of Australia and Asian monsoon (*Xu and Chan*, 2001), the induced thermocline feedback could trigger large magnitudes of deep convection over the eastern Pacific, as manifested by OLR troughs (*Chiodi and Harrison*, 2010), and the moisture divergence changes presented in this study for extreme El Niño (e.g. the first SOM neuron, Fig. 5.7a).

Similar concerns relate to the use of EOF analyses to classify ENSO behaviour – due to EOF orthogonality constraints, the pattern of variation covering La Niña to moderate El Niño events is mostly captured by EOF#1 but also partly represented in EOF#2, which in turn partly represents the contrasting moisture divergence response to moderate and extreme El Niños. Classifications need to consider this complexity and ideally use methods, such as the SOM presented here, that can represent them as separate patterns rather than the mixed form of the EOF analysis.

Third, the observed non-linear response highlights the need for a coupled Hadley-Walker cell view in explaining the different El Niño types. Although commonly interpreted as a meridional circulation cell, the Hadley cell is not zonally symmetric, but rather a 3D helix circulation where the zonal asymmetry is modulated by the Walker circulation. In neutral ENSO condition, the warm pool low and the subtropical highs to the east form a triangular shape (Fig. 5.5a, see also Fig.1 in *Zhang and Song* (2006)). In the mature phase of an extreme El Niño, strong eastern warming weakens or even reverses the Walker circulation, and compresses the equatorial-low-subtropical-high polarity (Fig. 5.6d); the pitch distance of the 3D Hadley-Walker helix circulation is reduced. As a result, the dry air intrusion from the subtropics becomes more effective, due to both a tighter pressure gradient and reduced opportunity for evaporation to replenish the moisture because of the shorter travel distance. The reduced trade winds and evaporation also play a role (*Su and Neelin*, 2002). As warming is more confined to the western-central Pacific in a moderate El Niño, the modulation of the Walker circulation is not strong enough to reverse the equatorial-low-subtropical-high polarity.

Finally, we note limitations to this study. The limited time span of ERA-I data allows only a small sample of seven El Niño events to be included. Other reanalysis products that assimilate only surface observations, for instance ERA-20C or 20th Century Reanalysis (20CR), cover a much longer period with more El Niño events. However, the accuracy of upper-air states is compromised prior the satellite era. Of the three extreme El Niños, two coincided with major volcanic eruptions (the March 1982 El Chichon and the June 1991 Mt. Pinatubo), and we did not address the possible role volcanic forcing may have on tropical moisture divergence. Moreover, the Pacific exhibits distinct decadal (PDO, Pacific Decadal Oscillation) to inter-decadal (IPO, Inter-decadal Pacific Oscillation) variations, with largely consistent manifestations in SST, sea level pressure, wind stress, thermocline evolution, Hadley circulation and ENSO

variability (*Power et al.*, 1999; *Mantua et al.*, 1997; *Folland*, 2002; *Wang and Lau*, 2006; *Quan et al.*, 2004; *Trenberth and Stepaniak*, 2001). The change in PDO/IPO phase around 1976/77 has been identified as a major "climate shift" (*Trenberth*, 1990; *Trenberth and Stepaniak*, 2001), after which El Niño activity increased and the structure of the SPCZ changed (*Folland*, 2002), possibly caused by the altered zonal SST structure (*van der Wiel et al.*, 2015). Therefore, the validity of the results presented here might be limited to positive PDO/IPO epochs. Further investigation with earlier datasets is needed to determine whether they hold in La Niña dominated periods.

5.5 Appendix

5.5.1 SOM algorithms

The input moisture divergence anomaly data are organized into an $(n \times p)$ matrix X:

$$X = \begin{bmatrix} \vec{x}^{(1)} \\ \vec{x}^{(2)} \\ ... \\ \vec{x}^{(n)} \end{bmatrix} \tag{5.2}$$

where $\vec{x}^{(i)} = (x_1^{(i)}, x_2^{(i)}, x_3^{(i)}, ..., x_p^{(i)})$ is the ith training sample (at the ith time point).

There are several initialization options, including using random vectors/training samples or using leading EOFs (*Hulle*, 2012). Different initial neurons could converge to slightly different final states, but the same overall pattern emerges at the end of training. Here, neurons were initialized by taking the first five samples from the training set X. Several SOM runs initialized with randomly chosen training samples were also performed, yielding very similar results. Therefore only results from the "first-5" initialized SOM are used here.

The inital neurons are adjusted iteratively to obtain the final neuron locations. There are two basic methods that neuron adjustments could use: incremental (or stochastic) adjustment and batch adjustment (*Hulle*, 2012). In the incremental approach, neurons are adjusted using each training sample individually and in sequence. This usually leads to stochastic behaviour in the convergence path

and requires large numbers of iterations to reach convergence, but is more suitable for real-time processing when a complete training set is not available beforehand. The batch mode, used here, uses all training samples together to calculate each iteration of neuron adjustment.

The training session consists of 300 iterations of neuron updates. In each iteration, each training sample is allocated to its closest neuron (in a Euclidean sense), which is called the "winner" neuron for that data sample. The training samples allocated to a particular "winner" neuron provide information on how to adjust that neuron, effectively moving its location in data space towards the weighted mean of the training samples allocated to it. However, these training samples are also used to adjust the neurons that are neighbours of the "winner", but subject to a weighting that depends on the topological distance between a neighbour and the "winner" neuron. This weighting is via a neighbourhood function, h_{ij}, between neurons i and j which ensures the topological relationships between neurons in the SOM. The location of each neuron i is therefore updated according to:

$$\vec{m}_i := \frac{\sum_j h_{ij} \bar{\vec{x}}_j n_j}{\sum_j h_{ij} n_j} \tag{5.3}$$

where the mean ($\bar{\vec{x}}_j$) of all training samples allocated to a neighboring neuron $\vec{m}_j$ is weighted by the corresponding number (n_j) of training samples, and the neighborhood function between neurons i and j. This overall mean is then updated to $\vec{m}_i$.

A Gaussian is a common choice for the neighbourhood function, and is adopted here:

$$h_{ij}(t) = \begin{cases} exp(-\frac{\|\vec{r}_i - \vec{r}_j\|^2}{2\sigma^2(t)}) & \sigma > 0 \\ 1 & \sigma = 0 \end{cases} \tag{5.4}$$

where $\vec{r}_i$ and $\vec{r}_j$ are the location vectors of the "winner" neuron i and the neighboring neuron j, respectively. A large kernel size, $\sigma(t)$, is necessary in the early stages of the training session for the global order to take shape, but this is then decreased monotonically during each iteration, t, of the training session:

$$\sigma(t) = [(\sigma_0 + 1) * (1 - \frac{t}{T})] \tag{5.5}$$

where [] is the floor function, and T is the total number of iterations for the training session, 300 in this case.

5.5.2 El Niño phase separation

The phase definitions for El Niños identified using the Niño 3.4 time series are shown in Fig. 5.9. The fast changes to Niño 3.4 and to the overlying atmosphere mean that the 70 % criterion used to define the times of transition between the "Starting", "Peak", and "Decaying" phases do not generally occur at a calendar monthly mean value. Instead, linear interpolation between monthly mean values was used to locate the transition time points:

$$\begin{cases} f_{01} = \frac{T_2 - T_t}{T_2 - T_0} \\ f_{12} = \frac{T_t - T_0}{T_2 - T_0} \\ t_t = f_{01} \cdot t_0 + f_{12} \cdot t_2 \end{cases} \tag{5.6}$$

where T is the normalized Niño 3.4 index; t is the time point represented by the number of days since a given reference time; f_{01} and f_{12} are the linear interpretation factors; subscripts 0 and 2 denote the two ends of the interpolation domain, and subscript t represents the target time/data point. Variables (e.g. moisture divergence) used to create composites for each phase were then interpolated to time point t using the same interpolation factors (f_{01} and f_{12}).

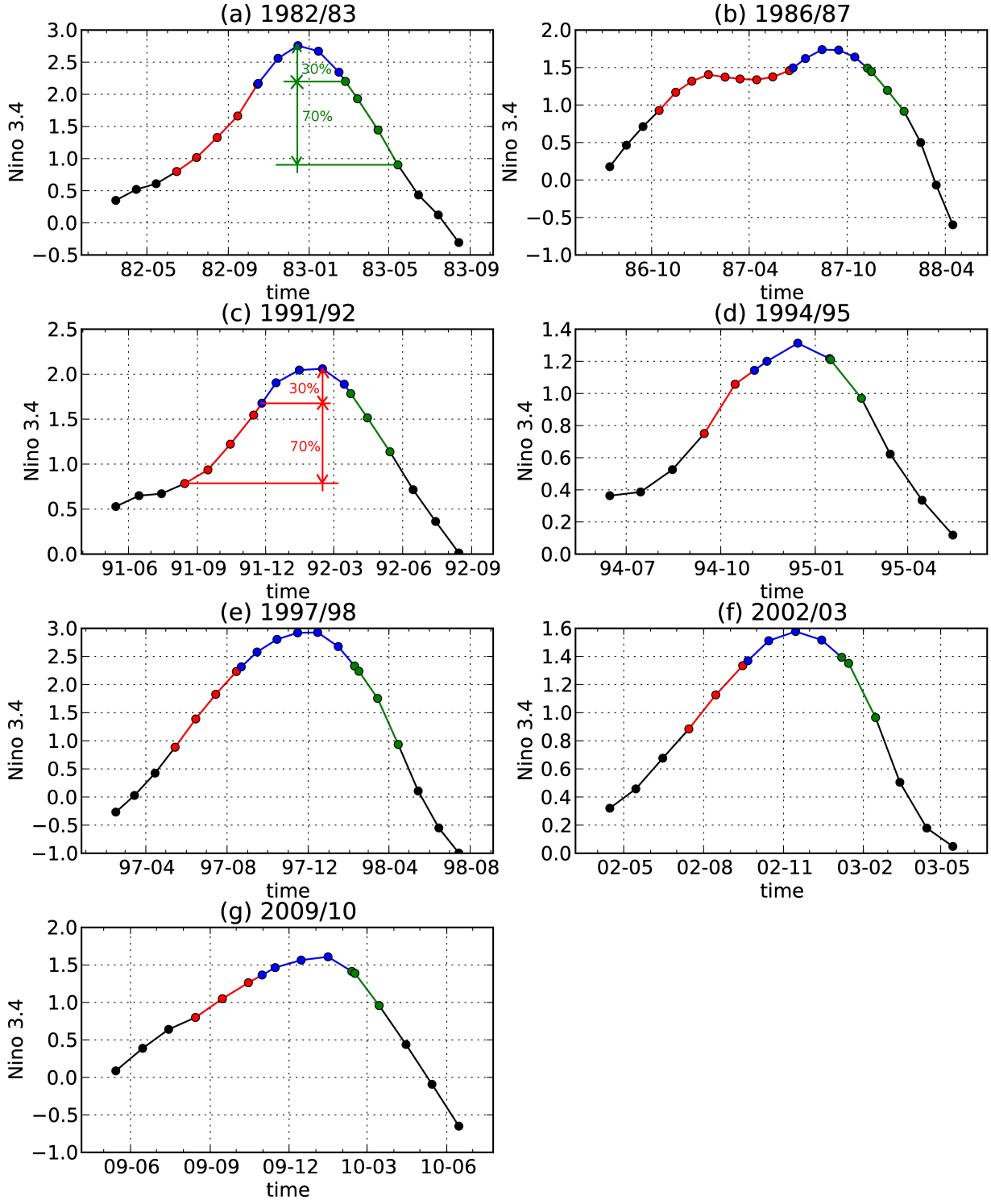

Figure 5.9: Normalized Niño 3.4 indices with phase separations for each El Niño event: (a) 1982/83, (b) 1986/87, (c) 1991/92, (d) 1994/95, (e) 1997/98, (f) 2002/03 and (g) 2009/10. Phase colors are: "Starting" (red), "Peak" (blue), "Decaying" (green), "Pre-event" and "Post-event" (both black). Panels (a) and (c) illustrate the phase separation from "Peak" to "Decaying" and from "Starting" to "Peak", respectively.

Chapter 6

Moisture transport by Atlantic tropical cyclones onto the North American continent

The contents of this chapter have been submitted for publication to the journal Climate Dynamics.

6.1 Introduction

Tropical cyclones (TCs: tropical depressions, storms and hurricanes) are powerful regional scale meteorological phenomena that are known for their extreme wind, intensive rainfall and often very costly economical and societal losses. Despite their destructive potential, TCs also serve as an important source of freshwater and carry a considerable amount of water from ocean to land, which plays an important role in modulating regional scale droughts. Using Palmer Drought Severity Index (PDSI) and daily rainfall records from the Cooperative Observer Network, *Maxwell et al.* (2012) suggested that up to 41 % of droughts over the southeastern United States during 1950 - 2008 were terminated by single TCs, thus the term "drought busters" was coined. During the dry years of 2006 - 2007, TC-related rainfall redressed the meteorological drought over the Atlantic Coastal Plain by $20-40$ %, and the water deficit was reduced by $50\,\%-90\,\%$ in the Carolinas watersheds (*Brun and Barros*, 2014). And for a dry continent like Australia, TC rainfall is as regarded a significant contributor to freshwater supplies for human communities, agriculture and the

health of ecosystems (*Dare et al.*, 2012).

Many studies have documented the contribution of TCs to rainfall at a regional (e.g. *Rodgers et al.* (2001); *Larson et al.* (2005); *Ren et al.* (2006); *Brun and Barros* (2014); *Konrad et al.* (2002); *Konrad and Perry* (2010); *Knight and Davis* (2007, 2009); *Prat and Nelson* (2013); *Dare et al.* (2012)) or global (e.g. *Jiang and Zipser* (2010)) scale. However, few studies have looked into the effects of TCs on continental scale onshore moisture transport, which helps set up a favorable environment for precipitation. *Schumacher and Galarneau* (2012) performed a quantification of the moisture transported ahead of two recurving TCs (Erin in 2007 and Ike in 2008), by contrasting ensemble members from THORPEX Interactive Grand Global Ensemble (TIGGE) where the TC recurved from those that did not. The results indicated that although being positively related, the tropical moisture transported by TCs is neither a strictly necessary or sufficient condition for the coincident heavy rainfalls. This illustrates the importance of a better quantification of this moisture transport, and a better understanding of its ultimate effect on precipitation. From a large scale water and energy budget point of view, TCs serve as an important balancing mechanism in redistributing tropical water and heat poleward. However, a good quantification of this aggregated role has not been fully addressed (*Hart et al.*, 2007).

In view of such a gap, this study develops a set of methods to isolate the TC-related moisture transport from ocean to land, and specific to this study, applies them to the North American continent. The column integrated moisture fluxes are estimated from ECMWF's ERA-Interim (ERA-I) reanalysis product (*Dee et al.*, 2011), and the best track observation from National Hurricane Center (NHC) (*Landsea and Franklin*, 2013) is used to track the TCs. To make the TC moisture flux attribution, a set of distance-based attribution methods is developed and pilot tested. Similar distance-based methods are commonly adopted by precipitation-focused studies, where the precipitation events within a certain radius of a TC is attributed to the TC's influence. Note that this kind of distance-based method in general is variable dependent: the necessary geographical vicinity for an effect to be experienced may vary from variable to variable. A typical choice among precipitation attribution studies is $500\,km$ (e.g. *Rodgers et al.* (2001); *Larson et al.* (2005); *Lau et al.* (2008); *Jiang and Zipser* (2010)). This provides helpful guidance to the spatial extent of TCs' influence on moisture fluxes, but should not be adopted directly without validation.

Section 6.2 describes the datasets and the TC flux attribution methods. Four different schemes, differing in their flexibility and adaptibility, are designed

to determine a critical TC influence radius. Section 6.3 displays the results of applying the attribution schemes to onshore moisture fluxes, by firstly giving an overview of the TC activities (Sec 6.3.1), followed by validations on two sample coastal grid cells (Sec. 6.3.2). Then the distrubtion, seasonal totals and inter-annual variabilities of TC transport are presented in Sec 6.3.3 - 6.3.5. Finally, Section 6.4 talks about the uncertainties in the estimate and a preliminary discussion on the relationship with ENSO.

6.2 Data and methods

6.2.1 Best track TC records

The best track records of North Atlantic tropical cyclones are obtained from the HURDAT2 (HURricane DATa 2nd generation) dataset compiled by National Hurricane Center (NHC) (*Landsea and Franklin*, 2013). This dataset is a Re-analysis effort to extend and revise the NHC's North Atlantic hurricane dataset (HURDAT) by utilizing an enhanced collection of historical meteorological observations in the context of an upgraded scientific understanding of hurricanes and analysis techniques. In addition to 6-hourly location and time tracks of TCs, observations that are not available in real time are synthesized, and some additional information is added onto the original HURDAT format, including non-synoptic (other than 00, 06, 12 and 18 UTC) best track times to help pin-point significant moments in a TC's lifetime (such as landfalling and maximum intensity times), and best track wind radii estimates that provide information on the shape and size of a cyclone (*Landsea and Franklin*, 2013). This radii information is explored and utilized in this study to design TC attribution schemes.

Best track records of East Pacific (EP) tropical cyclones are obtained from IBTrACS (International Best Track Archive for Climate Stewardship) (*Levinson et al.*, 2010), which is an objective combination of best track records from various regional data centers. The inclusion of East Pacific TCs gives a more complete view of the continental freshwater inputs from TCs. However, this study focuses mostly on Atlantic TCs.

6.2.2 Horizontal moisture fluxes

Six-hourly specific humidity (q) and horizontal winds (u and v) observations during 1979-Jan to 2012-Dec are obtained from ERA-I reanalysis (*Dee et al.*, 2011). Moisture fluxes on model levels 1 to 60 that cover the troposphere and stratosphere are vertically integrated to form the column moisture fluxes:

$$\begin{cases} F_u = \frac{1}{g}\int_1^{60} uqdP \\ F_v = \frac{1}{g}\int_1^{60} vqdP \end{cases} \tag{6.1}$$

where dP is the pressure increment between model levels. The annual cycles and anomalies of F_u and F_v are defined using the 1979-2012 long-term mean as climatology.

6.2.3 TC-flux attribution

The isolation of the moisture fluxes carried by a TC from the background flow in which the TC is embeded is not a trivial task and the answer is highly dependent on the definition and approach. The large scale vorticity condition is one of the important factors for TC genesis and development (*Bengtsson et al.*, 2007) and a clear boundary between the background flow and the TC flow does not usually exist, particularly when during the transition to an extra-tropical storm. Therefore it is important to inspect the results to make sure the method generates reasonable estimates. Furthermore, exploration of the sensitivity to methodological choices and quantification of uncertainties may be as valuable as the final estimated number. In view of such difficulty, an ensemble of estimates is produced based on a range of TC influence detecting schemes, as explained in the following.

The attribution of TC-related onshore moisture fluxes is designed following three main principles: 1) the TC-induced moisture flux is anomalous in nature and significant in magnitude, therefore should be separated from both the mean annual cycle and the background flow in the flux anomalies; 2) the spatial extent of the influence from a TC is a confined area following the movement of the TC, centered around the TC center, but not necessarily symmetrical in the four quadrants (NE, NW, SW and SE); 3) the temporal extent of the TC influence is limited to the lifetime of a TC, precedent or aftermath effects are not included.

Based on these principles we devised a set of distance-based TC-attribution schemes that use the distance from TC centers as the major decisive threshold, but also taking the underlying variability of moisture fluxes into consideration. Each decision made following the above principles inevitably incorporates some degree of subjectiveness and uncertainty, and sometimes the decision is a balanced compromise between targeted result, analysis objectiveness and limitations in the available data. For instance a conservative TC influence radius guarantees a more accurate effect detection, but is likely to miss the full extent and lead to underestimated results. A large radius can help capture as many affected grid boxes as possible, but at the risk of falsely detecting a TC's effect in some cases (making a type I error). In such cases, background flow filtering can help reduce the error by subtracting low-pass filtered flows from the flux anomalies, thus a large portion of the falsely detected TC-fluxes will be removed in the filtering process. However, the effectiveness of such time filtering can be sensitive to the TC-time masking: "correctly" masking out the time points when a grid box is TC-affected should give better estimates of the background moisture flow. However if the number of consecutive time points removed by masking gets too large (a common phenomenon with large radius schemes) and the filtering kernel becomes filled with missing values, the low-pass timeseries representing the background fluxes will be poorly estimated and can easily be contaminated by spurious variations near the missing sections. Enlarging the filtering window size can only help to a certain extent, as a too large kernel will lose track of variations in the underlying background flow. Finally, anomalous circulations associated with a TC may already be significant prior to the TC's approach , and may persist for some time after the TC dies away. In such cases the captured TC-fluxes will be incomplete based on the third principle. However, the incompleteness does not necessarily lead to low-biased overall estimate, as both the moistening and the drying flows may get underestimated.

A sequence of coastal boxes are first selected from ERA-I's land-sea-mask data, covering the coasts of Washington State in the northwest corner, down to the Mexican coasts in the south, the entire Gulf of Mexico, then up to Maine in the northeast (See the blue boxes later in Fig. 6.2). With the $0.75 \times 0.75°$ horizontal resolution of ERA-I, a grid box has a typical length of $70\,km$ at this latitude, and a total of 276 coastal grid boxes are identified. The collection encompasses all the equator-ward facing coastal lines of the North American continent, and the east- and west- ward sides where mid-latitude zonal flows are significant.

The inclusion of the latter helps quantifying the proportion of onshore moisture transport by TCs.

From HURDAT2 the TC events in the study region ($15-55°N$, $40-130°W$) that ever reached storm intensity (maximum sustained wind speed reaching $34\,knot$ or above) are selected. Following the movement of each TC, coastal grid boxes that are within a certain threshold radius are regarded as affected by the TC, and a label is attached to that grid box at that time point. Care has been taken to avoid duplicate labels when more than one TC is present. These labels separate the spaio-temporal coordinates affected by TCs and can then be applied onto a variable of interest, e.g. moisture fluxes. Whenever a non-synoptic hour in HURDAT2 is encountered, an additional record is inserted into the ERA-I fluxes via linear interpolation between the synoptic hours that encompass that time point.

To implement the first principle, the TC-related flux is detected from the column integrated zonal (F'_u) and meridional (F'_v) flux anomalies, which are obtained by subtracting the 34-year climatology of that 6-hour value. A background anomaly flow timeseries (F'_{ub} and F'_{vb}) is estimated by taking the timeseries of flux anomalies at a grid cell, replacing the TC-affected time points by zero anomalies, and applying a low-pass filter. The filter used is a Gaussian-weighted filter such that the amplitude of variations on 21-day timescales is reduced by half, while faster variations are reduced much more and slower variations much less:

$$\begin{cases} F'_{ub}(t) = F'_{u0}(t) * g(t;\sigma) \\ F'_{vb}(t) = F'_{v0}(t) * g(t;\sigma) \end{cases} \tag{6.2}$$

where F'_{u0} and F'_{v0} are the 0-replaced flux anomalies, $g(t;\sigma)$ is the Gaussian kernel to be convolved with. The scale parameter σ is determined using:

$$\sigma = T_{1/2}\sqrt{\frac{ln2}{2\pi^2}} \tag{6.3}$$

where $T_{1/2}$ is the period at which response amplitude is reduced by 50%, which in this case is set to three weeks. The choice of 21 days covers the lifetime of the majority of Atlantic TCs (*Bengtsson et al.*, 2007).

The preference of a Gaussian filter over a box-car filter is that the flux anomaly can have abrupt pulses under the impact of a TC, which can generate step-like changes in the box-car filtered low-pass flow prior to and after the TC incident,

due to the equal weights within the filtering kernel. The decision of replacing TC-affected time points with 0s is a compromised balance as disscussed above: removing these points can help improve the resultant low-pass flow but is susceptible to spuriousness due to too many missing values. If during a certain time period the majority are regarded as TC-affected, then it is justified to set the background flow anomaly to zero so that all the anomalous flux is attributed to TCs. However this will hamper the ability of background flow filtering to reduce the type I error. The technique is not perfect and uncertainties are expected.

After subtracting the background flow, the TC-related moisture flux is defined as the residual flux when a TC is nearby within a certain radius. Distances are computed as the great-circle distances, and four different schemes are explored to define this critical radius:

1. Scheme 1: Fixed radius in the NW, NE, SE and SW quadrants. Four distances were tried to test the sensitivity of the results: 300, 500, 700 and 900 km.
2. Scheme 2: The maximum 34 kt wind radii in all four quadrants through the life time of a TC, scaled by a scaling factor. Three scaling factors were considered in the sensitivity test: 2.0, 3.0, and 4.0.
3. Scheme 3: The maximum 34 kt wind radii in the corresonding quadrant through the lifetime of a TC, scaled by a scaling factor of 3.0. For example, if a coastal grid box is to the NW of the TC center, then the critical radius is 3 times the maximum 34 kt wind radii in the NW quadrant.
4. Scheme 4: The 34 kt wind radii in the corresonding quadrant at the corresonding time, scaled by a scaling factor of 3.0. For example, if a coastal grid box is to the NE of the TC center, then the critical radius is 3 times the NE 34 kt wind radii of the TC at that time point.

Going from Scheme 1 to 4, greater degrees of flexibility and adaptibility are incorporated: Scheme 1 applies a fixed radius to all TCs regardless of their differences in size, shape and temporal evolutions. The use of wind radii (the distance from the TC center where wind speeds remain at 34 kt or above) from HURDAT2 best track provides an observational basis for the radius definition that can vary according to the maximum size reached by each TC (Scheme 2). Scheme 3 extends this with quadrant dependency to account for shape asymmetry of TCs. Scheme 4 is the most dynamic of all and allows the critical radius to change over the lifetime of the TC according to observations.

Note that the wind radii data from HURDAT2 are only available from 2004 onwards, during which missing values may be present, in which case a backward relaxation scheme is implemented: in Scheme 4 if the wind radius in a given quadrant at a given time is missing, relax back to the maximum of the corresonding quadrant (Scheme 3); If all values in a quadrant are missing, relax back to the four-quadrant maximum (Scheme 2). There is no simple relationship between the size and central minimum pressure of TCs (*Emanuel*, 2005; *Knaff et al.*, 2007; *Knaff and Zehr*, 2007; *Ren et al.*, 2007), therefore we didn't attempt to predict the wind radii to extend Schemes 2-4 back in time. Analysis using Scheme 1 is extended back to 1980.

6.3 Results

6.3.1 Overview of TC activities

Fig. 6.1 displays the tracks of all *Atlantic* TCs during May-Nov that came within $700\,km$ of the North American continent in each of three 10- or 11-year periods during 1980-2012. These TCs are selected from a subset that ever reached storm intensity (maximum sustained surface wind $\geq 34\,kt$) within the study region. There are broadly two preferred pathways of TCs, one into the Gulf of Mexico from the Caribbean Sea and the other steers along the Gulf stream and recurves northeast ward (see also *Konrad and Perry* (2010)). Many of the TCs that follow the latter path did not make landfall but rather grazed the coastline at some distance; whether these TCs will be regarded as relevant to onshore transport depends on the attribution scheme selected, their sizes and the distances offshore. Moisture exchanges across the western coast may be affected by Atlantic TCs that came from the Gulf of Mexico or eastern coast, or occasional TCs originating from eastern Pacific. Based on the TC occurrences the coastal lines of North America can be divided into three sections: the western coast, Gulf of Mexico and the eastern coast (detailed definition will be introduced later). The Greater Antilles islands (many small islands are not represented in ERA-I.) are burried in the TC tracks and can experience impacts from both pathways. These grid boxes are treated as a fourth section, although estimates of TC fluxes may have larger errors due to the coarse resolution.

Increased TC activities can be observed from the track plots in Fig. 6.1 as well as the TC number timeseries in Fig. 6.1d. A linear trend during 1980-2005 is

evident, although after that the trend levelled off. The year 1994 seperates a relatively quiescent decade before and an active decade after that, reflecting the Atlantic multi-decadal mode (AMO) (*Goldenberg*, 2001). On top of that, strong inter-annual variability can be observed, largely consistent with that found by *Nogueira and Keim* (2011).

Fig. 6.2 displays the tracks of two major hurricanes: Rita and Katrina in 2005, based on best track records. It is important that the TC locations from best track and ERA-I are consistent. To evaluate the positional difference between the two, we detected TC centers from ERA-I for these two TCs. The detection only takes into account the relative vorticity (RV) field (at model level 48, approximately 840 hPa) and locates RV maxima via a Difference of Gaussians blob detection algorithm. The results displayed in Fig. 6.2 suggest a good agreement between the two, and the offsets of RV-detected centers are typically a few tens of kilometers, which is about the scale of ERA-I's horizontal resolution and relatively small compared to a typical TC detection radius (will be introduced later). However, this preliminary offset estimate may underestimate the errors found in earlier years (*Jourdain et al.*, 2014).

The distribution of 34 kt wind radii from best track is shown in Fig. 6.3. Consistent for all four quadrants the distribution is highly skewed to the right, with the maximum radii reaching up to 1185 km in the SW quadrant. As the detecting Schemes 2 to 4 favour maximum radii (Scheme 4 may relax back onto maximum radii in cases of missing values), these large radii records can lead to far-reaching TC influencing circles. The majority of the TC records have a 34 kt wind radii below 500 km, and the median value is 166 km in NW, 222 km in NE, 148 km in SW and 185 km in SE quadrant, respectively. There is a slight shape asymmetry with the eastern quadrants stretched further than the western half, consistent with literature (*Price et al.*, 1994; *Liu and Chan*, 1999; *Jourdain et al.*, 2014). Taking into account the cyclonic TC circulation and southeast-ward facing coastal line where TCs make landfall, this asymmetry may create a more extensive onshore transport branch than the offshore branch.

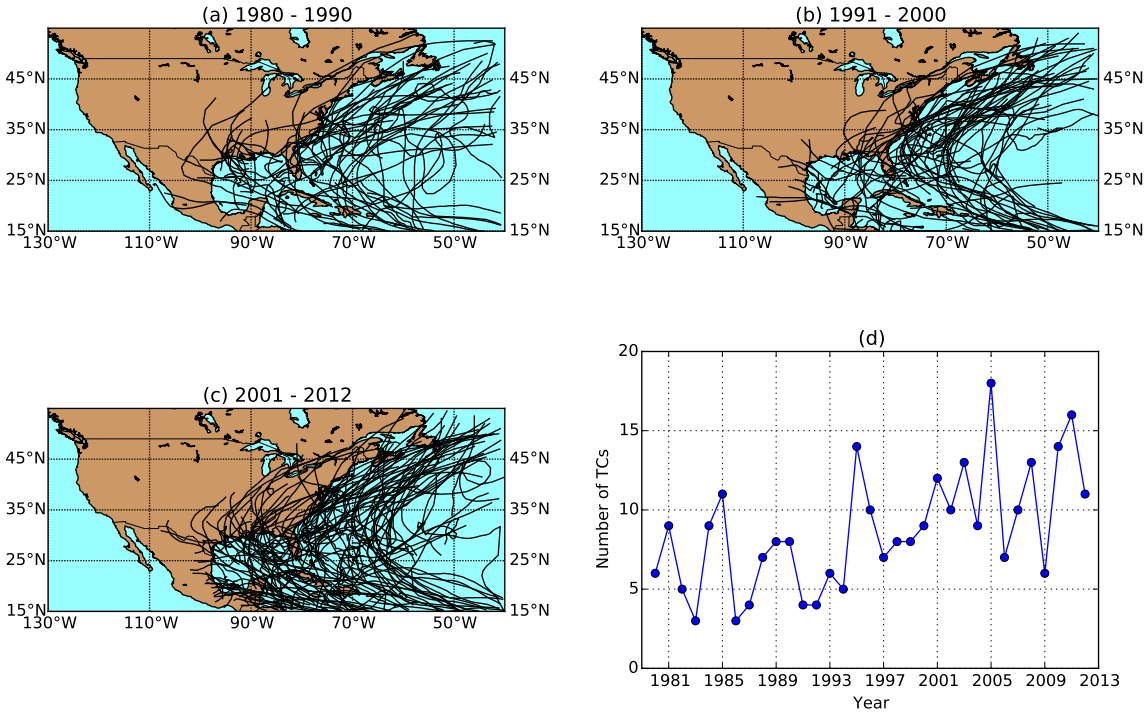

Figure 6.1: Atlantic TC tracks during (a) 1980-1990, (b) 1991-2000 and (c) 2001-2012 that reached storm intensity (maximum sustained surface wind $\geq$ 34 kt) within the study region and came within 700 km of the North American coast. (d) The number of TCs identified using the above criteria in May-Nov each year.

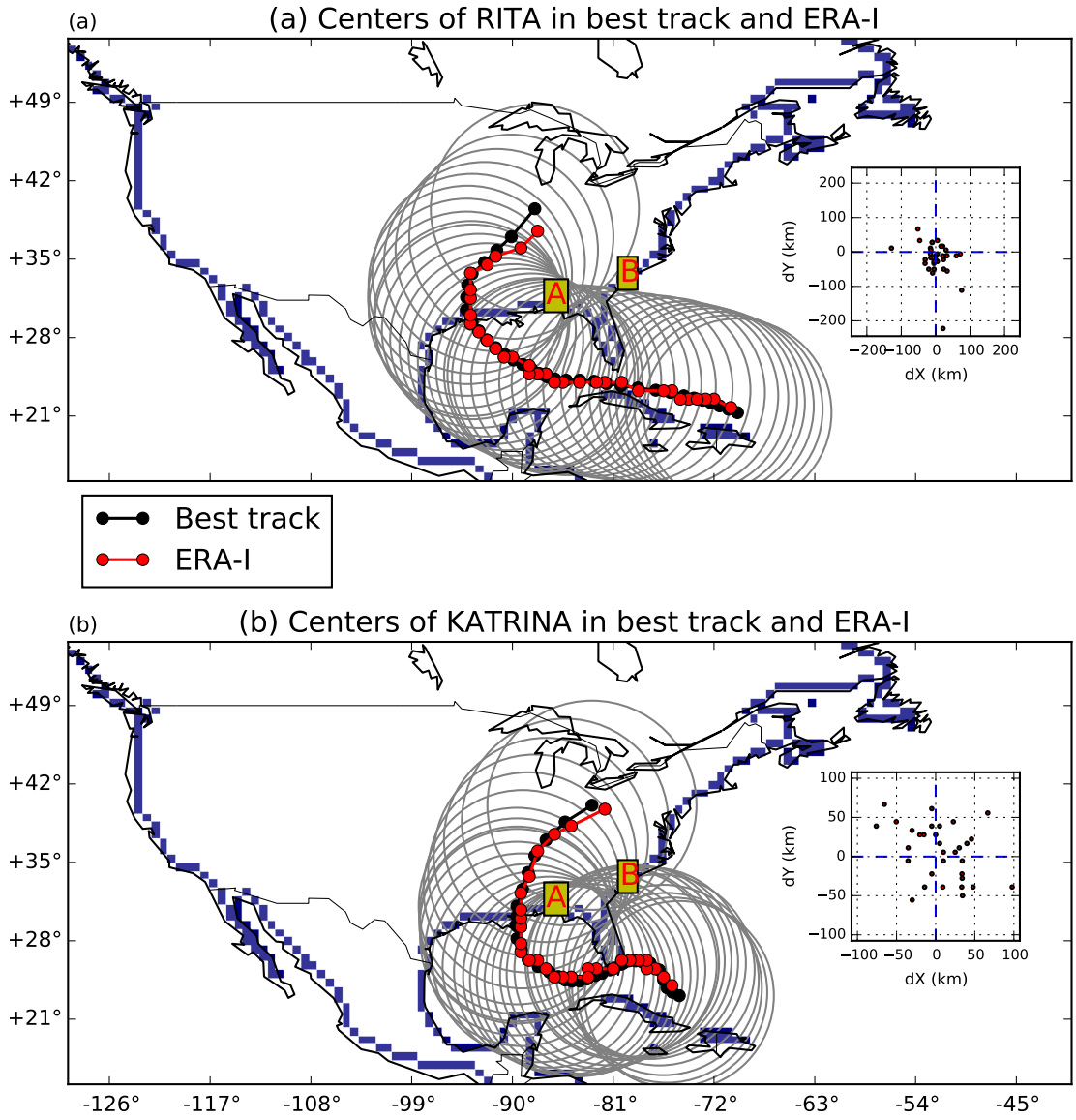

Figure 6.2: Coastal grid boxes of the North American continent and sample TC tracks. The coastal boxes defined from ERA-I land-sea-mask in the study region are plotted out in blue. The best track locations of TC Rita are plotted in black in (a) and Katrina in (b), both events occurred in 2005. The corresponding TC centers detected from relative vorticity maxima (at model level 48) using a Difference of Gaussians blob detection algorithm are plotted in red. A 900 km fixed radius circle is plotted following the movement of best track TC centers. The inset plots display the differences (in km) between the best track and blob detected TC centers, by centering the former at the origin. Two sample grid boxes are labelled on the map: A (31.0°N, 87.0°W) and B (33.0°N, 80.4°W).

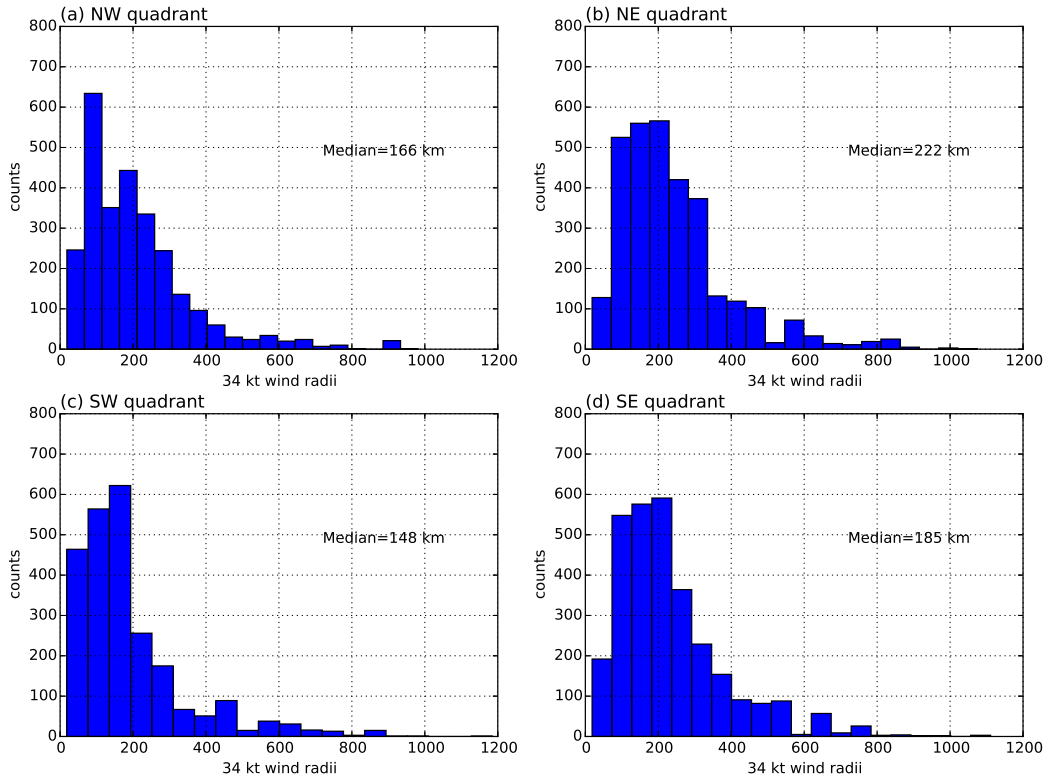

Figure 6.3: TC 34 kt wind radii distribution in four quadrants, for all Atlantic TC records within the study region of $15-55°N$, $40-130°W$ that reach storm intensity (maximum sustained wind speed $\geq 34\,kt$) during 1980-2012. The distribution in the NW, NE, SW and SE quadrant is shown in subplot (a), (b), (c) and (d), respectively.

6.3.2 TC flux attribution

The effectiveness of TC flux attribution is first tested on two sample grid boxes: box A at 31.0°N, 87.0°W in the Gulf of Mexico section, and box B at 33.0°N, 80.4°W in the eastern coast section (both labelled in Fig. 6.2). Nine different attribution schemes are tested and the setups are listed in Table 6.1. The fixed radius scheme (Scheme 1) includes 300 km and 500 km radii, covering the range many precipitation attribution studies have adopted (*Dare et al.*, 2012), and extend further to include 700 km and 900 km, to cover the possibly larger response areas in wind than in precipitation. Three scaling factors are applied to Scheme 2 to test the sensitivity to symetrical sizes. And Scheme 3 and 4 with a scaling factor 3.0 are included to test the sensitivity to shape asymmetry and size evolution during a TC's lifetime.

Table 6.1: TC flux attribution schemes. First column shows the detection schemes as introduced in Sec. 6.3.2. Second column lists the parameter, either a fixed radii for Scheme 1, or the scaling factor for Schemes 2-4. Column three indicates whether the scheme is retained for subsequent analyses.

Scheme	Parameter (radii or scaling)	Retained for subsequent analysis
1	300 km	No
1	500 km	No
1	700 km	Yes
1	900 km	Yes
2	2.0	Yes
2	3.0	Yes
2	4.0	Yes
3	3.0	Yes
4	3.0	Yes

The 2005 timeseries of meridional column-integrated moisture flux anomaly at box A is shown in Fig. 6.4 as the black curve. Based on Scheme 1 with a fixed 900 km radii (horizontal shaded band d in Fig. 6.4), the time points when a TC (or multiple TCs) is nearby are marked as dark green shading. Therefore the five most prominent spikes induced by TC Arlene, Cindy, Dennis, Katrina and Rita are correctly attributed. These abrupt pulses are all positive in sign, as the relevant TCs all passed to the west of box A (e.g. Katrina as shown in Fig. 6.2). Tammy (Oct-5 - Oct-7) induced a negative flux anomaly, as it approached the sample box from the east, before recurving southeast wards (not shown).

With these TC-affected time points replaced with zeros, the 21-day Gaussian filter generates an estimated background anomaly flow (red curve in Fig. 6.4).

Also included are the estimates from a box-car filter (blue line) and the same Gaussian filter (green line) on the original anomaly time series (not zero-replaced). All three estimates are based on scheme-1-radii-900. These three filters give largely consistent estimates during the TC-free periods, but show considerable differences in the vicinity of TCs. The box-car filter creates step-like changes before and after Katrina and Rita, suggesting insufficient resilience to abrupt changes. On the other hand, were the TC-affected fluxes not replaced with zeros, the Gaussian filter also gives an unsatisfactory result (green line). It is worth noting that the estimated background flow will be different if a different detection scheme is used, and so will the deviations from it that are attributed to TCs.

Despite the successful attribution of the five major TCs by the fixed 900 km scheme, the other two cases, Ophelia and Wilma, lack an obvious response in the flux, and therefore are likely to be false detections. This is because the fixed 900 km radius goes beyond the actual influencing extent of these TCs. When reduced to 700 km (shaded panel c in Fig. 6.4), the two false detections are eliminated. Further reduction in the radius starts to induce false negative errors, for instance the fixed 500 km (panel b) and 300 km (panel a) schemes fail to detect Rita, and other major TCs are detected for too short a duration.

Similarly, among the three wind radii based Scheme 2 setups (Scheme 2 with scaling factors of 2.0, 3.0 and 4.0, correponding to panel e, f and g in Fig. 6.4, respectively), a large scaling factor inflates the detecting radius of the grid box and tends to pick up faraway TCs whose influence cannot be discerned in this grid cell. Such errors are evident in the scheme-2-scale-4.0 case (panel g), which falsely detected a few periods when notable flux responses are lacking.

The more adaptive schemes (scheme-3-scale-3.0 in panel h, and scheme-4-scale-3.0 in panel i) create some closely spaced narrow and intermittent bins in the TC time shading (Fig. 6.4). This is a combined result of the movement of the TC and time-varying detecting radius, which can be dramatic between 6-h intervals (*Konrad et al.*, 2002). At least in this illustrated case the extra adaptibility does not provide much added value to attribution accuracy, as the underlying flux shows even more temporal coherency than the frequently alternating detecting bins. This also demonstrates the inherent deficiency of the binary, distance-based detection method in general.

Fig. 6.5 illustrates the attribution of zonal moisture flux at grid box B. Different to box A, the green curve shows the Gaussian filtered time series after the

shaded TC time points have been masked (effectively treated as missing), and the background flow estimates are based on Scheme 2 with scaling factor 4.0 (panel g in Fig. 6.5). Large differences are observed in the estimated background flows during late Aug-Sept, when the green curve shows spuriously high values, due to the 2-day gap between the masked values of Katrina and Ophelia. Remembered by its very erratic and slow moving track, Ophelia lingered for a long time along the eastern coast at storm and hurricane intensities. Such long-lasting effects post a big challenge to background flow estimates, as can be seen in the box-car filter (blue curve). In such cases, replacing the TC time points with zeros help create a better estimate (red curve).

Although false positive errors are found in the scheme-2-scale-4.0 scheme at box A, it is able to pick up some TC impacts at box B that other schemes failed to, for instance the full extent of Franklin, Katrina and Ophelia (when Maria and Nate may also contribute). The correctness of the Irene and Rita attribution may be controversial (though they are accompanied by brief spikes of on and offshore moisture transport), and the length of Wilma seems to be overestimated. However, this examination of individual grid cells is ad hoc, and fine-tuning a specific scheme may overfit the selected sample and lose generalizability. Therefore scheme-2-scale-4.0 is retained for subsequent analyses. But we exclude scheme-1-radii-300 and scheme-1-radii-500 from the selection, as both being too conservative. Again the highly variable scheme-3-scale-3.0 and scheme-4-scale-3.0 detect intermittent TC effects during Dennis and Katrina. They seem to improve the detection accuracy compared with their symmetrical counter-part (scheme-2-scale-3.0 scheme), by eliminating Irene from detection, but the omission of Franklin and earlier part of Wilma is arguable. These two schemes are also retained in the ensemble.

It is worth noting that at both box A and B, no scheme is able to fully capture the finishing stage of Katrina and Ophelia (Fig. 6.4, 6.5), even for the most expansive scheme (scheme-2-scale-4.0). And in the case of Tammy the schemes do not attribute the large negative (positive) zonal anomalies before (after) Oct-5 and Oct-6 (Fig. 6.5). This is because the lifetime of these TCs are defined by best track records, and the TC had either not existed before significant precedent flow occurred, or already died away before the strong flow anomalies dissipated. Relating back to the earlier discussion, these precedent and aftermath effects are not included and it is largely a subjective choice. However, enlarging the detection radius would be biased because the precedent effects would more likely be captured than the aftermath effects.

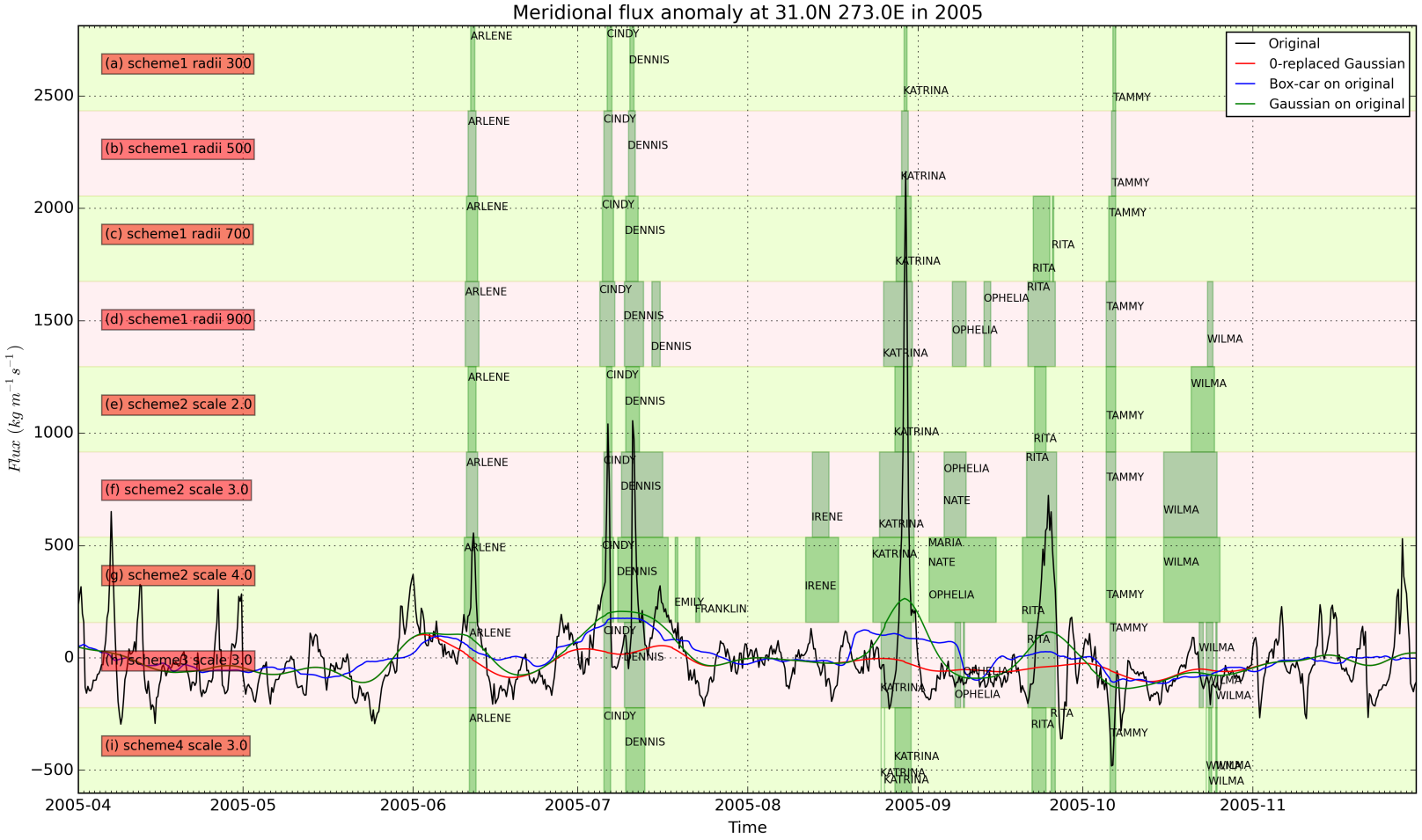

Figure 6.4: Illustration of the TC flux attribution at a costal box at 31.0°N, 87.0°W (A in Fig. 6.2). The black line shows the time series of column integrated meridional moisture flux anomalies (in $kgm^{-1}s^{-1}$) during April - Nov 2005. Red line shows the estimated background flow by applying a Gaussian filter after the TC-affected time points are replaced with zeros (using Scheme 1 with fixed 900 km radius). Blue (green) line is the result of a box-car (Gaussian) filtering with a kernel size of 21 days on the original time series. Each horizontal band of pink or green background shading shows a different radius definition scheme, from Scheme 1 with fixed 300 km radius at the top, to Scheme 4 with a scaling factor of 3.0 at the bottom. They are labelled on the figure. Within each scheme band, time points when this grid box is deemed as TC-affected are shown by dark green shading, with the relevant TC names labelled nearby.

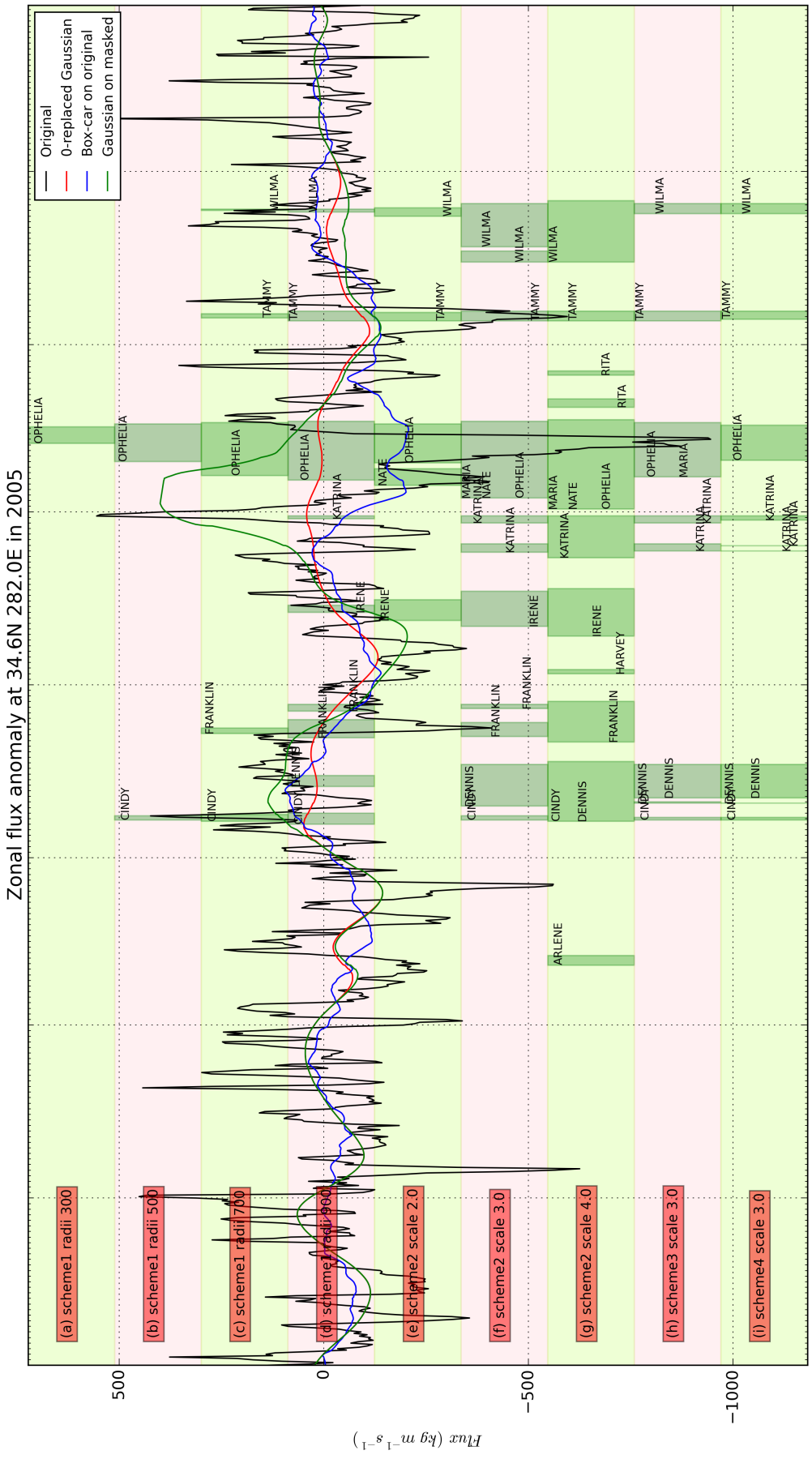

Figure 6.5: Same as Fig. 6.4 but for the zonal flux at grid box 33.0°*N*, 80.4°*W* (B in Fig. 6.2). And the estimated background flows are based on scheme 2 with scaling factor 4.0. Also note that the green line shows the low-pass by a 21-day Gaussian filter with TC-affected time points masked.

6.3.3 Spatial distribution of TC onshore transport

Following the discussion on the two case studies in the previous section, we included seven detection schemes in the ensemble collection (Table 6.1) and performed TC and non-TC flux separation for each coastal grid box using difference schemes. TC-related moisture flux is defined as the difference between the full flux anomaly and the background flow anomaly during the green-shaded time points. The same separation procedure is also repeated on the immediate oceanic grid boxes, whose fluxes, together with those from the adjacent land boxes, are used to compute the mean onshore flux F_u and F_v by averaging the two. The onshore moisture transport is computed as the negative of the dot product of the onshore flux and the relevant coastal length vector:

$$\begin{cases} T_{ui} = -\mathbf{F_{ui}} \cdot \mathbf{dy_i} \\ T_{vi} = -\mathbf{F_{vi}} \cdot \mathbf{dx_i} \end{cases} \tag{6.4}$$

where T_{ui} and T_{vi} are the TC onshore transport (in kg/s) at grid box i in the zonal and meridional direction, respectively. $\mathbf{dy_i}$ and $\mathbf{dx_i}$ are the meridional and zonal length of the grid box, with the vector direction pointing outwards from land. The negative sign implies net onshore transport has positive values, and vice versa. Note there exists a slight difference between the northern and the southern boundaries of a grid box, due to the shrinking latitudinal circles towards the pole.

To help portray the spatio-temporal distribution of TC moisture transport, the coastal grid boxes are numbered, sorted and segmented so that number 0 - 92 covers the western coast (plotted in green in Fig. 6.6 and Fig. 6.7), 93 - 166 for the Gulf of Mexico (including Florida, in yellow), 167 - 252 for the eastern coast (in orange) and 253 - 275 for the Greater Antilles (in brown).

Fig. 6.6 shows the TC moisture flux distribution during 2005 using the scheme1-radii-900 scheme. The western coast is mostly free from Atlantic TC influences, which is also observed in many other years (not shown). Much of the TC induced moisture exchange occurred in the Gulf of Mexico section, within which 17 TCs made landfall in 2005. A few TCs steered along the eastern coast and induced some onshore transport along the coast of North Carolina, South Carolina and Pennsylvania during Sept and Oct (grid cells 167 - 190). Previous studies have suggested inter-annual variations in prefered TC tracks,

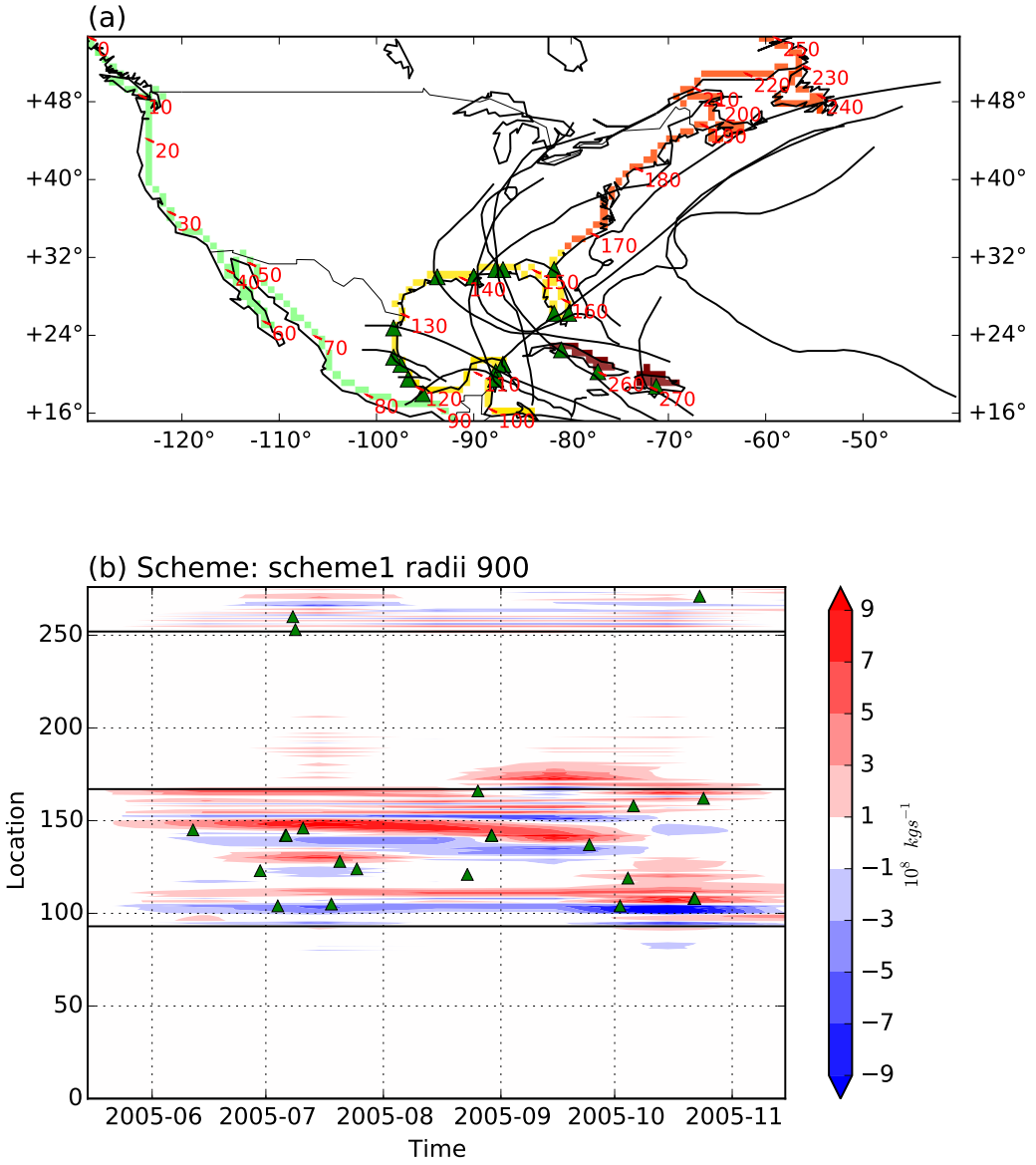

Figure 6.6: Spatio-temporal distribution of TC onshore fluxes (in $10^8\,kgs^{-1}$) during May-Nov 2005, using scheme1-radii-900. (a) gives a geographical reference of the coastal line, relevant TC tracks and their landfalling locations (if any, marked using a green triangle). The coastal boxes are numbered and ordered to represent the western coast section (0 - 92, in green), the Gulf of Mexico section (93 - 166, in yellow), the eastern coast section (167 - 252, in orange) and the Greater Antilles section (253 - 275, in brown). (b) shows the time-location distribution in a hovmoller plot, with TC onshore fluxes aggregated over calendar months. Horizontal solid lines indicate section boundaries, therefore the panels from top to bottom are the Greater Antilles, eastern coast, Gulf of Mexico and western coast, respectively. Landfalling locations are also marked (triangles) on the hovmoller plot.

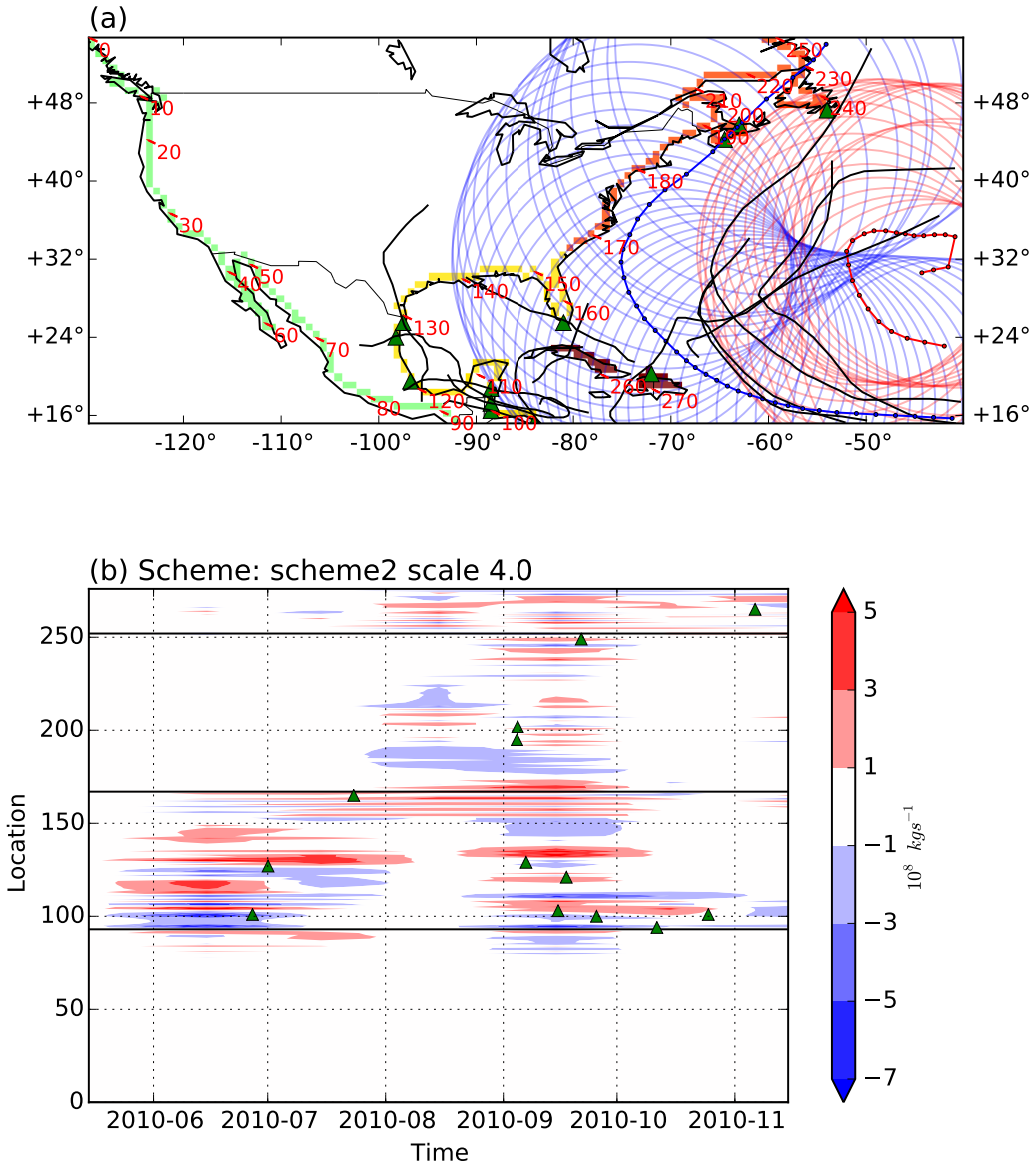

Figure 6.7: Same as Fig. 6.6 but for year 2010 using scheme2-scale-4.0. The tracks of TC Danielle and its 2667 *km* radii (after scaling by 4.0) are plotted in red, and Igor with its 3333 *km* radii (after scaling) are plotted in blue.

and 2005 witnessed more landfalls and tracks in the Gulf of Mexico and west of the Appalachian Mts, compared to 2004 when more TCs visited the Atlantic coastal plains east of the Appalachian Mts (*Brun and Barros*, 2014). Similar Gulf versus Atlantic differences are also reported in *Konrad and Perry* (2010), and are subject to influences from ENSO, Quasi-Biennial-Oscillation (QBO) and North Atlantic Oscillation (NAO) (*Gray*, 1984; *Pielke and Landsea*, 1999; *Dailey et al.*, 2009; *Kim et al.*, 2009).

In addition to moistening, TCs also have a drying effect that takes moisture away from the continent, usually by the western or southern branch of the spiral bands. Within the Gulf of Mexico section, this particularly active year had two long-lasting moisture export/import zones that span 5 - 6 months, one on the Yucatan Peninsula of Mexico and the other covering Florida. The export zones are located to the south/west of the import counter-parts, with the TCs travelling between (indicated by the landfalling locations in Fig. 6.6). This is consistent with the cyclonic circulation and the broad orientation of the coastal lines.

Due to the coarse resolution, small geographical area and island nature of the Greater Antilles, the flux response is very noisy.

The fixed 900 km scheme, although inflexible, constrains the TC's influence to a reasonable extent. When scaled by a large factor (e.g. 4.0), the scheme that picks the maximum wind radii of a TC can become very expansive for those large TCs. Fig. 6.7 shows the distribution of TC-fluxes during 2010 detected using scheme2-scale-4.0 scheme. Similar to the 2005 case, the Gulf of Mexico houses most of the TC-fluxes, however part of these may be falsely detected. Fig. 6.7a highlights two TCs that have relatively large sizes. After scaling by a factor of 4.0, Danielle's radius of influence goes up to 2667 km, and Igor's goes up to 3333 km, both are clearly overestimated and extend into the Gulf of Mexico. Consequently, distant fluxes, either onshore or offshore, are falsely attributed to TCs. As will be seen later, the overall effect is likely to be an overestimate of the offshore fluxes.

6.3.4 Coastally integrated TC onshore transport

The overall *Atlantic* TC contribution to continental scale onshore moisture transport is obtained by integrating along the coast lines:

$$T = \sum_{i=1}^{N} T_{ui} + T_{vi} \tag{6.5}$$

Applying the same computation to the absolute moisture flux (annual cycle plus anomaly) gives the total onshore transport onto the North American continent. The time series of TC and total onshore transport during the 2005 TC season are shown in Fig. 6.8.

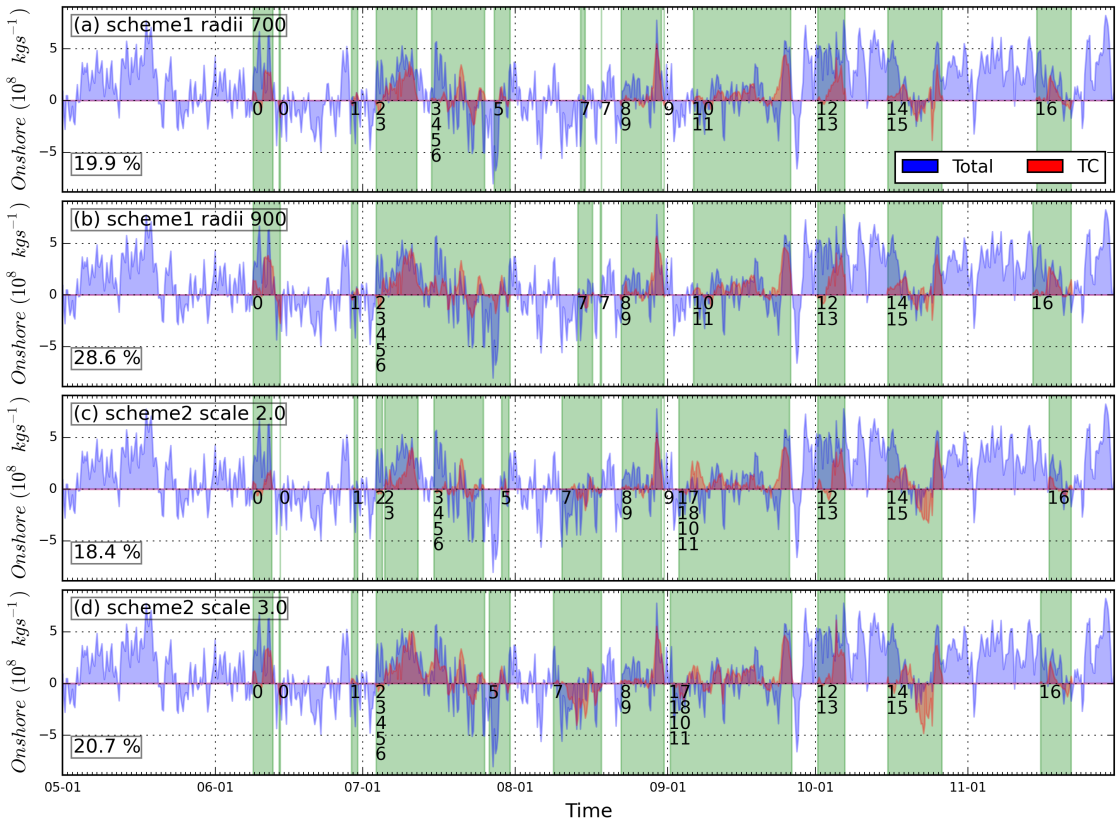

Figure 6.8: Time series of the total (blue) and TC-attributed (red) integrated onshore transport ($10^8\,kgs^{-1}$) during May-Nov 2005, by Atlantic TCs under (a) scheme-1-radii-700, (b) scheme-1-radii-900, (c) scheme-2-scale-2.0, (d) scheme-2-scale-3.0, (e) scheme-2-scale-4.0, (f) scheme-3-scale-3.0 and (g) scheme-4-scale-3.0 (see Table 6.1 for the schemes). The total moisture transport combines the annual cycle and anomaly fluxes. Time periods when any coastal grid boxes are affected by TCs are indicated by green shading, to which a numerical ID is attached for each relevant TC (the ID-name translation can be found in Table 6.2). The percentage contribution by TCs to the total transport is labelled at the lower left corner for each scheme.

Consistent with the results from the Section 6.3.2, a larger detection radius can

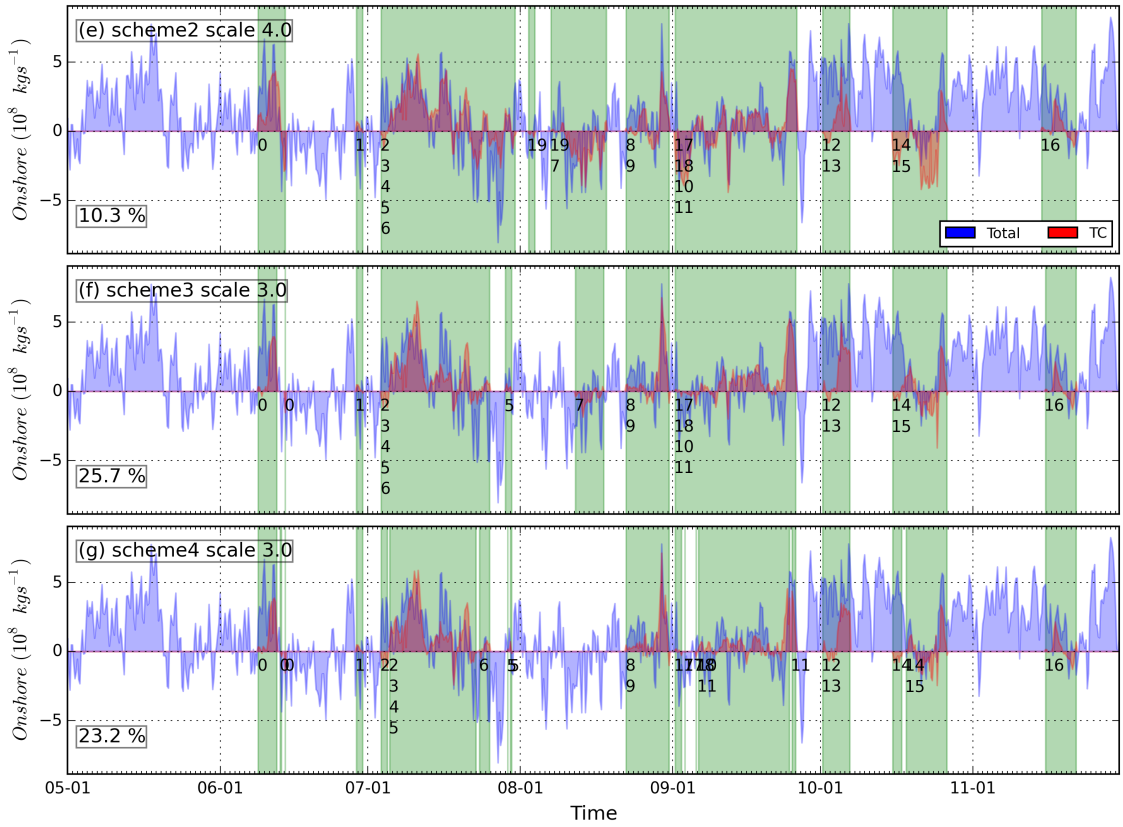

Figure 6.9: Fig. 6.8 continued.

pick up more distant TCs and create more long-lasting, continous TC transports, as indicated by the green shadings in Fig. 6.8. More adaptable schemes tend to create intermittent hits-and-misses in the TC impact detection, as in the case of scheme-4-scale-3.0 (Fig. 6.8g). Despite these differences, the detected TC moisture transports are largely consistent among schemes. The integrated total moisture transport that includes both annual cycle fluxes and flux anomalies are also shown. Note that the TC time series differ from the total time series by the sum of annual cycle and the estimated background flow, and the TC integration is over different subsets of spatio-temporal coordinates, therefore it is legitimate for the TC-related transport to be ocassionally larger than or opposite sign to the total transport.

In some cases the total onshore transport is dominated by TC effects, as during early July 2005 when TC Cindy, Dennis and Emily are present (Fig. 6.8, Table 6.2). The proportion is lower in more conservative schemes, but there is also an upper limit on the more aggressive schemes: a sensible background flow

estimation limits the highest TC flux estimate.

The occasional drying effect of TCs is indicated by the negative red filling in Fig. 6.8. In some cases, for instance during Oct-21 to Oct-25, this drying effect can overtake the total transport under some schemes (e.g. scheme-2-scale-2.0, scheme-2-scale-3.0 and scheme-2-scale-4.0). This is partly caused by the compensating fluxes across different coastal sections in the total transport integration, and the integration of TC fluxes usually takes only a confined coastal section where the signal is more coherent. The false attribution error discussed in the previous section may also contribute. Another factor is that annual cycle fluxes may work in the opposite direction to the anomalous fluxes, which will be discussed more later.

The seasonal onshore (offshore) moisture transport by either TCs or total fluxes are calculated by time-integrating the positive (negative) fluxes during the relevant time periods. The integrated amounts (in Eg, $1\,Eg = 10^{15} kg$) are shown in Table 6.2, and the percentage contributions from TCs are included in Fig. 6.8 and Table 6.2.

A total of $2.14\,Eg$ of water vapour was transported onto the North American continent from the western, southern and eastern coasts during May-Nov 2005, of which about 21 % was attributed to TCs (Table 6.2). The percentage varies from 28.6 % by scheme-1-radii-900, to 10.3 % by scheme-2-scale-4.0. This most aggressive scheme scored the lowest percentage because both the onshore and offshore transports are highest and the offshore amount is especially large in absolute amount. This large drying flow is most prominent during mid-Aug, early-Sept and mid-Oct (Fig. 6.9).

Repeating the costal integration using scheme-1-radii-900 over the study period of 1980-2012 gives an estimation of the TC moisture transport climatology, as shown in Fig. 6.10a. On average, September has the largest TC transport ($0.058\,Eg$), followed by August (0.047) and July (0.028) when the climatological annual cycle flux indicates net offshore transport (blue fillings in Fig. 6.10a). During the rest of the season, TC transport shows reduced intensity while the climatological annual cycle contributes much large quantities. Integrated across the entire season, *Atlantic* TC contributes around 13 % of total onshore moisture transport during May–Nov 1980–2012.

When quantifying the proportional contribution by TCs as shown above, we have used the total moisture transport as the denominator. Taking out the annual cycle component, the ratio of TC- and anomaly- onshore transport

gives a different view of the TC's contribution. Integrated over the very active 2005 season, the moisture transport by TCs detected by the scheme-1-radii-900 scheme constitutes 28.6 % of the total onshore transport (Fig. 6.10b, Fig. 6.8 and Table 6.2), and the percentage goes to 74.8 % if annual cycle fluxes are taken out. This high proportion of anomalous onshore flux is due to (i) the anomalous flux is mostly dominated by TC-fluxes during TC affected time periods, and (ii) the TC-induced flux is more systematically orientated as onshore, while the large compensating offshore flows are present in the total anomaly transport. As landfalling TCs are usually associated with enhanced precipitation on the left or right side of the track (*Konrad and Perry*, 2010; *Atallah et al.*, 2007), the air masses exiting the continent are more moisture-depleted. Lastly, during Oct-21 to Oct-25, the annual cycle flow is in the opposite direction to the anomalous flow (Fig. 6.10), which helps to create much larger (negative) TC-transport than the total transport as observed in Fig. 6.8.

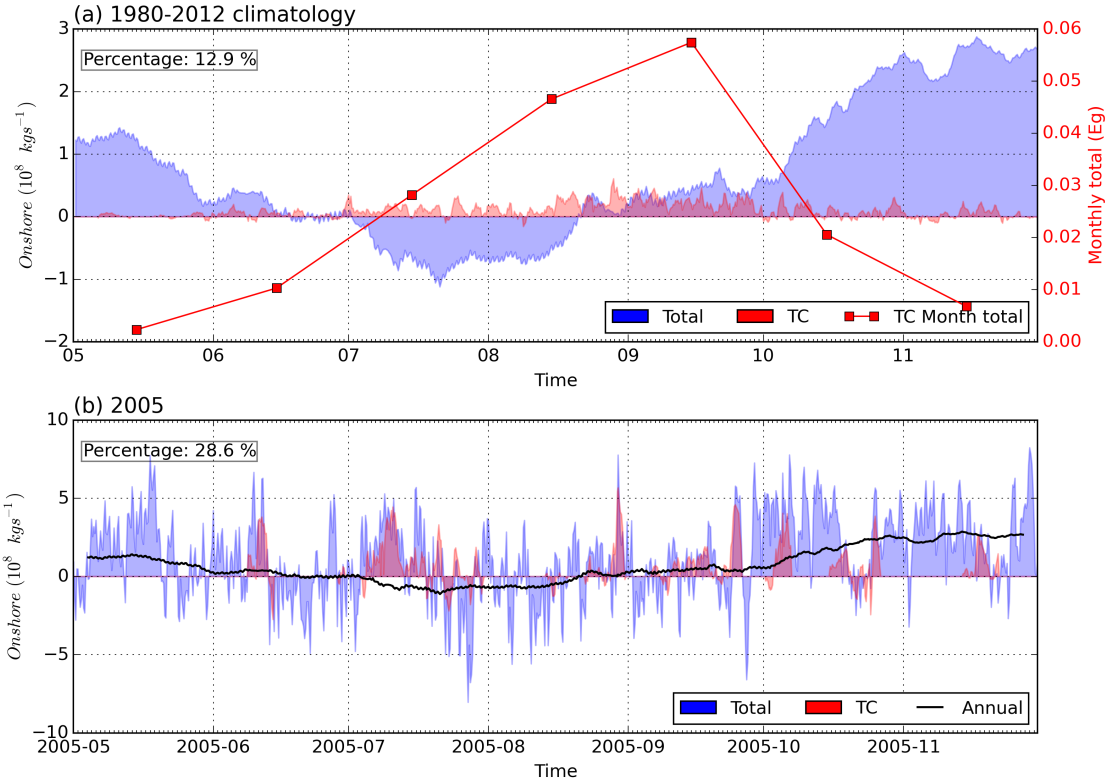

Figure 6.10: Coastal integral of moisture transport ($kg\,s^{-1}$) by Atlantic TCs (red) and the total moisture flux (blue), during May-Nov of the (a) 1980-2012 climatology and (b) year 2005. In both panels, the TC fluxes are computed using scheme-1-radii-900 scheme, and the total moisture flux includes annual cycle flux and flux anomalies. In (a), the monthly integral of TC moisture transport (in Eg) is plotted onto the y-axis on the right. The climatological annual cycle time series is smoothed by a 7-day filter, and the same time series is shown in (b) as the thick black line. The proportion of TC-transport to total seasonal transport is labelled at the top left corner in each panel.

Table 6.2: Seasonal onshore moisture transport (Eg) by TCs and total moisture flux during May-Nov 2005. The percentage contributed by TCs is obtained by dividing the net TC transport (column 4) by the net total transport (column 7). Names of the TCs labelled in Fig. 6.8 are given in the lower section of the table, with each TC ID associated with a name.

Scheme	TC positive (Eg)	TC negative	TC net	Total positive (Eg)	Total negative	Total net	TC percentage (%)
scheme-1-radii-700	0.55	-0.12	0.43	3.20	-1.06	2.14	19.9
scheme-1-radii-900	0.75	-0.13	0.61				28.6
scheme-2-scale-2.0	0.54	-0.15	0.39				18.4
scheme-2-scale-3.0	0.75	-0.31	0.44				20.7
scheme-2-scale-4.0	0.75	-0.53	0.22				10.3
scheme-3-scale-3.0	0.70	-0.15	0.55				25.7
scheme-4-scale-3.0	0.60	-0.11	0.49				23.2
Mean	0.66	-0.21	0.45	3.20	-1.06	2.14	21.0
TC ID	TC Name	TC ID	TC Name	TC ID	TC Name	TC ID	TC Name
0	Arlene	6	Gert	12	Stan	18	Nate
1	Bret	7	Irene	13	Tammy	19	Harvey
2	Cindy	8	Jose	14	Wilma		
3	Dennis	9	Katrina	15	Alpha		
4	Emily	10	Ophelia	16	Gamma		
5	Franklin	11	Rita	17	Maria		

6.3.5 Inter-annual variability in TC onshore transport

The previous section examines the TC onshore transport in 2005 and the 1980–2012 climatology. To investigate the inter-annual variation, the same computation is repeated for 2004–2012 for all schemes, and extended back to 1980 for the scheme1-radii-700 and scheme1-radii-900 schemes. To give a more thorough view of the total TC contribution, we also performed attributions to the East Pacific TCs using the scheme1-radii-700 and scheme1-radii-900 schemes, based on best track data from IBTrACS. Fig. 6.11 shows timeseries of seasonal onshore transport in total and the component attributed to Atlantic and East Pacific TCs, and the corresponding TC percentage of the total net transport.

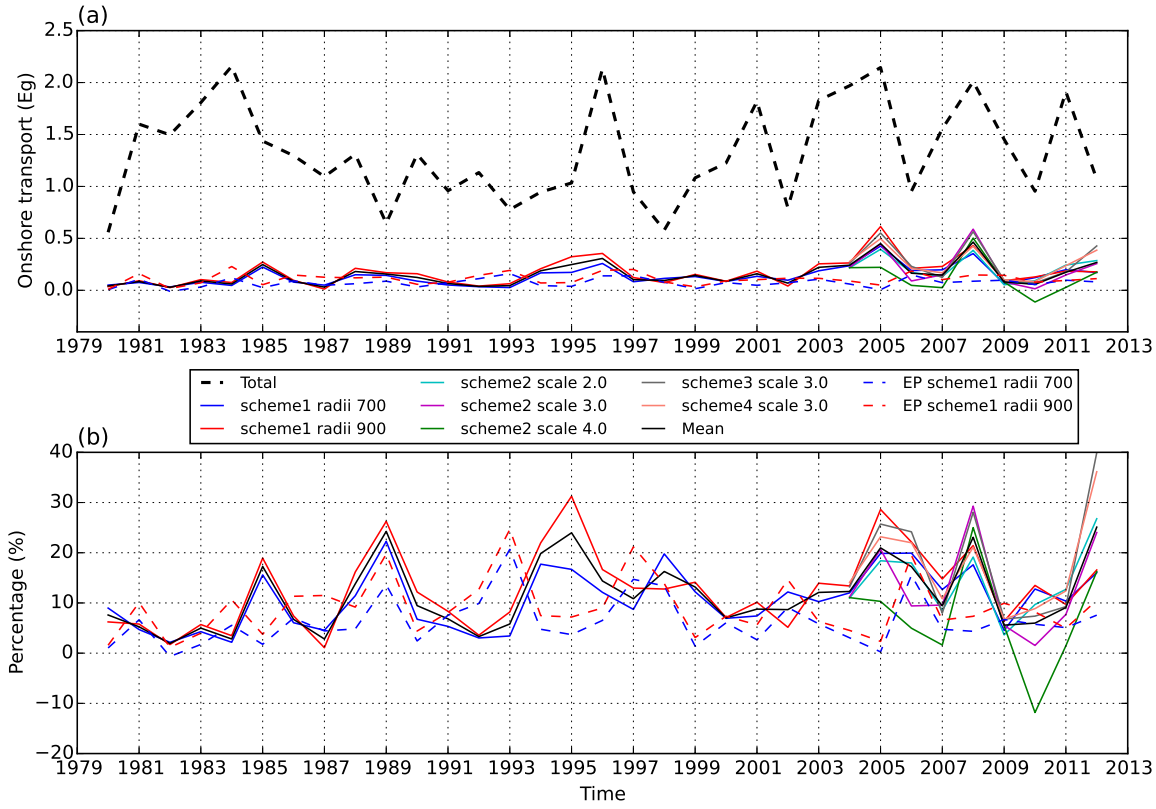

Figure 6.11: (a) Coastally-integrated seasonal (May-Nov) net onshore moisture transport (Eg) by the total moisture flux (thick dashed black line) and by fluxes attributed to TCs by the ensemble of schemes considered here. (thin colored lines). Schemes 2, 3 and 4 are restricted to 2004 onwards. (b) Percentage contribution of TCs to seasonal onshore transport accroding to each attribution scheme. In both panels, transports or percentages by East Pacific TCs attributed using scheme1-radii-700 (blue) and scheme1-radii-900 (red) are shown in long dashed lines.

Estimates from the full ensemble of attribution schemes are available during 2004 - 2012, within which good agreement is observed in 2004 and 2009. For the other seven years, there is a wide spread among them, typically 0.25 Eg but in 2005 the spread reaches 0.39 Eg (Fig. 6.11, Table 6.2). No scheme is always higher or lower than the others, but scheme2-scale-4.0 gives the lowest estimate for all years except 2008 and 2009, when it falls inside the ensemble range. In 2010 this latter scheme reports a negative net TC transport ($-0.11\,Eg$), likely caused by falsely attributed offshore fluxes discussed previously. Desipte the evident differences in the TC-attributed net transports, the schemes do agree on the years with greater or less TC transports. This is reflected in the significant correlations observed among all schemes during 2004–2012, with the lowest correlation being 0.64 ($p = 0.06$) bewteen scheme1-radii-900 and scheme2-scale-4.0, and highest correlation being 0.97 ($p < 0.01$) between scheme2-scale-2.0 and scheme4-scale-3.0. This suggests a consistent and robust inter-annual variability in TC transport that is relatively insensitive to the detection scheme.

During the period of 2004–2012, 2005 and 2008 stand out with large TC transport in both the absolute and percentage senses. Desipte the total transport in these two years being among the highest in the record, their percentage contributions still reach 21.0 % (ensemble mean, ensemble range is 10.3–28.8 %) and 23.1 % (ensemble mean, range: 17.6–29.3 %), respectively. Transports in 2007, 2009 and 2010 are lower than these two years by about 70 % to 87 % (based on ensemble means), and the 2010 mean is the lowest (0.06 Eg) during 2004–2012. 2006, 2011 and 2012 have moderate TC transport, with ensemble means of 0.16 Eg, 0.17 Eg and 0.27 Eg, respectively. These are mostly consistent with the variation in TC-attributed precipitation by *Brun and Barros* (2014). However, they identified 2004 as the most TC-impacted year during 2002-2011, exceeding 2005 despite the more activate major hurricanes in the latter. The difference was suggested to be related with the Atlantic versus Gulf of Mexico alignments of the storm tracks, where orographic effects can vary greatly correspondingly (*Konrad and Perry*, 2010; *Brun and Barros*, 2014). Here, moisture onshore transport is about 50 % lower in 2004 than in 2005 (Fig. 6.11). This discrepency illustrates that although a positive relationship is expected, the underlying processes of TC onshore moisture transport and precipitation are distinct (*Schumacher and Galarneau*, 2012). Responses of precipitation to TCs may vary substantially, which is controlled not only by the moisture plume advected by the TCs but also by interactions with extra-tropical features, including upper level divergence and

the presence of a front at the time of TC arrival (*Konrad and Perry*, 2010).

The use of fixed radii schemes allows the estimation to be made back to 1980. Scheme1-radii-700 and scheme1-radii-900 schemes report largely consistent TC onshore transport during 1980–2004 (Fig. 6.11), with a correlation coefficient of 0.96 ($p < 0.01$). The variability is also closely related to TC activity measurements, for instance a significant correlation ($R = 0.70$, $p < 0.01$) is found between the scheme1-radii-700 estimates and the TC number timeseries as shown in Fig. 6.1d, as well as with the Accumulated Cyclone Energy (ACE) index (shown in the next section and in Fig. 6.12). A weak increasing trend can be observed in both, although neither is statistically significant (by a Mann-Kendall trend test).

On average, 0.15 Eg (ensemble mean) of moisture, equivalent to 11.4 % (Table 6.3) of seasonal onshore moisture transport can be attributed to *Atlantic* TCs during 1980–2012, which is in good agreement with the precipitation percentages (10 % of Florida's annual rainfall (*Knight and Davis*, 2007); $4 - 15$ % of the South East US (*Rodgers et al.*, 2001; *Knight and Davis*, 2009; *Konrad and Perry*, 2010; *Prat and Nelson*, 2013)). The mean value for 1980–1994, a relatively quiet TC period (*Goldenberg*, 2001), is 8.8 %, and the mean for the more active 1994–2012 period is 14.1 %. However, the percentage variation is affected by both the TC-attributed and the total transport. The relatively high percentage values during the 1985–1995 decade are partly caused by lower total transport (Fig. 6.11). Similarly, the 2012 percentage in some of the schemes exceeds that in 2005, as the total transport is much lower in 2012.

Although not a focus of the study, we also give an estimation on the contributions by East Pacific TCs (Fig. 6.11, Table 6.3), using the two fixed radii schemes. In general, less moisture is transported by East Pacific TCs (7.8 %, Table 6.3) than by the Atlantic ones (11.4 %). However, in some cases the amounts are comparable, or even higher, such as in 1993 and 1997. Timeseries of the East Pacific TC transport have mixed positive and negative correlations with their Atlantic counter-parts during different periods, and overall no significant correlation is observed. With this component added, moisture transport by TCs from both basins constitutes around 0.24 Eg (19.1 % of total) during 1980–2012.

Table 6.3: Percentage (%) contribution to hurricane-season ocean-to-land moisture transport attributed to TCs according to period and attribution scheme. *: the 1980–2012 climatology is the weighted average of the two sub-periods including all schemes available: $(10.3 \times 24 + 14.3 \times 9)/33 = 11.4$.

	Atlantic	Atlantic	Atlantic	East Pacific
Scheme	2004–2012	1980–2003	1980–2012	1980–2012
Scheme1-700	14.0	9.4	10.6	6.3
Scheme1-900	16.3	11.3	12.7	9.2
Scheme1 mean	15.2	10.3	11.7	7.8
Scheme2-2.0	14.2	N/A	N/A	N/A
Scheme2-3.0	13.2	N/A	N/A	N/A
Scheme2-4.0	7.1	N/A	N/A	N/A
Scheme3-3.0	18.1	N/A	N/A	N/A
Scheme4-3.0	17.3	N/A	N/A	N/A
Mean over all schemes	14.3	10.3	11.4*	7.8

6.4 Conclusions and disscussion

6.4.1 TC onshore flux and its inter-annual variability

In this study we designed a range of distance-based schemes to quantify the TC-related moisture transport. A collection of multiple schemes is included to form an ensemble of estimates. Much as expected, TC-related moisture transports across the continental coasts correspond well with TC tracks, either around landfalling areas or along the Atlantic coast. The Gulf of Mexico coast and the eastern Atlantic coast housed the majority of influcencing TCs, and onshore (offshore) transport is typically observed on the right (left) side of the TC center. As the land usually experiences heavy precipiation in response to a TC's landfall, the air masses leaving the continent from the south-west side are more moisture depleted. Combined with slightly weaker winds on the western quadrants, the TC-related net moisture transport is more systematically orientated as onshore. After integration along the coast line, impacts from TCs can dominate the total onshore transport during affected periods.

Contribution from *Atlantic* TCs to seasonal onshore transport across the western, southern and eastern coasts of North American is around 11.4 % for the 1980–2012 period, and based on the TC activity and the total seasonal transport amount, the percentage can reach 25.1 % (ensemble mean in 2012). During 2004 - 2012, all ensemble members show largely consistent inter-annual varability, which is also broadly consistent with TC-related precipitation changes (*Brun and Barros*, 2014). Among the ensemble members, no scheme constantly produces higher or lower estimates than the others, but one attribution scheme (scheme2-scale-4.0) produces lower estimates in all but two years and this contributes strongly to an average ensemble spread of 0.25 *Eg* during 2004–2012. The latter scheme is perhaps the most "aggressive" one, taking the quadruple of 34 kt wind radii of a TC as the attribution threshold. This was shown to be an overestimate for large-sized TCs, and the overall effect is influenced more by the offshore flows, giving a lower net TC transport.

6.4.2 Uncertainties in the TC flux attribution

The size of a TC's impact area is a critical parameter in the attribution process, and giving an objective definition of the TC size is a difficult task (*Liu and Chan*, 1999). Several different definitions have been used in previous studies, including

the radius of the outer closed isobar (ROCI) (*Liu and Chan*, 1999; *Merrill*, 1984; *Konrad et al.*, 2002; *Konrad and Perry*, 2010), the radial extent of 15, 17 and 25 m/s winds (R-15, R-17 and R-25) (*Weatherford and Gray*, 1988), and radial extent of a threshold relative vorticity (*Liu and Chan*, 1999). A fixed 500 km radius has been commonly used in precipitation-TC studies (*Rodgers et al.*, 2001; *Larson et al.*, 2005; *Lau et al.*, 2008; *Jiang and Zipser*, 2010), or as a buffer zone for the landfalling TCs (*Nogueira and Keim*, 2011). Pilot tests on two sample locations suggest that the commonly used $500\,km$ impact radius is too conservative to capture the full extent of moisture flux responses. In fact, the same concern has been raised in relation to precipitation attributions (*Dare et al.*, 2012; *Rodgers et al.*, 2001). As the detection radius increases, so does the risk of false positive errors. In such cases, the removal of an estimated background flow can help reduce the error. However, the accuracy of the background estimation drops as the duration of TC's impact increases, which is a natural response to an inflated detecting radius. Incorporating extra flexibility into the detecting radius, by addressing shape asymmetry of TCs or their time varying sizes, has limited added value in improving the detection accuracy. The current method is a compromised balance and further improvements are needed. For instance, all distance-based attribution methods resort to a binary type detection strategy: a grid box at any time is either affected or not by a nearby TC, and can jump between the two states, either due to changes in the distance from a TC, or a different scheme is used. Instead a smooth kernel with decreasing weights, e.g. multivariate Gaussian, may help reduce the sensitivity to threshold radius definition, and the risks of false positive errors as well.

In the attribution process, the temporal extent has been restricted to the life time of TCs. This decision can lead to a scenario that significant anomalous flows are ignored because a TC has not yet fully developed (and not yet entered into best track records) or has already dissipated. Whether or not the preceding and aftermath flows should be associated with a TC is an ambiguous question and should always be made clear moving from one context to another. Some studies have identified precedent precipitation events (PREs) that are closely related to moisture transport prior to the arrival of a landfalling TC (*Galarneau et al.*, 2010; *Schumacher and Galarneau*, 2012). In some cases, these PREs lead the TC arrival time by 36 hours, or 1000 km poleward of the TC (*Galarneau et al.*, 2010). However, not every landfalling TC is associated with such PRE events. A robust detection scheme should have the flexibility to adjust to different situations, and ideally make the adjustment automatically. Therefore in future work, we

plan to perform sensitivity experiments by extending forward and backward in time from detected TC time points by an adjustable period of time (e.g. extend backward by 3 days to capture the moisture transport that supplies PREs).

To evaluate the uncertainties associated with misalignment of TC centers in ERA-I and best track, we performed a test by detecting RV maxima from the vicinity of two selected TCs. Although the results suggest overall good agreement with best track, the misalignment is likely to be underestimated for ERA-I. Using a similar detection method, *Jourdain et al.* (2014) reported increasing TC postional errors in ERA-I back to the 1980s, when compared with the records from International Best Track Archive for Climate Stewardship (IBTRACS). The largest offsets are around 180 km for the less intense TCs (see their Fig. 3). Assuming random directional distribution in the offsets, the uncertainty range due to reanalysis positional error could be similar to the differences between fixed 700 km and 900 km schemes. Considering the overall good agreement between the two (Fig. 6.11), this positional error is not contributing much to the estimation uncertainty.

Another source of error comes from the TC wind field in reanalyses. The maximum wind speed in the vicinity of TCs was found to be underestimated in magnitude (*Bengtsson et al.*, 2007; *Jourdain et al.*, 2014) but overestimated in its lateral extent (*Jourdain et al.*, 2014). For ERA-I, the bias of maximum wind speed is about $-9\,m/s$ for storms and $-27\,m/s$ for hurricanes. While the sizes of the TCs are overestimated by about $210\,km$ (*Jourdain et al.*, 2014). Both suggest a significant deficit in realistically depicting TCs by reanalysis products. The resultant uncertainty in the integrated moisture flux is difficult to estimate, as the latter is column integrated over the entire atmosphere not only the surface. Although it is heavily weighted towards the boundary layer, the moisture transport associated with TCs can extend up to the tropopause (*Schumacher and Galarneau*, 2012). Assuming the low biased wind speed and high biased radial extent are systematic within the troposphere, the combined effect is likely to be qualitatively similar to an overly aggressive attribution scheme (e.g. scheme-2-scale-4.0), which tends to give a lower seasonal transport.

6.4.3 Relationship with TC precipitation

In this study we attempted to quantify the ocean to land moisture transport directly related to TC activity. Like TC-related precipitation, this is a form of freshwater influx to the land so these two quantities should be positively

related but will not be identical because additional physical processes play a role in converting atmospheric moisture to precipitation. Firstly, enhanced precipitation due to a TC does not originate only from additional ocean-to-land water vapour transport: contributions may also be made from water vapour that is already present in the atmosphere before the TC approaches, from convergence of water vapour from land (*Schumacher and Galarneau*, 2012), and to a lesser extent from anomalous evapotranspiration during the passage of the TC. Secondly, additional moisture transport by the TC is favourable to enhanced precipitation but does not guarantee it. Hurricane Hugo in 1989 made landfall in South Carolina causing around one billion dollars of damage by its strong winds, but only produced modest rainfall (*Konrad and Perry*, 2010; *Cline*, 2002). On the other hand, not every heavy rainfall event coinciding with TCs can be attributed to TCs (*Konrad and Perry*, 2010; *Schumacher and Galarneau*, 2012). The timing, location, and magnitude of ascent associated with synoptic-scale features such as baroclinic zones and upper-level shortwaves are just as important in determining when and where heavy rain will occur (*Konrad and Perry*, 2010; *Schumacher and Galarneau*, 2012).

Lastly, the atmospheric moisture exchange across the coastline is relevant to the continental-scale water budget, but this moisture can then have two different fates. It can contribute to enhanced precipitation and return to the ocean via land runoff, but it could also leave the continent via atmospheric transport over another part of the coastline away from (and therefore not attributed to) the TC and/or after some time has elapsed and the TC has dissipated. Precipitation responses are relevant in both coastal and inland areas. Landfalling TCs and their associated rainfall generally weaken quickly due to the isolation of the inner core from the warm, moist ocean surface (*Ren et al.*, 2007; *Knight and Davis*, 2009; *Dare et al.*, 2012). Despite this general weakening, interactions with other synoptic systems (*Konrad and Perry*, 2010; *Dare et al.*, 2012), or local orography (*Brun and Barros*, 2014) may continue to produce rainfall further inland.

6.4.4 Relationship with ENSO and future work

It is of great importance to investigate the relations of TC moisture transport with well known modes of climate variability, including ENSO, NAO and QBO. As this is planned in a future work we will only give some shorter comments on the ENSO relationship here.

Previous studies have documented an ENSO influcence on Atlantic TC activity

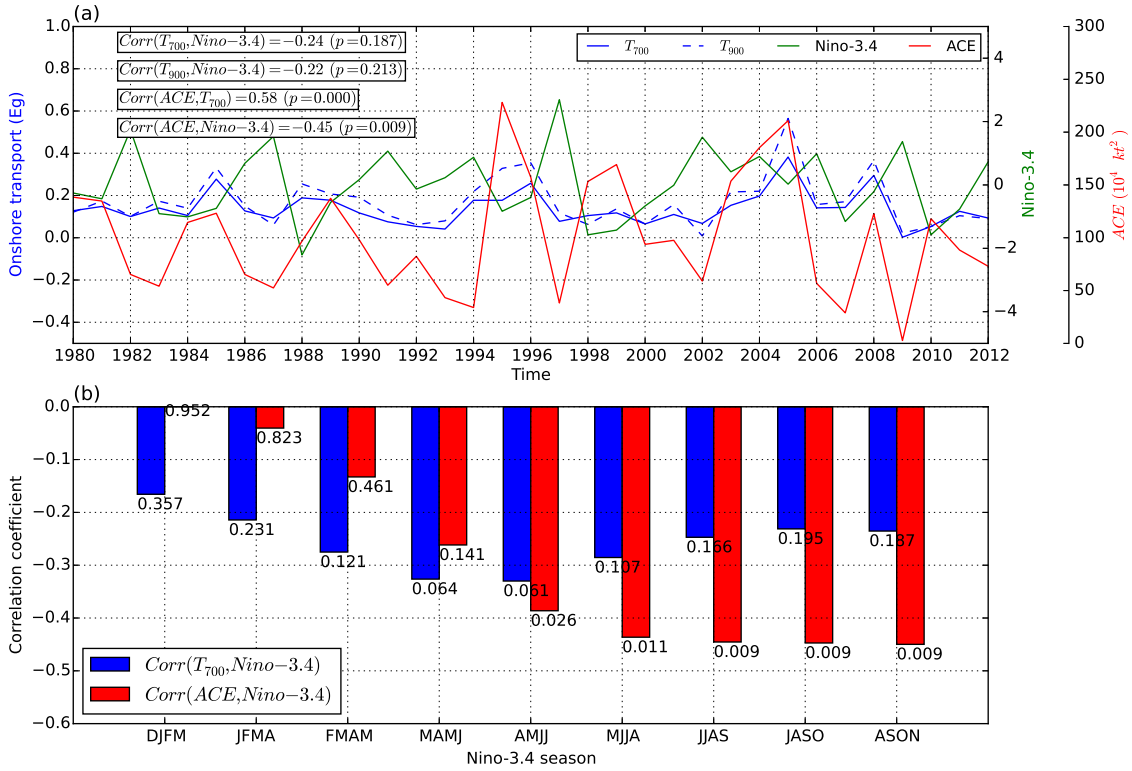

Figure 6.12: (a) Time series of seasonal TC onshore transport (Eg) during 1980 - 2012, detected using scheme1-radii-700 (T_{700}, blue solid line) and scheme1-radii-900 scheme (T_{900}, blue dashed line). The seasonal ACE indices ($10^4\,kt^2$) are plotted in red onto the rightmost y-axis. Seasonal average (Aug-Nov, ASON) Niño 3.4 indices are plotted in green onto the second y-axis from right. Linear trends in all time series have been removed. Some correlation results are shown at the top-left corner. (b) The blue (red) bars show correlation coefficients between the May-Nov seasonal T_{700} (ACE) and Niño 3.4 indices computed using different season definitions, ranging from the DJFM season prior to the TC season, to ASON during the later part of the same TC season. p values of the correlations are labelled correspondingly.

(e.g. *Gray* (1984); *Pielke and Landsea* (1999); *Goldenberg* (2001); *Smith et al.* (2007); *Bengtsson et al.* (2007)). Enhanced subsidence and vertical wind shear develop over the tropical Atlantic, in response to anomalous central/eastern Pacific warming during El Niños. Consequently, surpressed Atlantic TC activity is observed during warm years, and the opposite for cold years (*Gray*, 1984). This negative relationship bewteen TC activity (represented by ACE) and central Pacific SST (represented by Niño 3.4 index) can be observed in Fig. 6.12. Correspondingly one might expect a similar negative relationship between Niño 3.4 and the seasonal TC moisture transport. However, this relationship is much weaker and not statistically significant. Besides, there seems to be a time shift

bewteen these two relationships: ACE is most sensitive to the Aug-Nov (ASON) season Niño 3.4 SST ($R = -0.45$, $p = 0.01$, see Fig. 6.12a, b), while peak correlation with TC transport is observed in MAMJ Niño 3.4 index. This lack of correspondence is partially because, in addition to anomalous TC activity, effective onshore transport also requires properly aligned tracks, therefore landfalling locations in different ENSO phases need to be incorporated. *Smith et al.* (2007) noticed that despite generally enhanced TCs during cold years, there is little difference in the probability of hurricane landfalls in Florida or along the Gulf coast compared with neutral years, and these areas are most conducive to onshore transport as shown in our results. Lastly, the conventional El Niño versus La Niña way of looking at ENSO variability needs to be updated. Many studies have reported a systematic difference between an Eastern Pacific (EP) El Niño and a Central Pacific (CP) El Niño with distinct features in many aspects (*Kao and Yu*, 2009; *Kug et al.*, 2009; *Xu et al.*, 2015), including Atlantic TC activities (*Kim et al.*, 2009; *Wang et al.*, 2014). In particular, the CP El Niños were found to enhance Atlantic TCs in contrast to surpressing by EP El Niños (*Kim et al.*, 2009). Taking into account the observed increasing frequency of CP El Niños after 1990s (*Kim et al.*, 2009), greater complexity is added to the discussion on ENSO variability.

6.4.5 Concluding remarks about further applications

The TC moisture flux attribution method proposed in the study is designed to facilitate continental scale onshore moisture flux quantification, but can be tailored to country or basin scales to cater to different purposes, although suitable data and further improvements may be necessary. For instance, some systematic differences in the size of TCs have been documented (*Jiang and Zipser*, 2010) between ocean basins, and in particular TCs in the Atlantic typically have smaller sizes compared with those in NWP, SPA and IO regions. Therefore care should be taken in applying the methods to other basins.

Chapter 7

Conclusions and discussion

7.1 Key findings

This thesis assesses some important aspects of the atmospheric hydrological cycle in our modern day climate, including the climatological distributions and variations of precipitation, evaporation, the moisture budget and the horizontal moisture transports. These variables constitute key components of the climatic system, bridging the water and energy cycles, and thus their changes have global scale impacts. The most noteworthy findings of this study are summarised here.

7.1.1 Observations of atmospheric hydrology are still insufficient, unevenly distributed, and have homogeneity issues, biases and internal consistency deficiencies.

Chapter 2 identifies some deficiencies in precipitation observations: ground-based observation is sparse where precipitation is most intense, in tropical deep convection regions both over ocean and land. Rain gauge networks have much better coverage and timely data exchanges in north hemisphere mid-latitude regions, particularly in North America and European countries, while in most of other regions routine gauge observation exchange has dropped during the most recent decades. Case studies over the warm pool, Amazon, Gulf stream and Indian sub-continent regions revealed that discrepancies among datasets are mostly related to the annual cycle. The Amazonian dry biases are still present even in the new JRA-55 reanalysis, despite improvements over its predecessor identified

by earlier studies. Discrepancies amongst reanalyses and observations are found over the western coast of the Indian sub-continent, and the problem was traced down to disagreement between gauge (from GPCC) and satellite estimates (from GPCP). Comparison with observations from the Indian Institute of Tropical Meteorology (ITM) gauge network suggest that the GPCC estimates may be too high by above 50 %.

A bench-mark global scale land evaporation observation dataset is still lacking. The most recent effort is a compilation by *Mueller et al.* (2013), which synthesized estimates from four categories including diagnostics, reanalyses, land surface models and GCMs. Estimates from the same category tend to cluster and the overall result is sensitive to the number of members each category contains, therefore the compilation is regarded as non-robust and uncertainties are large. In terms of the climatological annual mean land evaporation/evapotranspiration (E/ET), both ERA-I and JRA-55 fall within, but near the higher end, of the range of estimates from literature.

Atmospheric reanalysis products have gone through three major iterations (*Trenberth et al.*, 2011), and new products keep being created. However, limitations remain. The gaps from conventional in situ observations are filled by adding information from forecast models, but not without uncertainty. This is particularly true for hydrological cycle related variables such like precipitation and evaporation. Parameters are usually constrained indirectly by observations, and approximations used in the model's representation of moist processes strongly affect the quality and consistency of the hydrological cycle (*Dee et al.*, 2011). In many respects it is better to provide seperated datasets (gauges versus satellites) rather than combining them. Presenting more complete datasets by infilling gives the view that there aren't issues with data access, and may also prohibit easy discrepancy diagnosis, as in the case of the Indian precipitation analysis. For the ERA-I and JRA-55 reanalyses evaluated here, both improvements over earlier products and residual deficiencies are found. For the latter, tropical precipitation and evaporation are overestimated, and their temporal variability are incorrect. Accurate representation of the hydrological cycle in reanalyses is still a difficult challenge.

7.1.2 Spin-down, analysis increment and budget imbalance in ERA-I and JRA-55 reanalyses.

Following on from the previous discussion, analyses in Chapters 2 and 3 confirmed the analysis increment errors in ERA-I and JRA-55, which are responsible for the high biases observed in tropical precipitation. Reanalysis assimilation schemes introduce artificial sources or sinks of moisture into the atmospheric water budget. This is particularly evident in the tropics where the reanalyses have a preferred over-active state that tends to spin-down during the rest of the forecast cycle. Assimilation of observed humidity then replenishes the atmosphere, serving as an artificial moisture source, and creating a positive analysis increment. The problem existed in earlier versions (ERA-40 and JRA25), was reduced by the upgrade from 3DVAR to 4DVAR (*Andersson et al.*, 2005; *Trenberth et al.*, 2011; *Kobayashi et al.*, 2015), but still persists in ERA-I and JRA-55. Such a problem can become even more severe when the assimilated observations contain biases, one example being the MERRA reanalysis: during the 2000s, the atmosphere was over-moistened by an artificial vapour source from the AMSU-A channels, leading to excessive oceanic precipitation (*Bosilovich et al.*, 2011). More analyses of the sources going into reanalyses are needed. One of such efforts is ECMWF's on-going Observational Feedback Archive (OFA) project, which will provide an open-access database to facilitate retrieval of the observations used in reanalyses and other climate data products, along with information on instrumental characterization, data quality, reanalysis departures and data sources, etc..

The analysis increment problem has far reaching implications in various aspects, but for the examination of the hydrological cycle we emphasize only two: firstly, positive increment errors render a "leaking" atmosphere that generates excessive moisture outputs compared to inputs. Similarly, negative increments give rise to a "flooding" atmosphere where inputs overtake outputs. In either case, the water budget is not closed, as represented by the non-zero budget residuals quantified in Chapter 3. A cluster analysis was used to quantify and examine these residuals at a regime (seasons and regions across the globe sharing similar hydrological characteristics) level rather than grid cell level, allowing the residuals to be associated with the contextual hydrological cycle. Consistent for both ERA-I and JRA-55, the regime with the largest fractional residual (as a percentage of mean precipitation) was constituted by the tropical savanna in central Africa and South America, the dry winter monsoon season in

south Asia, and some arid parts of central Asia during summer. In addition to strong seasonality, this regime also features low levels of precipitation (mean $\leq$ 1 mm/day), high (almost entire) dependency of rainfall on local ET, and a strong net moisture export by moisture divergence. A non-closed budget combines errors from all budget terms (with possible cancellations among them), however in this case we show the major cause appears to be the moisture divergence field: the low mean precipitation makes the fractional residual in this regime sensitive to small errors, though it is only the second driest of the six regimes and the driest has a budget that is much closer to being closed. Terrestrial E/ET from reanalyses contains considerable uncertainties, however the spatial distribution is relatively uniform in the tropics, therefore it is less likely to be an effective distinguishing factor. The high correlations between the timeseries of absolute residuals with moisture divergence support the hypothesis that anomalous divergence is associated with large negative residuals and vice versa. ERA-I and JRA-55 show largely consistent results, suggesting that some shared errors cause them to both overestimate the moisture divergence.

Secondly, analysis increments violate the internal physical consistency of the reanalysis system. Artificial moisture sources or sinks give moisture increments which in turn alter the heat increment, energy balance, and then circulation (*Bosilovich et al.*, 2011). Putting the energy coupling aside, we observed higher precipitation levels in both reanalyses maintained at a lower level of humidity load, which is related to the increment and spin-down problem discussed above, and may lead to an impression that the circulation, or hydrological cycle, in reanalyses is more intense than in observations. In fact, a spinning-down model tends to slow down the circulation by the extra latent heat added to the atmosphere (*Andersson et al.*, 2005). This "apparent" intensification effect has no physical root, therefore violates the internal consistency. The energy component was not explicitly addressed here, but more discussions of the hydrological cycle intensity are included in the next section.

7.1.3 A baseline diurnal cycle in atmospheric total column water and moisture transport.

In Chapter 4 we diagnosed the diurnal variability in the horizontal moisture fluxes from reanalysis, and identified one dynamic and one thermodynamic mode. The former is driven by the interactions between semi-diurnal wind and surface pressure cycles stemmed from atmospheric tides. When scaled

by mean background humidity load, it generates a westward propagating moisture convergence/divergence wave along the equator. The thermodynamic mode represents the diurnal moisture flux due to diurnal humidity variations advected by mean annual winds (largely zonal). Atmospheric tidal theories can predict the dynamic mode quite well, therefore we put more emphasis on the thermodynamic component here.

First of all, the analyses did not provide a conclusive result on the causes of the diurnal cycle in Total Column Water (TCW). Objectively this is due to limitations in the reanalysis data (insufficient temporal resolution), and the approach the analysis takes (identifying diurnal cycles from annual harmonics). Furthermore, the non-closed water budget hampers budget analysis at this time scale. Nevertheless we are able to diagnose the existence of a global scale TCW diurnal cycle that is broadly meridionally uniform (although much less uniform than the atmospheric tides), with a phase largely consistent with the local maximum solar heating, and to the first order of approximation, relatively quantitively consistent with the enhanced moisture inputs from oceanic evaporation. On the other hand, examining the vertical profiles at a few selected regions indicated better correspondence between specific humidity and wind divergence, particularly over mid-latitude land areas. The correspondence is much less clear over ocean. However, this is not necessarily inconsistent with the surface evaporation feedback, and it is likely that both effects are required to explain the diurnal cycle.

Despite the uncertain cause, the observed TCW diurnal cycle is likely to be very robust, as the diagnosis is performed on fitted harmonics where inter-annual, intra-seasonal and high frequency variability are filtered out. This frequency isolation has some important implications. Previous studies have suggested that the enhanced oceanic convective activity (positively correlated with TCW) has an early morning maximum (*Yang and Slingo*, 2001; *Kawai and Wada*, 2007; *Sui et al.*, 1997), and others suggest a secondary afternoon maximum (*McGarry and Reed*, 1978; *Augustine*, 1984; *Janowiak et al.*, 1994; *Sui et al.*, 1997; *Fu et al.*, 1990). The major distinguishing factor here seems to be the large-scale circulation conditions: disturbed or undisturbed (*Sui et al.*, 1997) and intra-seasonal variability (e.g. MJO). However, these variabilities are removed by the harmonic fitting, therefore the results suggest a baseline TCW diurnal cycle that can be isolated from such intra-seasonal changes, with a peak-to-trough magnitude of $\sim 0.4\,mm$, and a peak phase of $\sim 1800 - 2100$ local time.

7.1.4 El Niño complexity: the moisture divergence perspective.

The re-organisation of the large-scale atmospheric circulation in response to ENSO has been explained by classical theories for the altered Walker circulation (*Bjerknes*, 1966, 1969), and the Hadley cell was found to strengthen and shift during warm events (*Oort and Yienger*, 1996; *Quan et al.*, 2004; *Hu and Fu*, 2007; *Wang*, 2002). However, recent studies have identified distinct responses to two different types of El Niños in various aspects including ocean heat content, SST, salinity, precipitation, horizontal winds and Outgoing Long-wave Radiation (OLR) (*Xu and Chan*, 2001; *Yu and Kao*, 2007; *Kao and Yu*, 2009; *Kug et al.*, 2009; *Chiodi and Harrison*, 2010; *Singh et al.*, 2011). This classification has some correspondence with warming strengths but structural differences are also evident, suggesting a large-scale non-linear response pattern. Chapter 4 looked into this complexity from a moisture divergence perspective, and confirmed the Extreme and Moderate El Niño classification (also commonly referred to as Eastern Pacific (EP) and Central Pacific (CP) events). Following the eastward shifted warming center in an Extreme El Niño, the zonal SST gradient is weakened or even reversed, and the meridional gradient over the eastern Pacific is weakened. In response, the Southern Pacific Convergence Zone (SPCZ) swings further equator-ward, westerly anomalies develop over the eastern Pacific to help maintain the warming, and the northern hemisphere branch of the Hadley cell gets compressed and shifted equator-ward more than in a Moderate El Niño. These atmospheric responses develop swiftly during the peak-to-decaying phase of an Extreme event, when the underlying SST anomaly plateaus at its maximum, suggesting a highly non-linear ocean-atmosphere coupling mechanism. Each El Niño has its own characteristics, and we learn something new from each event. Implications of such differences between an Extreme and Moderate El Niños keep being documented, including their distinct impacts on tropical cyclone tracks and intensities (*Kim et al.*, 2009; *Wang et al.*, 2014). With frequency variations in decadal to inter-decadal time scales and potential future changes, this classification constitutes an important factor in our understanding of ENSO.

7.1.5 Extreme onshore moisture transports by tropical cyclones: a methodological discussion.

Having addressed the climatological annual and diurnal cycles of moisture transports, we moved on to quantify a special form of extreme moisture fluxes: onshore moisture transport by tropical cyclones (TCs). Previous studies have looked into the attribution of precipitation to TCs, but there has been almost no discussion of continental scale moisture transport by TCs. In Chapter 6 we designed an ensemble of attribution schemes that use the best track TC location records and reanalysis moisture fluxes to estimate onshore transport. Similar to many precipitation attribution studies, the attribution is fundamentally distance-based (using geographical vicinity to a TC centre as the major attribution criterion), but with consideration of variations in TC size and asymmetry, and also takes into account underlying background flow from which the TC attributed fluxes are identified. Schemes with various degrees of complexity and flexibility offer us an ensemble estimate from which uncertainty and sensitivity are analyzed.

The results suggest that onshore moisture transport onto the North American continent by Atlantic TCs has large inter-annual variability, directly caused by variations in TC activity and their tracks. On average (1980-2012 mean across the ensemble of estimates), Atlantic TCs alone contribute about 0.15 Eg, or 11 % of total hurricane season moisture transport, with most of the TC transport occurring in the Gulf of Mexico and along the eastern coast. With contributions from Eastern Pacific TCs included, the value rises to 0.24 Eg (or 19 % of the total). TCs form an important moisture input for the North American and many other continents: in some cases, a single TC can alleviate or terminate a sustained drought.

From a methodological perspective, we found that the appropriate attribution size for moisture fluxes appears to be much larger than the 500 km radius commonly used in precipitation attributions, and the $700 - 900\,km$ range serves as a good reference. Including detailed information about a TC, such as their transient size and shape variations, gives limited added value in the attribution. This allows estimations to be extended further back in time, before TC size observations were available, and also makes it easier to combine best track records from different data centres, which may offer records of different completeness and use different measures of TC sizes.

7.1.6 Development of analysis techniques

As well as conventional, well-established analysis methods, some new techniques were needed to answer the scientific questions that are the focus of this thesis.

Taylor diagrams provide a powerful visual device for performance evaluations, where the agreements on variation strength, pattern correlations and biases can be summarized into a single plot. However, uncertainty estimation of the observational reference has been fairly rudimentary: by adding another independent, or often only partly independent, observation. Most of the time, a truly independent alternative is not available. Therefore we devised a method to incorporate the random errors estimated by the data provider into the Taylor diagram. Introduction of this not only makes good use of this valuable first-hand information, but also allows a more objective interpretation. An example of the additional insight obtained by representing this uncertainty information on the Taylor diagram is that the differences between reanalysis precipitation (ERA-I and JRA-55) and GPCP data, while comparable in magnitude for the tropical and extra-tropcal oceans, and clearly more robust for the tropics due to the much larger uncertainty estimates provided by GPCP for the extra-tropical regions (see Chapter 2). Application to climate model evaluations is also meaningful and helpful: one could easily visualize the overlap between the model uncertainty range (perhaps encompassed by different realizations) and the observation uncertainty range (by utilizing the method introduced here). In addition to GPCP and OAFlux that provide uncertainty estimates along with their data, other observations also have such information, such as CRUTEM4, and also for ERA-20C and 20th Century Reanalysis (20CR) with their ensembles (10 and 56, respectively).

Empirical Orthogonal Function (EOF) analysis is a commonly used technique in climatic studies, however the orthogonal constraint can sometimes hamper clear and easy physical interpretations, particularly when non-linear response patterns are the main interest. One example is the Extreme versus Moderate El Niño complexity discussed above, where we demonstrated in Chapter 5 that the leading two EOFs are clearly related to each other, albeit in a non-linear manner. The EOF patterns are orthogonal, as required by the method, but their associated Principal Components (PCs), while also required to be nominally independent as measured by zero linear correlation, are in fact related but in a non-linear way. The combination of their lack of independence with the orthogonality

constraints of the EOF method, can hamper their physical interpretation: neither of the leading EOFs of tropical Pacific moisture divergence is able to capture on its own the pattern of response to a La Niña, or to a Moderate El Niño, or to an Extreme El Niño event. Instead, different combinations of the two EOFs are needed to capture each of these events. The first EOF captures most of the transition from La Niña to Moderate El Niño, but this is also partly represented by the second EOF, which in turn also partly represents the contrasting moisture divergence response to Moderate and Extreme El Niños. To overcome this limitation, we explored the Self-organizing map (SOM) algorithm in describing the non-linear ENSO transitions. The results suggest it is a powerful tool, not only in the synoptic circulation and downscaling analyses where it has been mostly applied, but also to complement EOF analysis in the diagnosis of large-scale climatic modes. A classification of ENSO atmospheric moisture divergence modes finds that the separation between Extreme and Moderate El Niños can be as large as from Moderate El Niños to La Niñas.

7.2 Limitations and future work

One study can not, of course, address all parts of the hydrological cycle, and limitations exist that need to be acknowledged and that could form the basis for future work:

1. The variability in the hydrological and energy cycles are closely coupled: latent heat transfer vertically between the surface and the atmosphere modulates the energy balance of both, and also has implications for cloud cover distribution and radiative forcing of the atmosphere, which subsequently alter the entire climatic responses to both natural and anthropogenic drivers (*Wielicki et al.*, 2002). Particularly over long time scales, the hydrological cycle intensity is controlled more by energy constraints than by mass constraints (*Allen and Ingram*, 2002). Such energy constraint perspectives have laid the foundation for many important understandings of hydrological responses to a changing climate at global (e.g. *Allen and Ingram* (2002); *Held and Soden* (2006); *Chou and Neelin* (2004); *Allan et al.* (2014)), and at regional scales as well (*Levermann et al.* (2009); *Muller and O'Gorman* (2011)). Over inter-annual and intra-seasonal time scales, large-scale circulation is closely coupled with the radiative responses, one example being the different dynamic-thermodynamic mechanisms responsible for the observed circulation patterns during CP versus EP El Niños as

introduced in Chapter 5 (see also *Su and Neelin* (2002)). From an internal consistency point of view, inconsistency is found in reanalysis products between their hydrological and energy cycles, possibly due to parameterization schemes that produce too much rainfall prematurely, or due to the assimilation of questionable observations. This thesis largely considers only the water mass circulations without explicitly addressing the energy component. The climate system is highly holistic, as should be its study, particularly when physical explanation is the ultimate goal. Serving as an observation-based analysis, this thesis was intended to have a narrower scope, but more involvement of other components including the energy cycle should be addressed in future studies.

2. During the diagnosis of the major characteristics of the modern day hydrological cycle, we have put more attention on the horizontal moisture transport, for a few reasons: firstly the far-reaching nature of moisture fluxes is most representative of the atmospheric branch of hydrological cycle. Secondly, in most cases the variability of precipitation can be captured quite well by the horizontal moisture divergence/convergence. Lastly the power of reanalysis can be better utilized in the quantification of wind and humidity fields compared with precipitation and evaporation estimates, which both contain model and increment errors. In the analysis of precipitation, we have restricted the scope to climatological mean states with only brief discussion on its temporal variability. The long-term mean distribution is a useful summary indicator of the precipitation patterns and the quality of the datasets being evaluated, but detailed analysis over time scales, for instance, the frequency/intensity distributions and variations in precipitation, including extreme rainfall and sustained droughts, are also necessary from a societal impact and risk assessment point of view. Analyses on precipitation frequency/intensity in reanalysis and the possible link with analysis increment distributions were considered initially, but could not be pursued due to time limitations. Future work could undertake modelling experiments to explore the sensitivity of the simulated surface runoff to input rainfall frequency/intensity, an analysis on the sensitivity of oceanic moisture transport to data resolution, and a vertical profiling of the moisture exchange between tropics and extra-tropics.

3. Long-term changes in hydrological cycle intensity are controversial. Previously we mentioned internal consistency issues in reanalysis products and their association with the energy cycle. The greatest implication of such problems perhaps lies in the quantification of long-term changes of the

hydrological cycle. Although not included as a major topic of the thesis, this has been a fairly active area in the research community and has raised some controversy in the literature (*Quan et al.*, 2004; *Mitas and Clement*, 2005; *Vecchi et al.*, 2006; *Zhang and Song*, 2006; *Sohn and Park*, 2010; *Zahn and Allan*, 2011).

Firstly, hydrological cycle intensity can be "viewed" in different ways. Increased precipitation and evaporation, both being freshwater fluxes between the surface and the atmosphere, imply intensification, and this has been confirmed by evidence following the rising global mean temperature. However, theoretical thermodynamic arguments suggest that precipitation increases are constrained to a slower rate than humidity increases (*Held and Soden*, 2006; *Allen and Ingram*, 2002; *Allan et al.*, 2014), meaning the overall circulation must slow as mean temperature rises. In addition, circulation strength has also been measured by quantifying the streamfunction (whose maximum value can be used as an indicator of Hadley circulation strength, e.g. *Quan et al.* (2004); *Mitas and Clement* (2005)), vertical wind shear (*Quan et al.*, 2004), effective wind (*Sohn and Park*, 2010), Sea Level Pressure (SLP) gradient (*Vecchi et al.*, 2006; *Sohn and Park*, 2010; *Zhang and Song*, 2006) and the moisture fluxes in ascending versus descending branches of the circulation (*Zahn and Allan*, 2011). Despite different time periods selected by studies that may lead to different conclusions (in some cases this has a great impact, e.g. the inclusion of the fast increasing SLP anomalies during 2003-2007 makes a big difference in the resultant trend in *Sohn and Park* (2010)), there seems to be a discrepancy between wind-based and pressure gradient based circulation strength: analyses using reanalysis wind fields (streamfunction, vertical wind shear) tend to give a strengthening result, while SLP gradient analyses tend to show overall weakening. The discrepancy is related to internal consistency issues: in reanalysis systems, vertical velocity was derived, based on mass conservation, from the divergence of horizontal winds, which are in turn strongly coupled with convective processes (*Zhang and Song*, 2006). On the other hand, surface pressure is directly observed without obvious sources of trend biases, while biases in the trends of the input radiosonde temperature can affect the wind fields via altering the static stability (*Santer*, 2005; *Zhang and Song*, 2006). Therefore, the dynamic relationship between sea level pressure and vertical velocity is not guaranteed (*Zhang and Song*, 2006).

Inconsistency in reanalysis system can lead to contradicting conclusions that depend on the very definition and the perspective one subsequently chooses. Either result (strengthening or weakening) depicts only one incomplete aspect

of the system and therefore is not robust. Reanalysis, and to some extent all existing observations, suffer heterogeneity and consistency issues, therefore making a robust diagnosis of long-term change challenging. Future studies need to take this into account, by making a closer combination of observation and model evidence and explicitly promoting the component that is physically consistent among various aspects. Finally, a more encompassing framework that can incorporate different interpretations of hydrological intensity is needed.

References

Adam, J. C. (2003), Adjustment of global gridded precipitation for systematic bias, *Journal of Geophysical Research*, *108*(D9), 1–15, doi:10.1029/2002JD002499.

Adler, R. F., C. Kidd, G. Petty, M. Morissey, and H. M. Goodman (2001), Intercomparison of global precipitation products: The third precipitation intercomparison project (PIP-3), *Bulletin of the American Meteorological Society*, *82*(7), 1377–1396.

Akaike, H. (1974), A new look at the statistical model identification, *Automatic Control, IEEE Transactions on*, *19*(6), 716–723, doi:10.1109/TAC.1974.1100705.

Allan, R. P. (2012), The Role of Water Vapour in Earth's Energy Flows, *Surveys in Geophysics*, *33*(3-4), 557–564, doi:10.1007/s10712-011-9157-8.

Allan, R. P., C. Liu, M. Zahn, D. A. Lavers, E. Koukouvagias, and A. Bodas-Salcedo (2014), Physically Consistent Responses of the Global Atmospheric Hydrological Cycle in Models and Observations, *Surveys in Geophysics*, *35*(3), 533–552, doi:10.1007/s10712-012-9213-z.

Allen, M. R., and W. J. Ingram (2002), Constraints on future changes in climate and the hydrologic cycle., *Nature*, *419*(September), 224–232, doi:10.1038/nature01092.

Andersson, A., K. Fennig, C. Klepp, S. Bakan, H. Graßl, and J. Schulz (2010), The Hamburg Ocean Atmosphere Parameters and Fluxes from Satellite Data - HOAPS-3, *Earth Syst. Sci. Data*, *2*(2), 215–234, doi:10.5194/essd-2-215-2010.

Andersson, A., C. Klepp, K. Fennig, S. Bakan, H. Grassl, and J. Schulz (2011), Evaluation of HOAPS-3 ocean surface freshwater flux components, *Journal of Applied Meteorology and Climatology*, *50*(2), 379–398, doi:10.1175/2010JAMC2341.1.

Andersson, E., P. Bauer, A. Beljaars, F. Chevallier, E. Hólm, M. Janisková, P. Kallberg, G. Kelly, P. Lopez, A. McNally, E. Moreau, A. J. Simmons, J. N. Thépaut, and A. M. Tompkins (2005), Assimilation and modeling of the atmospheric hydrological cycle in the ECMWF forecasting system, *Bulletin of the American Meteorological Society*, *86*(3), 387–402, doi:10.1175/BAMS-86-3-387.

Ashok, K., S. K. Behera, S. A. Rao, H. Weng, and T. Yamagata (2007), El Nino

Modoki and its possible teleconnection, *Journal of Geophysical Research: Oceans*, *112*(11), C11,007, doi:10.1029/2006JC003798.

Atallah, E., L. F. Bosart, and A. R. Aiyyer (2007), Precipitation Distribution Associated with Landfalling Tropical Cyclones over the Eastern United States, *Monthly Weather Review*, *135*(6), 2185–2206, doi:10.1175/MWR3382.1.

Augustine, J. a. (1984), The Diurnal Variation of Large-Scale Inferred Rainfall over the Tropical Pacific Ocean during August 1979, *Monthly Weather Review*, *112*(9), 1745–1751.

Baldocchi, D., E. Falge, L. H. Gu, R. Olson, D. Hollinger, S. Running, P. Anthoni, C. Bernhofer, K. Davis, R. Evans, J. Fuentes, A. Goldstein, G. Katul, B. Law, X. H. Lee, Y. Malhi, T. Meyers, W. Munger, W. Oechel, K. T. P. U, K. Pilegaard, H. P. Schmid, R. Valentini, S. Verma, T. Vesala, K. Wilson, and S. Wofsy (2001), FLUXNET: A new tool to study the temporal and spatial variability of ecosystem-scale carbon dioxide, water vapor, and energy flux densities, *Bulletin American Meteorological Society*, *82*(11), 2415–2434.

Becker, A., P. Finger, A. Meyer-Christoffer, B. Rudolf, K. Schamm, U. Schneider, and M. Ziese (2013), A description of the global land-surface precipitation data products of the global precipitation climatology centre with sample applications including centennial (trend) analysis from 1901-present, *Earth System Science Data*, *5*(1), 71–99, doi:10.5194/essd-5-71-2013.

Bengtsson, L., S. Hagemann, and K. I. Hodges (2004), Can climate trends be calculated from reanalysis data?, *Journal of Geophysical Research D: Atmospheres*, *109*(11), D11,111, doi:10.1029/2004JD004536.

Bengtsson, L., K. I. Hodges, and M. Esch (2007), Tropical cyclones in a T159 resolution global climate model: Comparison with observations and re-analyses, *Tellus, Series A: Dynamic Meteorology and Oceanography*, *59 A*(4), 396–416, doi:10.1111/j.1600-0870.2007.00236.x.

Biemans, H., R. W. a. Hutjes, P. Kabat, B. J. Strengers, D. Gerten, and S. Rost (2009), Effects of Precipitation Uncertainty on Discharge Calculations for Main River Basins, *Journal of Hydrometeorology*, *10*(August 2015), 1011–1025, doi:10.1175/2008JHM1067.1.

Bjerknes, J. (1966), A possible response of the atmospheric Hadley circulation to equatorial anomalies of ocean temperature, *Tellus A*, *18*(4), 820.

Bjerknes, J. (1969), Atmospheric Teleconnections From The Equatorial Pacific, *Monthly Weather Review*, *97*(3), 163–172.

Bosc, C., and T. Delcroix (2008), Observed equatorial Rossby waves and ENSO-related warm water volume changes in the equatorial Pacific Ocean, *Journal of Geophysical Research*, *113*(C6), 1–14, doi:10.1029/2007JC004613.

Bosilovich, M., S. Schubert, and G. Walker (2005), Global changes of the water cycle intensity., *Journal of Climate*, *18*, 1591–1608, doi:10.1175/JCLI3357.1.

Bosilovich, M. G., J. Chen, F. R. Robertson, and R. F. Adler (2008), Evaluation of global precipitation in reanalyses, *Journal of Applied Meteorology and Climatology*, *47*(9), 2279–2299, doi:10.1175/2008JAMC1921.1.

Bosilovich, M. G., F. R. Robertson, and J. Chen (2011), Global energy and water budgets in MERRA, *Journal of Climate*, *24*(22), 5721–5739, doi:10.1175/2011JCLI4175.1.

Bourras, D. (2006), Comparison of five satellite-derived latent heat flux products to moored buoy data, *Journal of Climate*, *19*(24), 6291–6313, doi:10.1175/JCLI3977.1.

Brönnimann, S., J. L. Annis, C. Vogler, and P. D. Jones (2007), Reconstructing the quasi-biennial oscillation back to the early 1900s, *Geophysical Research Letters*, *34*(22), L22,805, doi:10.1029/2007GL031354.

Brown, P. J., and C. D. Kummerow (2014), An assessment of atmospheric water budget components over tropical oceans, *Journal of Climate*, *27*(5), 2054–2071, doi:10.1175/JCLI-D-13-00385.1.

Bruce, J. G., and E. Firing (1974), Temperature measurements in the upper 10 m with modified expendable bathythermograph probes, *Journal of Geophysical Research*, *79*(27), 4110–4111.

Brun, J., and A. P. Barros (2014), Mapping the role of tropical cyclones on the hydroclimate of the southeast United States: 2002-2011, *International Journal of Climatology*, *34*(2), 494–517, doi:10.1002/joc.3703.

Cai, W., M. Lengaigne, S. Borlace, M. Collins, T. Cowan, M. J. McPhaden, A. Timmermann, S. B. Power, J. Brown, C. Menkes, A. Ngari, E. M. Vincent, and M. J. Widlansky (2012), More extreme swings of the South Pacific convergence zone due to greenhouse warming., *Nature*, *488*(7411), 365–9, doi:10.1038/nature11358.

Cai, W., S. Borlace, M. Lengaigne, P. van Rensch, M. Collins, G. Vecchi, A. Timmermann, A. Santoso, M. J. McPhaden, L. Wu, M. H. England, G. Wang, E. Guilyardi, and F.-F. Jin (2014), Increasing frequency of extreme El Niño events due to greenhouse warming, *Nature Climate Change*, *5*(2), 1–6, doi:10.1038/nclimate2100.

Capotondi, A. (2013), ENSO diversity in the NCAR CCSM4 climate model, *Journal of Geophysical Research: Oceans*, *118*(10), 4755–4770, doi:10.1002/jgrc.20335.

Capotondi, A., A. T. Wittenberg, M. Newman, E. Di Lorenzo, J.-Y. Yu, P. Braconnot, J. Cole, B. Dewitte, B. Giese, E. Guilyardi, F.-F. Jin, K. Karnauskas, B. Kirtman, T. Lee, N. Schneider, Y. Xue, and S.-W. Yeh (2015), Understanding ENSO Diversity, *Bulletin of the American Meteorological Society*, *96*(6), 921–938, doi:10.1175/BAMS-D-13-00117.1.

Castillo, R., R. Nieto, A. Drumond, and L. Gimeno (2014), The role of the

ENSO cycle in the modulation of moisture transport from major oceanic moisture sources, *Water Resources Research*, *50*(2), 1046–1058, doi:10.1002/2013WR013900.

Cavazos, T. (1999), Large-scale circulation anomalies conducive to extreme precipitation events and derivation of daily rainfall in northeastern Mexico and southeastern Texas, *Journal of Climate*, *12*(5 II), 1506–1523.

Chang, C. P., Y. Lei, C. H. Sui, X. Lin, and F. Ren (2012), Tropical cyclone and extreme rainfall trends in East Asian summer monsoon since mid-20th century, *Geophysical Research Letters*, *39*(17), 1–6, doi:10.1029/2012GL052945.

Chen, M., P. Xie, J. E. Janowiak, and P. a. Arkin (2002), Global Land Precipitation: A 50-yr Monthly Analysis Based on Gauge Observations, *Journal of Hydrometeorology*, *3*(3), 249–266.

Chiodi, A. M., and D. E. Harrison (2010), Characterizing Warm-ENSO variability in the equatorial pacific: An OLR perspective, *Journal of Climate*, *23*(9), 2428–2439, doi:10.1175/2009JCLI3030.1.

Chou, C., and J. D. Neelin (2004), Mechanisms of Global Warming Impacts on Regional Tropical Precipitation, *Journal of Climate*, *17*(13), 2688–2701, doi:10.1175/1520-0442(2004)017<2688:MOGWIO>2.0.CO;2.

Clayson, C. A., and D. Weitlich (2005), Diurnal warming in the tropical Pacific and its interannual variability, *Geophysical Research Letters*, *32*(21), 1–4, doi:10.1029/2005GL023786.

Clayson, C. A., and D. Weitlich (2007), Variability of tropical diurnal sea surface temperature, *Journal of Climate*, *20*(2), 334–352, doi:10.1175/JCLI3999.1.

Cline, J. (2002), Surface-Based Rain, Wind, and Pressure Fields in Tropical Cyclones over North Carolina Since 1989, *Tech. rep.*, National Weather Service Offic, Bohemia, New York.

Crane, R. G., and B. C. Hewitson (1998), Double CO2 Precipitation Changes for the Sisquehanna Basin: Down-Scaling from the Genesis General Circulation Model, *International Journal of Climatology*, *18*(1), 65–76.

Dai, A. (2001), Global Precipitation and Thunderstorm Frequencies. Part I: Seasonal and Interannual Variations, *Journal of Climate*, *14*(6), 1092–1111.

Dai, A., and K. E. Trenberth (2002), Estimates of Freshwater Discharge from Continents: Latitudinal and Seasonal Variations, *Journal of Hydrometeorology*, *3*(6), 660–687.

Dai, A., and K. E. Trenberth (2004), The diurnal cycle and its depiction in the community climate system model, *Journal of Climate*, *17*(5), 930–951.

Dai, A., and J. Wang (1999), Diurnal and Semidiurnal Tides in Global Surface Pressure Fields, *Journal of the Atmospheric Sciences*, *56*(22), 3874–3891.

Dai, A., X. Lin, and K. L. Hsu (2007), The frequency, intensity, and diurnal cycle of precipitation in surface and satellite observations over low- and mid-latitudes, *Climate Dynamics*, *29*(7-8), 727–744, doi:10.1007/s00382-007-0260-y.

Dailey, P. S., G. Zuba, G. Ljung, I. M. Dima, and J. Guin (2009), On the relationship between North Atlantic sea surface temperatures and U.S. hurricane landfall risk, *Journal of Applied Meteorology and Climatology*, *48*(1), 111–129, doi:10.1175/2008JAMC1871.1.

Dare, R. a., N. E. Davidson, and J. L. McBride (2012), Tropical Cyclone Contribution to Rainfall over Australia, *Monthly Weather Review*, *140*(2006), 120522063439,001, doi:10.1175/MWR-D-11-00340.1.

Dee, D. P., and S. Uppala (2009), Variational bias correction of satellite radiance data in the ERA-Interim reanalysis, *Quarterly Journal of the Royal Meteorological Society*, *135*(644), 1830–1841, doi:10.1002/qj.493.

Dee, D. P., S. M. Uppala, A. J. Simmons, P. Berrisford, P. Poli, S. Kobayashi, U. Andrae, M. A. Balmaseda, G. Balsamo, P. Bauer, P. Bechtold, A. C. M. Beljaars, L. van de Berg, J. Bidlot, N. Bormann, C. Delsol, R. Dragani, M. Fuentes, A. J. Geer, L. Haimberger, S. B. Healy, H. Hersbach, E. V. Hólm, L. Isaksen, P. Kållberg, M. Köhler, M. Matricardi, A. P. McNally, B. M. Monge-Sanz, J.-J. Morcrette, B.-K. Park, C. Peubey, P. de Rosnay, C. Tavolato, J.-N. Thépaut, and F. Vitart (2011), The ERA-Interim reanalysis: configuration and performance of the data assimilation system, *Quarterly Journal of the Royal Meteorological Society*, *137*(656), 553–597, doi:10.1002/qj.828.

Demory, M. E., P. L. Vidale, M. J. Roberts, P. Berrisford, J. Strachan, R. Schiemann, and M. S. Mizielinski (2014), The role of horizontal resolution in simulating drivers of the global hydrological cycle, *Climate Dynamics*, *42*(7-8), 2201–2225, doi:10.1007/s00382-013-1924-4.

Deschamps, P. Y., and R. Frouin (1984), Large Diurnal Heating of the Sea Surface Observed by the HCMR Experiment, *Journal of Physical Oceanography*, *14*(1), 177–184.

Deser, C., and C. Smith (1998), Diurnal and semidiurnal variations of the surface wind field over the tropical Pacific Ocean, *Journal of climate*, *11*, 1730–1748.

Dirmeyer, P. A., X. Gao, M. Zhao, Z. Guo, T. Oki, and N. Hanasaki (2006), GSWP-2: Multimodel analysis and implications for our perception of the land surface, *Bulletin of the American Meteorological Society*, *87*(10), 1381–1397, doi:10.1175/BAMS-87-10-1381.

Dreyfus, G. (2005), *Neural Networks: Methodology and Applications*, Springer Berlin Heidelberg.

Ebita, A., S. Kobayashi, Y. Ota, M. Moriya, R. Kumabe, K. Onogi, Y. Harada, S. Yasui, K. Miyaoka, K. Takahashi, H. Kamahori, C. Kobayashi, H. Endo,

M. Soma, Y. Oikawa, and T. Ishimizu (2011), The Japanese 55-year Reanalysis âĂIJJRA-55âĂİ: An Interim Report, *Sola*, *7*, 149–152, doi:10.2151/sola.2011-038.

Edwards, J. M. (2007), Oceanic latent heat fluxes: Consistency with the atmospheric hydrological and energy cycles and general circulation modeling, *Journal of Geophysical Research*, *112*(D6), D06,115, doi:10.1029/2006JD007324.

Emanuel, K. (2005), Increasing destructiveness of tropical cyclones over the past 30âĂL'years, *Nature*, *436*(7051), 686–688, doi:10.1038/nature03906.

Fekete, B., C. Vörösmarty, and W. Grabs (2000), Global Composite Runoff Fields on Observed River Discharge and Simulated Water Balances, *Tech. Rep. 22*, Complex Systems Research Center, University of New Hampshire, doi:10.1017/CBO9781107415324.004.

Flato, G., J. Marotzke, B. Abiodun, P. Braconnot, S. C. Chou, W. Collins, P. Cox, F. Driouech, S. Emori, V. Eyring, C. Forest, P. Gleckler, E. Guilyardi, C. Jakob, V. Kattsov, C. Reason, and M. Rummukainen (2013), *Evaluation of Climate Models*, book section 9, pp. 741–866, Cambridge University Press, Cambridge, United Kingdom and New York, NY, USA, doi:10.1017/CBO9781107415324.020.

Folland, C. K. (2002), Relative influences of the Interdecadal Pacific Oscillation and ENSO on the South Pacific Convergence Zone, *Geophysical Research Letters*, *29*(13), 2–5, doi:10.1029/2001GL014201.

Fu, C., H. F. Diaz, and J. O. Fletcher (1986), Characteristics of the Response of Sea Surface Temperature in the Central Pacific Associated with Warm Episodes of the Southern Oscillation, *Monthly Weather Review*, *114*(9), 1716–1739.

Fu, R., D. Genio, D. Anthony, and W. B. Rossow (1990), Behavior of deep convective clouds in the tropical Pacific deduced from ISCCP radiances, *Journal of Climate*, *3*(10), 1129–1152.

Galarneau, T. J., L. F. Bosart, and R. S. Schumacher (2010), Predecessor Rain Events ahead of Tropical Cyclones, *Monthly Weather Review*, *138*(8), 3272–3297, doi:10.1175/2010MWR3243.1.

Gentemann, C., C. Donlon, A. Stuart-Menteth, and F. Wentz (2003), Diurnal signals in satellite sea surface temperature measurements, *Geophysical Research Letters*, *30*(3), 1140, doi:10.1029/2002GL016291.

Giese, B. S., and S. Ray (2011), El Niño variability in simple ocean data assimilation (SODA), 1871-2008, *Journal of Geophysical Research*, *116*(C2), C02,024, doi:10.1029/2010JC006695.

Gimeno, L., A. Drumond, R. Nieto, R. M. Trigo, and A. Stohl (2010), On the origin of continental precipitation, *Geophysical Research Letters*, *37*(13), L13,804, doi:10.1029/2010GL043712.

Gimeno, L., A. Stohl, R. M. Trigo, F. Dominguez, K. Yoshimura, L. Yu, A. Drumond, A. M. Durn-Quesada, and R. Nieto (2012), Oceanic and terrestrial sources of continental precipitation, *Reviews of Geophysics*, *50*(4), RG4003, doi:10.1029/2012RG000389.

Goldenberg, S. B. (2001), The Recent Increase in Atlantic Hurricane Activity: Causes and Implications, *Science*, *293*(5529), 474–479, doi:10.1126/science.1060040.

Gray, W. M. (1984), Atlantic Seasonal Hurricane Frequency. Part I: El Niño and 30 mb Quasi-Biennial Oscillation Influences.

Hagemann, S., K. Arpe, and L. Bengtsson (2005), *Validation of the hydrological cycle of ERA-40*, vol. 24, era rep. s ed., 42pp pp., ECMWF.

Harris, I., P. D. Jones, T. J. Osborn, and D. H. Lister (2014), Updated high-resolution grids of monthly climatic observations - the CRU TS3.10 Dataset, *International Journal of Climatology*, *34*(3), 623–642, doi:10.1002/joc.3711.

Harrison, D. E., and P. S. Schopf (1984), Kelvin-Wave-Induced Anomalous Advection and the Onset of Surface Warming in El Niño Events, *Monthly Weather Review*, *112*(5), 923–933.

Hart, R. E., R. N. Maue, and M. C. Watson (2007), Estimating local memory of tropical cyclones through MPI anomaly evolution, *Monthly Weather Review*, *135*(12), 3990–4005, doi:Doi10.1175/2007mwr2038.1.

Hartmann, D. L., A. M. G. Klein Tank, M. Rusticucci, L. V. Alexander, S. BroÌĹnnimann, Y. Charabi, F. J. Dentener, E. J. Dlugokencky, D. R. Easterling, A. Kaplan, B. J. Soden, P. W. Thorne, M. Wild, and P. M. Zhai (2013), *Observations: Atmosphere and Surface*, book section 2, pp. 159–254, Cambridge University Press, Cambridge, United Kingdom and New York, NY, USA, doi:10.1017/CBO9781107415324.008.

Haurwitz, B., and A. D. Cowley (1973), The diurnal and semidiurnal barometric oscillations global distribution and annual variation, *Pure and Applied Geophysics PAGEOPH*, *102*(1), 193–222, doi:10.1007/BF00876607.

Hegerl, G. C., E. Black, R. P. Allan, W. J. Ingram, D. Polson, K. E. Trenberth, R. S. Chadwick, P. A. Arkin, B. B. Sarojini, A. Becker, A. Dai, P. J. Durack, D. Easterling, H. J. Fowler, E. J. Kendon, G. J. Huffman, C. Liu, R. Marsh, M. New, T. J. Osborn, N. Skliris, P. A. Stott, P. L. Vidale, S. E. Wijffels, L. J. Wilcox, K. M. Willett, and X. Zhang (2015), Challenges in quantifying changes in the global water cycle, *Bulletin of the American Meteorological Society*, *96*(7), 1097–1115, doi:10.1175/BAMS-D-13-00212.1.

Held, I. M., and B. J. Soden (2006), Robust responses of the hydrological cycle to global warming, *Journal of Climate*, *19*(21), 5686–5699, doi:10.1175/JCLI3990.1.

Hewitson, B. C., and R. G. Crane (1994), *Neural Nets: Applications in Geography: Applications for Geography*, vol. 29, 194 pp., Springer.

Hewitson, B. C., and R. G. Crane (2002), Self-organizing maps: Applications to synoptic climatology, *Climate Research*, *22*(1), 13–26, doi:10.3354/cr022013.

Hoerling, M. P., A. Kumar, and M. Zhong (1997), El Nino, La Nina, and the nonlinearity of their teleconnections, *Journal of Climate*, *10*(8), 1769–1786.

Hu, Y., and Q. Fu (2007), Observed poleward expansion of the Hadley circulation since 1979, *Atmospheric Chemistry and Physics Discussions*, *7*(19), 5229–5236, doi:10.5194/acpd-7-9367-2007.

Huffman, G., and D. Bolvin (2011), GPCP version 2 combined precipitation data set documentation, *Tech. rep.*, NASA Goddard Space Flight Center.

Hulle, M. M. V. (2012), *Self-organizing Maps*, Physics and astronomy online library, 585–622 pp., Springer Berlin Heidelberg.

Janowiak, J. E., P. A. Arkin, and M. Morrissey (1994), An Examination of the Diurnal Cycle in Oceanic Tropical Rainfall Using Satellite and in-Situ Data, *Monthly Weather Review*, *122*(10), 2296–2311.

Janowiak, J. E., A. Gruber, C. R. Kondragunta, R. E. Livezey, and G. J. Huffman (1998), A comparison of the NCEP-NCAR reanalysis precipitation and the GPCP rain gauge-satellite combined dataset with observational error considerations, *Journal of Climate*, *11*(11), 2960–2979.

Jiang, H., and E. J. Zipser (2010), Contribution of Tropical Cyclones to the Global Precipitation from Eight Seasons of TRMM Data: Regional, Seasonal, and Interannual Variations, *Journal of Climate*, *23*(2005), 1526–1543, doi:10.1175/2009JCLI3303.1.

Jiménez, C., C. Prigent, B. Mueller, S. I. Seneviratne, M. F. McCabe, E. F. Wood, W. B. Rossow, G. Balsamo, A. K. Betts, P. A. Dirmeyer, J. B. Fisher, M. Jung, M. Kanamitsu, R. H. Reichle, M. Reichstein, M. Rodell, J. Sheffield, K. Tu, and K. Wang (2011), Global intercomparison of 12 land surface heat flux estimates, *Journal of Geophysical Research Atmospheres*, *116*(2), D02,102, doi:10.1029/2010JD014545.

Johnson, N. C. (2013), How many enso flavors can we distinguish?, *Journal of Climate*, *26*(13), 4816–4827, doi:10.1175/JCLI-D-12-00649.1.

Jourdain, N. C., B. Barnier, N. Ferry, J. Vialard, C. E. Menkes, M. Lengaigne, and L. Parent (2014), Tropical cyclones in two atmospheric (re)analyses and their response in two oceanic reanalyses, *Ocean Modelling*, *73*(2014), 108–122, doi:10.1016/j.ocemod.2013.10.007.

Jung, M., M. Reichstein, and a. Bondeau (2009), Towards global empirical upscaling of FLUXNET eddy covariance observations: validation of a model

tree ensemble approach using a biosphere model, *Biogeosciences Discussions*, *6*(3), 5271–5304, doi:10.5194/bgd-6-5271-2009.

Jung, M., M. Reichstein, P. Ciais, S. I. Seneviratne, J. Sheffield, M. L. Goulden, G. Bonan, A. Cescatti, J. Chen, R. de Jeu, A. J. Dolman, W. Eugster, D. Gerten, D. Gianelle, N. Gobron, J. Heinke, J. Kimball, B. E. Law, L. Montagnani, Q. Mu, B. Mueller, K. Oleson, D. Papale, A. D. Richardson, O. Roupsard, S. Running, E. Tomelleri, N. Viovy, U. Weber, C. Williams, E. Wood, S. Zaehle, and K. Zhang (2010), Recent decline in the global land evapotranspiration trend due to limited moisture supply, *Nature*, *467*(7318), 951–954, doi:10.1038/nature09396.

Kalnay, E., M. Kanamitsu, R. Kistler, W. Collins, D. Deaven, L. Gandin, M. Iredell, S. Saha, G. White, J. Woollen, Y. Zhu, M. Chelliah, W. Ebisuzaki, W. Higgins, J. Janowiak, K. C. Mo, C. Ropelewski, J. Wang, A. Leetmaa, R. Reynolds, R. Jenne, and D. Joseph (1996), The NCEP/NCAR 40-year reanalysis project, *Bulletin of the American Meteorological Society*, *77*(3), 437–471.

Kao, H. Y., and J. Y. Yu (2009), Contrasting Eastern-Pacific and Central-Pacific types of ENSO, *Journal of Climate*, *22*(3), 615–632, doi:10.1175/2008JCLI2309.1.

Kawai, Y., and H. Kawamura (2002), Evaluation of the diurnal warming of sea surface temperature using satellite-derived marine meteorological data, *Journal of Oceanography*, *58*(6), 805–814, doi:10.1023/A:1022867028876.

Kawai, Y., and A. Wada (2007), Diurnal sea surface temperature variation and its impact on the atmosphere and ocean: A review, *Journal of Oceanography*, *63*(5), 721–744, doi:10.1007/s10872-007-0063-0.

Kim, H.-M., Webster Peter J., and J. A. Curry (2009), Impact of Shifting Patterns of Pacific Ocean Warming on North Atlantic Tropical Cyclones, *Science*, *325*(5936), 77–80, doi:10.1126/science.1174062.

Kirtman, B., S. B. Power, J. A. Adedoyin, G. J. Boer, R. Bojariu, I. Camilloni, F. J. Doblas-Reyes, A. M. Fiore, M. Kimoto, G. A. Meehl, M. Prather, A. Sarr, C. SchaÌĹr, R. Sutton, G. J. van Oldenborgh, G. Vecchi, and H. J. Wang (2013), *Near-term Climate Change: Projections and Predictability*, book section 11, pp. 953–1028, Cambridge University Press, Cambridge, United Kingdom and New York, NY, USA, doi:10.1017/CBO9781107415324.023.

Kistler, R., E. Kalnay, W. Collins, S. Saha, G. White, J. Woollen, M. Chelliah, W. Ebisuzaki, M. Kanamitsu, V. Kousky, H. Van Den Dool, R. Jenne, and M. Fiorino (2001), The NCEP-NCAR 50-year reanalysis: Monthly means CD-ROM and documentation, *Bulletin of the American Meteorological Society*, *82*(2), 247–267.

Klepp, C., K. Bumke, S. Bakan, and P. Bauer (2010), Ground validation of oceanic snowfall detection in satellite climatologies during LOFZY, *Tellus, Series A: Dynamic Meteorology and Oceanography*, *62*(4), 469–480, doi:10.1111/j.1600-0870.2010.00459.x.

Knaff, J. A., and R. M. Zehr (2007), Reexamination of tropical cyclone wind-pressure relationships, *Bulletin of the American Meteorological Society*, *88*(3), 71–88, doi:10.1175/WAF965.1.

Knaff, J. a., C. R. Sampson, M. DeMaria, T. P. Marchok, J. M. Gross, and C. J. McAdie (2007), Statistical Tropical Cyclone Wind Radii Prediction Using Climatology and Persistence, *Weather and Forecasting*, *22*(4), 781–791, doi:10.1175/WAF1026.1.

Knight, D. B., and R. E. Davis (2007), Climatology of Tropical Cyclone Rainfall in the Southeastern United States, *Physical Geography*, *28*(2), 126–147, doi:10.2747/0272-3646.28.2.126.

Knight, D. B., and R. E. Davis (2009), Contribution of tropical cyclones to extreme rainfall events in the southeastern United States, *Journal of Geophysical Research*, *114*(D23), 1–17, doi:10.1029/2009JD012511.

Knippertz, P., and H. Wernli (2010), A lagrangian climatology of tropical moisture exports to the northern hemispheric extratropics, *Journal of Climate*, *23*(4), 987–1003, doi:10.1175/2009JCLI3333.1.

Knippertz, P., H. Wernli, and G. Gläser (2013), A global climatology of tropical moisture exports, *Journal of Climate*, *26*(10), 3031–3045, doi:10.1175/JCLI-D-12-00401.1.

Kobayashi, S., Y. Ota, Y. Harada, A. Ebita, M. Moriya, H. Onoda, K. Onogi, H. Kamahori, C. Kobayashi, H. Endo, K. Miyaoka, and K. Takahashi (2015), The JRA-55 Reanalysis: General Specifications and Basic Characteristics, *Journal of the Meteorological Society of Japan. Ser. II*, *93*(1), 5–48, doi:10.2151/jmsj.2015-001.

Kohonen, T. (1990), The Self-Organizing Map, *Proceedings of the IEEE*, *78*(9), 1464–1480, doi:10.1109/5.58325.

Konrad, C. E., and L. B. Perry (2010), Relationships between tropical cyclones and heavy rainfall in the Carolina region of the USA, *International Journal of Climatology*, *30*(4), 522–534, doi:10.1002/joc.1894.

Konrad, C. E., M. F. Meaux, and D. A. Meaux (2002), Relationships between tropical cyclone attributes and precipitation totals: Considerations of scale, *International Journal of Climatology*, *22*(2), 237–247, doi:10.1002/joc.721.

Koster, R. D., P. A. Dirmeyer, Z. Guo, G. Bonan, E. Chan, P. Cox, C. T. Gordon, S. Kanae, E. Kowalczyk, D. Lawrence, P. Liu, C.-H. Lu, S. Malyshev, B. McAvaney, K. Mitchell, D. Mocko, T. Oki, K. Oleson, A. Pitman, Y. C. Sud, C. M. Taylor, D. Verseghy, R. Vasic, Y. Xue, and T. Yamada (2004), Regions of Strong Coupling Between Soil Moisture and Precipitation, *Science*, *305*(5687), 1138–1140, doi:10.1126/science.1100217.

Kug, J. S., F. F. Jin, and S. I. An (2009), Two types of El Niño events: Cold

tongue El Niño and warm pool El Niño, *Journal of Climate*, *22*(6), 1499–1515, doi:10.1175/2008JCLI2624.1.

Kumar, A., L. Zhang, and W. Wang (2013), Sea Surface TemperatureâĂŞPrecipitation Relationship in Different Reanalyses, *Monthly Weather Review*, *141*(3), 1118–1123, doi:10.1175/MWR-D-12-00214.1.

Kumar, B. P., J. Vialard, M. Lengaigne, V. S. N. Murty, and M. J. McPhaden (2012), TropFlux: Air-sea fluxes for the global tropical oceans-description and evaluation, *Climate Dynamics*, *38*(7-8), 1521–1543, doi:10.1007/s00382-011-1115-0.

Landsea, C. W., and J. L. Franklin (2013), Atlantic Hurricane Database Uncertainty and Presentation of a New Database Format, *Monthly Weather Review*, *141*(10), 3576–3592, doi:10.1175/MWR-D-12-00254.1.

Larkin, N. K. (2005a), Global seasonal temperature and precipitation anomalies during El Niño autumn and winter, *Geophysical Research Letters*, *32*(16), L16,705, doi:10.1029/2005GL022860.

Larkin, N. K. (2005b), On the definition of El Niño and associated seasonal average U.S. weather anomalies, *Geophysical Research Letters*, *32*(13), L13,705, doi:10.1029/2005GL022738.

Larson, J., Y. Zhou, and R. W. Higgins (2005), Characteristics of landfalling tropical cyclones in the United States and Mexico: Climatology and interannual variability, *Journal of Climate*, *18*(8), 1247–1262, doi:10.1175/JCLI3317.1.

Lau, K. M., Y. P. Zhou, and H. T. Wu (2008), Have tropical cyclones been feeding more extreme rainfall?, *Journal of Geophysical Research Atmospheres*, *113*(23), 1–12, doi:10.1029/2008JD009963.

Lee, D. E., and M. Biasutti (2014), Climatology and variability of precipitation in the Twentieth-Century Reanalysis, *Journal of Climate*, *27*(15), 5964–5981, doi:10.1175/JCLI-D-13-00630.1.

Legates, D. R. (1987), A climatology of global precipitation, *Publ. Climatol.*, *40*(1), 86 pp.

Levermann, A., J. Schewe, V. Petoukhov, and H. Held (2009), Basic mechanism for abrupt monsoon transitions., *Proceedings of the National Academy of Sciences of the United States of America*, *106*(49), 20,572–20,577, doi:10.1073/pnas.0901414106.

Levinson, D. H., K. R. Knapp, M. C. Kruk, J. H. Howard, and J. P. Kossin (2010), The International Best Track Archive for Climate Stewardship (IBTrACS) project: Overview of methods and Indian ocean statistics, *Indian Ocean Tropical Cyclones and Climate Change*, *91*(3), 215–221, doi:10.1007/978-90-481-3109-9{_}26.

Lindzen, R. (1967), Thermally driven diurnal tide in the atmosphere, *Quarterly Journal of the Royal Meteorological*, *93*(395), 18–42, doi:10.1002/qj.49709339503.

Liu, C., R. P. Allan, P. Berrisford, M. Mayer, P. Hyder, N. Loeb, D. Smith, P. L. Vidale, and J. M. Edwards (2015), Combining satellite observations and reanalysis energy transports to estimate global net surface energy fluxes 1985-2012, *Journal of Geophysical Research: Atmospheres*, *120*(18), 9374–9389, doi:10.1002/2015JD023264.

Liu, K. S., and J. C. L. Chan (1999), Size of Tropical Cyclones as Inferred from ERS-1 and ERS-2 Data, *Monthly Weather Review*, *127*(12), 2992–3001.

Liu, Y., R. H. Weisberg, and C. N. K. Mooers (2006), Performance evaluation of the self-organizing map for feature extraction, *Journal of Geophysical Research: Oceans*, *111*(5), C05,018, doi:10.1029/2005JC003117.

Lorenz, C., and H. Kunstmann (2012), The hydrological cycle in three state-of-the-art reanalyses: Intercomparison and performance analysis, *Journal of Hydrometeorology*, *13*(5), 1397–1420, doi:10.1175/JHM-D-11-088.1.

Mantua, N. J., S. R. Hare, Y. Zhang, J. M. Wallace, and R. C. Francis (1997), A Pacific Interdecadal Climate Oscillation with Impacts on Salmon Production, *Bulletin of the American Meteorological Society*, *78*(6), 1069–1079.

Matthews, A. J., D. B. Baranowski, K. J. Heywood, P. J. Flatau, and S. Schmidtko (2014), The surface diurnal warm layer in the Indian ocean during CINDY/DYNAMO, *Journal of Climate*, *27*(24), 9101–9122, doi:10.1175/JCLI-D-14-00222.1.

Maxwell, J. T., P. T. Soulé, J. T. Ortegren, and P. a. Knapp (2012), Drought-Busting Tropical Cyclones in the Southeastern Atlantic United States: 1950-2008, *Annals of the Association of American Geographers*, *102*(2), 259–275, doi:10.1080/00045608.2011.596377.

McGarry, M. M., and R. J. Reed (1978), Diurnal Variations in Convective Activity and Precipitation During Phases II and III of GATE, *Monthly Weather Review*, *106*(1), 101–113.

Merrill, R. T. (1984), A Comparison of Large and Small Tropical Cyclones, *Monthly Weather Review*, *112*(7), 1408–1418.

Mitas, C. M., and A. Clement (2005), Has the Hadley cell been strengthening in recent decades?, *Geophysical Research Letters*, *32*(3), 1–5, doi:10.1029/2004GL021765.

Mitas, C. M., and A. Clement (2006), Recent behavior of the Hadley cell and tropical thermodynamics in climate models and reanalyses, *Geophysical Research Letters*, *33*(1), L01,810, doi:10.1029/2005GL024406.

Mo, K. C., and R. W. Higgins (1996), Large-scale atmospheric moisture transport

as evaluated in the NCEP/NCAR and the NASA/DAO reanalyses, *Journal of Climate*, *9*(7), 1531–1545.

Mueller, B., S. I. Seneviratne, C. Jimenez, T. Corti, M. Hirschi, G. Balsamo, P. Ciais, P. Dirmeyer, J. B. Fisher, Z. Guo, M. Jung, F. Maignan, M. F. McCabe, R. Reichle, M. Reichstein, M. Rodell, J. Sheffield, A. J. Teuling, K. Wang, E. F. Wood, and Y. Zhang (2011), Evaluation of global observations-based evapotranspiration datasets and IPCC AR4 simulations, *Geophysical Research Letters*, *38*(6), L06,402, doi:10.1029/2010GL046230.

Mueller, B., M. Hirschi, C. Jimenez, P. Ciais, P. A. Dirmeyer, A. J. Dolman, J. B. Fisher, M. Jung, F. Ludwig, F. Maignan, D. G. Miralles, M. F. McCabe, M. Reichstein, J. Sheffield, K. Wang, E. F. Wood, Y. Zhang, and S. I. Seneviratne (2013), Benchmark products for land evapotranspiration: LandFlux-EVAL multi-data set synthesis, *Hydrology and Earth System Sciences*, *17*(10), 3707–3720, doi:10.5194/hess-17-3707-2013.

Muller, C. J., and P. a. O'Gorman (2011), An energetic perspective on the regional response of precipitation to climate change, *Nature Climate Change*, *1*(8), 266–271, doi:10.1038/nclimate1169.

National Research Council (2009), *Observing Weather and Climate from the Ground Up: A Nationwide Network of Networks*, The National Academies Press, Washington, DC.

New, M., M. Hulme, and P. Jones (1999), Representing Twentieth-Century Space âĂŞ Time Climate Variability . Part I : Development of a 1961-90 Mean Monthly Terrestrial Climatology, *Journal of Climate*, *12*(3), 829–856.

New, M., D. Lister, M. Hulme, and I. Makin (2002), A high-resolution data set of surface climate over global land areas, *Climate Research*, *21*(1), 1–25, doi:10.3354/cr021001.

Nogueira, R. C., and B. D. Keim (2011), Contributions of Atlantic tropical cyclones to monthly and seasonal rainfall in the eastern United States 1960-2007, *Theoretical and Applied Climatology*, *103*(1), 213–227, doi:10.1007/s00704-010-0292-9.

Oort, A. H., and J. J. Yienger (1996), Observed interannual variability in the Hadley circulation and its connection to ENSO, *Journal of Climate*, *9*(11), 2751–2767.

Pan, M., A. K. Sahoo, T. J. Troy, R. K. Vinukollu, J. Sheffield, and E. F. Wood (2012), Multisource Estimation of Long-Term Terrestrial Water Budget for Major Global River Basins, *Journal of Climate*, *25*(9), 3191–3206, doi:10.1175/JCLI-D-11-00300.1.

Parker, J., S. Longmuir, and W. Stoll (2000), Closing the water cycle, *Water*, *27*(1), 35–36.

Peel, M. C., B. L. Finlayson, and T. A. McMahon (2006), Updated world map of

the K ÌĹoppen-Geiger climate classification, *Meteorologische Zeitschrift*, *15*(3), 259–263, doi:10.1127/0941-2948/2006/0130.

Pepin, N. C., and J. D. Lundquist (2008), Temperature trends at high elevations: Patterns across the globe, *Geophysical Research Letters*, *35*(14), L14,701, doi:10.1029/2008GL034026.

Pielke, R. A., and C. N. Landsea (1999), La Niña, El Niño and Atlantic Hurricane Damages in the United States, *Bulletin of the American Meteorological Society*, *80*(10), 2027–2033.

Power, S., T. Casey, C. Folland, A. Colman, and V. Mehta (1999), Inter-decadal modulation of the impact of ENSO on Australia, *Climate Dynamics*, *15*(5), 319–324, doi:10.1007/s003820050284.

Prat, O. P., and B. R. Nelson (2013), Precipitation contribution of tropical cyclones in the southeastern united states from 1998 to 2009 using TRMM satellite data, *Journal of Climate*, *26*(3), 1047–1062, doi:10.1175/JCLI-D-11-00736.1.

Prat, O. P., and B. R. Nelson (2014), Characteristics of annual, seasonal, and diurnal precipitation in the Southeastern United States derived from long-term remotely sensed data, *Atmospheric Research*, *144*, 4–20, doi:10.1016/j.atmosres.2013.07.022.

Price, J. F., R. A. Weller, C. M. Bowers, and M. G. Briscoe (1987), Diurnal response of sea surface temperature observed at the long-term upper ocean study (34N, 70W) in the Sargasso Sea, *Journal of Geophysical Research*, *92*(C13), 14,480, doi:10.1029/JC092iC13p14480.

Price, J. F., T. B. Sanford, and G. Z. Forristall (1994), Forced Stage Response to a Moving Hurricane, *Journal of Physical Oceanography*, *24*(2), 233–260.

Qian, T., A. Dai, K. E. Trenberth, and K. W. Oleson (2006), Simulation of Global Land Surface Conditions from 1948 to 2004. Part I: Forcing Data and Evaluations, *Journal of Hydrometeorology*, *7*(5), 953–975, doi:10.1175/JHM540.1.

Quan, X.-w., H. F. Diaz, and M. P. Hoerling (2004), Change of the Tropical Hadley Cell Since 1950, in *The Hadley Circulation: Present, Past and Future*, edited by H. Diaz and R. Bradley, pp. 85–120, Kluwer Academic Publishers, Dordrecht.

Ren, F., G. Wu, W. Dong, X. Wang, Y. Wang, W. Ai, and W. Li (2006), Changes in tropical cyclone precipitation over China, *Geophysical Research Letters*, *33*(20), L20,702, doi:10.1029/2006GL027951.

Ren, F., Y. Wang, X. Wang, and W. Li (2007), Estimating tropical cyclone precipitation from station observations, *Advances in Atmospheric Sciences*, *24*(4), 700–711, doi:10.1007/s00376-007-0700-y.

Reusch, D. B., R. B. Alley, and B. C. Hewitson (2007), North Atlantic climate

variability from a self-organizing map perspective, *Journal of Geophysical Research*, *112*(D2), 1–20, doi:10.1029/2006JD007460.

Roads, J. (2003), The NCEP-NCAR, NCEP-DOE, and TRMM Tropical Atmosphere Hydrologic Cycles, *Journal of Hydrometeorology*, *4*(5), 826–840.

Robertson, F. R., M. G. Bosilovich, J. Chen, and T. L. Miller (2011), The effect of satellite observing system changes on MERRA water and energy fluxes, *Journal of Climate*, *24*(20), 5197–5217, doi:10.1175/2011JCLI4227.1.

Rodell, M., H. K. Beaudoing, T. S. L'Ecuyer, W. S. Olson, J. S. Famiglietti, P. R. Houser, R. Adler, M. G. Bosilovich, C. A. Clayson, D. Chambers, E. Clark, E. J. Fetzer, X. Gao, G. Gu, K. Hilburn, G. J. Huffman, D. P. Lettenmaier, W. T. Liu, F. R. Robertson, C. A. Schlosser, J. Sheffield, and E. F. Wood (2015), The observed state of the water cycle in the early twenty-first century, *Journal of Climate*, *28*(21), 8289–8318, doi:10.1175/JCLI-D-14-00555.1.

Rodgers, E. B., R. F. Adler, and H. F. Pierce (2001), Contribution of Tropical Cyclones to the North Atlantic Climatological Rainfall as Observed from Satellites, *Journal of Applied Meteorology*, *40*(11), 1785–1800.

Rodríguez, J. M., T. C. Johns, R. B. Thorpe, and A. Wiltshire (2011), Using moisture conservation to evaluate oceanic surface freshwater fluxes in climate models, *Climate Dynamics*, *37*(1-2), 205–219, doi:10.1007/s00382-010-0899-7.

Roll, H. U. (1991), *Physics of the Marine Atmosphere*, *International Geophysics*, vol. 55, 305–308 pp., Academic Press, New York.

Ruane, A. C., and J. O. Roads (2007), 6-Hour to 1-year variance of five global precipitation sets, *Earth Interactions*, *11*(11), 1–29, doi:10.1175/EI225.1.

Santer, B. D. (2005), Amplification of Surface Temperature Trends and Variability in the Tropical Atmosphere, *Science*, *309*(5740), 1551–1556, doi:10.1126/science.1114867.

Schiller, a., and J. Godfrey (2003), Indian Ocean intraseasonal variability in an ocean general circulation model, *Journal of climate*, *16*(1999), 21–39.

Schiller, A., and J. S. Godfrey (2005), A diagnostic model of the diurnal cycle of sea surface temperature for use in coupled ocean-atmosphere models, *Journal of Geophysical Research: Oceans*, *110*(11), 1–9, doi:10.1029/2005JC002975.

Schumacher, R. S., and T. J. Galarneau (2012), Moisture Transport into Midlatitudes ahead of Recurving Tropical Cyclones and Its Relevance in Two Predecessor Rain Events, *Monthly Weather Review*, *140*(6), 1810–1827, doi:10.1175/MWR-D-11-00307.1.

Schwarz, G. (1978), Estimating the dimension of a model, *Ann. Statist.*, *6*(2), 461–464, doi:10.1214/aos/1176344136.

Seager, R., and N. Henderson (2013), Diagnostic computation of moisture

budgets in the ERA-interim reanalysis with reference to analysis of CMIP-archived atmospheric model data, *Journal of Climate*, *26*(20), 7876–7901, doi:10.1175/JCLI-D-13-00018.1.

Serreze, M. C., and R. G. Barry (2011), Processes and impacts of Arctic amplification: A research synthesis, *Global and Planetary Change*, *77*(1-2), 85–96, doi:10.1016/j.gloplacha.2011.03.004.

Shepherd, T. G. (2014), Atmospheric circulation as a source of uncertainty in climate change projections, *Nature Geoscience*, *7*(10), 703–708, doi:10.1038/ngeo2253.

Simmons, A. J., K. M. Willett, P. D. Jones, P. W. Thorne, and D. P. Dee (2010), Low-frequency variations in surface atmospheric humidity, temperature, and precipitation: Inferences from reanalyses and monthly gridded observational data sets, *Journal of Geophysical Research Atmospheres*, *115*(1), D01,110, doi:10.1029/2009JD012442.

Singh, A., T. Delcroix, and S. Cravatte (2011), Contrasting the flavors of El Niño-Southern Oscillation using sea surface salinity observations, *Journal of Geophysical Research: Oceans*, *116*(6), C06,016, doi:10.1029/2010JC006862.

Smith, S. R., J. Brolley, J. J. O'Brien, and C. A. Tartaglione (2007), ENSO's impact on regional U.S. hurricane activity, *Journal of Climate*, *20*(7), 1404–1414, doi:10.1175/JCLI4063.1.

Soden, B. J. (2000), The sensitivity of the tropical hydrological cycle to ENSO, *Journal of Climate*, *13*(3), 538–549.

Sohn, B. J., and S. C. Park (2010), Strengthened tropical circulations in past three decades inferred from water vapor transport, *Journal of Geophysical Research Atmospheres*, *115*(15), D15,112, doi:10.1029/2009JD013713.

Sontakke, N. A., G. B. Pant, and N. Singh (1993), Construction of all-india summer monsoon rainfall series for the period 1844âĂŞ1991, *Journal of Climate*, *6*(9), 1807–1811, doi:10.1175/1520-0442(1993)006<1807:COAISM>2.0.CO;2.

Stuart-Menteth, A. C. (2003), A global study of diurnal warming using satellite-derived sea surface temperature, *Journal of Geophysical Research*, *108*(C5), 3155, doi:10.1029/2002JC001534.

Su, H., and J. D. Neelin (2002), Teleconnection Mechanisms for Tropical Pacific Descent Anomalies during El Niño*, *Journal of the Atmospheric Sciences*, *59*(18), 2694–2712.

Sui, C.-H., K.-M. Lau, Y. N. Takayabu, and D. a. Short (1997), Diurnal Variations in Tropical Oceanic Cumulus Convection during TOGA COARE, *Journal of the Atmospheric Sciences*, *54*(5), 639–655.

Sverdrup, H., M. Johnson, and R. Fleming (1942), *The Oceans: Their Physics,*

Chemistry and General Biology, 1104 pp., Prentice-Hall, New York, doi:10.2307/210609.

Sykes, P., J. While, A. Sellar, and M. Martin (2011), Diurnal Variability in Sea Surface Temperature: Observation and model assessment, *Tech. Rep. June*, Met Office, Exeter.

Taylor, K. (2001), Summarizing multiple aspects of model performance in a single diagram, *Journal of Geophysical Research: Atmospheres*, *106*, 7183–7192.

Tian, B., B. J. Soden, and X. Wu (2004), Diurnal cycle of convection, clouds, and water vapor in the tropical upper troposphere: Satellites versus a general circulation model, *Journal of Geophysical Research D: Atmospheres*, *109*(10), 1–16, doi:10.1029/2003JD004117.

Trenberth, K. E. (1990), Recent Observed Interdecadal Climate Changes in the Northern Hemisphere, *Bulletin of the American Meteorological Society*, *71*(7), 988–993.

Trenberth, K. E. (1997a), Using Atmospheric Budgets as a Constraint on Surface Fluxes, *Journal of Climate*, *10*(11), 2796–2809.

Trenberth, K. E. (1997b), The Definition of El Niño, *Bulletin of the American Meteorological Society*, *78*(August), 2771–2777.

Trenberth, K. E. (2011), Changes in precipitation with climate change, *Climate Research*, *47*(1), 123–138, doi:10.3354/cr00953.

Trenberth, K. E., and C. J. Guillemot (1995), Evaluation of the Global Atmospheric Moisture Budget as Seen from Analyses, *Journal of Climate*, *8*(9), 2255–2272.

Trenberth, K. E., and C. J. Guillemot (1998), Evaluation of the atmospheric moisture and hydrological cycle in the NCEP/NCAR reanalyses, *Climate Dynamics*, *14*(3), 213–231, doi:10.1007/s003820050219.

Trenberth, K. E., and L. Smith (2006), The vertical structure of temperature in the tropics: Different flavors of El Niño., *Journal of climate*, *19*(2005), 4956–4970.

Trenberth, K. E., and D. P. Stepaniak (2001), Indices of El Niño Evolution, *Journal of Climate*, *14*(8), 1697–1701.

Trenberth, K. E., A. Dai, R. M. Rasmussen, and D. B. Parsons (2003), The Changing Character of Precipitation, *Bulletin of the American Meteorological Society*, *84*(9), 1205–1217, doi:10.1175/BAMS-84-9-1205.

Trenberth, K. E., L. Smith, T. Qian, A. Dai, and J. T. Fasullo (2007), Estimates of the Global Water Budget and Its Annual Cycle Using Observational and Model Data, *Journal of Hydrometeorology*, *8*(4), 758–769, doi:10.1175/JHM600.1.

Trenberth, K. E., J. T. Fasullo, and J. Kiehl (2009), Earth's Global Energy Budget,

Bulletin of the American Meteorological Society, *90*(3), 311–323, doi:10.1175/2008BAMS2634.1.

Trenberth, K. E., J. T. Fasullo, and J. Mackaro (2011), Atmospheric Moisture Transports from Ocean to Land and Global Energy Flows in Reanalyses, *Journal of Climate*, *24*(18), 4907–4924, doi:10.1175/2011JCLI4171.1.

Ueyama, R., and C. Deser (2008), A climatology of diurnal and semidiurnal surface wind variations over the tropical Pacific Ocean based on the tropical atmosphere ocean moored buoy array, *Journal of Climate*, *21*, 593–607, doi:10.1175/2007JCLI1666.1.

van der Ent, R. J., H. H. G. Savenije, B. Schaefli, and S. C. Steele-Dunne (2010), Origin and fate of atmospheric moisture over continents, *Water Resources Research*, *46*(9), W09,525, doi:10.1029/2010WR009127.

van der Schrier, G., J. Barichivich, K. R. Briffa, and P. D. Jones (2013), A scPDSI-based global data set of dry and wet spells for 1901-2009, *Journal of Geophysical Research: Atmospheres*, *118*(10), 4025–4048, doi:10.1002/jgrd.50355.

van der Wiel, K., A. J. Matthews, D. P. Stevens, and M. M. Joshi (2015), A dynamical framework for the origin of the diagonal south pacific and south atlantic convergence zones, *Quarterly Journal of the Royal Meteorological Society*, pp. 1997–2010, doi:10.1002/qj.2508.

Vaughan, D. G., J. C. Comiso, I. Allison, J. Carrasco, G. Kaser, R. Kwok, P. Mote, T. Murray, F. Paul, J. Ren, E. Rignot, O. Solomina, K. Steffen, and T. Zhang (2013), *Observations: Cryosphere*, book section 4, pp. 317–382, Cambridge University Press, Cambridge, United Kingdom and New York, NY, USA, doi:10.1017/CBO9781107415324.012.

Vecchi, G. a., and B. J. Soden (2007), Global Warming and the Weakening of the Tropical Circulation, *Journal of Climate*, *20*(17), 4316–4340, doi:10.1175/JCLI4258.1.

Vecchi, G. a., B. J. Soden, A. T. Wittenberg, I. M. Held, A. Leetmaa, and M. J. Harrison (2006), Weakening of tropical Pacific atmospheric circulation due to anthropogenic forcing., *Nature*, *441*(7089), 73–6, doi:10.1038/nature04744.

Verdon-Kidd, D. C., and A. S. Kiem (2009), On the relationship between large-scale climate modes and regional synoptic patterns that drive Victorian rainfall, *Hydrology and Earth System Sciences*, *13*(4), 467–479, doi:10.5194/hess-13-467-2009.

Verdon-Kidd, D. C., a. S. Kiem, and R. Moran (2014), Links between the big dry in Australia and hemispheric multi-decadal climate variability-implications for water resource management, *Hydrology and Earth System Sciences*, *18*(6), 2235–2256, doi:10.5194/hess-18-2235-2014.

Vinukollu, R. K., R. Meynadier, J. Sheffield, and E. F. Wood (2011), Multi-model, multi-sensor estimates of global evapotranspiration:

climatology, uncertainties and trends, *Hydrological Processes*, *25*(26), 3993–4010, doi:10.1002/hyp.8393.

Wang, C. (2002), Atmospheric Circulation Cells Associated with the El Niño-Southern Oscillation, *Journal of Climate*, *15*(4), 399–419.

Wang, H., and K. M. Lau (2006), Atmospheric hydrological cycle in the tropics in twentieth century coupled climate simulations, *International Journal of Climatology*, *26*(5), 655–678, doi:10.1002/joc.1279.

Wang, H., L. Long, A. Kumar, W. Wang, J.-K. E. Schemm, M. Zhao, G. A. Vecchi, T. E. Larow, Y.-K. Lim, S. D. Schubert, D. A. Shaevitz, S. J. Camargo, N. Henderson, D. Kim, J. A. Jonas, and K. J. E. Walsh (2014), How Well Do Global Climate Models Simulate the Variability of Atlantic Tropical Cyclones Associated with ENSO?, *Journal of Climate*, *27*(15), 5673–5692, doi:10.1175/JCLI-D-13-00625.1.

Wang, K., and R. E. Dickinson (2012), A review of global terrestrial evapotranspiration: Observation, modeling, climatology, and climatic variability, *Reviews of Geophysics*, *50*(2), 1–54, doi:10.1029/2011RG000373.

Weatherford, C. L., and W. M. Gray (1988), Typhoon structure as revealed by aircraft reconnaissance. Part I: data analysis and climatology, *Monthly Weather Review*, *116*, 1032–1043.

Webster, P. J., C. A. Clayson, and J. A. Curry (1996), Clouds, Radiation, and the Diurnal Cycle of Sea Surface Temperature in the Tropical Western Pacific, *Journal of Climate*, *9*(8), 1712–1730.

Wielicki, B. a., T. Wong, R. P. Allan, A. Slingo, J. T. Kiehl, B. J. Soden, C. T. Gordon, A. J. Miller, S.-K. Yang, D. a. Randall, F. Robertson, J. Susskind, and H. Jacobowitz (2002), Evidence for large decadal variability in the tropical mean radiative energy budget., *Science (New York, N.Y.)*, *295*(5556), 841–844, doi:10.1126/science.1065837.

Wilks, D. S. (2011), *Statistical methods in the atmospheric sciences*, vol. 100, Academic press.

Xie, P., and P. A. Arkin (1997), Global Precipitation : A 17-Year Monthly Analysis Based on Gauge Observations , Satellite Estimates , and Numerical Model Outputs, *Bulletin of the American Meteorological Society*, *78*(11), 2539–2558.

Xu, G., T. J. Osborn, A. J. Matthews, and M. M. Joshi (2015), Different atmospheric moisture divergence responses to extreme and moderate El Niños, *Climate Dynamics*, doi:10.1007/s00382-015-2844-2.

Xu, J., and J. Chan (2001), The role of the Asian-Australian monsoon system in the onset time of El Niño events., *Journal of climate*, *14*, 418–433.

Yang, G., and J. Slingo (2001), The diurnal cycle in the tropics, *Monthly Weather Review*, *129*, 784–801.

Yin, X., A. Gruber, and P. Arkin (2004), Comparison of the GPCP and CMAP Merged Gauge-Satellite Monthly Precipitation Products for the Period 1979-2001, *Journal of Hydrometeorology*, *5*(6), 1207–1222, doi:10.1175/JHM-392.1.

Yokoyama, R., and M. Konda (1996), Sea surface effects on the sea surface temperature estimation by remote sensing-Part 2, *International Journal of Remote Sensing*, *17*(7), 1293–1302, doi:10.1080/01431169608948704.

Yu, J.-Y., and H.-Y. Kao (2007), Decadal changes of ENSO persistence barrier in SST and ocean heat content indices: 1958-2001, *Journal of Geophysical Research*, *112*(D13), D13,106, doi:10.1029/2006JD007654.

Yu, L., X. Jin, and R. A. Weller (2008), Multidecade Global Flux Datasets from the Objectively Analyzed Air-sea Fluxes (OAFlux) Project: Latent and Sensible Heat Fluxes, Ocean Evaporation, and Related Surface Meteorological Variables.

Zahn, M., and R. P. Allan (2011), Changes in water vapor transports of the ascending branch of the tropical circulation, *Journal of Geophysical Research*, *116*(D18), D18,111, doi:10.1029/2011JD016206.

Zeng, X., and R. E. Dickinson (1998), Impact of diurnally-varying skin temperature on surface fluxes over the tropical Pacific, *Geophysical Research Letters*, *25*(9), 1411–1414, doi:10.1029/98GL51097.

Zhang, K., J. S. Kimball, R. R. Nemani, and S. W. Running (2010), A continuous satellite-derived global record of land surface evapotranspiration from 1983 to 2006, *Water Resources Research*, *46*(9), 1–21, doi:10.1029/2009WR008800.

Zhang, M., and H. Song (2006), Evidence of deceleration of atmospheric vertical overturning circulation over the tropical Pacific, *Geophysical Research Letters*, *33*(12), L12,701, doi:10.1029/2006GL025942.